

**Fast 3D Inhomogeneous Radiative Transfer Model  
Incorporating Aspherical Frozen Hydrometeors with  
Application to Precipitation Locking**

by

**Kun Zhang**

B.S., Beijing University of Aeronautics and Astronautics,

Beijing, China, 1997

M.S., University of Florida, Gainesville, Florida, U.S.A., 2000

A thesis submitted to the  
Faculty of the Graduate School of the  
University of Colorado in partial fulfillment  
of the requirements for the degree of  
Doctor of Philosophy  
Department of Electrical, Computer, and Energy Engineering

2019

This thesis entitled:  
Fast 3D Inhomogeneous Radiative Transfer Model Incorporating Aspherical Frozen Hydrometeors  
with Application to Precipitation Locking  
written by Kun Zhang  
has been approved for the Department of Electrical, Computer, and Energy Engineering

---

Prof. Albin J. Gasiewski

---

Prof. Dejan Filipovic

---

Prof. Julie Lundquist

---

Dr. Alexander Voronovich

---

Dr. Kwo-Sen Kuo

Date \_\_\_\_\_

The final copy of this thesis has been examined by the signatories, and we find that both the content and the form meet acceptable presentation standards of scholarly work in the above mentioned discipline.

Zhang, Kun (Ph.D., Electrical Engineering with Expertise in Remote Sensing)

Fast 3D Inhomogeneous Radiative Transfer Model Incorporating Aspherical Frozen Hydrometeors  
with Application to Precipitation Locking

Thesis directed by Prof. Albin J. Gasiewski

A horizontally inhomogeneous unified microwave radiative transfer (HI-UMRT) model incorporating aspherical frozen hydrometeors based on the NASA/GSFC OpenSSP database is presented to study 3-dimensional (3D) effects of horizontal inhomogeneous clouds on computed microwave radiances and facilitate satellite radiance assimilation over horizontally inhomogeneous weather conditions. HI-UMRT provides a coupled two-Stokes parameter numerical radiance solution of the 3D radiative transfer equation by embedding the existing 1D UMRT algorithm into an iterative perturbation scheme. The horizontal derivatives in radiances of lower perturbation order are treated as the source functions of the azimuthal harmonic perturbation radiative transfer equations that are readily solved by the planar-stratified 1D UMRT algorithm.

The 1D UMRT algorithm requires symmetry of the transition matrix for the discretized planar-stratified radiative transfer equation to realize numerically stable and accurate matrix operations as required by the discrete-ordinate eigenanalysis method. In this thesis, the necessary block-diagonal structure of the full Stokes matrix for randomly oriented OpenSSP aspherical hydrometeors is shown to be maintained, albeit with small asymmetric deviations which introduce small asymmetric components into the transition matrix that are negligible for most passive microwave remote sensing applications. An upper bound of the brightness temperature error calculated by neglecting the asymmetric components of the transition matrix under even extreme atmospheric conditions is shown to be small. Hence the OpenSSP hydrometeor database can be reliably used within the UMRT model.

Block-diagonal Stokes matrix elements along with other single-scattering parameters of OpenSSP hydrometeors were subsequently used in radiative simulations of multi-stream dual-

polarization radiances for a simulated hurricane event to demonstrate the inherent numerical stability and utility of the extended 1D UMRT algorithm. An intercomparison of computed upwelling radiances for a multiphase distribution of aspherical OpenSSP hydrometeors versus a mass-equivalent Mie hydrometeor polydispersion for key sensing frequencies from 10 to 874 GHz shows the considerable impact of complex (versus simple spherical) hydrometeors on predicted microwave radiances.

Further, a numerical performance assessment shows that the increase in computing time for the 3D HI-UMRT model relative to the 1D UMRT model is moderate since (i) the computationally efficient UMRT engine is applied only to the perturbation equations with non-trivial solutions, and (ii) the layer parameters for the 1D solution are reused for all higher perturbation orders. Numerical simulations using HI-UMRT based on 3D cloud profiles simulated by the WRF numerical weather model illustrate the convergence of the iterative perturbation series. An intercomparison of top-of-atmosphere brightness temperature images for HI-UMRT versus the planar-stratified UMRT model illustrates the considerable impact of cloud horizontal inhomogeneities on computed upwelling microwave radiances.

The microwave radiances simulated using UMRT at 118 and 183 GHz based on the Orbital Micro Systems Inc. Global Earth Monitoring System (GEMS) CubeSat constellation concept have been used in an all-weather microwave data assimilation scheme to facilitate precipitation locking of hydrometeor state variables in severe weather. The capability of first frame precipitation locking can be achieved based on constrained extended Kalman filtering (XKF), statistical estimation of a flow-dependent background error covariance matrix, and appropriate update of state variables using nonlinear iterative method. Preliminary simulation results demonstrate the potential for assimilating both thermodynamic and hydrometeor variables in first-frame locking iterations.

To my wife, Lily

To my parents

To my sons, Joshua and Noah

## Acknowledgements

First I would like to express my sincere gratitude to Professor Albin J. Gasiewski for serving as my Ph.D. advisor, and for his continuous support and guidance throughout my tenure as a Ph.D. graduate student at University of Colorado at Boulder. He graciously shared with me his immense knowledge, rich experience and rigorous approach in the research field of remote sensing. His innovative research ideas in succinct passages gave me confidence in achieving the goals of my Ph.D. graduate research. I also really appreciated he offered me opportunities in teaching courses and instructing graduate students. Such an intensive training equipped me for my future academic career.

Second, I would like to thank Professors Dejan Filipovic and Julie Lundquist, Drs. Alexander Voronovich and Kwo-Sen Kuo for serving on my Ph.D. Dissertation Committee, for their insightful comments and encouragement. I am grateful to Dr. Kwo-Sen Kuo for providing access to the NASA/GSFC OpenSSP database and helpful discussions. His valuable suggestions and careful review for my research paper are really appreciated. Special thanks must also be given to Professor Julie Lundquist for useful suggestions about technical writing and bibliographic management. I also thank Dr. Gail Skofronick Jackson and Dr. Andrew Heymsfield for many constructive comments.

I am also grateful to Drs. Ke Chen and Jiaying He for helpful discussions concerning my research based on their professional remote sensing background during their visit to the Center for Environmental Technology (CET). I will miss the company and conversation of my colleagues and friends at CET, including Omkar Pradhan, Eryan Dai, Lavanya Periasamy, David Kraft and Michael Hurowitz.

Last but not the least, I would like to thank my family, my parents Shoukang Zhang and Sujun Zuo for their unfailing love and encouragement in my life, and my parents-in-law Bingyun Zhang and Danliang Zhu for their daily care about me. I especially would like to express my gratitude to my dear wife Min Lily Zhu for supporting me spiritually and caring for me in every possible way to see the completion of this work.

In addition, my work used the RMACC Summit supercomputer, which is supported by the National Science Foundation, the University of Colorado Boulder, and Colorado State University. Financial support from the NASA grant NNX15AQ24G is also acknowledged.

## Contents

<b>Chapter</b>		
<b>1</b>	Introduction	<b>1</b>
<b>2</b>	Microwave Single-Scattering Parameters of Atmospheric Hydrometeors	<b>10</b>
2.1	Simple Mie Spheres . . . . .	12
2.2	Complex Aspherical Hydrometeors . . . . .	14
2.2.1	Database of Geometrically Symmetric Frozen Hydrometeors . . . . .	15
2.2.2	OpenSSP Database of Ice and Snow Particles with Asymmetric Geometry . .	16
2.3	Extension of Scattering Parameters for Selected OpenSSP Hydrometeors . . . . .	17
2.3.1	Discrete Dipole Approximation Code (DDSCAT v7.3.1) . . . . .	19
2.3.2	Full Stokes Matrix of Randomly-Oriented OpenSSP Hydrometeors . . . . .	20
2.3.3	Scalar Radiative Efficiencies of Randomly-Oriented OpenSSP Hydrometeors .	23
<b>3</b>	The Planar-Stratified 1D UMRT Model Incorporating Aspherical Hydrometeors	<b>26</b>
3.1	Planar-Stratified Radiative Transfer Model . . . . .	27
3.1.1	Radiative Transfer Equation . . . . .	27
3.1.2	The Unified Microwave Radiative Transfer (UMRT) Model . . . . .	28
3.1.3	Generic Method of Incorporation Aspherical Hydrometeors into RT Model . .	30
3.2	UMRT Transition Matrix Symmetry . . . . .	32
3.2.1	Requirements of Transition Matrix Symmetry . . . . .	35
3.2.2	Transition Matrix Symmetry Based on OpenSSP Hydrometeors . . . . .	36



3.2.3	Theoretical Analysis of Transition Matrix Perturbation . . . . .	38
3.3	Incorporation of OpenSSP Aspherical Hydrometeors . . . . .	42
3.3.1	Gamma Function Distribution of Particle Size . . . . .	43
3.3.2	Conservation of Mass in WRF-based Simulations . . . . .	45
3.3.3	Maximum Entropy Principle for Ice Habit Probabilities Estimation . . . . .	45
3.4	Analysis of Dual-Polarized Microwave Radiances using 1D UMRT . . . . .	48
3.5	Analysis of Multi-stream Microwave Radiances using 1D UMRT . . . . .	52
<b>4</b>	<b>Fast 3D Inhomogeneous Radiative Transfer Model</b>	<b>55</b>
4.1	Review of Existing 3D Radiative Transfer Models . . . . .	55
4.2	Horizontal Perturbation Series . . . . .	57
4.2.1	Iterative Perturbation Scheme . . . . .	57
4.2.2	Perturbation Source Analysis . . . . .	63
4.3	HI-UMRT Numerical Solution . . . . .	66
4.3.1	Angular Discretization of the Radiative Transfer Equations . . . . .	66
4.3.2	Solution for 3D Spatially Inhomogeneous Sparse Media . . . . .	69
4.3.3	Convergence Criterion . . . . .	73
<b>5</b>	<b>Simulations of Microwave Radiances using 3D HI-UMRT Model</b>	<b>75</b>
5.1	Convergent Perturbation Series . . . . .	76
5.2	Azimuthally Dependent 3D Radiation Effects . . . . .	78
<b>6</b>	<b>Microwave Radiances Assimilation Scheme: Precipitation Locking</b>	<b>82</b>
6.1	Precipitation Locking Concept . . . . .	83
6.2	Simulations of High-temporal Resolution Observations . . . . .	84
6.3	First-Frame Locking . . . . .	90
6.3.1	Primary Goals . . . . .	90
6.3.2	Assimilation Method: Extended Kalman Filtering . . . . .	95

6.3.3	Background Error Covariance Modeling . . . . .	97
6.3.4	Constrained Extended Kalman Filtering . . . . .	101
6.3.5	Preliminary Results . . . . .	105
6.4	Suggested Future Research on Precipitation Locking . . . . .	111
<b>7</b>	<b>Conclusions</b>	<b>118</b>
	<b>Bibliography</b>	<b>121</b>
	<b>Appendix</b>	
<b>A</b>	<b>Example Input Files for DDSCAT v7.3.1</b>	<b>132</b>
<b>B</b>	<b>Transition Matrix Symmetry Induced by Block-diagonal Stokes Matrix</b>	<b>134</b>
<b>C</b>	<b>Small Valued Asymmetric Components of the OpenSSP Stokes Matrix</b>	<b>137</b>
<b>D</b>	<b>Calculations of Atmospheric Prognostic Variables Based on WRF Simulations</b>	<b>142</b>

## Tables

### Table

2.1	List of frequencies included in this study. . . . .	18
2.2	Selected snow aggregates (ap-) and ice pristine crystals (p-) with varying range of maximum diameters $D_{\max}$ . An interdipole distance of $\sim 50 \mu\text{m}$ is used for frequencies below 200 GHz and $\sim 17 \mu\text{m}$ for 300 GHz up to 874 GHz in DDSCAT v7.3.1. . . . .	19
5.1	Evolution of 3D HI-UMRT originating from 1D discrete-ordinate tangent linear RT (DOTLRT) model [127] . . . . .	81
6.1	List of frequencies used for the precipitation locking study. . . . .	92

## Figures

### Figure

- |     |  |    |
|-----|--|----|
| 1.1 | Precipitation locking simulation system under development at Center for Environmental Technology (CET) at University of Colorado at Boulder. . . . .   | 2  |
| 2.1 | Population of aspherical frozen hydrometeor habits and sizes in the current (ca. 2018) OpenSSP database. . . . .   | 17 |
| 2.2 | Random orientation-averaged Stokes matrix elements $\langle L_{vv} \rangle_o$ and $\langle L_{hh} \rangle_o$ compared with $L_{vv}$ and $L_{hh}$ of mass-equivalent spherical ice particle respectively as a function of forward scattering angle $\Theta$ at 659.8 GHz for: (a) aggregates of classic dendrites (ap-14) with $D_{\max} = 2002 \mu\text{m}$ versus ice spheres of $902 \mu\text{m}$ in diameter, (b) aggregates of dendrites with broadening arms (ap-19) with $D_{\max} = 1810 \mu\text{m}$ versus ice spheres of $751 \mu\text{m}$ in diameter, (c) aggregates of needles (ap-29) with $D_{\max} = 1645 \mu\text{m}$ versus ice spheres of $648 \mu\text{m}$ in diameter and (d) aggregates of sandwich plates (ap-43) with $D_{\max} = 1951 \mu\text{m}$ versus ice spheres of $757 \mu\text{m}$ in diameter. . . . . | 21 |
| 2.3 | Similar to Figure 2.2, but for four habits of ice pristine crystals at 659.8 GHz, (a) classic dendrites (p-14) with $D_{\max} = 354 \mu\text{m}$ versus ice spheres of $267 \mu\text{m}$ in diameter, (b) dendrites with broadening arms (p-19) with $D_{\max} = 403 \mu\text{m}$ versus ice spheres of $278 \mu\text{m}$ in diameter, (c) solid columns (p-31) with $D_{\max} = 353 \mu\text{m}$ versus ice spheres of $301 \mu\text{m}$ in diameter and (d) sandwich plates (p-43) with $D_{\max} = 403 \mu\text{m}$ versus ice spheres of $216 \mu\text{m}$ in diameter. . . . .  | 22 |

2.4	Random orientation-averaged single-scattering parameters of (a) extinction efficiency ( $Q_{\text{ext}}$ ), (b) absorption efficiency ( $Q_{\text{abs}}$ ), (c) scattering efficiency ( $Q_{\text{sca}}$ ), and (d) backscattering efficiency ( $Q_{\text{bk}}$ ) as a function of maximum diameter $D_{\text{max}}$ at 874 GHz for four habits of snow aggregates. These efficiencies are normalized by the hydrometeor effective area of an equal-volume sphere (see Equation 2.14). . . . .	23
2.5	Similar to Figure 2.4, but for four habits of ice pristine crystals, (a) extinction efficiency ( $Q_{\text{ext}}$ ), (b) absorption efficiency ( $Q_{\text{abs}}$ ), (c) scattering efficiency ( $Q_{\text{sca}}$ ), and (d) backscattering efficiency ( $Q_{\text{bk}}$ ). These efficiencies are normalized by the hydrometeor effective area of an equal-volume sphere (see Equation 2.14). . . . .	24
3.1	Calculation of the reduced phase matrix for spherical particle polydispersions. . . . .	30
3.2	Perturbation bound for a scalar function $\phi(z)$ used to determine relative errors of radiative transfer solutions introduced by asymmetric component of the transition matrix for OpenSSP snow aggregates. The perturbation bound varies with frequencies and snow particle types. . . . .	42
3.3	Simulations of dual-polarization brightness temperature imagery over hurricane Sandy at $53^\circ$ view, the conical scanning angle selected by multiple microwave satellite missions (e.g. ICI). Left column: Vertical polarization brightness temperatures $T_{\text{BV}}$ at 315.65, 321.65, 323.65, and 440.8 GHz, respectively. Middle column: Brightness temperature differences between vertical and horizontal polarization $\Delta T_{\text{B,V-H}}$ at the same respective frequencies to the left. Right column: Histogram of $\Delta T_{\text{B,V-H}}$ with mean and standard deviation. . . . .	49
3.4	Similar to Figure 3.3, but simulations at frequencies of 445.0, 446.6, 659.8, and 874 GHz. The $\Delta T_{\text{B,V-H}}$ histogram exhibits a strong peak at 2-3 Kelvin for the two highest frequencies. . . . .	50

3.5	Statistics of $\Delta T_{B,V-H}$ on top of hurricane Sandy across key microwave frequencies between 10 and 874 GHz. (a) The maximum (curve with square markers) and the mean (curve with error bars) in the presence of bulk aspherical hydrometeors. Both curves are consistent. The error bars indicate half of the standard deviations. (b) Comparison of the maximum $\Delta T_{B,V-H}$ between aspherical hydrometeors (solid line) and a mass-equivalent polydispersion of Mie spheres (dashed line). . . . .	51
3.6	Statistics of $\Delta T_{BV,Mie-DDA}$ for selected viewing angles at (a) 315.65 GHz, (b) 420.763 GHz, (c) 659.8 GHz, and (d) 874.0 GHz. The curves with square markers show maximum brightness temperature differences and the curves with error bars show the mean differences. Error bars indicate difference standard deviations. . . . .	53
3.7	Similar to Figure 3.6, but the maximum $\Delta T_{BV,Mie-DDA}$ is shown with respect to both key microwave remote sensing frequency from 10 to 874 GHz and discrete viewing angles between zenith and the horizon. . . . .	54
4.1	A flowchart of the HI-UMRT algorithm based on the existing 1D UMRT engine embedded within an iterative perturbation scheme. . . . .	62
4.2	HI-UMRT perturbation source diagram for illustration of non-trivial RT solutions under the assumption of a specular surface as the lower boundary condition required calculations exist only at non-trivial azimuthal harmonics of order $m$ and perturbation order $n$ . . . . .	64
4.3	Calculation of the azimuthal harmonic reflection and transmission operators $(\bar{r}_m, \bar{t}_m)$ , and the azimuthal harmonic perturbation self-radiation fields $(\bar{u}_{m,*}^{(n)}, \bar{v}_{m,*}^{(n)})$ for a horizontal inhomogeneous layer with thickness $h$ . . . . .	70

5.1	Relationship between the maximum perturbation correction and the perturbation order for upwelling brightness temperature simulations for hurricane Sandy at 166.31 GHz and 240.70 GHz. The maximum $T_B$ change with the 15 <sup>th</sup> order perturbation correction reaches the convergence threshold of 0.2 K. The solid curve for the perturbation corrections computed using HI-UMRT and the dashed curve for the predicted perturbation corrections. . . . .	77
5.2	Simulation of 3D radiative transfer through opaque and horizontally inhomogeneous clouds in a simulation domain over hurricane Sandy 2012 at 166.31 GHz. The angular variables of the radiative transfer equation are set to be $\theta = 50^\circ$ and $\phi = 45^\circ$ . (a) 1D UMRT top-of-atmosphere brightness temperature image obtained using HI-UMRT with $m = 0$ and $n = 0$ ; (b) 3D HI-UMRT brightness temperature image computed up to 15 <sup>th</sup> order perturbation corrections; (c) Difference between 3D and 1D radiative transfer solution (i.e. (b)-(a)). . . . .	78
5.3	Simulation of brightness temperature differences for the Sandy 2012 event between 3D and 1D radiative transfer solutions at four different azimuth angles: (a) $\phi = 0^\circ$ , (b) $\phi = 90^\circ$ , (c) $\phi = 180^\circ$ , (d) $\phi = 270^\circ$ . . . . .	80
6.1	Precipitation locking simulation system under development at Center for Environmental Technology (CET) at University of Colorado at Boulder. . . . .	84
6.2	Sub-hourly repeat times for a 36-satellite CubeSat constellation [44]. . . . .	86
6.3	Simulated rotated linear polarization antenna temperature images for four selected MiniRad channels: (a) 118.05 GHz, (b) 117.65 GHz, (c) 117.25 GHz, (d) 116.65 GHz. . . . .	87
6.4	Brightness temperature images computed within two hours at intervals of 30 minutes: (a) 01:15:00, (b) 01:45:00, (c) 02:15:00, (d) 02:45:00. . . . .	88
6.5	Innovations of 117.25 GHz channel. The observations were simulated based on two PolarCube or GEMS satellites flying over Hurricane Sandy at (a) October 29th, 00:45:00 and (b) October 29th, 01:15:00 on two different orbits. . . . .	89

6.6	Brightness temperature innovations of 12 selected channels at nadir viewing angle. (a)-(f) sounding channels offset to the 118.7503 GHz oxygen absorption line center, (g) window channel at 166.31 GHz, and (h)-(l) sounding channels offset to the 183.310 GHz water vapor absorption line center. . . . .	93
6.7	Comparisons of the state variable between the truth and forecast in a selected atmospheric column with the grid indexes ( $x = 175$ , $y = 128$ ) in the simulation domain: (a) temperature in Kelvin, (b) water vapor bulk density in $\text{g/m}^3$ , and (c)-(g) the bulk density of hydrometeor in $\text{g/m}^3$ of five microphysical phases. . . . .	94
6.8	Sample precipitation cell modes, e.g. stratified and convective modes in a 15-dimensional H-space for estimating the background error covariance matrix under flow-dependent conditions. . . . .	99
6.9	Cloud vertical profiles in NAM reanalyses classified into 20 clusters using the K-means algorithm based on the altitude-density model. . . . .	102
6.10	Schematic diagram of the background error covariance matrix for cloud hydrometeor variables at 32 vertical levels. Red squares on the diagonal represent variances and covariances among multivariate states in the same level. Black squares along the off-diagonal are variances and covariances between adjacent levels. The enlarged table illustrates variances and covariances of seven state variables at a given level: temperature $t$ , vapor density $v$ , cloud water density $c$ , rain droplet density $r$ , cloud ice density $i$ , snow density $s$ , and graupel density $g$ . . . . .	103
6.11	Schematic flowchart of constrained extended Kalman filtering used for iterative update for atmospheric state vectors. Modified from Skofronick-Jackson [112]. . . . .	106
6.12	Residual $T_B$ innovations of 12 selected channels at nadir viewing angle after 20 XKF iterates. (a)-(f) sounding channels offset to the 118.7503 GHz oxygen absorption line center, (g) window channel at 166.31 GHz, and (h)-(l) sounding channels offset to the 183.310 GHz water vapor absorption line center. . . . .	107



6.13	Statistics of the innovation variations with XKF iterations. Each figure shows mean, standard deviation, minimum and maximum value of the innovations over the entire testing scene for (a) - (l) sounding/imaging channels centered at 118.7503 GHz and 183.310 GHz. The standard deviation of residual $T_B$ innovations after 20 iterations is shown in each sub-figure title. . . . .	109
6.14	Comparisons of atmospheric state variables for thin clouds between the mean truth (line with stars), the mean first guess (line with triangles), and the 20 <sup>th</sup> iterate mean and STD profiles (line with error bars), (a) temperature in Kelvin, (b) water vapor bulk density in $\text{g}/\text{m}^3$ , (c)-(g) the bulk density of hydrometeor in $\text{g}/\text{m}^3$ of five microphysical phases. The minimum and maximum values of temperature and vapor density in the 20 <sup>th</sup> iterate are shown in (a) and (b). Only the minimum values of hydrometeor density in the 20 <sup>th</sup> iterate are included in (c)-(g) for good display. . . .	113
6.15	Similar to Figure 6.14, but comparisons of atmospheric state variables for thick clouds.	114
6.16	Prognostic variable errors at the 20 <sup>th</sup> iterate used for assessing the degree of precipitation locking, (a) mean temperature error evaluated from surface to 1 km height, (b) temperature error at 500 mb, (c) temperature error at 700 mb, (d) integrated vapor content error in $\text{kg}/\text{m}^2$ , (e) integrated cloud water path error in $\text{kg}/\text{m}^2$ , (f) integrated rain error in $\text{kg}/\text{m}^2$ , (g) integrated cloud ice path error in $\text{kg}/\text{m}^2$ , (h) integrated snow path error in $\text{kg}/\text{m}^2$ , (i) integrated graupel path error in $\text{kg}/\text{m}^2$ . . . . .	115
6.17	Statistics of prognostic variable errors changed during XKF iterate. Each figure shows the error mean, standard deviation, minimum and maximum values calculated using atmospheric profiles categorized as thin clouds. (a) mean temperature error evaluated from surface to 1 km height, (b) temperature error at 500 mb, (c) temperature error at 750 mb, (d) integrated vapor content error in $\text{g}/\text{m}^2$ , (e) integrated cloud water path error in $\text{g}/\text{m}^2$ , (f) integrated rain error in $\text{g}/\text{m}^2$ , (g) integrated cloud ice path error in $\text{g}/\text{m}^2$ , (h) integrated snow path error in $\text{g}/\text{m}^2$ , (i) integrated graupel path error in $\text{g}/\text{m}^2$ . . . . .	116

6.18	Similar to Figure 6.17 but for statistics of prognostic variable errors calculated using profiles of thick clouds. . . . .	117
B.1	Geometry of the scattering problem by a single aspherical particle with random orientations at origin. The incident wave propagates along $\hat{k}_i$ defined by $(\theta_i, \phi_i)$ and the scattered wave along $\hat{k}_s$ defined by $(\theta_s, \phi_s)$ is considered. The forward scattering angle $\Theta$ is defined in a scattering plane spanned by $\hat{k}_i$ and $\hat{k}_s$ . The polarization vectors of the incident and the scattered wave in the scattering plan are drawn in red arrows. . . . .	134
C.1	Scattering coordinate system wherein DDSCAT computes complex scattering function matrix. (a) Forward scattering angles $(\theta', \phi')$ and the particle orientation $(\beta', \Theta', \Phi')$ are redefined in a forward scattering coordinate system. (b) Transform of DDSCAT-based scattered electric fields (dashed arrows) into the required scattered components in vertical and horizontal polarization. . . . .	139
C.2	Mean fractional errors between the pairs of Stokes matrix elements with simultaneous permutation of angular and up-/down-welling indexes. . . . .	141
D.1	Horizontal and vertical grids of the WRF (known as the C grid) where thermodynamic and hydrometeor state variables $\theta_{ij}$ are defined at the center of the grid cell, and the components of winds $(U_{ij}, V_{ij}, W_{ij})$ are defined along the normal cell face. $\Delta x$ and $\Delta y$ are the east-west resolution and the north-south resolution of the grid (respectively). The vertical grid length $\Delta\eta$ is not a constant and is specified in the WRF model initialization. . . . .	142
D.2	Atmospheric state variables defined at the center of the WRF grid cell. (a) height in meters, (b) temperature in Kelvins, (c) pressure in mb, (d) relative humidity in %, (e) water vapor density in $g/m^3$ , and (f) hydrometeor bulk density in $g/m^3$ . . . . .	143

## Chapter 1

### Introduction

The National Research Council (NRC) during the Decadal Survey (DS) [1] in 2007 identified the Precipitation and All-weather Temperature and Humidity (PATH) as one of the ten critical Earth science missions. The PATH mission identified the use of a microwave array spectrometer to provide all-weather temperature and humidity sounding with spatial resolution comparable to AMSU-A/B (i.e.  $\sim 15\text{-}30$  km) and at  $\sim 15\text{-}30$  minutes temporal resolution for improved forecasting of hurricanes and severe storms. At least three candidates of geostationary microwave array spectrometer concepts (i.e. the GEostationary Microwave observatory (GEM) [116], the Geostationary Synthetic Thinned Aperture Radiometer (GeoSTAR) [77], and the Geostationary Interferometric Microwave Sounder (GIMS) [80]) have been recognized to make such high spatio-temporal observations achievable, albeit at costs in the range of \$200-600 million [45, 139]. Due to recent advances in microwave receiver and filter technology, the concept of a low-Earth orbiting (LEO) constellation of  $\sim 30\text{-}50$  CubeSat small satellites with payload consisting of cross-track scanning microwave spectrometers using sounding channels at both the 118.7503 GHz oxygen line and the 183.310 GHz water vapor line has been identified as an alternative cost effective means of achieving these observation goals [94]. This constellation is being developed by Orbital Micro Systems Inc., and is called the Global Earth Monitoring Systems (GEMS).

While the specific hardware implementation of GEMS is to be determined, the observed microwave data at such high spatio-temporal resolution provide the potential for precipitation locking of large individual precipitation cells in numerical weather prediction (NWP) models under conditions

of rapidly evolving mesoscale convection and widely varying cloud opacity. Precipitation locking is analogous to the process underlying a phase-locked loop (PLL) wherein linear phase differencing is achieved only when the oscillator and signal phases remain within the same cycle [40]. Similarly, stable linear NWP model updates can be achieved provided that the cloud and precipitation state does not de-correlate between satellite observations. This potential of precipitation locking is being explored in this thesis at the University of Colorado at Boulder in an all-weather microwave radiances assimilation system called precipitation assimilation system (PAS) [139]. Figure 1.1 illustrates the schematic diagram of the precipitation locking algorithm based on short-term NWP models and extended Kalman filtering (XKF).

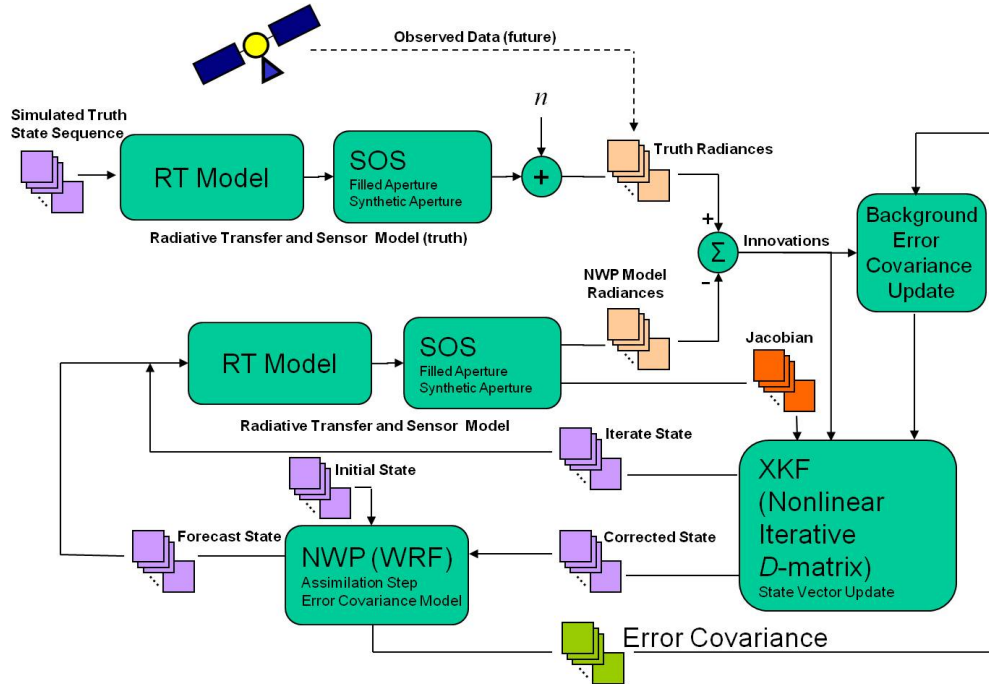


Figure 1.1: Precipitation locking simulation system under development at Center for Environmental Technology (CET) at University of Colorado at Boulder.

five modules in the simulation system are required to be implemented with an extended capability. These modules are: 1) computationally efficient and accurate radiative transfer model with the capability to provide the sensitivity functions (Jacobians) that describe the tangent linear response of each observable (e.g. brightness temperature,  $T_B$ ) to each atmospheric variable, 2) high-temporal

observation data simulations based on a passive microwave sensor constellation or geostationary imager/sounder concept, 3) estimation of *a priori* error covariance matrices for all thermodynamic and hydrometeor state variables for first-frame locking, 4) atmospheric state vector update based on constrained extended Kalman filtering (XKF), and 5) continual estimation of background error covariance matrices for all variables for continuous assimilation.

The existing one-dimensional (1D) Unified Microwave Radiative Transfer (UMRT) model [122, 127] developed at the Center for Environmental Technology (CET) at University of Colorado at Boulder (CU) offers several advantages to meet the needs of the precipitation locking simulator. The UMRT algorithm provides a fast layer-adding dual-polarization solution to the differential radiative transfer equation in a planar-stratified multilayer medium under all single-scattering albedo conditions along with a fast Jacobian calculation that reuses previously computed matrix operators. Importantly, the UMRT model takes advantage of the transition matrix symmetry of the radiative transfer equation based on spherical scattering hydrometeors to realize unconditional numerical stability and computational efficiency for all matrix operations required by the discrete-ordinate eigenanalysis method [118, 91, 127]. In this thesis, the UMRT model was extended by incorporating complex hydrometeors to extend the applicability of UMRT over a wide range of aspherical ice hydrometeor habits and frequencies from 10 GHz to  $\sim 1$  THz.

Microwave dual-polarization sounding and imaging data from spaceborne atmospheric sensors such as the Tropical Rainfall Measuring Mission (TRMM) [64] and the Global Precipitation Measurement (GPM) mission [25] are widely used in both precipitation retrieval algorithms (e.g., for nowcasting) and in microwave radiance assimilation methods for optimal update of numerical weather prediction models. It has been shown that both sounding and window channels above  $\sim 90$  GHz are sensitive to scattering by frozen hydrometeors [41, 36], and exhibit significant polarization differences from ice clouds at moderate off-nadir (e.g. at  $53^\circ$ ) viewing angles [26, 114]. For these reasons, the Ice Cloud Imager (ICI) instrument for MetOp-SG [16, 9] is being developed for ice cloud parameter retrievals using 12 dual-polarized channels from 183 GHz to 664 GHz and conical scanning at  $53^\circ$  incidence. At the same time, CubeSat-based small satellites are being developed

to demonstrate the potential of ice cloud measurements using a submillimeter-wave radiometer operating at 670 GHz. The small satellite constellation concept has been identified as a cost effective means to provide global severe weather observations with high spatio-temporal resolution for 4D-Var assimilation [139] and is being demonstrated in the MicroMAS [11] and PolarCube [94] temperature sounding cross-track radiometer missions at 118.75 GHz.

Radiative transfer models for cirrus parameter retrieval algorithms have been developed for cirrus clouds composed of aspherical ice crystals with multiple shapes and size distributions. Brightness temperature depressions caused by non-zero ice water path (IWP) at 85.5, 157, 220 and 340 GHz for cirrus clouds containing five habits of ice crystals was studied by Evans and Stephens [32, 33]. The study was extended to 880 GHz for scattering properties of cirrus clouds using models with additional ice crystal shapes, size distributions and atmospheric profiles, along with the development of a Bayesian retrieval algorithm for cirrus cloud IWP and mean particle size [34]. The performance of the retrieval algorithm was later evaluated based on airborne flights of the Submillimeter-Wave Cloud Ice Radiometer (SWCIR) [35] and the Compact Scanning Submillimeter Imaging Radiometer (CoSSIR) [36]. Concurrently, the Atmospheric Radiative Transfer Simulator (ARTS) code developed by Emde et al. [26] was used to study microwave radiances over cirrus clouds comprising spheroids of varying aspect ratio at off-nadir viewing angles.

The radiative impact of aspherical frozen hydrometeors in severe weather (e.g. hurricanes) radiance modeling was also investigated by comparing the computed brightness temperatures with observations from four instruments (e.g., the High Altitude Monolithic Microwave Integrated Circuit Scanning Radiometer (HAMSR)) on the NASA ER-2 aircraft [113]. A single ice crystal habit of a bullet rosette shape was chosen to represent frozen cloud hydrometeors. Comparisons of the resultant brightness temperatures based on either this aspherical habit or Mie spheres suggested that multiple habits and size distributions of aspherical hydrometeors are needed for accurate simulations of upwelling radiances. A similar case study on stratiform snowfall [93] based on aspherical ice crystals and snow aggregates presented in the OpenSSP database [68] showed general consistency between observations from the Conical Scanning Millimeter-Wave Imaging Radiometer (CoSMIR)

and computed upwelling radiances at 165.50 GHz and nadir viewing for radar retrieved profiles of observed precipitation during the Midlatitude Continental Convective Clouds Experiment (MC3E).

In this thesis, the UMRT model is first extended by incorporating aspherical frozen hydrometeor information derived from the OpenSSP database, which provides relevant geophysical frozen hydrometeor data for a variety of pristine ice crystals and snow aggregates of widely varying sizes [68]. Based on the morphological structures of those particles, the single-scattering parameters at key passive sensing frequencies between 10 and 874 GHz are calculated using the Discrete Dipole Approximation code (DDSCAT v7.3.1) [24]. DDSCAT is an open-source software package. It was compiled at CU CET and modified to calculate the extinction, absorption, and scattering efficiency along with the full  $(4 \times 4)$  Stokes matrix for 203 selected hydrometeor habits with random orientations. This extended UMRT model addresses a fundamental requirement of near-symmetry of the DRTE transition matrix to ensure that the model maintains the properties of numerical stability and computational efficiency for randomly oriented aspherical hydrometeors [140]. Upon the proof of this transition matrix property, the extended UMRT model is used to simulate microwave radiances at the top of the atmosphere over hurricane Sandy (2012) based on atmospheric profiles simulated using the Weather Research and Forecasting (WRF v3.5) model. The resulting top-of-atmosphere brightness temperatures are compared with the analogous results for mass-equivalent Mie spheres for quantitative assessment of the impact of aspherical frozen hydrometeors on the simulated microwave radiances.

One of the challenges in assimilating all-weather satellite microwave data into numerical weather prediction (NWP) models is to rapidly and accurately compute radiation fields over clouds and precipitation [7, 135]. However, real clouds exhibit strong radiative variations in both the horizontal and vertical directions [130]. These three-dimensional (3D) radiative effects have been observed in optical and infrared cloud parameter retrievals (e.g. cloud optical thickness) by statistical analysis of uncertainties in one-dimensional (1D) retrievals [128, 129, 130]. The 3D effects of clouds in the microwave range have similarly been observed in estimating rain rates over water surfaces using satellite microwave observations [81]. By comparing brightness temperature differences between 3D

and 1D radiative transfer models, it has been shown that horizontally homogeneous cloud models (i.e. 1D planar-stratified radiative transfer models) underestimate retrieved rain rates [81].

A horizontally inhomogeneous unified microwave radiative transfer (HI-UMRT) model based on the existing 1D UMRT model was developed in this thesis to facilitate forward radiative simulations for 3D inhomogeneous clouds in severe weather (e.g. hurricanes). The HI-UMRT model provides a 3D analytic radiative transfer solution by embedding a planar-stratified 1D UMRT algorithm for the first two Stokes parameters [122, 127] within a horizontally inhomogeneous iterative perturbation scheme. The solution to the 3D radiative transfer equation using 1D UMRT can be found by perturbation theory applied to the azimuthal harmonics of the radiation field, where the horizontal gradients of radiances of lower order perturbations are treated as source functions of the equation. The UMRT engine is subsequently used to solve each azimuthal harmonic and iterative perturbation equation starting from the zeroth order. During each successive order of iteration, the basic UMRT radiative parameters (e.g. emission, reflection, and transmission matrices) need to be computed only once for each 1D vertical profile, and are subsequently reused for all azimuthal and perturbation series corrections. The necessary number of perturbation iterations can be determined based on the required precision of the computed upwelling microwave radiances. The converged 3D HI-UMRT simulations of the top-of-atmosphere brightness temperature images compared with the corresponding 1D UMRT results show that the accuracy of radiative transfer computations can be considerably improved by correcting for the error caused by neglecting horizontal cloud inhomogeneities.

Observing system simulation experiments (OSSEs) of CubeSat constellation microwave observations are required to demonstrate the basic features of the constellation concept and provide experimental data for facilitating the systematic development of the precipitation locking concept in many aspects. To this end, efforts have been carried out to simulate upwelling microwave radiances based on NWP atmosphere state reanalyses as would be observed by a constellation of small passive microwave satellites. The GEMS system under development is selected to provide the necessary simulation parameters. GEMS utilizes  $\sim 30$ -50 PolarCube-based small satellites deployed



in multiple orbital planes (e.g. the GPS orbit with inclination  $55^\circ$  or NASA A-train orbit with inclination  $98.14^\circ$ ) to achieve sub-hourly revisit times. A mesoscale severe weather event (e.g. hurricane Sandy, 2012) in the North American Mesoscale (NAM) model reanalysis is selected as the primary case study of simulations in this thesis. The WRF model is a mesoscale numerical weather prediction system designed to serve both atmospheric research and operational forecasting needs [59]. The output of WRF model runs sampled at 5 km in space and at 30 minutes in time provides a series of atmospheric state inputs to the radiative transfer model (e.g. UMRT) used to compute top-of-atmosphere brightness temperature imagery. The observed antenna temperatures based on the PolarCube specifications [94] were further simulated by considering randomized orbit geometry, received polarization vector rotation, antenna beam patterns, and the designed channel passband responses. A two-dimensional antenna temperature scan image of Sandy was constructed during the overflight of a single GEMS satellite. Repetition of this simulation process for other satellites which overflew the event every 15 minutes was used to generate a sequence of microwave images of hurricane Sandy at the representative time intervals.

Previous studies using the MM5 model [45] have shown that cloud ice parameters in the NWP model can be adjusted iteratively close to the true state using unconstrained extended Kalman filtering, thus markedly causing the innovation field to decrease. However, thermodynamic variables (e.g. temperature and water vapor content), which are less directly observable, diverged during these first-frame observation iterations. In order to engage precipitation locking a means of stabilizing the first-frame update process for both thermodynamic and hydrometeor state variables by adding inequality constraints to the extended Kalman filter gains [39] and use of an appropriate *a priori* state variable error covariance matrix is essential. The technique of Kalman filtering with inequality constraints has been used for turbofan engine health estimation [110], where it has been shown that the variance of constrained estimates is smaller than unconstrained estimates with the average error reduced by 50%.

Also essential to the precipitation locking process is the need to generate accurate estimates of the background error covariance matrices for both thermodynamic (e.g. temperature, water vapor)

and hydrometeor (e.g., rain, cloud liquid water, cloud ice, snow, and graupel density) variables. The background error covariance matrix plays a central role in meteorological variational data assimilation systems based on passive microwave satellite data and iterative extended Kalman filtering [5]. The atmospheric state variable statistics embodied in this matrix impact the Kalman gain significantly, and incorrect error statistics can result in instabilities that amplify noise among unobservable prognostic modes. This thesis focuses on the development of flow-dependent error covariances for thermodynamic and hydrometeor variables, which can be assumed to be Brownian processes whose error covariances grow linearly with time. Under the Brownian assumption the covariance matrix is developed from increments in the forecast state variables, which are themselves jointly Gaussian for short enough time periods.

The thesis is organized as follows. Section 2 describes single-scattering parameters of aspherical atmosphere hydrometeors computed using DDSCAT v7.3.1 code and compared with those of presumed spherical hydrometeors computed based on Mie theory. Section 3 discussed the simulation efforts of multi-stream dual-polarized microwave radiances using the 1D UMRT algorithm incorporating the OpenSSP aspherical hydrometeor database. The degree of transition matrix symmetry based on aspherical OpenSSP hydrometeors is examined in this section along with a theoretical analysis of transition matrix perturbations introduced by the arbitrary geometrical structure of OpenSSP hydrometeors. Sections 4 and 5 present the new 3D HI-UMRT algorithm based on an iterative perturbation scheme using the existing 1D UMRT engine. The computation efficiency and theoretical computing time are discussed using the continuous form of the differential radiative transfer equation. The angular and spatial discretization of the radiative transfer equation is provided along with the numerical solution for terms of the azimuthal harmonic iterative perturbation series. Numerical simulations are performed to demonstrate the convergent perturbation corrections and further evaluate the 3D radiative effects by comparing the simulated upwelling brightness temperature imagery for 3D HI-UMRT versus the planar-stratified 1D UMRT model. Section 6 focuses on the development of a precipitation locking simulation system along with an introduction to the concept of precipitation locking. The simulation results of high-temporal resolution observations

based on the proposed GEMS constellation were used to demonstrate precipitation locking for the first observation frame. The Brownian-based estimation of flow-dependent background error covariance matrices is also discussed in this section with some preliminary results. Conclusions and future work discussion are provided in the last section.

## Chapter 2

### Microwave Single-Scattering Parameters of Atmospheric Hydrometeors

In passive atmospheric remote sensing the electromagnetic energy radiated from the Earth's atmosphere [123] is precisely measured. The radiation field observed from the top of the atmosphere is sensitive to both thermodynamic and hydrometeor parameters such as pressure, temperature, water vapor, and cloud hydrometeor content [62, 41]. Hydrometeors suspended or falling in the atmosphere are water particles that can be in solid, liquid, or mixed (liquid and solid) phases. Atmospheric hydrometeors can be characterized by their microphysical properties, such as maximum dimension, fractional volume, morphological structure, orientation, and permittivity [123]. In numerical weather prediction (NWP) models, microphysical parameterizations [37, 98] are used to classify hydrometeors into five categories: 1) non-precipitating cloud liquid droplets with radius less than  $\sim 50 \mu\text{m}$ , 2) precipitating rain of radius less than  $\sim 5 \text{ mm}$ , 3) cloud ice of maximum dimensions less than  $\sim 1 \text{ mm}$  and exhibiting a variety of morphological structures (e.g. plates, dendrites, columns, needles, etc.), 4) snow of size between  $\sim 1 \text{ mm}$  and  $\sim 10 \text{ mm}$  with complex aggregation structures, and 5) graupel of size typically less than  $\sim 10 \text{ mm}$ .

Within the microwave frequency range, cloud hydrometeors affect electromagnetic propagation by absorbing and scattering radiation along with the background gases that primarily absorb (e.g. oxygen and water vapor). Absorbing hydrometeors also emit microwaves due to the local thermal equilibrium between hydrometeors and the surrounding atmosphere [41]. The absorption, scattering, and emission by cloud hydrometeors can considerably impact microwave brightness measurements made at atmospheric sounding frequencies. Observations of brightness temperature can be used to

determine cloud and precipitation properties via either retrieval or radiance assimilation schemes [41, 84, 59].

In order to model microwave radiance fields propagating through clouds, the radiative single-scattering properties of individual hydrometeors need to be determined. The properties are based on presumed particle geometries, dielectric constitution, and the ambient thermodynamic temperature [68, 41]. The single-scattering parameters which are important for passive remote sensing can be organized into two groups: 1) scalar quantities which represent the total power loss from the incident radiation field due to the scattering and/or absorption by particles [123], including the extinction cross section ( $\sigma_e$ ), the scattering cross section ( $\sigma_s$ ), and the absorption cross section ( $\sigma_a$ ), and 2) matrix quantities which are angularly-dependent and relate the scattered radiation field to the incident field. The scattering function matrix ( $\overline{\overline{F}}$ ), a complex  $2 \times 2$  matrix, is a key element of the radiative transfer theory since nearly all quantities required by the differential radiative transfer equation can be expressed in terms of this complex matrix. For example, the real  $4 \times 4$  Stokes matrix ( $\overline{\overline{L}}$ ) is derived from the scattering function matrix using the definition of Stokes parameters of the radiation field. Another commonly used single-scattering parameter is the asymmetry parameter ( $g$ ) calculated based on the scattering function matrix. The asymmetry parameter represents the amount of power scattered into the forward versus backward directions.

In this chapter, the numerical calculation of single-scattering parameters for both simple Mie spheres and complex aspherical hydrometeors are discussed. Mie theory provides a closed-form series solution leading to all necessary radiative parameters for spherical hydrometeors. However, numerical methods are required for general aspherical particles. The Discrete Dipole Approximation (DDA) algorithm [24] is one commonly used numerical method that can be applied to aspherical frozen hydrometeors such as those defined within the OpenSSP hydrometeor database [68]. Scalar extinction, scattering and absorption efficiencies for selected general hydrometeor shapes and for random orientations were computed using DDSCAT v7.3.1 at key passive sensing frequencies from 10 to 874 GHz. These calculations extended the maximum frequencies of scattering and absorption properties considered within the current OpenSSP database. The random orientation-averaged

full Stokes matrices for these selected OpenSSP hydrometeors were also computed using DDSCAT v7.3.1, averaging over 6,156 different particle orientations. These scalar efficiencies are useful because they are independent of propagation direction and polarization of the incident wave [90].

## 2.1 Simple Mie Spheres

The electromagnetic field perturbed by a dielectric sphere has been well studied beginning with the work of Mie (1906, 1908), later clarified by Stratton [119]. In Mie theory, vector spherical mode (VSM) expansions [125, 12, 41] of the incident, internal, and scattered fields are expressed to arbitrary precision. All unknown VSM expansion coefficients are determined by applying boundary conditions at the spherical particle radius. The VSM coefficients for the scattered fields are commonly known as the *Mie coefficients*:

$$a_n = -\frac{j_n(mx) [xj_n(x)]' - j_n(x) [mxj_n(mx)]'}{j_n(mx) [xh_n(x)]' - h_n(x) [mxj_n(mx)]'} \quad (2.1)$$

$$b_n = -\frac{j_n(x) [mxj_n(mx)]' - m^2 j_n(mx) [xj_n(x)]'}{h_n(x) [mxj_n(mx)]' - m^2 j_n(mx) [xh_n(x)]'} \quad (2.2)$$

where  $j_n(\cdot)$  is the spherical Bessel function of first kind,  $h_n(\cdot)$  is the spherical Hankel function of first kind (corresponding to outwardly propagating spherical waves), and  $[\cdot]'$  denotes differentiation with respect to the parameter  $x$ . In practice, Mie coefficients are computable using recursive series formulae [12, 90]. The parameter  $x$  is the electrical size of the sphere, which is the ratio of sphere circumference to wavelength.

$$x \triangleq \frac{\pi D}{\lambda} \quad (2.3)$$

where  $D$  is the sphere diameter, and  $\lambda$  is the wavelength. The parameter  $m$  is the complex refractive index of the sphere:

$$m \triangleq \sqrt{\frac{\epsilon_s}{\epsilon}} \quad (2.4)$$

where  $\epsilon_s$  and  $\epsilon$  are the dielectric constant of the sphere and the background medium (respectively).

Applying Mie theory to spherical hydrometeors, the scalar extinction efficiency  $\eta_e$ , scattering

efficiency  $\eta_s$ , and absorption efficiency  $\eta_a$  [12, 41] are defined and computed as:

$$\eta_e(x, m) \triangleq \frac{\sigma_e}{\pi D^2/4} = \frac{2}{x^2} \sum_{n=1}^{n_{max}} (2n+1) \text{Re}\{a_n + b_n\} \quad (2.5)$$

$$\eta_s(x, m) \triangleq \frac{\sigma_s}{\pi D^2/4} = \frac{2}{x^2} \sum_{n=1}^{n_{max}} (2n+1) (|a_n|^2 + |b_n|^2) \quad (2.6)$$

$$\eta_a(x, m) \triangleq \frac{\sigma_a}{\pi D^2/4} = \eta_e(x, m) - \eta_s(x, m) \quad (2.7)$$

where the efficiencies are normalized by the sphere's physical cross-section [12]. The maximum truncation order  $n_{max}$  is commonly determined by  $n_{max} = \text{round}(x + 4x^{\frac{1}{3}} + 2)$  [41]. It can be shown that the scattering cross section computed using Mie theory becomes equal to the Rayleigh scattering cross section for dielectric spheres with small radii. The Rayleigh-Mie transition occurs for hydrometeor diameters  $D \gtrsim 0.1\lambda/\pi$ .

Similarly, the non-zero elements of the complex scattering function matrix of a sphere using the linear polarization basis ( $v$  for the vertical polarization and  $h$  for the horizontal polarization) can be expressed in terms of Mie coefficients [125, 12]:

$$f_{vv}(\Theta) = \frac{-j}{k} \sum_{n=1}^{n_{max}} \frac{2n+1}{n(n+1)} [a_n \pi_n(\cos \Theta) + b_n \tau_n(\cos \Theta)] \quad (2.8)$$

$$f_{hh}(\Theta) = \frac{-j}{k} \sum_{n=1}^{n_{max}} \frac{2n+1}{n(n+1)} [a_n \tau_n(\cos \Theta) + b_n \pi_n(\cos \Theta)] \quad (2.9)$$

where  $k$  is the wavenumber in vacuum, and  $\Theta$  denotes the forward scattering angle spanned by the propagation vectors of the incident and scattered fields. The angle-dependent functions  $\pi_n$  and  $\tau_n$  are defined by upward recursion as:

$$\pi_n(\Theta) = \frac{2n-1}{n-1} \cos \Theta \pi_{n-1} - \frac{n}{n-1} \pi_{n-2} \quad (2.10)$$

$$\tau_n(\Theta) = n \cos \Theta \pi_n - (n+1) \pi_{n-1} \quad (2.11)$$

with  $\pi_0 = 0$  and  $\pi_1 = 1$ . The Stokes matrix of a sphere using the modified Stokes parameter

representation  $[I_v, I_h, U, V]^T$  can be computed as:

$$\bar{\bar{L}}(\Theta) = \begin{bmatrix} |f_{vv}(\Theta)|^2 & 0 & 0 & 0 \\ 0 & |f_{hh}(\Theta)|^2 & 0 & 0 \\ 0 & 0 & \text{Re}\{f_{vv}(\Theta)f_{hh}^*(\Theta)\} & -\text{Im}\{f_{vv}(\Theta)f_{hh}^*(\Theta)\} \\ 0 & 0 & \text{Im}\{f_{vv}(\Theta)f_{hh}^*(\Theta)\} & \text{Re}\{f_{vv}(\Theta)f_{hh}^*(\Theta)\} \end{bmatrix} \quad (2.12)$$

Note that for spheres only four independent real-valued elements are present in (2.12), and that the sub-spaces  $[I_v, I_h]$  and  $[U, V]$  are decoupled. The decoupled block-diagonal structure of the Stokes matrix for spheres facilitates numerical microwave radiative transfer modeling, as will be discussed in the next chapter.

The above calculations of the radiative parameters (2.5) - (2.12) are based on Mie coefficients, which depend highly on the electrical size  $x$  and the complex refractive index  $m$  of the sphere. In this thesis, the complex dielectric constant of water droplets (e.g. cloud liquid water and rain) is calculated with the Debye model as defined in the atmospheric Millimeter-Wave Propagation Model (MPM) (1985) by Liebe [75]. Other commonly used models for computing the complex permittivity of liquid water include the Klein-Swift model (1977) [61] and the Meissner-Wentz model (2004) [86]. However, for consistency with previous works [41, 127] the MPM model is used in this thesis. The ice refractive index for microwave frequencies is obtained based on Warren and Brandt's model (2008) of optical constants of ice calculated at a single temperature of 266 Kelvin [132]. Finally, the complex dielectric constant for hydrometeors composed of ice, water, and air (e.g. graupel or wet snow) is calculated based on the dielectric mixing theory described by Sadiku (1985) [104].

## 2.2 Complex Aspherical Hydrometeors

Real hydrometeors exhibit falling, advecting, convecting, and dynamically evolving motion in clouds. The morphological structure of atmospheric hydrometeors varies dramatically in real cloud processes. For example, the shape of precipitating rain droplets are slightly oblate due to viscous forces. Cloud ice crystals naturally grow into a variety of aspherical forms with facets and branches



based on the diffusion of water vapor and anisotropic attachment [99, 47]. These ice crystals also collide during motion within a cloud and in doing so can form larger aggregates.

### 2.2.1 Database of Geometrically Symmetric Frozen Hydrometeors

The geometrical structure of hydrometeors plays a key role in remote sensing measurements and has a significant impact on cloud and precipitation property retrieval, particularly when the hydrometeor size is comparable to or greater than the wavelength of the electromagnetic field (i.e. electrically large particles). This impact has been widely studied for backscattering and extinction by aspherical ice and snow particles [71, 54, 95, 13, 124]. The results of these studies have motivated the modeling of complex ice and snow particles according to their ice crystal habits, which depend on aggregation, riming, and melting history.

Four publicly released databases are available for modeling aspherical but symmetric ice crystals, generating aggregates, and calculating the single-scattering parameters of individual particles. It should be noted that these databases model pristine ice crystals as aspherical symmetric particles in idealized habits with multiple-fold symmetry, and include (for example) hexagonal columns, hexagonal plates, and multi-bullet rosettes. These databases are:

- (1) Icepart-mod: polarimetric scattering database for ice particles at microwave frequencies  
(<http://www.arm.gov/data/data-sources/icepart-mod-120/>) [13, 83]
- (2) SCATDB: scattering database for ice crystals and aggregates by Liu et al.  
(<http://cirrus.met.fsu.edu/research/scatdb.html>) [79, 92]
- (3) Database of microwave single-scattering properties of falling snow  
(<http://helios.fmi.fi/~tyynelaj/database.html>) [124]
- (4) ARTS microwave single-scattering properties database  
(<https://zenodo.org/record/1175589>) [30]

The discrete dipole approximation (DDA) method is commonly used to calculate the scattering

properties of the ice and snow particles in the above databases, with the exception of the icepart-mod database which uses both the DDA algorithm and the generalized multi-particle Mie method (GMM) [134]. Note that two different open-source implementations of the DDA algorithm exists, 1) the Amsterdam DDA (ADDA) [137] used in the ARTS database, and 2) the Discrete Dipole Approximation Code (DDSCAT) [24] as used in Liu’s database.

### 2.2.2 OpenSSP Database of Ice and Snow Particles with Asymmetric Geometry

Realistic ice particle geometries, rather than purely pristine shapes, are required to model diverse ice habits. Since radiative extinction by electrically large ice particles is highly geometry dependent [48, 74], the OpenSSP database of microwave single-scattering parameters of aspherical and asymmetric ice hydrometeors has been generated and released by Kuo et al. at NASA/GSFC (<https://storm.pps.eosdis.nasa.gov/storm/OpenSSP.jsp>) [68]. The OpenSSP ice crystals are simulated based on a three-dimensional physical model [47] to represent the natural diffusional growth of pristine ice crystals in clouds. The OpenSSP asymmetric snow particles are subsequently generated by simulating the natural aggregation of these pristine ice crystals of various sizes.

At the time of this writing, the OpenSSP database contained nearly 10,000 samples of simulated frozen hydrometeors categorized into 20 habits of pristine ice crystals and 9 families of snow aggregates based on commonly observed cloud ice habits (e.g., dendrites, needles, and plates). Using a dot to represent a particular habit with its effective spherical volume-equivalent radius, the entire OpenSSP frozen hydrometeor population is illustrated in Figure 2.1.

The DDSCAT v7.1 software package was used by NASA/GSFC to calculate the single-scattering parameters of OpenSSP frozen hydrometeors. Partial Stokes matrices (e.g. six elements only) at fifteen frequencies up to 190 GHz along with scalar efficiencies (e.g.  $Q_{ext}$ ,  $Q_{sca}$ , and  $Q_{abs}$ ) were provided in the OpenSSP database (see [68]). These calculated quantities were extended for this thesis as described below.

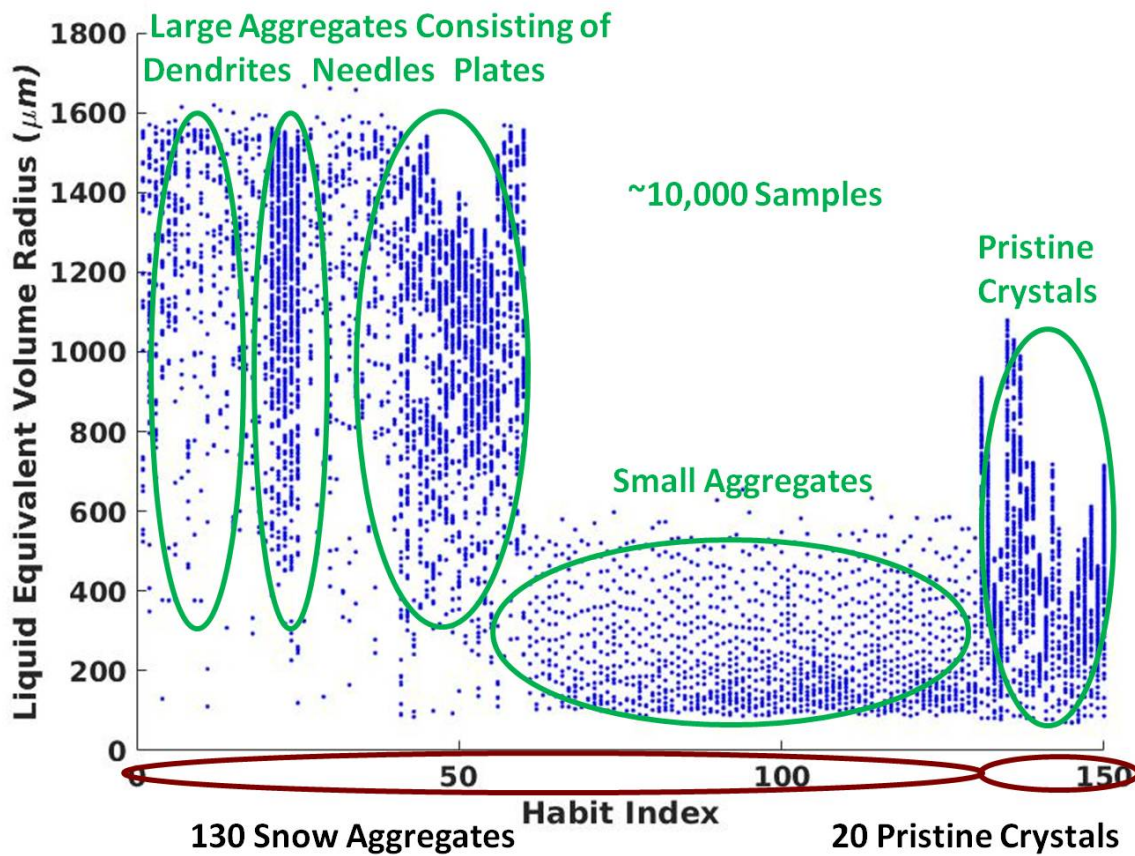


Figure 2.1: Population of aspherical frozen hydrometeor habits and sizes in the current (ca. 2018) OpenSSP database.

### 2.3 Extension of Scattering Parameters for Selected OpenSSP Hydrometeors

For this study of microwave radiative transfer through clouds, efforts were made to augment the OpenSSP database in two aspects. First, the extension of single-scattering parameters to frequencies beyond 190 GHz corresponding to important sensing channels (see Table 2.1) on both current and future missions (e.g., the ICI mission, the Geosynchronous Microwave (GEM) sounder/imager [120], the Orbital Micro Systems (OMS) Global Earth Monitoring Systems (GEMS) constellation, and NASA airborne CoSSIR campaigns [36]) was done. Second, the full ( $4 \times 4$ ) Stokes matrix for randomly-oriented selected representative OpenSSP hydrometeors was computed.

Table 2.2 identifies several of the 203 selected snow aggregates and ice pristine crystals for

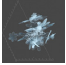
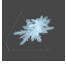

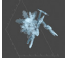

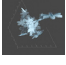
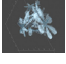

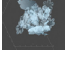




Table 2.1: List of frequencies included in this study.

	Frequency (GHz)
OpenSSP Database	3.00, 5.00, 10.66, 13.61, 18.71, 23.82, 35.53, 89.06, 94.07, 150.10, 165.62, 176.42, 180.43, 186.43, 190.43
Added by This Study	10.65, 23.80, 36.50, 52.80, 54.40, 56.92, 57.07, 89.00, 113.75, 115.75, 117.25, 117.65, 118.05, 118.35, 166.31, 176.31, 178.31, 180.31, 181.66, 182.41, 315.65, 321.65, 323.65, 371.20, 420.76, 440.80, 445.00, 446.60, 659.80, 874.00

this study. Although these shapes comprise only a small portion of the entire database (i.e.  $\sim 3\%$  of the total number of samples), this selection is representative of the entire population of OpenSSP habits, including all of the nine families of snow aggregates with inscribing sphere (i.e., maximum) diameter  $D_{\max}$  up to 6,000  $\mu\text{m}$  and four of the most commonly observed ice crystal habits with  $D_{\max}$  up to 8,000  $\mu\text{m}$ . The maximum diameters of particles are stored in the OpenSSP database along with other geometrical properties (e.g., liquid volume-equivalent radius). The minimum value of  $D_{\max}$  for any habit is the smallest size of that particle habit in the database. The maximum value of  $D_{\max}$  used in this study was chosen based on the computational time needed for the discrete dipole approximation (DDA) algorithm at the highest frequency (874 GHz). The increment  $\Delta D_{\max}$  in  $D_{\max}$  for any habit was selected to be the discretized archival size for simulated particle growth using the self-collection algorithm [68].

In order to maintain the accuracy of the DDA algorithm, DDSCAT v7.3.1 requires that  $|m|kd < 0.5$  [24], where  $m$  is the complex refractive index of ice at frequency of interest,  $k$  is the free space wave number, and  $d$  is the interdipole distance of a simulated OpenSSP hydrometeor. Accordingly, the spatial-averaged interdipole distance of  $\sim 50 \mu\text{m}$  as specified in the current OpenSSP database was used for the calculations at frequencies below 200 GHz. A smaller interdipole distance of  $\sim 16.7 \mu\text{m}$  was needed for frequencies above 200 GHz. This finer interdipole distance was selected to meet the accuracy requirement of DDSCAT v7.3.1 for frequencies up to  $\sim 800$  GHz. At the highest frequency of 874 GHz, the interdipole distance requirement was barely satisfied resulting in some minor loss of accuracy in computing the scattering function matrix.

Table 2.2: Selected snow aggregates (ap-) and ice pristine crystals (p-) with varying range of maximum diameters  $D_{\max}$ . An interdipole distance of  $\sim 50 \mu\text{m}$  is used for frequencies below 200 GHz and  $\sim 17 \mu\text{m}$  for 300 GHz up to 874 GHz in DDSCAT v7.3.1.

OpenSSP Habit Identifier	Sample Depiction	Description	Min. $D_{\max}$ ( $\mu\text{m}$ )	Max. $D_{\max}$ ( $\mu\text{m}$ )	Avg. $\Delta D_{\max}$ ( $\mu\text{m}$ )	# Particles
ap-04		Dendrite with facets	324	2530	$\sim 700$	4
ap-13		Fern dendrite	260	3396	$\sim 250$	14
ap-14		Classic dendrite	270	5863	$\sim 350$	19
ap-16		Star-shaped dendrite	260	5011	$\sim 300$	18
ap-29		Needle	1012	5066	$\sim 1000$	24
ap-19		Dendrite with broadening arms	287	3338	$\sim 150$	5
ap-44		Dendrite with broadening arms	273	3941	$\sim 200$	25
ap-46		Dendrite with broadening arms	324	6189	$\sim 250$	27
ap-43		Sandwich plate	353	3434	$\sim 200$	18
p-14		Classic dendrite	250	8100	$\sim 800$	11
p-19		Dendrite with broadening arms	223	4510	$\sim 350$	13
p-31		Solid column	206	2018	$\sim 150$	13
p-43		Sandwich plate	250	3950	$\sim 350$	12

### 2.3.1 Discrete Dipole Approximation Code (DDSCAT v7.3.1)

DDSCAT v7.3.1 [24] was compiled and installed on the CU "Summit" research supercomputer with message passing interface (MPI) enabled to perform parallel computations of the single-

scattering parameters (e.g. extinction efficiency, scattering efficiency, absorption efficiency and full Stokes matrix) for all selected ice and snow particles at the selected frequencies (see Tables 2.1 and 2.2). DDSCAT v7.3.1 computes the orientational average of these scattering parameters for each randomly-oriented particle.

Three input files are mandatory for executing DDSCAT v7.3.1 for OpenSSP hydrometeors: 1) a target file `shape.dat` specifying the target geometry with the location and composition of each dipole, 2) an external file (e.g. `ior-266K.dat`) containing the ice refractive index as a function of frequency, 3) a parameter file `ddscat.par` providing all necessary parameters to run the core program `ddscat`. The target files can be obtained from the OpenSSP database (<https://storm.pps.eosdis.nasa.gov/storm/OpenSSP.jsp>) by request. The file for the ice refractive index was created based on the Warren and Brandt revised model [132] (see Appendix A for the dielectric constant of ice between 10 and 1000 GHz).

The sample parameter file `ddscat.par` attached in the DDSCAT v7.3.1 software package was modified to meet the requirements for DDSCAT outputs in this study. A key modification is to change the number of output Stokes matrix elements to 9, including all upper triangle elements except  $L_{VV}$ , so that the full Stokes matrix of a randomly-oriented particle can be obtained [125]. Note that the Stokes matrix element  $L_{VV}$  defined using the Stokes parameter representation  $[I, Q, U, V]^T$  can be computed [12]:

$$L_{VV} = L_{UU} + (L_{II} - L_{QQ}) \quad (2.13)$$

An example of the modification of the parameter file is shown in Appendix A.

### 2.3.2 Full Stokes Matrix of Randomly-Oriented OpenSSP Hydrometeors

The random orientation-averaged full Stokes matrices  $\overline{\langle \bar{L} \rangle}_o(\Theta)$  for selected OpenSSP hydrometeors were computed using DDSCAT v7.3.1 by averaging over 6,156 different particle orientations. These orientations considered  $18 \times 19 \times 18$  samples over the three Eulerian angles  $(\beta, \Theta, \Phi)$ . Figure 2.2 shows comparisons of the random orientation-averaged Stokes matrix elements  $\langle L_{vv} \rangle_o$  and  $\langle L_{hh} \rangle_o$  for four families of snow aggregates (i.e. classic dendrite, dendrite with broadening arms, needles,

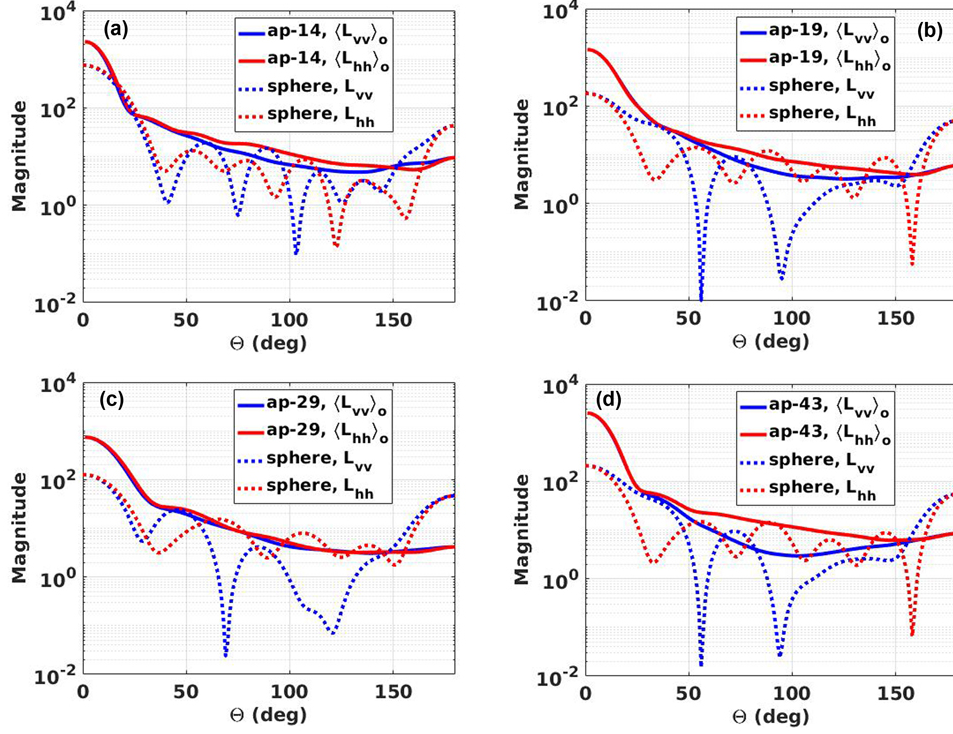


Figure 2.2: Random orientation-averaged Stokes matrix elements  $\langle L_{vv} \rangle_o$  and  $\langle L_{hh} \rangle_o$  compared with  $L_{vv}$  and  $L_{hh}$  of mass-equivalent spherical ice particle respectively as a function of forward scattering angle  $\Theta$  at 659.8 GHz for: (a) aggregates of classic dendrites (ap-14) with  $D_{\max} = 2002 \mu\text{m}$  versus ice spheres of  $902 \mu\text{m}$  in diameter, (b) aggregates of dendrites with broadening arms (ap-19) with  $D_{\max} = 1810 \mu\text{m}$  versus ice spheres of  $751 \mu\text{m}$  in diameter, (c) aggregates of needles (ap-29) with  $D_{\max} = 1645 \mu\text{m}$  versus ice spheres of  $648 \mu\text{m}$  in diameter and (d) aggregates of sandwich plates (ap-43) with  $D_{\max} = 1951 \mu\text{m}$  versus ice spheres of  $757 \mu\text{m}$  in diameter.

and "sandwich" plates) at 659.8 GHz versus  $L_{vv}$  and  $L_{hh}$  for the mass-equivalent Mie ice spheres. The intrinsic densities of the ice spheres are identical to the solid portions of the OpenSSP snow aggregates, and are constant ice densities with  $\rho_h = 0.9167 \text{ g/cm}^3$ . The comparisons exhibit good general agreement in angular variation trend, although the ice spheres exhibit deep scattering resonances at several forward scattering angles, and are generally (though not always) of smaller scattering value. The comparisons reveal approximately one order of magnitude stronger forward scattering within  $\Theta \lesssim 25^\circ$  for the aspherical snow aggregates than the mass-equivalent frozen spheres, and approximately one order of magnitude less at backscattering angles  $\Theta \gtrsim 160^\circ$ .

Figure 2.3 shows similar examples for four habits of ice pristine crystals at 659.8 GHz. Solid

columns are a more commonly observed habit than needles in ice clouds [51, 52, 36, 70, 78] and are chosen along with dendrites and plates to represent cloud ice. According to Schmitt and Heymsfield [106], a  $D_{\max}$  of  $\sim 400 \mu\text{m}$  is a typical transition size between simple ice crystals and complex aggregates. Therefore, slightly smaller size pristine ice crystals than this transition size are used for comparisons.

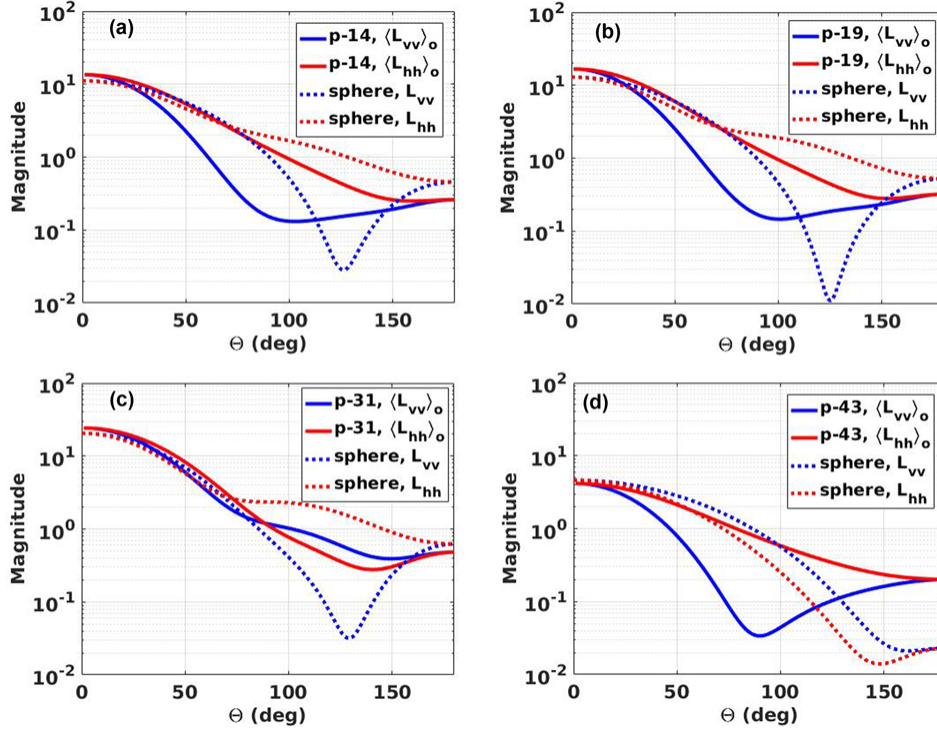


Figure 2.3: Similar to Figure 2.2, but for four habits of ice pristine crystals at 659.8 GHz, (a) classic dendrites (p-14) with  $D_{\max} = 354 \mu\text{m}$  versus ice spheres of  $267 \mu\text{m}$  in diameter, (b) dendrites with broadening arms (p-19) with  $D_{\max} = 403 \mu\text{m}$  versus ice spheres of  $278 \mu\text{m}$  in diameter, (c) solid columns (p-31) with  $D_{\max} = 353 \mu\text{m}$  versus ice spheres of  $301 \mu\text{m}$  in diameter and (d) sandwich plates (p-43) with  $D_{\max} = 403 \mu\text{m}$  versus ice spheres of  $216 \mu\text{m}$  in diameter.

From Figure 2.3, the element  $\langle L_{vv} \rangle_o$  for crystals with planar morphology exhibits a strong depression in scattering at  $90^\circ$ . This is not observed for randomly oriented column-like ice crystals of habit p-31. Both aspherical ice crystals and the mass-equivalent Mie spheres exhibit the same order of magnitude of forward scattering within  $\Theta \lesssim 25^\circ$  due to the smaller particle diameter than the wavelength at 659.8 GHz, where it is expected that the morphological structure of aspherical



ice particles would have small impact on forward scattering within this Rayleigh regime. At backscattering angles  $\Theta \gtrsim 160^\circ$ , aspherical ice particles exhibit slightly smaller scattering than Mie spheres except for the orientation-averaged plate shaped ice crystals of habit p-43, where approximately one order of magnitude stronger backscattering is exhibited.

### 2.3.3 Scalar Radiative Efficiencies of Randomly-Oriented OpenSSP Hydrometeors

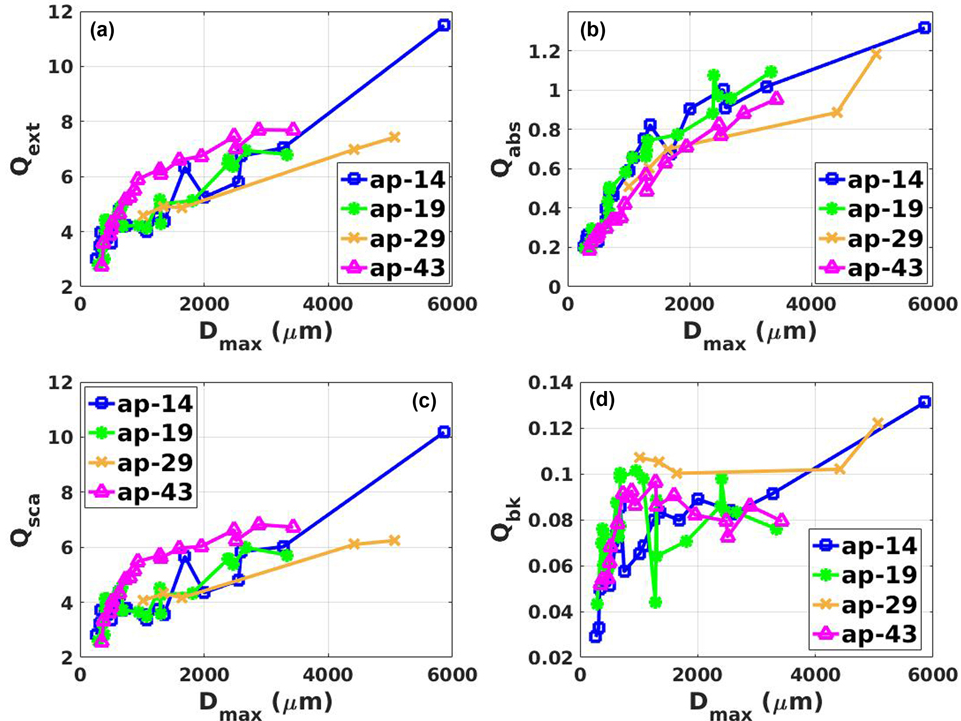


Figure 2.4: Random orientation-averaged single-scattering parameters of (a) extinction efficiency ( $Q_{\text{ext}}$ ), (b) absorption efficiency ( $Q_{\text{abs}}$ ), (c) scattering efficiency ( $Q_{\text{sca}}$ ), and (d) backscattering efficiency ( $Q_{\text{bk}}$ ) as a function of maximum diameter  $D_{\max}$  at 874 GHz for four habits of snow aggregates. These efficiencies are normalized by the hydrometeor effective area of an equal-volume sphere (see Equation 2.14).

DDSCAT v7.3.1 was also used to compute scalar extinction, scattering, and absorption efficiencies for the selected hydrometeors. These efficiencies  $Q_{\text{ext}}$ ,  $Q_{\text{sca}}$ , and  $Q_{\text{abs}}$  are defined by

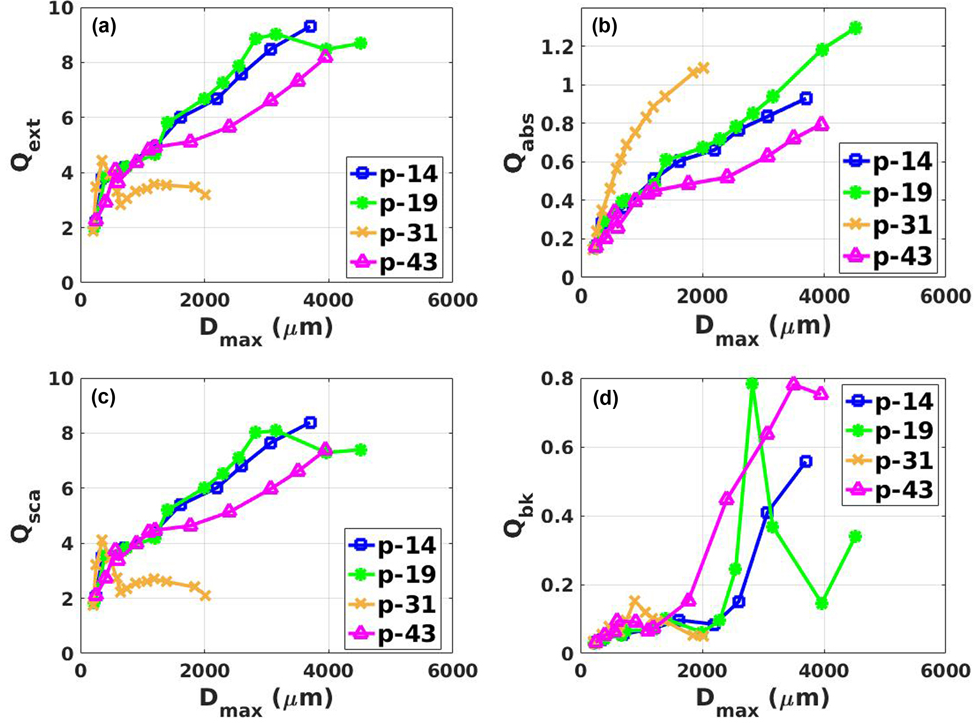


Figure 2.5: Similar to Figure 2.4, but for four habits of ice pristine crystals, (a) extinction efficiency ( $Q_{\text{ext}}$ ), (b) absorption efficiency ( $Q_{\text{abs}}$ ), (c) scattering efficiency ( $Q_{\text{sca}}$ ), and (d) backscattering efficiency ( $Q_{\text{bk}}$ ). These efficiencies are normalized by the hydrometeor effective area of an equal-volume sphere (see Equation 2.14).

Draine and Flatau [24] in the DDSCAT v7.3.1 code as:

$$\begin{aligned}
 Q_{\text{sca}} &= \sigma_{\text{sca}} / \pi a_{\text{eff}}^2 \\
 Q_{\text{abs}} &= \sigma_{\text{abs}} / \pi a_{\text{eff}}^2 \\
 Q_{\text{ext}} &= Q_{\text{sca}} + Q_{\text{abs}}
 \end{aligned} \tag{2.14}$$

where  $\sigma_{\text{sca}}$  is the scattering cross section,  $\sigma_{\text{abs}}$  is the absorption cross section and  $a_{\text{eff}}$  is the effective radius of an equal-volume sphere. Note that the efficiencies in (2.14) are normalized using the effective area of an equal-volume sphere. Thus, multiplying the efficiencies by the hydrometeor effective area (also calculated using DDSCAT v7.3.1 code) yields respective scalar coefficients. Figure 2.4 shows the efficiencies as a function of the maximum diameter at 874 GHz for the same four families of snow aggregates, and Figure 2.5 shows analogous efficiencies for the same four habits

of ice crystals. At submillimeter-wavelength, the scattering efficiency of an orientation-averaged plate-like ice crystal (including needles) or snow aggregate increases monotonically with  $D_{\max}$  and is typically  $\sim 10$  times larger than the corresponding absorption efficiency. Thus, in general, a single-scattering ice particle albedo close to unity is to be expected. However, we note that the scattering efficiency of a column-like ice crystal (e.g. habit p-31) exhibits only small variations between  $500 \mu\text{m}$  and  $2,000 \mu\text{m}$  size, while the absorption efficiency increases faster than that of plate-like ice crystals. The corresponding single-scattering hydrometeor albedo is thus significantly less than unity for column-like ice crystals relative to aggregates or larger dendrites and plates.

## Chapter 3

### The Planar-Stratified 1D UMRT Model Incorporating Aspherical Hydrometeors

It has been shown that the 1D UMRT model maintains unconditional numerical stability and computational efficiency for plane-parallel multilayer clouds composed of spherical polydisperse hydrometeors [122]. Extending UMRT to incorporate randomly-oriented aspherical hydrometeor scattering matrices requires: 1) a proof of transition matrix symmetry as required by the UMRT algorithm, and 2) explicit specification of particle size distributions and phase matrices for multiple habits of aspherical hydrometeors. In this chapter, we first discuss UMRT transition matrix symmetry in the context of the use of the aspherical OpenSSP hydrometeor database. The required transition matrix symmetry is shown to be fulfilled because any OpenSSP Stokes matrix exhibits the necessary block-diagonal structure, albeit with small asymmetric deviations which are negligible for most remote sensing applications. A gamma size distribution for OpenSSP frozen hydrometeors and comparable exponential size distribution for Mie spheres are determined based on the law of mass conservation. A new method for estimating ice habit probabilities based on the principle of maximum entropy is also developed. Finally, simulation results for dual-polarized multi-stream microwave radiances using the extended UMRT model are presented along with an intercomparison of brightness temperature imagery computed for Mie spherical particles versus aspherical OpenSSP hydrometeors at frequencies from 10 to  $\sim 1$  THz.

### 3.1 Planar-Stratified Radiative Transfer Model

#### 3.1.1 Radiative Transfer Equation

The differential radiative transfer equation describes the propagation of polarimetric radiation fields in an arbitrary medium. For a sparse medium (e.g. the atmosphere) under incoherent addition of Stokes parameters and local thermodynamic equilibrium, the radiation field is governed by:

$$\frac{d\bar{I}}{ds} \triangleq \hat{s} \cdot \nabla \bar{I} = -\bar{\kappa}_e(\bar{r}, \hat{s}) \cdot \bar{I}(\bar{r}, \hat{s}) + \bar{\kappa}_a(\bar{r}, \hat{s}) \cdot B(f, T(\bar{r})) + \int_{4\pi} \bar{P}(\bar{r}, \hat{s}, \hat{s}') \cdot \bar{I}(\bar{r}, \hat{s}') d\Omega' \quad (3.1)$$

where  $\bar{\kappa}_e$  is the extinction matrix that describes the attenuation rates in coherent wave propagation due to absorption and scattering,  $\bar{\kappa}_a$  is the absorption vector for both the scatterers and the background medium,  $B(f, T(\bar{r}))$  is the Planck function at thermodynamic temperature  $T$  and frequency  $f$ , and  $\bar{P}(\bar{r}, \hat{s}, \hat{s}')$  is the scattering phase matrix coupling the radiation field from direction  $\hat{s}'$  into the direction  $\hat{s}$  [123, 41]. The radiation field  $\bar{I}$  in (3.1) can be represented by a four-element modified Stokes vector defined as:

$$\bar{I}(\bar{r}, \hat{s}, f) = \begin{bmatrix} I_v \\ I_h \\ U \\ V \end{bmatrix} \triangleq \frac{1}{\eta} \begin{bmatrix} \langle |E_v|^2 \rangle \\ \langle |E_h|^2 \rangle \\ 2\text{Re}\langle E_v E_h^* \rangle \\ 2\text{Im}\langle E_v E_h^* \rangle \end{bmatrix} \left( \frac{\text{W}}{\text{m}^2 - \text{sr} - \text{Hz}} \right) \quad (3.2)$$

where  $I_v$  and  $I_h$  are the specific intensities of the vertically and horizontally polarized electromagnetic fields  $E_v$  and  $E_h$  (respectively), and  $\eta$  is the wave impedance.

The general radiative transfer equation (3.1) cannot be solved analytically for several reasons [84]. First, the equation is in a mixed integro-differential form. Second, only the incident radiances are known at each boundary, but the scattered radiances remain unknown. Third, the solution of the RT equation exists in a five dimensional space of four coupled radiation components, that is, three independent spatial variables to determine the position  $\bar{r}$  and two angular variables to determine the propagation direction  $\hat{s}$  for each of the four Stokes parameters.

Methods for finding either the deterministic solution or the statistical solution of the RT

equation (3.1) were developed by Chandrasekhar [18] with additional methods applicable to terrestrial plane-parallel atmospheres, followed by Ishimaru, 1978 [57], van de Hulst, 1980 [125], Tsang et al., 1985 [123], Gasiewski, 1993 [41], Matzler 2006 [90], Marshak and Davis 2006 [84], and Stamnes et al., 2015 [117].

### 3.1.2 The Unified Microwave Radiative Transfer (UMRT) Model

The UMRT algorithm developed by *Tian and Gasiewski* [122] provides a fast and numerically stable solution to the 1D radiative transfer equation for the first two Stokes parameters based on the planar-stratified approximation with the azimuthal symmetry, where a horizontally homogeneous medium with sparse dielectric spheres is assumed for the atmosphere. The radiation field in the radiative transfer equation is represented by the first two Stokes parameters (i.e.  $I_v$  and  $I_h$ ), which are functions of elevation angle  $\theta$ , height  $z$  and frequency  $f$ . The elevation angle  $\theta$  is the angle of the propagation direction defined relative to the zenith direction. Applying the Rayleigh-Jean's approximation, the 1D radiative transfer equation for the UMRT model can be simplified as:

$$\cos\theta \frac{d\bar{T}_B(z, \theta, f)}{dz} = -\bar{\kappa}_e(z, \theta)\bar{T}_B(z, \theta, f) + \bar{\kappa}_a(z, \theta)T(z) + \int_0^\pi \bar{P}'(z, \theta, \theta', f)\bar{T}_B(z, \pi - \theta', f) \sin\theta' d\theta' \quad (3.3)$$

where  $T(z)$  is the temperature at height  $z$ , and  $\bar{T}_B$  is the brightness temperature vector and related to the radiation field by:

$$\bar{T}_B \triangleq \frac{\lambda^2 \bar{I}}{K} = \frac{\lambda^2}{K} \begin{bmatrix} I_v \\ I_h \end{bmatrix} \quad (\text{Kelvin}) \quad (3.4)$$

where  $\lambda$  is the wavelength and  $K$  is Boltzmann's constant (i.e.  $1.38 \times 10^{-23}$  Joule/Kelvin). The matrix  $\bar{P}'(z, \theta, \theta', f)$  is the azimuthally reduced  $2 \times 2$  phase matrix:

$$\bar{P}'(z, \theta, \theta', f) \triangleq \int_0^{2\pi} \bar{P}(z, \theta, \theta', \Delta\phi, f) d\Delta\phi \quad (3.5)$$

The above differential radiative transfer equation (DRTE) is most effectively solved for meteorological applications using a discrete set of upwelling and downwelling radiation streams. Before the discretization of the DRTE over a set of quadrature angles the key elements of the DRTE

(i.e.  $\overline{\kappa}_e$ ,  $\overline{\kappa}_a$ , and  $\overline{P}$ ) must be determined based on the single-scattering parameters of Mie spheres and the spherical particle size distributions.

Two well-known particle size distributions are commonly used to model the size statistics of Mie spheres. Liquid hydrometeors have been shown to closely follow the Marshall-Palmer size distribution function [85]:

$$n(D) = N_o e^{-\Lambda D} \quad \text{where} \quad \begin{cases} N_o = 8 \times 10^3 \text{ (m}^{-3} \cdot \text{mm}^{-1}) \\ \Lambda = 4.1 R^{-0.21} \text{ (mm}^{-1}) \end{cases} \quad (3.6)$$

where  $R$  is the rain rate in mm/hr. Snowflakes have been shown to closely follow the Sekhon-Srivastava (SS) size distribution function [107]:

$$n(D) = N_o e^{-\Lambda D} \quad \text{where} \quad \begin{cases} N_o = 2.50 \times 10^3 R^{-0.94} \text{ (m}^{-3} \cdot \text{mm}^{-1}) \\ \Lambda = 2.29 R^{-0.45} \text{ (mm}^{-1}) \end{cases} \quad (3.7)$$

where  $R$  is the liquid equivalent precipitation rate in mm/hr. An exponential size distribution function can be used for spherical graupel with a fixed number density  $N_o$  and a variable mean particle size to account for the total graupel mass content of a cloud layer [103, 121].

For spherical particles the extinction matrix  $\overline{\kappa}_e$  is diagonal with identical elements of the scalar extinction coefficient [123]. The absorption vector  $\overline{\kappa}_a$  is reduced to the scale absorption coefficient. These scalar coefficients including the scattering coefficient  $\kappa_s$  are determined as:

$$\kappa_e = \int_0^\infty \eta_e \left( \frac{\pi D}{\lambda}, m \right) \frac{\pi D^2}{4} n(D) dD \quad (3.8)$$

$$\kappa_s = \int_0^\infty \eta_s \left( \frac{\pi D}{\lambda}, m \right) \frac{\pi D^2}{4} n(D) dD \quad (3.9)$$

$$\kappa_a = \kappa_e - \kappa_s \quad (3.10)$$

where  $D$  is the diameter of a sphere, and the efficiencies  $\eta_e$  and  $\eta_s$  are calculated by (2.5) and (2.6). The reduced phase matrix  $\overline{P}'(z, \theta, \theta', f)$  can be determined by the steps in Figure 3.1. The modified Stokes matrix as a function of incident and scattering angles is obtained by pre- and post-rotation of the polarization basis of Stokes matrix  $\overline{L}(\Theta)$  (2.12) computed within forward scattering coordinates

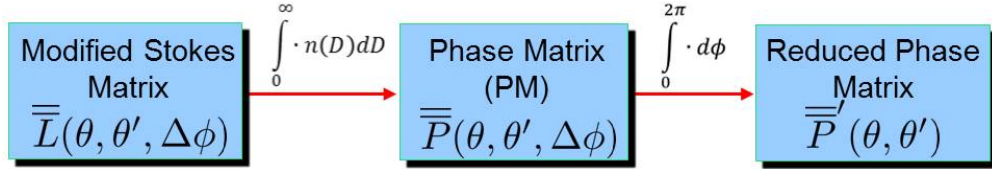


Figure 3.1: Calculation of the reduced phase matrix for spherical particle polydispersions.

(see Appendix B for details). In this study, we use Reinser’s microphysical model for hydrometeors with five categories (i.e., cloud liquid, rain, cloud ice, snow, and graupel). The total effective radiative parameters in the RT equation (3.3) are the sum of the respective calculations for each of the five categories.

The UMRT radiative transfer equation is discretized using an arbitrary number of up- and down-welling streams. The UMRT algorithm provides a level-centric planar-stratified multi-stream forward RT solution along with a fast top-of-atmosphere Jacobian calculation by reusing the layer matrix operators computed in forward RT calculations [122]. One of the key features of the UMRT algorithm is that it takes advantage of the symmetric properties of the reduced Mie phase matrix for dual-polarization radiances to realize unconditional numerical stability and high computational efficiency for all matrix operations required by the discrete-ordinate eigenanalysis method [118].

### 3.1.3 Generic Method of Incorporation Aspherical Hydrometeors into RT Model

Determining the radiative parameters of aspherical hydrometeor polydispersions is the first task for calculating forward microwave radiances using a radiative transfer model. In general, the extinction matrix for aspherical particles is no longer a diagonal matrix. Also, in general, the elements of the absorption vector are non-zero. The phase matrix can be obtained based on an ensemble averaged Stokes matrix over particle sizes, habits, and prescribed orientation distributions [123].

A generic routine for the extinction matrix, absorption vector, and the phase matrix for aspherical particles has been discussed by Tsang et al. [123], where the complex  $2 \times 2$  scattering function matrix of a single scatterer is first required to be determined using techniques for calculation



of scattered and internal electromagnetic fields from arbitrarily shaped finite object (e.g. DDA [24], GMM [134], and FDTD [66] etc.). The expression of the scattering function matrix  $\overline{\overline{F}}(\theta, \phi, \theta', \phi')$  in the vertical-horizontal polarization basis can be written as:

$$\overline{\overline{F}}(\theta, \phi, \theta', \phi') = \begin{bmatrix} f_{vv}(\theta, \phi, \theta', \phi') & f_{vh}(\theta, \phi, \theta', \phi') \\ f_{hv}(\theta, \phi, \theta', \phi') & f_{vv}(\theta, \phi, \theta', \phi') \end{bmatrix} \quad (3.11)$$

where  $(\theta', \phi')$  are the incident directions and  $(\theta, \phi)$  are the scattering directions.

For a monodispersion of aspherical particles, the extinction matrix can subsequently be determined using the coherent wave propagation theory with Foldy's approximation:

$$\overline{\overline{\kappa}}_e = \begin{bmatrix} -2\text{Re}\{M_{vv}\} & 0 & -\text{Re}\{M_{vh}\} & -\text{Im}\{M_{vh}\} \\ 0 & -2\text{Re}\{M_{hh}\} & -\text{Re}\{M_{hv}\} & \text{Im}\{M_{hv}\} \\ -2\text{Re}\{M_{hv}\} & -2\text{Re}\{M_{vh}\} & -(\text{Re}\{M_{vv}\} + \text{Re}\{M_{hh}\}) & (\text{Im}\{M_{vv}\} - \text{Im}\{M_{hh}\}) \\ 2\text{Im}\{M_{hv}\} & -2\text{Im}\{M_{vh}\} & -(\text{Im}\{M_{vv}\} - \text{Im}\{M_{hh}\}) & -(\text{Re}\{M_{vv}\} + \text{Re}\{M_{hh}\}) \end{bmatrix} \quad (3.12)$$

where

$$M_{jl} = \frac{i2\pi n_o}{k} \langle f_{jl}(\theta', \phi', \theta', \phi') \rangle_o \quad j, l = v, h \quad (3.13)$$

with  $n_o$  is the number of particles per unit volume,  $k$  is the wavenumber in vacuum, and  $\langle f_{jl}(\theta', \phi', \theta', \phi') \rangle_o$  denotes the ensemble average over the orientation and size distribution of the particles [123], and  $i = \sqrt{-1}$ . Similarly, the phase matrix can be calculated by multiplying the ensemble averaged Stokes matrix with  $n_o$ :

$$\overline{\overline{P}}(\theta, \phi, \theta', \phi') = n_o \langle \overline{\overline{L}}(\theta, \phi, \theta', \phi') \rangle_o \quad (3.14)$$

where

$$\langle \bar{L}(\theta, \phi, \theta', \phi') \rangle_o = \begin{bmatrix} \langle |f_{vv}|^2 \rangle_o & \langle |f_{vh}|^2 \rangle_o & \langle \text{Re}\{f_{vv}f_{vh}^*\} \rangle_o & \langle -\text{Im}\{f_{vv}f_{vh}^*\} \rangle_o \\ \langle |f_{hv}|^2 \rangle_o & \langle |f_{hh}|^2 \rangle_o & \langle \text{Re}\{f_{hv}f_{hh}^*\} \rangle_o & \langle -\text{Im}\{f_{hv}f_{hh}^*\} \rangle_o \\ \langle 2\text{Re}\{f_{vv}f_{hv}^*\} \rangle_o & \langle 2\text{Re}\{f_{vh}f_{hh}^*\} \rangle_o & \langle \text{Re}\{f_{vv}f_{hh}^* + f_{vh}f_{hv}^*\} \rangle_o & \langle -\text{Im}\{f_{vv}f_{hh}^* - f_{vh}f_{hv}^*\} \rangle_o \\ \langle 2\text{Im}\{f_{vv}f_{hv}^*\} \rangle_o & \langle 2\text{Im}\{f_{vh}f_{hh}^*\} \rangle_o & \langle \text{Im}\{f_{vv}f_{hh}^* + f_{vh}f_{hv}^*\} \rangle_o & \langle \text{Re}\{f_{vv}f_{hh}^* - f_{vh}f_{hv}^*\} \rangle_o \end{bmatrix} \quad (3.15)$$

Finally, the absorption vector can be determined using (3.12) and (3.14):

$$\bar{\kappa}_a = \begin{bmatrix} \kappa_{e11} - \int [P_{11} + P_{21}] d\Omega_s \\ \kappa_{e22} - \int [P_{12} + P_{22}] d\Omega_s \\ 2\kappa_{e13} + 2\kappa_{e23} - 2 \int [P_{13} + P_{23}] d\Omega_s \\ -2\kappa_{e14} - 2\kappa_{e24} + 2 \int [P_{14} + P_{24}] d\Omega_s \end{bmatrix} \quad (3.16)$$

where  $\kappa_{eij}$  and  $P_{ij}$  are the  $(ij)^{\text{th}}$  element of the extinction matrix and phase matrix.

### 3.2 UMRT Transition Matrix Symmetry

The symmetry of the transition matrix of the one-dimensional discrete ordinate DRTE is based on phase matrix reciprocity, as considered in the discrete-ordinate matrix-operator method developed by Nakajima and Tanaka [91] and summarized by Stamnes [118]. This method improves the computational stability of the radiative transfer solution but introduces rounding errors in the approximation of the symmetric transition matrices. These early works also failed to theoretically address the matrix inversion instability in the discrete-ordinate eigenanalysis method implementation for high albedo cloud layers. The transition matrix of the normalized DRTE in the DOTLRT and UMRT framework [127, 122] addresses this numerical instability for planar-stratified multilayer media composed of spherical scatterers. The transition matrix is implicitly defined as the following

$4M \times 4M$  square matrix.

$$\underbrace{\frac{d}{dz} \begin{bmatrix} \bar{u}_v \\ \bar{u}_h \\ \bar{v}_v \\ \bar{v}_h \end{bmatrix}}_{4M \times 1} = \underbrace{\begin{bmatrix} -\bar{U} & -\bar{D} \\ \bar{D} & \bar{U} \end{bmatrix}}_{4M \times 4M} \underbrace{\begin{bmatrix} \bar{u}_v \\ \bar{u}_h \\ \bar{v}_v \\ \bar{v}_h \end{bmatrix}}_{4M \times 1} + \underbrace{\begin{bmatrix} \bar{f} \\ \bar{f} \\ -\bar{f} \\ -\bar{f} \end{bmatrix}}_{4M \times 1} \quad (3.17)$$

where  $\bar{u}_v$  and  $\bar{u}_h$  are the vectors of the normalized upwelling (+) radiation streams for vertical (subscript  $v$ ) and horizontal (subscript  $h$ ) polarization,  $\bar{v}_v$  and  $\bar{v}_h$  are (similarly) the vectors of the downwelling (-) streams,  $M$  is the number of radiation streams between zenith and the horizon, and  $\bar{f}$  is the source term representing thermal emission from the medium of interest. The submatrices  $\bar{U}$  and  $\bar{D}$  of the transition matrix are shown in (3.18) and (3.19) respectively, and constructed by using the elements of the azimuthally averaged reduced Mie phase matrix and the scalar extinction coefficient  $\kappa_e$ :

$$\bar{U} = \begin{bmatrix} g_{11}P_{vv11}^{++} & \cdots & g_{1M}P_{vv1M}^{++} & g_{11}P_{vh11}^{++} & \cdots & g_{1M}P_{vh1M}^{++} \\ \vdots & \ddots & \vdots & \vdots & \ddots & \vdots \\ g_{M1}P_{vvM1}^{++} & \cdots & g_{MM}P_{vvMM}^{++} & g_{M1}P_{vhM1}^{++} & \cdots & g_{MM}P_{vhMM}^{++} \\ \hline g_{11}P_{hv11}^{++} & \cdots & g_{1M}P_{hv1M}^{++} & g_{11}P_{hh11}^{++} & \cdots & g_{1M}P_{hh1M}^{++} \\ \vdots & \ddots & \vdots & \vdots & \ddots & \vdots \\ g_{M1}P_{hvM1}^{++} & \cdots & g_{MM}P_{hvMM}^{++} & g_{M1}P_{hhM1}^{++} & \cdots & g_{MM}P_{hhMM}^{++} \end{bmatrix} + \begin{bmatrix} \frac{\kappa_e}{\mu_1} & \cdots & 0 & 0 & \cdots & 0 \\ \vdots & \ddots & \vdots & \vdots & \ddots & \vdots \\ 0 & \cdots & \frac{\kappa_e}{\mu_M} & 0 & \cdots & 0 \\ \hline 0 & \cdots & 0 & \frac{\kappa_e}{\mu_1} & \cdots & 0 \\ \vdots & \ddots & \vdots & \vdots & \ddots & \vdots \\ 0 & \cdots & 0 & 0 & \cdots & \frac{\kappa_e}{\mu_M} \end{bmatrix} \quad (3.18)$$

$$\overline{\overline{D}} = \begin{bmatrix} g_{11}P_{vv11}^{+-} & \cdots & g_{1M}P_{vv1M}^{+-} & g_{11}P_{vh11}^{+-} & \cdots & g_{1M}P_{vh1M}^{+-} \\ \vdots & \ddots & \vdots & \vdots & \ddots & \vdots \\ g_{M1}P_{vvM1}^{+-} & \cdots & g_{MM}P_{vvMM}^{+-} & g_{M1}P_{vhM1}^{+-} & \cdots & g_{MM}P_{vhMM}^{+-} \\ \hline g_{11}P_{hv11}^{+-} & \cdots & g_{1M}P_{hv1M}^{+-} & g_{11}P_{hh11}^{+-} & \cdots & g_{1M}P_{hh1M}^{+-} \\ \vdots & \ddots & \vdots & \vdots & \ddots & \vdots \\ g_{M1}P_{hvM1}^{+-} & \cdots & g_{MM}P_{hvMM}^{+-} & g_{M1}P_{hhM1}^{+-} & \cdots & g_{MM}P_{hhMM}^{+-} \end{bmatrix} \quad (3.19)$$

where the reduced Mie phase matrix elements are defined as:

$$\begin{aligned} P_{\alpha\beta ji}^{++} &= P_{\alpha\beta}(+\mu_j, +\mu_i) \\ P_{\alpha\beta ji}^{+-} &= P_{\alpha\beta}(+\mu_j, -\mu_i) \\ P_{\alpha\beta ji}^{-+} &= P_{\alpha\beta}(-\mu_j, +\mu_i) \\ P_{\alpha\beta ji}^{--} &= P_{\alpha\beta}(-\mu_j, -\mu_i) \end{aligned} \quad j = 1, 2, \dots, M \quad i = 1, 2, \dots, M \quad (3.20)$$

where  $\alpha$  and  $\beta$  denote either vertical ( $v$ ) or horizontal ( $h$ ) polarization, the subscripts  $i$  and  $j$  are the indexes of those radiation streams which coincide with the Gauss-Legendre quadrature angles,  $\mu_j = \cos \theta_j$  is the cosine of the  $j^{\text{th}}$  scattered quadrature angle, and  $\mu_i$  is the cosine of the  $i^{\text{th}}$  incident quadrature angle. The normalization factors are computed as  $g_{ji} = -\sqrt{\frac{\gamma_j \gamma_i}{\mu_j \mu_i}}$ , where  $\gamma_j$  and  $\gamma_i$  are the Christoffel weights.

Provided that the extinction coefficient is greater than or equal to the corresponding scattering coefficient which is always the case for passive lossy media, it was shown [122] that the subblock sum and difference  $\overline{\overline{U}} + \overline{\overline{D}}$  and  $\overline{\overline{U}} - \overline{\overline{D}}$  matrices are both symmetric and positive definite for the first two coupled Stokes parameters (i.e.,  $v$  and  $h$ ) for Mie spherical scatterers. The study by Tian and Gasiewski was based on the discrete ordinate tangent linear radiative transfer model (DOTLRT) developed by Voronovich et al. [127] for a single polarization. By applying analytic factorization of the symmetric and positive definite matrices an inherently stable and computationally accurate radiative transfer solution to compute dual-polarization multi-stream reflectivity and transmissivity

matrices of each vertically stacked slab resulted.

### 3.2.1 Requirements of Transition Matrix Symmetry

The transition matrix subblock sum and difference (SBSD) symmetry in the UMRT framework, including symmetry of the subblock matrices  $\overline{\overline{U}}$  and  $\overline{\overline{D}}$ , requires that the elements of the reduced phase matrix satisfy two sets of symmetric relationships:

$$P_{\alpha\beta ji}^{++} = P_{\alpha\beta ji}^{--}, \quad P_{\alpha\beta ji}^{+-} = P_{\alpha\beta ji}^{-+} \quad (3.21)$$

$$P_{\alpha\beta ji}^{++} = P_{\beta\alpha ij}^{++}, \quad P_{\alpha\beta ji}^{+-} = P_{\beta\alpha ij}^{-+} \quad (3.22)$$

The relationship (3.21) requires that the reduced phase matrix elements remain unchanged by inversion of the signs of  $\mu_i$  and  $\mu_j$ . Relationship (3.22) requires that the phase matrix elements also remain unchanged by permutation of both angular indexes and polarizations.

The UMRT model was developed for planar-stratified multilayer media and requires only the vertical and horizontal polarized Stokes parameters to represent the radiation field. The reduced phase matrix based on a multiphase distribution of aspherical hydrometeors can be related to the Stokes matrix of a single hydrometeor by:

$$\overline{\overline{P}}(\theta_s, \theta_i) = \sum_{i_s=1}^{N_s} p_{i_s} \int_0^\infty \langle \overline{\overline{L}} \rangle_o(\theta_s, \theta_i; D, i_s) n(D, i_s) dD \quad (3.23)$$

where  $\theta_i$  is the incident angle,  $\theta_s$  is the scattering angle,  $i_s$  is an index denoting hydrometeor habit,  $N_s$  is the total number of habits considered,  $p_{i_s}$  is the probability of hydrometeor habit  $i_s$ ,  $\langle \cdot \rangle_o$  denotes an average over random orientations,  $\langle \overline{\overline{L}} \rangle_o(\theta_s, \theta_i; D, i_s)$  is the reduced orientation-averaged Stokes matrix of a single hydrometeor with maximum diameter  $D$  and habit index of  $i_s$ , and  $n(D, i_s)$  are particle size distributions (PSDs) of each habit  $i_s$ .

It is evident from (3.23) that the requirements of transition matrix SBSB symmetry (3.21) and (3.22) can be rewritten in terms of the discretized Stokes matrix elements of any OpenSSP

hydrometeor as shown in (3.24) and (3.25) as:

$$L_{\alpha\beta ji}^{++} = L_{\alpha\beta ji}^{--}, \quad L_{\alpha\beta ji}^{+-} = L_{\alpha\beta ji}^{-+} \quad (3.24)$$

$$L_{\alpha\beta ji}^{++} = L_{\beta\alpha ij}^{++}, \quad L_{\alpha\beta ji}^{+-} = L_{\beta\alpha ij}^{-+} \quad (3.25)$$

where

$$\begin{aligned} L_{\alpha\beta ji}^{++} &= \langle L_{\alpha\beta} \rangle_o(+\mu_j, +\mu_i) \\ L_{\alpha\beta ji}^{+-} &= \langle L_{\alpha\beta} \rangle_o(+\mu_j, -\mu_i) \\ L_{\alpha\beta ji}^{-+} &= \langle L_{\alpha\beta} \rangle_o(-\mu_j, +\mu_i) \\ L_{\alpha\beta ji}^{--} &= \langle L_{\alpha\beta} \rangle_o(-\mu_j, -\mu_i) \\ j &= 1, 2, \dots, M \quad i = 1, 2, \dots, M \\ \alpha, \beta &= v \text{ or } h \end{aligned} \quad (3.26)$$

### 3.2.2 Transition Matrix Symmetry Based on OpenSSP Hydrometeors

Consider first a Stokes matrix in the block-diagonal form for a randomly oriented particle with at least one plane of symmetry [18, 125, 89, 90, 88, 117]:

$$\overline{\overline{L}}_o(\Theta) = \begin{bmatrix} \langle L_{vv} \rangle_o & \langle L_{vh} \rangle_o & 0 & 0 \\ \langle L_{vh} \rangle_o & \langle L_{hh} \rangle_o & 0 & 0 \\ 0 & 0 & \langle L_{UU} \rangle_o & \langle L_{UV} \rangle_o \\ 0 & 0 & -\langle L_{UV} \rangle_o & \langle L_{VV} \rangle_o \end{bmatrix} \quad (3.27)$$

where we use the modified Stokes vector representation  $[I_v, I_h, U, V]^T$  and  $\Theta$  is the forward scattering angle as illustrated in Figure B.1. The off-diagonal zero values follow from the presumed single plane of symmetry. It can be shown (see Appendix B) that the transition matrix SBSD symmetry requirements (3.24) and (3.25) are fulfilled by any Stokes matrix in the above block-diagonal form (3.27).

Consider now aspherical hydrometeors with random orientations but without the requirement of any necessary planes of symmetry. Such hydrometeors are well represented in the OpenSSP

database. For a simulated OpenSSP snow aggregate of any size, there is in general a lack of an intrinsic plane of symmetry due to the randomness in the self-collection particle growth model [68]. The corresponding Stokes matrix  $\langle \bar{\bar{L}} \rangle_o(\Theta)$  exhibits small but fundamental nonzero elements in the off-diagonal  $2 \times 2$  submatrix blocks which introduce an asymmetric component into the SBSD matrices of the transition matrix (3.17). In order to analyze this asymmetric component, the Stokes matrix  $\langle \bar{\bar{L}} \rangle_o(\theta_s, \theta_i)$  can be decomposed into two parts, one symmetric matrix  $\langle \bar{\bar{L}} \rangle_{o,\text{sym}}(\theta_s, \theta_i)$  that meets the requirements of (3.24) and (3.25), and the other asymmetric matrix  $\langle \bar{\bar{L}} \rangle_{o,\text{asym}}(\theta_s, \theta_i)$  that does not but can be treated as a perturbation matrix in the DRTE (3.17) due to its small valued elements:

$$\begin{aligned}
\langle \bar{\bar{L}} \rangle_o(\theta_s, \theta_i) &= \langle \bar{\bar{L}} \rangle_{o,\text{sym}}(\theta_s, \theta_i) + \langle \bar{\bar{L}} \rangle_{o,\text{asym}}(\theta_s, \theta_i) \\
&= \int_0^{2\pi} \bar{\bar{R}}(-i_2) \langle \bar{\bar{L}} \rangle_{o,\text{sym}}(\Theta) \bar{\bar{R}}(-i_1) d\Delta\phi \\
&\quad + \int_0^{2\pi} \bar{\bar{R}}(-i_2) \langle \bar{\bar{L}} \rangle_{o,\text{asym}}(\Theta) \bar{\bar{R}}(-i_1) d\Delta\phi
\end{aligned} \tag{3.28}$$

where  $\bar{\bar{R}}(-i_{1,2})$  is the rotation matrix defined in (B.1) and

$$\begin{aligned}
\langle \bar{\bar{L}} \rangle_{o,\text{sym}}(\Theta) &= \\
&\begin{bmatrix} \langle L_{vv} \rangle_o & \langle L_{vh} \rangle_o & 0 & 0 \\ \langle L_{vh} \rangle_o & \langle L_{hh} \rangle_o & 0 & 0 \\ 0 & 0 & \langle L_{UU} \rangle_o & \langle L_{UV} \rangle_o \\ 0 & 0 & -\langle L_{UV} \rangle_o & \langle L_{VV} \rangle_o \end{bmatrix}
\end{aligned} \tag{3.29}$$

$$\begin{aligned}
\langle \bar{\bar{L}} \rangle_{o,\text{asym}}(\Theta) &= \\
&\begin{bmatrix} 0 & 0 & \langle L_{vU} \rangle_o & \langle L_{vV} \rangle_o \\ 0 & 0 & \langle L_{hU} \rangle_o & \langle L_{hV} \rangle_o \\ -2\langle L_{vU} \rangle_o & -2\langle L_{hU} \rangle_o & 0 & 0 \\ 2\langle L_{vV} \rangle_o & 2\langle L_{hV} \rangle_o & 0 & 0 \end{bmatrix}
\end{aligned} \tag{3.30}$$

As discussed in Section 2, the random orientation-averaged full Stokes matrix  $\langle \bar{\bar{L}} \rangle_o(\Theta)$  of 203 selected OpenSSP hydrometeors was calculated using DDSCAT v7.3.1 at key passive remote sensing frequencies from 10 to 874 GHz and averaging over 6,156 particle orientations. Applying (3.28), the matrices  $\langle \bar{\bar{L}} \rangle_{o,\text{sym}}(\theta_s, \theta_i)$  and  $\langle \bar{\bar{L}} \rangle_{o,\text{asym}}(\theta_s, \theta_i)$  were calculated for the selected hydrometeors and frequencies of this thesis. It was found that the first  $2 \times 2$  matrix subblock elements of  $\langle \bar{\bar{L}} \rangle_{o,\text{asym}}(\theta_s, \theta_i)$  are typically four orders of magnitude smaller than the corresponding elements of  $\langle \bar{\bar{L}} \rangle_{o,\text{sym}}(\theta_s, \theta_i)$  for any of the OpenSSP hydrometeors selected for use in this study. It is thus reasonable to treat the asymmetric component of the Stokes matrix as a small perturbation to the symmetric component. In addition, a numerical calculation of the entrywise ratios of the first  $2 \times 2$  matrix subblock elements of  $\langle \bar{\bar{L}} \rangle_{o,\text{asym}}(\theta_s, \theta_i)$  and  $\langle \bar{\bar{L}} \rangle_{o,\text{sym}}(\theta_s, \theta_i)$  was performed. By averaging over 1,008 scattering function matrix calculations at discrete orientations on selected snow aggregates, it was shown that the mean entrywise ratios due to non-zero elements of  $\langle \bar{\bar{L}} \rangle_{o,\text{asym}}(\theta_s, \theta_i)$  are limited to  $< 4 \times 10^{-4}$  (see Appendix C).

### 3.2.3 Theoretical Analysis of Transition Matrix Perturbation

The impact of the asymmetric component  $\langle \bar{\bar{L}} \rangle_{o,\text{asym}}(\theta_s, \theta_i)$  of the orientation-averaged Stokes matrix on the DRTE solution can be bounded for the selected OpenSSP hydrometeors through a perturbation analysis of the transition matrix. Taking both  $\langle \bar{\bar{L}} \rangle_{o,\text{sym}}(\theta_s, \theta_i)$  and  $\langle \bar{\bar{L}} \rangle_{o,\text{asym}}(\theta_s, \theta_i)$  from (3.28) into (3.23) and constructing the transition matrix for aspherical hydrometeors, the DRTE (3.17) can be rewritten as:



$$\begin{aligned}
\underbrace{\frac{d}{dz} \begin{bmatrix} \bar{u}_v \\ \bar{u}_h \\ \bar{v}_v \\ \bar{v}_h \end{bmatrix}}_{4M \times 1} &= \left( \underbrace{\begin{bmatrix} -\bar{U} & -\bar{D} \\ \bar{D} & \bar{U} \end{bmatrix}}_{4M \times 4M} + \underbrace{\begin{bmatrix} \bar{E}_1 & \bar{E}_2 \\ \bar{E}_3 & \bar{E}_4 \end{bmatrix}}_{4M \times 4M} \right) \underbrace{\begin{bmatrix} \bar{u}_v \\ \bar{u}_h \\ \bar{v}_v \\ \bar{v}_h \end{bmatrix}}_{4M \times 1} + \underbrace{\begin{bmatrix} \bar{f} \\ \bar{f} \\ -\bar{f} \\ -\bar{f} \end{bmatrix}}_{4M \times 1} \\
&= \left( \bar{T}_{sym} + \bar{T}_{asym} \right) \underbrace{\begin{bmatrix} \bar{u}_v \\ \bar{u}_h \\ \bar{v}_v \\ \bar{v}_h \end{bmatrix}}_{4M \times 1} + \underbrace{\begin{bmatrix} \bar{f} \\ \bar{f} \\ -\bar{f} \\ -\bar{f} \end{bmatrix}}_{4M \times 1}
\end{aligned} \tag{3.31}$$

where  $\bar{T}_{sym}$  is constructed out of the symmetric component of Stoke matrix  $\langle \bar{L} \rangle_{o,sym}(\theta_s, \theta_i)$  and  $\bar{T}_{asym}$  is constructed out of the asymmetric component  $\langle \bar{L} \rangle_{o,asym}(\theta_s, \theta_i)$ . The sub-matrices  $\bar{E}_1$  through  $\bar{E}_4$  are small block elements of  $\bar{T}_{asym}$ . Note that the  $4M$  diagonal elements of  $\bar{T}_{asym}$  are zero.

Applying (3.31) to a planar-stratified layer of aspherical hydrometeors, the dual-polarized radiation streams at the top of the layer can be obtained using the matrix exponential operator by:

$$\begin{aligned}
\begin{bmatrix} \bar{u}_v(z) \\ \bar{u}_h(z) \\ \bar{v}_v(z) \\ \bar{v}_h(z) \end{bmatrix} &= e^{(\bar{T}_{sym} + \bar{T}_{asym})z} \begin{bmatrix} \bar{u}_v(0) \\ \bar{u}_h(0) \\ \bar{v}_v(0) \\ \bar{v}_h(0) \end{bmatrix} + \bar{C} \\
&= e^{(\bar{T}_{sym} + \bar{T}_{asym})z} \bar{X}(0) + \bar{C}
\end{aligned} \tag{3.32}$$

$$\bar{X}(0) \triangleq \begin{bmatrix} \bar{u}_v(0) \\ \bar{u}_h(0) \\ \bar{v}_v(0) \\ \bar{v}_h(0) \end{bmatrix} \tag{3.33}$$

where  $\bar{C}$  is a constant vector determined by the source vector of (3.31), and  $\bar{X}(0)$  is a set of layer bottom radiation streams (i.e. lower boundary conditions at  $z = 0$ ).

Thus, for an arbitrary set of layer bottom radiation streams  $\bar{X}(0)$ , the worst case impact of neglecting  $\bar{\bar{T}}_{asym}$  on the radiative solution is now determinable. To quantize this error caused by neglecting  $\langle \bar{L} \rangle_{o,asym}(\theta_s, \theta_i)$ , we examine how the matrix exponential  $e^{(\bar{\bar{T}}_{sym} + \bar{\bar{T}}_{asym})z}$  is affected by the perturbation matrix  $\bar{\bar{T}}_{asym}$ . This problem has been well studied [126, 100, 60], where the perturbation bounds for a scalar error function  $\phi(z)$  that is directly applicable to the above transition matrix perturbation problem (3.32) were found:

$$\phi(z) \triangleq \frac{\left\| e^{(\bar{\bar{T}}_{sym} + \bar{\bar{T}}_{asym})z} - e^{\bar{\bar{T}}_{sym}z} \right\|}{\left\| e^{\bar{\bar{T}}_{sym}z} \right\|} \leq z \cdot \left\| \bar{\bar{T}}_{asym} \right\| \cdot e^{(\mu(\bar{\bar{T}}_{sym}) - \alpha(\bar{\bar{T}}_{sym}) + \left\| \bar{\bar{T}}_{asym} \right\|)z} \quad (3.34)$$

where  $\|\cdot\|$  denotes the below-defined 2-norm of a square matrix,  $\mu(\bar{\bar{T}}_{sym})$  is the log norm of  $\bar{\bar{T}}_{sym}$  with respect to the 2-norm, and  $\alpha(\bar{\bar{T}}_{sym})$  is defined using the maximum eigenvalue of  $\bar{\bar{T}}_{sym}$ . Following [126], these quantities in (3.34) are explicitly defined as:

$$\begin{aligned} \left\| \bar{\bar{T}}_{asym} \right\| &= \max\{|\lambda| \mid \lambda^2 \in \text{Eigenvalues of } (\bar{\bar{T}}_{asym}^\dagger \bar{\bar{T}}_{asym})\} \\ \mu(\bar{\bar{T}}_{sym}) &= \max\{\mu \mid \mu \in \text{Eigenvalues of } ((\bar{\bar{T}}_{sym}^\dagger + \bar{\bar{T}}_{sym})/2)\} \\ \alpha(\bar{\bar{T}}_{sym}) &= \max\{\text{Re}(\lambda) \mid \lambda \in \text{Eigenvalues of } \bar{\bar{T}}_{sym}\} \end{aligned} \quad (3.35)$$

where  $\dagger$  denotes the Hermitian transpose.

Without the loss of generality, consider a unitary vector of radiation streams  $\bar{X}_i(0)$ . The radiative error introduced by the perturbation matrix  $\bar{\bar{T}}_{asym}$  is thus computed using  $\bar{X}_i(0)$  as:

$$\bar{\mathcal{E}}(z) = \left( e^{(\bar{\bar{T}}_{sym} + \bar{\bar{T}}_{asym})z} - e^{\bar{\bar{T}}_{sym}z} \right) \bar{X}_i(0) \quad (3.36)$$

The maximum root square energy eigenvector error is defined below and coincides with the numerator of the function  $\phi(z)$ :

$$\max \left( \sqrt{\bar{\mathcal{E}}^\dagger \bar{\mathcal{E}}} \right) = \left\| e^{(\bar{\bar{T}}_{sym} + \bar{\bar{T}}_{asym})z} - e^{\bar{\bar{T}}_{sym}z} \right\| \quad (3.37)$$

Thus, the maximum root square fractional error can be defined using  $\phi(z)$  and  $\bar{X}_i(0)$  as:

$$\phi'(z) = \frac{\phi(z) \left\| e^{\bar{T}_{sym} z} \right\|}{\sqrt{\bar{X}_i^\dagger(0) \left( e^{\bar{T}_{sym} z} \right)^\dagger \left( e^{\bar{T}_{sym} z} \right) \bar{X}_i(0)}} \quad (3.38)$$

Since the perturbation matrix  $\bar{T}_{asym}$  has only a small influence on the eigenvectors and eigenvalues of  $\bar{T}_{sym}$  [46], the maximum root square fractional error  $\phi'(z)$  is approximately equal to  $\phi(z)$ . Therefore, the upper bound of  $\phi(z)$  can be interpreted as the maximum relative root mean square (RMS) error of the radiation solution at  $z$  introduced by the asymmetric component of the transition matrix  $\bar{T}_{asym}$  for any initial values of radiation at  $z = 0$ .

As an example, the upper bound of the function  $\phi(z)$  is calculated for selected OpenSSP snow aggregates at five sensing frequencies greater than 180 GHz under several atmospheric cloud hydrometeor habits for a cloud thickness of 1 km, a constant temperature at 260 K, and with ice water content for any given type of OpenSSP snow hydrometeor set to 1 g/m<sup>3</sup>. The OpenSSP hydrometeor particle size distribution used is discussed in Section 3. The upper bound of  $\phi(z)$  varies with OpenSSP hydrometeor type and frequency as shown in Figure 3.2. It is evident that the perturbation bound (i.e. maximum relative error) of the radiation solution is always less than 0.01% for frequencies below 420 GHz. This error is doubled at 659.8 GHz and reaches maximum of  $\sim 0.1\%$  at 874 GHz. Furthermore, the error depends heavily on the morphological structure of snow particles at the two highest frequencies. Nevertheless, the small relative error value (i.e.  $< 0.1\%$ ) introduced by the asymmetric transition matrix  $\bar{T}_{asym}$  has little impact for the first two Stokes parameters on the overall radiative transfer solution for any of the habits studied (e.g.,  $< 0.3$  K deviation from the nominal terrestrial temperature of 300 K). We note that this impact might not be negligible for the third and fourth Stokes parameters, which are often relevant at the 0.1 K and lower level of error [96].

Therefore, the random orientation-averaged Stokes matrix of an OpenSSP aspherical hydrometeor exhibits the block-diagonal structure for use in UMRT as shown in (3.27) with negligible off-diagonal block matrices. The block-diagonal form of the symmetric Stokes matrix thus accurately

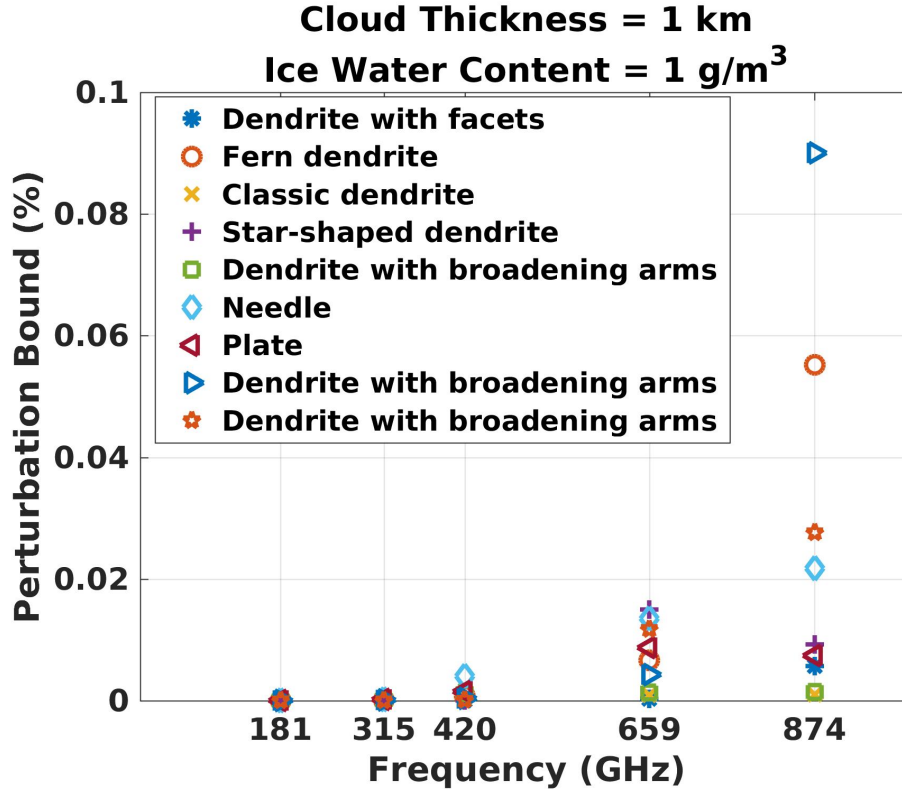


Figure 3.2: Perturbation bound for a scalar function  $\phi(z)$  used to determine relative errors of radiative transfer solutions introduced by asymmetric component of the transition matrix for OpenSSP snow aggregates. The perturbation bound varies with frequencies and snow particle types.

fulfills the transition matrix SBSD symmetry requirements for the UMRT model incorporating aspherical frozen hydrometeors based on the OpenSSP database for the first two Stokes parameters.

### 3.3 Incorporation of OpenSSP Aspherical Hydrometeors

In this study, cloud liquid water, rain and graupel are assumed to have spherical shapes and their single-scattering parameters were calculated based on Mie scattering [41]. Cloud liquid water and rain droplets follow the Marshall-Palmer particle size distributions [85], and exponential size distributions are used for graupel with a fixed number density and a variable mean particle size to account for the total graupel mass content of a cloud layer [103, 121]. The cloud ice and snow hydrometeors are represented by multi-habit mixtures of randomly oriented aspherical OpenSSP hydrometeors. Warren and Brandt's model of the ice refractive index for microwave frequencies is

used in the OpenSSP database as well as in the UMRT Mie scattering calculations for a spherical shaped particle.

### 3.3.1 Gamma Function Distribution of Particle Size

In this study, a gamma particle size distribution function [53, 41] is used for cloud ice and snow. The general form is:

$$n(D, i_s) = N_{o_{i_s}} D^{\mu(T)} e^{-\lambda(T)D} \quad (3.39)$$

where  $D$  is the maximum diameter of a frozen hydrometeor,  $i_s$  is habit index,  $N_{o_{i_s}}$  is (as discussed by Heymsfield et al. [53]) the intercept,  $\mu(T)$  is the dispersion, and  $\lambda(T)$  is the slope of the gamma distribution. The dispersion and slope are expressed as functions of temperature  $T$  and obtained by log-normal fitting to in-situ observed data. The fitted results used in the Heymsfield et al. study are:

$$\mu(T) = \begin{cases} -14.09 - 0.248T, & T < -61^\circ C, \\ -0.59 - 0.030T, & T \geq -61^\circ C, \end{cases} \quad (3.40)$$

$$\lambda(T) = \begin{cases} 9.88e^{-0.060T}, & T < -58^\circ C, \\ 0.75e^{-0.1057T}, & T \geq -58^\circ C, \end{cases} \quad (3.41)$$

and are independent of habit. By applying the above gamma distribution in (3.23), the phase matrix can be written as

$$\overline{\overline{P}}(\theta_s, \theta_i) = \sum_{i_s=1}^{N_s} p_{i_s} N_{o_{i_s}} \int_0^\infty \langle \overline{\overline{L}} \rangle_o(\theta_s, \theta_i; D, i_s) D^{\mu(T)} e^{-\lambda(T)D} dD \quad (3.42)$$

where  $N_s$  is the number of particle habits (e.g.  $N_s = 20$  for all OpenSSP pristine ice crystals and  $N_s = 9$  for all OpenSSP snow aggregates). The intercept for each particle habit  $N_{o_{i_s}}$  along with the probability of the specific frozen hydrometeor habit  $p_{i_s}$  need to be specified based on two constraints: i) conservation of mass consistent with the bulk ice density  $\rho_f$  in  $\text{g/m}^3$  (3.43) and ii) unitarity of particle probabilities (3.44), where

$$\rho_f = \sum_{i_s=1}^{N_s} p_{i_s} N_{o_{i_s}} \int_0^\infty D^{\mu(T)} e^{-\lambda(T)D} m(D, i_s) dD \quad (3.43)$$

$$\sum_{i_s=1}^{N_s} p_{i_s} = 1 \quad (3.44)$$

In the above  $m(D, i_s)$  is the specific mass of particle habit  $i_s$  and maximum diameter  $D$  which is derived from characteristic morphological records in the OpenSSP database. In this work the bulk density is obtained from the WRF model for a layer of clouds. Assuming that  $p_{i_s} = 1$  for a given habit, the first constraint is used to determine each corresponding  $N_{o_{i_s}}$ . However, the actual  $p_{i_s}$  values deserve careful consideration. Although ice habit mixture models [8, 78] developed from in-situ observed data are available, these models do not distinguish between dendrites and plates, thus they cannot be readily used to determine  $p_{i_s}$  values. Furthermore, an equal probability assumption (i.e.  $p_{i_s} = 1/N_s$ ) is not consistent with in-situ observations [8].

Instead, in this thesis, the frozen habit probabilities  $p_{i_s}$  are set to be random variables with uniform distributions between zero and one then normalized to satisfy (3.44) while maintaining consistency with (3.43). By this procedure the simulated upwelling radiances are statistical quantities due to the randomness of the underlying microphysical probability distribution. The statistics of the computed radiances are then obtained by calculating the histogram of brightness temperatures over the simulation domain. The resulting statistical data are discussed in the following two sections. Physics of the time history of the distribution extend beyond the scope of this paper. We note that both time dynamic and distribution entropy of cloud ice are being separately studied [136].

Finally, the upper limit of integration in (3.42) needs to be determined. This limit can be based on the transition size of ice particles from simple crystals to complex aggregates [106] and the maximum sizes of aggregates based upon the underlying OpenSSP growth model. According to Schmitt and Heymsfield [106], complex aggregates occur in ice clouds when crystals grow  $3.3 \pm 0.9$  times larger than the transition size  $D_t$ . This transition size can be modeled as a function of temperature  $T$  as:

$$D_t = 1.69T + 235 \quad (3.45)$$

where  $T$  is in  $^{\circ}\text{C}$  and  $D_t$  is in  $\mu\text{m}$ . For snow aggregates, the upper integration limits in (3.42) are

the maximum diameters provided in Table 2.2.

### 3.3.2 Conservation of Mass in WRF-based Simulations

The intensified hurricane Sandy on October 29, 2012 over the north Atlantic Ocean was selected as the target severe weather event in this study. The WRF model was initialized with a  $1500 \times 1500$  km simulation domain discretized into 5 km horizontal grid spacing with 60 vertical levels. Using the high-resolution North American Mesoscale (NAM) gridded reanalysis data as initial and boundary conditions the WRF model provided state vector forecasts of Sandy over 24 hours and generated the atmospheric vertical profiles of the prognostic variables of temperature, water vapor along with five bulk hydrometeor densities. The bulk densities of cloud ice and snow are used as key parameters for providing the mass conservation constraint in the simulations and assuring mass-equivalent comparisons of radiative transfer results for aspherical hydrometeors and spherical particles according to:

$$\rho_f = \rho_{sphere} = \int_0^{\infty} \frac{\pi D^3 \rho_h}{6} N_h e^{-\Lambda_h D} dD \quad (3.46)$$

where  $\rho_f$  is defined in (3.43),  $\rho_h$  is the volume averaged density of two types of spherical frozen particles for which  $\rho_h = 9.167 \times 10^{-4} \text{g/mm}^3$  for cloud ice and  $\rho_h = 2.5 \times 10^{-4} \text{g/mm}^3$  for snow [121]. The quantities  $N_h$  and  $\Lambda_h$  are parameters of an exponential size distribution, and  $D$  is the diameter of a sphere. For spherical cloud ice particles, a constant mean particle size of  $\Lambda_h = 50 \text{mm}^{-1}$  is assumed and  $N_h$  is obtained by imposing (3.46). For spherical snow particles, a constant intercept of  $N_h = 8000 \text{mm}^{-4}$  is used [103, 121] and  $\Lambda_h$  is imposed by (3.46). By (3.46), the bulk densities of multiple habits of aspherical frozen hydrometeors are thus equal to the bulk densities of analogous spherical particle polydispersion at any layer of a vertical profile.

### 3.3.3 Maximum Entropy Principle for Ice Habit Probabilities Estimation

Rather than being treated as uniformly distributed random variables, the estimation of ice habit probabilities  $p_{i_s}$  in (3.42) based on the maximum entropy principle is considered. The

principle of maximum entropy can be applied to any physical system and aims to find the best distribution that maximizes the number of partitions among all possible system states [102]. This general physically-based principle has been considered in determining the hydrometeor particle size distributions by Yano et al. [136], where the preliminary analysis identifies the hydrometeor mass as the best candidate variable restricted by the laws of conservation of total hydrometeor mass and total vertical flux as the physical constraints to the particle size distribution function. The maximum entropy principle is applicable to the problem of determining ice habit probabilities  $p_{i_s}$  since the various ice habits are specified by OpenSSP hydrometeor database along with the mass of each OpenSSP particle.

Consider a layer of ice clouds composed of multiple habits of OpenSSP frozen hydrometeors. The entropy of the cloud layer can be defined conveniently using ice habit probabilities  $p_{i_s}$ :

$$H(p_{i_s}) = - \sum_{i_s=1}^{N_s} p_{i_s} \ln \left( \frac{1}{p_{i_s}} \right) \quad (3.47)$$

where  $N_s$  is the number habits of ice particles, and  $p_{i_s}$  can be interpreted as the probability of occupancy in the  $i_s$  habit. Without any constraint,  $p_{i_s} = 1/N_s$  to achieve the maximum entropy.

Now, one physical constraint can be introduced to the ice particles in the cloud layer based on the law of mass conservation:

$$\rho_f = \sum_{i_s=1}^{N_s} N'_{o_{i_s}} \int_0^{\infty} D^{\mu(T)} e^{-\lambda(T)D} m(D, i_s) dD \quad (3.48)$$

where  $\rho_f$  is the bulk ice density of the cloud layer in  $\text{g/m}^3$  and is obtained from the WRF model simulation as discussed in (3.43), and  $N'_{o_{i_s}}$  is the number of ice particles in the  $i_s$  habit per unit volume. The number density  $N'_{o_{i_s}}$  can be determined based on the total ice concentration model developed by Heymsfield et al. [53]:

$$p_{i_s} N_t(T) = \int_0^{\infty} n(D, i_s) dD = N'_{o_{i_s}} \frac{\Gamma(\mu + 1)}{\lambda^{\mu+1}} \quad (3.49)$$

where  $N_t(T)$  is the total ice concentration per liter in clouds parameterized by temperature  $T$ , and

$$N_t(T) = \begin{cases} 27, & T \leq -60^\circ\text{C}, \\ 3.304e^{-0.04607T}, & T > -60^\circ\text{C}, \end{cases} \quad (3.50)$$



The number density  $N'_{o_{i_s}}$  is subsequently calculated as:

$$N'_{o_{i_s}} = p_{i_s} \frac{N_t \lambda^{\mu+1}}{\Gamma(\mu+1)} \quad (3.51)$$

Bringing (3.51) into (3.48), the constraint based on the law of mass conservation is rewritten as:

$$\begin{aligned} \rho_f &= \sum_{i_s=1}^{N_s} p_{i_s} \frac{N_t \lambda^{\mu+1}}{\Gamma(\mu+1)} \int_0^\infty D^\mu e^{-\lambda D} m(D, i_s) dD \\ &= \sum_{i_s=1}^{N_s} p_{i_s} \rho_{i_s} \end{aligned} \quad (3.52)$$

where the parameters  $\rho_f$  and  $T$  are obtained by WRF, the parameters of the size distribution function are determined by the temperature  $T$ , and the particle mass  $m(D, i_s)$  can be found from the OpenSSP database. Thus, the quantity  $\rho_{i_s}$  on the right hand of (3.52) is known for each habit  $i_s$ .

The ice habit probabilities  $p_{i_s}$  can be found using Lagrange multipliers [102] so that the cloud layer entropy  $H(p_{i_s})$  is maximized. The Lagrangian function  $L$  along with two Lagrangian multipliers  $\alpha$  and  $\beta$  is defined as:

$$L = H(p_{i_s}) + (\alpha - 1) \left( \sum_{i_s=1}^{N_s} p_{i_s} - 1 \right) + \beta \left( \sum_{i_s=1}^{N_s} p_{i_s} \rho_{i_s} - \rho_f \right) \quad (3.53)$$

It has been shown that if  $\alpha$ ,  $\beta$ , and each  $p_{i_s}$  are found so that  $L$  is maximized, then the same values of  $p_{i_s}$  also maximize the entropy  $H(p_{i_s})$  subject to the constraint (3.52). The procedure to find the solution can be found in either the text by Rosenkrantz [102] or Penfield's lecture notes at MIT (<http://www-mtl.mit.edu/Courses/6.050/notes/>). The ice habit probabilities  $p_{i_s}$  based on the principle of maximum entropy are then found as:

$$p_{i_s} = e^{-\alpha - \beta \rho_{i_s}} \quad (3.54)$$

where

$$\alpha = \ln \left( \sum_{i_s=1}^{N_s} e^{-\beta \rho_{i_s}} \right) \quad (3.55)$$

and  $\beta$  is the solution of the fundamental equation below:

$$f(\beta) = \sum_{i_s=1}^{N_s} (\rho_{i_s} - \rho_f) e^{-\beta(\rho_{i_s} - \rho_f)} = 0 \quad (3.56)$$

The computational difficulty associated with the maximum entropy principle usually resides in finding the solution of the equation  $f(\beta) = 0$  when multiple physical constraints exist.

This method for estimating  $p_{i_s}$  based on the maximum entropy principle was not used for the subsequent simulations of microwave radiances for two reasons: 1) the parameters obtained from three independent sources (i.e., WRF, OpenSSP database, and Heymsfield's PSDs) might violate mass conservation (3.52) when  $\rho_f$  is less than the smallest  $\rho_{i_s}$  or greater than the largest  $\rho_{i_s}$ , and 2) only one physical constraint is considered in the problem, which may not be sufficient for the optimal estimation of  $p_{i_s}$ . However, this method is worthy of a separate and more in-depth study in the future.

### 3.4 Analysis of Dual-Polarized Microwave Radiances using 1D UMRT

Many Earth observation missions focusing on the measurement of ice cloud or snowfall mass choose a view angle of approximately  $53^\circ$ , and receive linear vertical and horizontal polarizations (e.g., GPM operating at  $52.8^\circ$  incidence angle [114], ICI using a nominal incidence angle of  $53^\circ$  [9], and the CoSSIR airborne instrument performing a conical scan at  $50^\circ$  during the CRYSTAL FACE mission [36]). Those missions utilize a wide range of atmospheric sounding/imaging channels from 10 to 874 GHz. Accordingly, broadband simulations of dual polarization radiances were carried out using the UMRT model incorporating aspherical OpenSSP hydrometeors to facilitate the development of microwave radiance assimilation and ice cloud retrieval algorithms using upcoming submillimeter-wave observation data (e.g., from the ICI mission).

The computed upwelling brightness temperatures in vertical ( $T_{BV}$ ) polarization at  $53^\circ$  view angle covering the entire area of intensified hurricane Sandy and at frequencies aligned with ICI channels plus 874 GHz are shown on the left column of Figure 3.3 and Figure 3.4. We see that brightness temperatures are as low as 180 Kelvin near hurricane rain bands at 315.65 GHz. The bulk scattering of ice and snow hydrometeors within clouds at 5 - 6 km altitude causes strong reflection of the cold cosmic background temperature [114, 62] to produce these effects. Similar cold brightness temperatures near rain bands are observed at 874 GHz owing to the high scattering

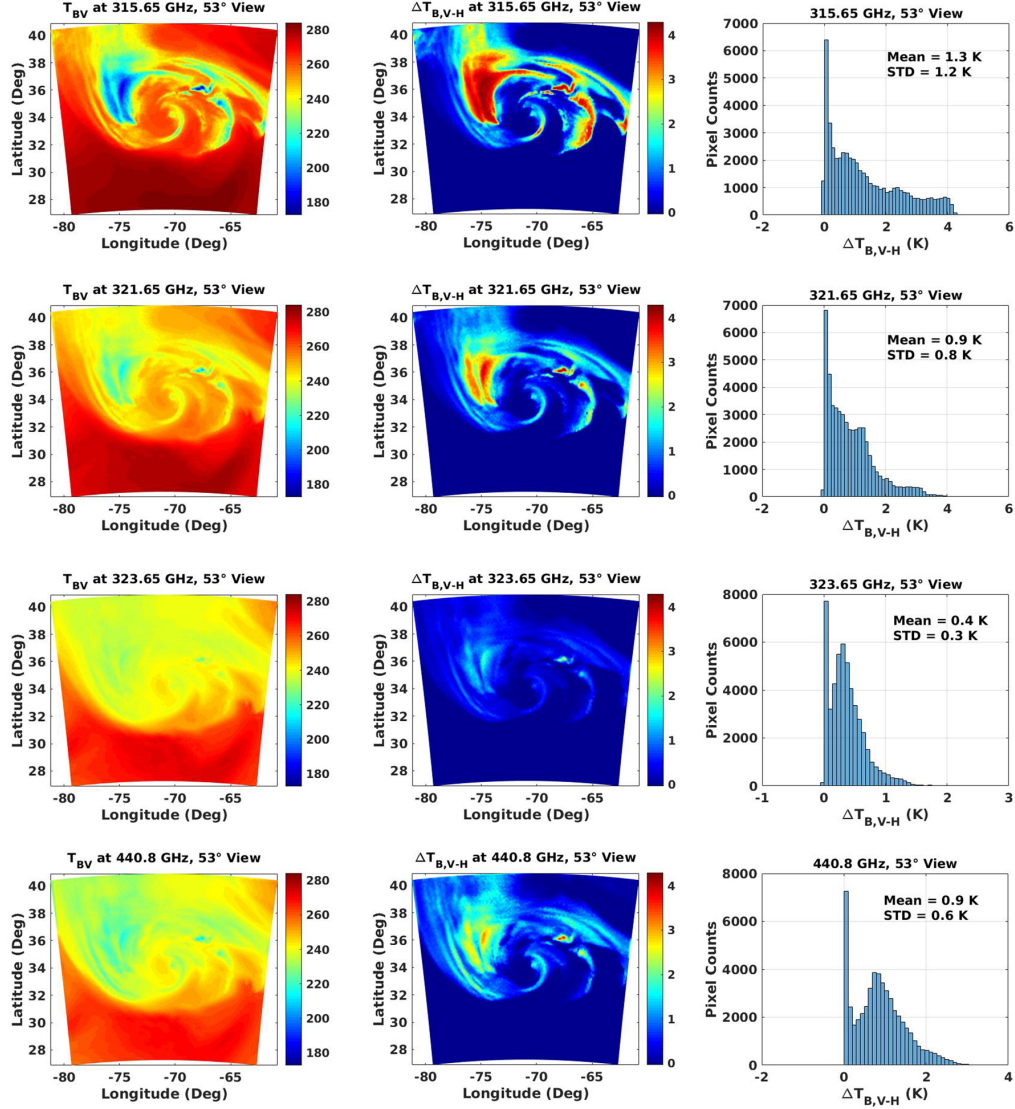


Figure 3.3: Simulations of dual-polarization brightness temperature imagery over hurricane Sandy at 53° view, the conical scanning angle selected by multiple microwave satellite missions (e.g. ICI). Left column: Vertical polarization brightness temperatures  $T_{BV}$  at 315.65, 321.65, 323.65, and 440.8 GHz, respectively. Middle column: Brightness temperature differences between vertical and horizontal polarization  $\Delta T_{B,V-H}$  at the same respective frequencies to the left. Right column: Histogram of  $\Delta T_{B,V-H}$  with mean and standard deviation.

efficiency of the aspherical OpenSSP hydrometeors (Figures 2.4 and 2.5).

The brightness temperature differences between vertical and horizontal polarization  $\Delta T_{B,V-H} = T_{BV} - T_{BH}$  at 53° viewing angle are shown in the middle column of Figure 3.3 and Figure 3.4 along with the histogram of  $\Delta T_{B,V-H}$  in the right column. The statistical mean of  $\Delta T_{B,V-H}$  over

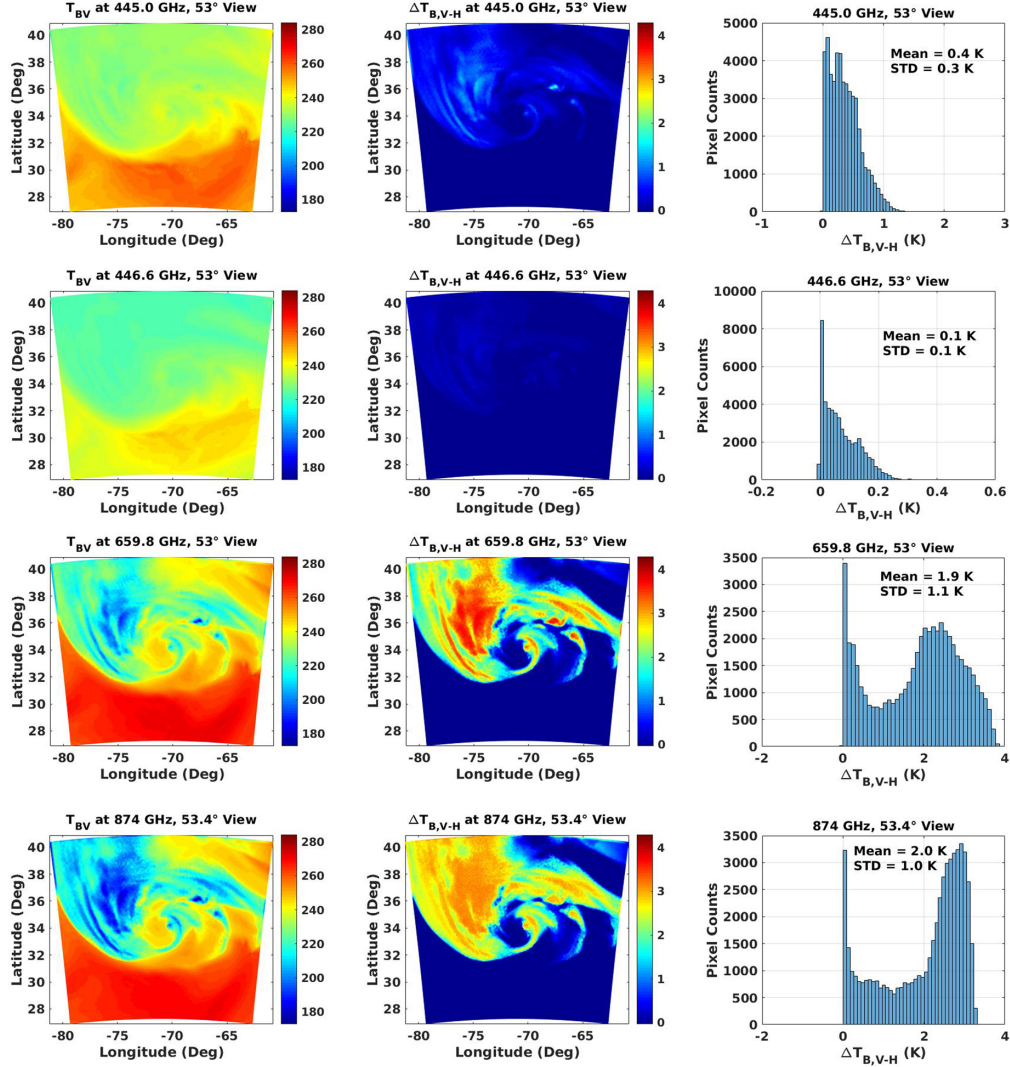


Figure 3.4: Similar to Figure 3.3, but simulations at frequencies of 445.0, 446.6, 659.8, and 874 GHz. The  $\Delta T_{B,V-H}$  histogram exhibits a strong peak at 2-3 Kelvin for the two highest frequencies.

the entire simulation domain shows good agreement with the maximum  $\Delta T_{B,V-H}$  across a wide range of sensing channels. The maximum difference  $\Delta T_{B,V-H}$  of  $\sim 4$  Kelvin reveals that the vertical polarized radiances are more sensitive to the complex structure of ice and snow particles. The two window channels of 659.8 GHz and 874 GHz exhibit a  $\sim 2$  Kelvin histogram mean in  $\Delta T_{B,V-H}$ . Such differences are considerable in microwave radiance assimilation practice.

Figure 3.5 (a) summarizes the maximum and mean value of  $\Delta T_{B,V-H}$  for a broad range of sensing channels between 10 and 874 GHz for the Sandy simulation. The maximum  $\Delta T_{B,V-H}$

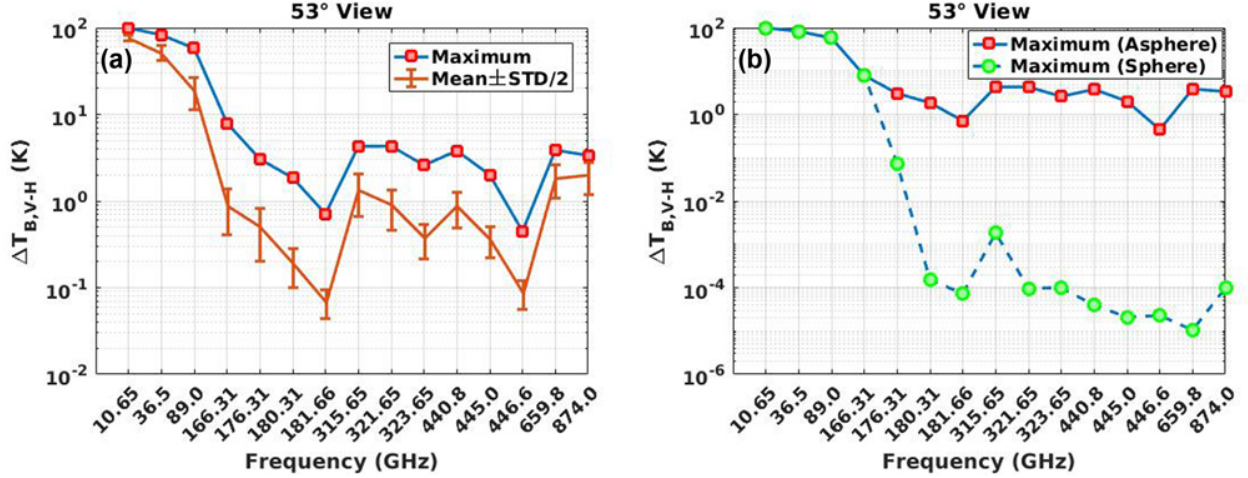


Figure 3.5: Statistics of  $\Delta T_{B,V-H}$  on top of hurricane Sandy across key microwave frequencies between 10 and 874 GHz. (a) The maximum (curve with square markers) and the mean (curve with error bars) in the presence of bulk aspherical hydrometeors. Both curves are consistent. The error bars indicate half of the standard deviations. (b) Comparison of the maximum  $\Delta T_{B,V-H}$  between aspherical hydrometeors (solid line) and a mass-equivalent polydispersion of Mie spheres (dashed line).

of more than 10 K observed in the window channels below 166.31 GHz is due to the significant impact of ocean surface reflectivity on linear polarized microwave radiances. For simplicity, the simulations assume a specular ocean surface as a lower boundary condition. The corresponding Fresnel surface reflection coefficient for the vertical polarization is much smaller than that of the horizontal polarization at  $53^\circ$  incidence, thus resulting in generally warmer brightness temperatures for the vertical polarization. On the other hand, the few K values of the maximum  $\Delta T_{B,V-H}$  at higher frequencies (e.g.,  $\geq 183$  GHz) show the impact of cloud aspherical frozen hydrometeors on polarimetric microwave radiances. At these higher frequencies the influence of the ocean surface on the upwelling brightness temperature is attenuated by cloud and strong water vapor absorption.

An intercomparison of the maximum  $\Delta T_{B,V-H}$  based on aspherical hydrometeors and mass-equivalent polydispersions of ice spheres (Figure 3.5 (b)) illustrates that the simplified spherical hydrometeor model produce milli-Kelvin level polarimetric brightness temperature differences for sounding channels near 183 GHz and above. However, the complex physical structure of aspherical

hydrometeors results in appreciable polarization differences and is expected to impact applications of dual-polarimetric microwave radiances at frequencies above 183 GHz in, for example, ICI ice cloud mass and mean size property retrievals [9].

### 3.5 Analysis of Multi-stream Microwave Radiances using 1D UMRT

The impact of using aspherical hydrometeors on forward multi-stream radiance calculations can be quantitatively assessed by comparing simulated upwelling radiances for a multiple habit mixture of aspherical OpenSSP hydrometeors against a polydispersion of mass-equivalent Mie spheres. Using the WRF-based atmospheric states for hurricane Sandy and simulating microwave imagery in the vertical polarization observed from space, this intercomparison provides statistical assessment of brightness temperatures at discrete stream angles and frequencies. For practical purposes, the comparison is performed at eight discrete stream angles between nadir and the horizon. The simulations provide insights into microwave radiance assimilation and ice cloud parameter retrieval using, for example, cross-track scanning radiometer data.

Figure 3.6 shows the statistics of simulated multi-stream brightness temperature differences  $\Delta T_{\text{BV,Mie-DDA}} \triangleq T_{\text{BV,Mie}} - T_{\text{BV,DDA}}$  for Mie spherical particles relative to aspherical OpenSSP hydrometeors at four different frequencies over the Sandy simulation. The sounding channel at 315.65 GHz is most affected by the complex structure of frozen hydrometeors, wherein the maximum  $\Delta T_{\text{BV,Mie-DDA}}$  reaches 50 - 60 K at all view angles. The three window channels at 420.763, 659.8 and 874 GHz are also considerably sensitive to aspherical hydrometeors with maximum brightness temperature differences of  $\sim 40$  K at most off-nadir viewing angles. Furthermore, the maximum impact of OpenSSP aspherical hydrometeors on brightness temperatures at 659.8 GHz occurs at viewing angles greater than  $14^\circ$  with up to 15 - 20 Kelvin differences. In contrast, the minimum impact at 420.763 GHz occurs at the largest viewing angle  $84^\circ$  with more than 20 Kelvin depression. Repeating the procedure for the key microwave sensing frequencies studied in this thesis, a summary of maximum  $\Delta T_{\text{BV,Mie-DDA}}$  corrections at discrete viewing angles and frequencies is shown in Figure 3.7. The impact of bulk aspherical frozen hydrometeors on the computed upwelling radiances

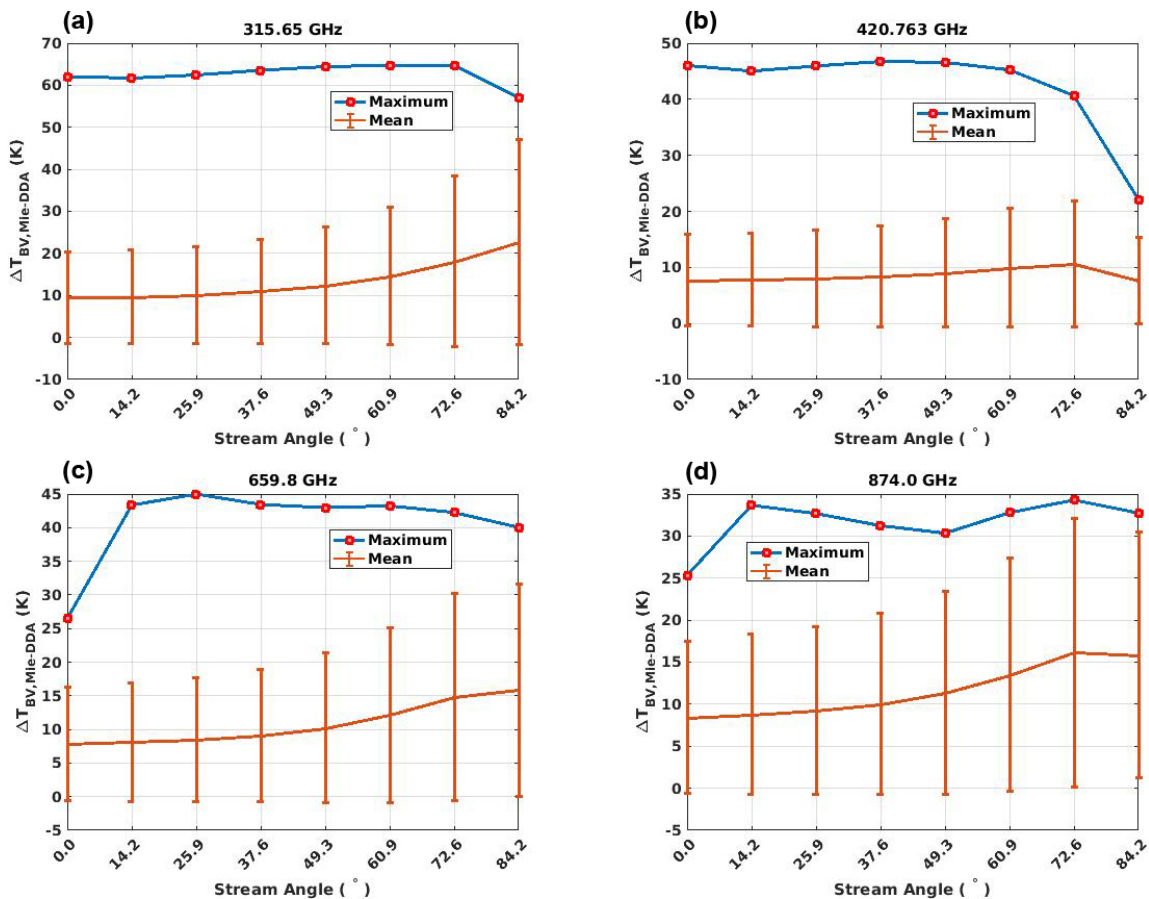


Figure 3.6: Statistics of  $\Delta T_{BV, Mie-DDA}$  for selected viewing angles at (a) 315.65 GHz, (b) 420.763 GHz, (c) 659.8 GHz, and (d) 874.0 GHz. The curves with square markers show maximum brightness temperature differences and the curves with error bars show the mean differences. Error bars indicate difference standard deviations.

compared to polydisperse Mie spheres varies with frequency and view angle.

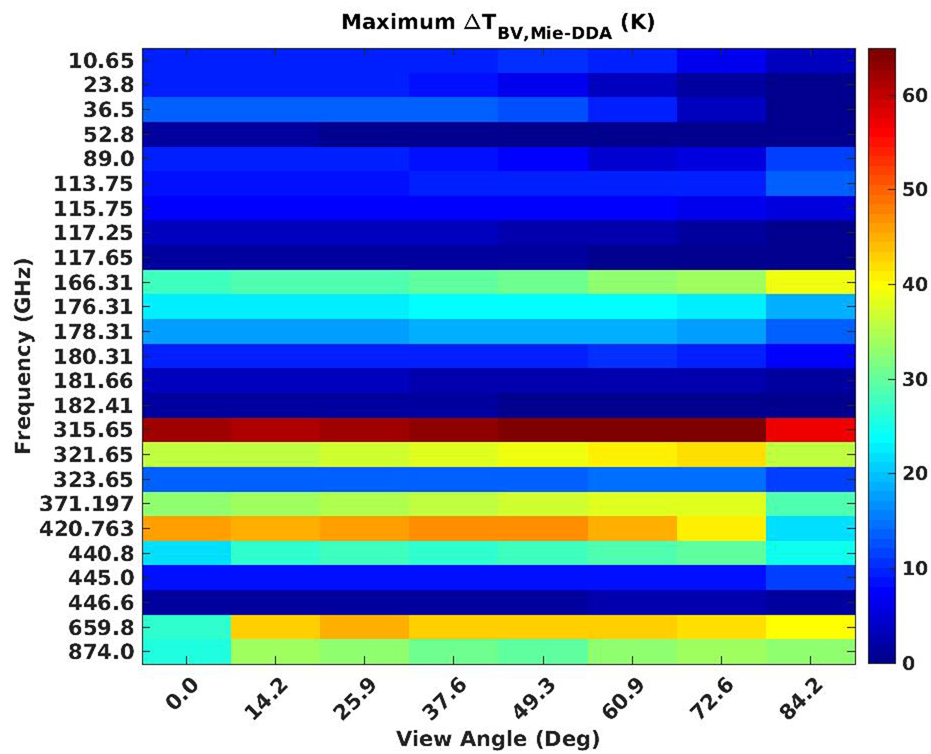


Figure 3.7: Similar to Figure 3.6, but the maximum  $\Delta T_{BV, \text{Mie-DDA}}$  is shown with respect to both key microwave remote sensing frequency from 10 to 874 GHz and discrete viewing angles between zenith and the horizon.



## Chapter 4

### Fast 3D Inhomogeneous Radiative Transfer Model

In this chapter, the existing 3D radiative transfer (RT) models are reviewed based on the fundamental solution methods of either (i) statistical or (ii) deterministic differential RT equation solutions. The new 3D Horizontally Inhomogeneous Unified Microwave Radiative Transfer (HI-UMRT) model of this thesis provides a deterministic solution of the 3D radiative transfer equation using an iterative perturbation scheme based on the 1D UMRT algorithm. The required number of 1D UMRT calculations is determined based on the number of perturbation iterations required for three dimensions. The numerical perturbation solution of the RT equation in azimuthal harmonics is obtained based on the angular and spatial discretization of the Stokes vector. The convergence criterion of the perturbation series is discussed at the end of this chapter.

#### 4.1 Review of Existing 3D Radiative Transfer Models

For all-weather assimilation of satellite microwave radiances into NWP models [84, 6], 3D cloud radiation fields are necessary to be rapidly and accurately computed. Both passive remote sensing retrieval algorithms and microwave radiance assimilation methods require computationally efficient radiative transfer models which limit radiative errors caused by horizontal inhomogeneities [29]. However, few 3D models have been extensively studied using radiative transfer model intercomparisons, for example, those undertaken by the International Polarized Radiative Transfer (IPRT) working group of the International Radiation Commission (IRC) [28, 29]. According to the recent IPRT report, nearly all of these numerical 3D models (e.g. 3DMCPOL [20], MSCART

[131], and MYSTIC [27]) are based on the Monte Carlo solution method. However, Monte Carlo methods are generally less efficient and accurate than deterministic numerical methods in repetitive operational usage, such as in radiance assimilation [31].

The sole deterministic numerical method studied in IPRT intercomparisons is the spherical harmonics discrete ordinate method (SHDOM) [31], which is widely used within the optical and infrared communities [84]. SHDOM is based on solving the integral form of the 3D discrete radiative transfer equation (DRTE) using Picard iteration which models the radiation streams along discrete angles through a 3D spatial grid [69]. Spherical harmonics are chosen to represent the source function of the DRTE for efficient computation purposes. Some drawbacks of the SHDOM method are: (i) the algorithm lacks a fast and efficient Jacobian computation for microwave radiance assimilation, and (ii) slow convergence occurs within opaque and/or high albedo scattering media. These difficulties have precluded the application of SHDOM to high albedo 3D clouds with strong horizontal variability.

Other techniques to solve the 3D radiative transfer equation include an iterative discrete ordinate method, which is applicable to low albedo cloud layers but without a Jacobian solution. This method is used within the 3D polarized Atmospheric Radiative Transfer Simulator (ARTS) [26]. Radiative perturbation theory based on solving both the plane-parallel 1D radiative transfer equation and the associated adjoint transport equation has been discussed where the horizontal variability along with the Green's function for the transport operator treated as a perturbation of the Dyson equation [141, 14]. Although this perturbation-based method provides a means for the solution of radiative transfer through 3D inhomogeneous clouds, this method fails to derive an explicit Green's function solution, thus making the computational accuracy and efficiency unspecified [73, 14, 15].

## 4.2 Horizontal Perturbation Series

### 4.2.1 Iterative Perturbation Scheme

The microwave radiation fields within 3D inhomogeneous clouds such as hurricane rain bands and convective towers can be represented by a Stokes vector  $\bar{I}(x, y, z, \theta, \phi)$  as a function of location (i.e.  $x, y, z$  in Cartesian coordinates), elevation angle  $\theta$ , and azimuth angle  $\phi$ . The HI-UMRT model uses a new means to solve the radiative transfer equation in a 3D medium by embedding the 1D UMRT algorithm into an iterative perturbation scheme, where higher order 1D radiative transfer equations perturbed by the horizontal derivatives in radiances of lower order correct accumulatively the zeroth order 1D UMRT result. The radiation fields are governed by the 3D differential radiative transfer equation:

$$\begin{aligned} \frac{d\bar{I}}{ds} &\triangleq \cos\theta \frac{\partial\bar{I}(x, y, z, \theta, \phi)}{\partial z} + \sin\theta \cos\phi \frac{\partial\bar{I}(x, y, z, \theta, \phi)}{\partial x} + \sin\theta \sin\phi \frac{\partial\bar{I}(x, y, z, \theta, \phi)}{\partial y} \\ &= -\bar{\kappa}_e(x, y, z, \theta) \bar{I}(x, y, z, \theta, \phi) + \bar{\kappa}_a(x, y, z, \theta) B(f, T(x, y, z)) \\ &\quad + \int_0^{2\pi} \int_0^\pi \bar{P}(x, y, z, \theta, \theta', \phi, \phi') \cdot \bar{I}(x, y, z, \theta', \phi') \sin\theta' d\theta' d\phi' \end{aligned} \quad (4.1)$$

where  $\bar{\kappa}_e$  is the extinction matrix,  $\bar{\kappa}_a$  is the absorption vector,  $\bar{P}$  is the phase matrix coupling the incident radiation field propagating in the direction of  $(\theta', \phi')$  with the scattered field propagating in  $(\theta, \phi)$ , and  $B(f, T)$  is the Planck function of thermal spectral radiance at thermodynamic temperature  $T$  and frequency  $f$ .

The Stokes vector  $\bar{I}(x, y, z, \theta, \phi)$  in (4.1) is an azimuthal periodic function with a period of  $2\pi$ . It can thus be represented by an azimuthal harmonic series based on a Fourier expansion. By harmonic balancing, the 3D differential radiative transfer equation (4.1) is thus decomposed into a series of azimuthal harmonic differential equations (4.2), (4.3), and (4.4).

$$\begin{aligned} \cos\theta \frac{\partial\bar{I}_{0c}}{\partial z} &= -\bar{\kappa}_e(x, y, z, \theta) \bar{I}_{0c} + \bar{\kappa}_a(x, y, z, \theta) B(f, T(x, y, z)) \\ &\quad + \int_0^\pi \bar{P}(x, y, z, \theta, \theta') \bar{I}_{0c}(x, y, z, \theta') \sin\theta' d\theta' \\ &\quad - \sin\theta \frac{\partial\bar{I}_{1c}}{\partial x} - \sin\theta \frac{\partial\bar{I}_{1s}}{\partial y} \end{aligned} \quad (4.2)$$

$$\begin{aligned}
\cos\theta \frac{\partial \bar{I}_{mc}}{\partial z} &= -\bar{k}_e(x, y, z, \theta) \bar{I}_{mc} \\
&+ \int_0^\pi \bar{P}_m(x, y, z, \theta, \theta') \cdot \bar{I}_{mc}(x, y, z, \theta') \sin\theta' d\theta' \\
&- \frac{1}{2} \sin\theta \frac{\partial}{\partial x} (\bar{I}_{(m+1)c} + \bar{I}_{(m-1)c}) \\
&- \frac{1}{2} \sin\theta \frac{\partial}{\partial y} (\bar{I}_{(m+1)s} - \bar{I}_{(m-1)s}), \\
&m = 1, 2, \dots
\end{aligned} \tag{4.3}$$

$$\begin{aligned}
\cos\theta \frac{\partial \bar{I}_{ms}}{\partial z} &= -\bar{k}_e(x, y, z, \theta) \bar{I}_{ms} \\
&+ \int_0^\pi \bar{P}_m(x, y, z, \theta, \theta') \cdot \bar{I}_{ms}(x, y, z, \theta') \sin\theta' d\theta' \\
&- \frac{1}{2} \sin\theta \frac{\partial}{\partial x} (\bar{I}_{(m+1)s} + \bar{I}_{(m-1)s}) \\
&- \frac{1}{2} \sin\theta \frac{\partial}{\partial y} (\bar{I}_{(m-1)c} - \bar{I}_{(m+1)c}), \\
&m = 1, 2, \dots
\end{aligned} \tag{4.4}$$

where  $m$  is the order of each azimuthal harmonic, and  $\bar{I}_{mc}$  and  $\bar{I}_{ms}$  are the cosine and sine harmonics (respectively).  $\bar{P}_m(x, y, z, \theta, \theta')$  is the  $m^{\text{th}}$  azimuthal cosine harmonic phase matrix defined as:

$$\begin{aligned}
\bar{P}_m(x, y, z, \theta, \theta') &= \int_0^{2\pi} \bar{P}(x, y, z, \theta, \theta', \Delta\phi) \cos(m\Delta\phi) d\Delta\phi, \\
\Delta\phi &= \phi - \phi'
\end{aligned} \tag{4.5}$$

For either spherical or randomly oriented aspherical hydrometeors, the phase matrix  $\bar{P}$  is an even function of  $\Delta\phi = \phi - \phi'$ . Accordingly, there is no need for a sine harmonic in this decomposition. In the case of oriented particles, the phase matrix will not in general be an even function of  $\Delta\phi$ , necessitating the introduction of a  $m^{\text{th}}$  azimuthal sine harmonic phase matrix.

Note that horizontal derivatives of radiances in azimuthal harmonics of order  $(m+1)$  and  $(m-1)$  are treated as source functions in (4.3) and (4.4). The zeroth order azimuthal harmonic equation (4.2) has a source function comprised of the atmospheric thermal emission and horizontal

derivatives of the first order azimuthal harmonics  $\bar{I}_{1c}$  and  $\bar{I}_{1s}$ . To accommodate the coupling of the azimuthal harmonic derivatives, we seek a perturbation series solutions of the form:

$$\bar{I}_{mc}(x, y, z, \theta) = \sum_{n=0}^{\infty} \bar{I}_{mc}^{(n)}(x, y, z, \theta) \quad (4.6)$$

$$\bar{I}_{ms}(x, y, z, \theta) = \sum_{n=0}^{\infty} \bar{I}_{ms}^{(n)}(x, y, z, \theta) \quad (4.7)$$

where  $n$  is the perturbation order. By the above approach, it is presumed that the horizontal derivatives of each of the azimuthal harmonic radiances introduce relatively small changes to the 1D planar-stratified solution. Applying perturbation theory to the azimuthal harmonic differential radiative transfer equations (4.2) - (4.4), we obtain a perturbation series of equations for the sine and cosine harmonic radiances that depend on both  $m$  and  $n$ :

1)  $m = 0, n = 0$

$$\cos \theta \frac{\partial \bar{I}_{0c}^{(0)}}{\partial z} = -\bar{\kappa}_e \bar{I}_{0c}^{(0)} + \bar{\kappa}_a B + \int_0^\pi \bar{P} \cdot \bar{I}_{0c}^{(0)} \sin \theta' d\theta' \quad (4.8)$$

2)  $m = 0, n > 0$

$$\begin{aligned} \cos \theta \frac{\partial \bar{I}_{0c}^{(n)}}{\partial z} &= -\bar{\kappa}_e \bar{I}_{0c}^{(n)} + \int_0^\pi \bar{P} \cdot \bar{I}_{0c}^{(n)} \sin \theta' d\theta' \\ &\quad - \sin \theta \frac{\partial}{\partial x} \bar{I}_{1c}^{(n-1)} - \sin \theta \frac{\partial}{\partial y} \bar{I}_{1s}^{(n-1)} \end{aligned} \quad (4.9)$$

3)  $m > 0, n = 0$

$$\cos \theta \frac{\partial \bar{I}_{mc}^{(0)}}{\partial z} = -\bar{\kappa}_e \bar{I}_{mc}^{(0)} + \int_0^\pi \bar{P}_m \cdot \bar{I}_{mc}^{(0)} \sin \theta' d\theta' \quad (4.10)$$

$$\cos \theta \frac{\partial \bar{I}_{ms}^{(0)}}{\partial z} = -\bar{\kappa}_e \bar{I}_{ms}^{(0)} + \int_0^\pi \bar{P}_m \cdot \bar{I}_{ms}^{(0)} \sin \theta' d\theta' \quad (4.11)$$

4)  $m > 0, n > 0$

$$\begin{aligned}
\cos \theta \frac{\partial \bar{I}_{mc}^{(n)}}{\partial z} &= -\bar{\kappa}_e \bar{I}_{mc}^{(n)} + \int_0^\pi \bar{P}_m \cdot \bar{I}_{mc}^{(n)} \sin \theta' d\theta' \\
&\quad - \frac{1}{2} \sin \theta \frac{\partial}{\partial x} \left( \bar{I}_{(m+1)c}^{(n-1)} + \bar{I}_{(m-1)c}^{(n-1)} \right) \\
&\quad - \frac{1}{2} \sin \theta \frac{\partial}{\partial y} \left( \bar{I}_{(m+1)s}^{(n-1)} - \bar{I}_{(m-1)s}^{(n-1)} \right)
\end{aligned} \tag{4.12}$$

$$\begin{aligned}
\cos \theta \frac{\partial \bar{I}_{ms}^{(n)}}{\partial z} &= -\bar{\kappa}_e \bar{I}_{ms}^{(n)} + \int_0^\pi \bar{P}_m \cdot \bar{I}_{ms}^{(n)} \sin \theta' d\theta' \\
&\quad - \frac{1}{2} \sin \theta \frac{\partial}{\partial x} \left( \bar{I}_{(m+1)s}^{(n-1)} + \bar{I}_{(m-1)s}^{(n-1)} \right) \\
&\quad - \frac{1}{2} \sin \theta \frac{\partial}{\partial y} \left( \bar{I}_{(m-1)c}^{(n-1)} - \bar{I}_{(m+1)c}^{(n-1)} \right)
\end{aligned} \tag{4.13}$$

The boundary condition at the top-of-atmosphere can be modeled as the downward propagating radiance field at a constant cosmic background temperature  $T_{cb} = 2.73$  K. Accordingly, the azimuthal harmonic upper boundary conditions for radiances  $\bar{I}_{mc}^{(n)}$  and  $\bar{I}_{ms}^{(n)}$  are zero for  $m > 0$  or  $n > 0$ . At the surface  $z = 0$ , the upwelling radiance field comprises the surface reflected and emitted radiation. The boundary condition is in general governed by:

$$\begin{aligned}
\bar{I}(x, y, 0, \mu, \phi) &= \int_0^{2\pi} \int_0^1 \bar{\gamma}(x, y, \mu, \mu', \phi, \phi') \bar{I}(x, y, 0, -\mu', \phi') d\mu' d\phi' \\
&\quad + \bar{e}_s(x, y, 0, \mu, \phi) \bar{B}(T_s)
\end{aligned} \tag{4.14}$$

where  $\mu = \cos \theta$ ,  $\bar{B}(T_s)$  is the Planck function vector at the surface thermodynamic temperature  $T_s$ , and  $\bar{\gamma}(x, y, \mu, \mu', \phi, \phi')$  is the surface bistatic scattering matrix whose elements are functions of incident direction  $(\mu', \phi')$ , scattered direction  $(\mu, \phi)$ , and polarization. The surface emissivity matrix  $\bar{e}_s$  is defined based on the Kirchoff law:

$$\bar{e}_s(x, y, 0, \mu, \phi) = \bar{I} - \int_0^{2\pi} \int_0^1 \bar{\gamma}(x, y, \mu, \mu', \phi, \phi') d\mu' d\phi' \tag{4.15}$$

where  $\bar{I}$  is an identity matrix.

For simplicity, a specular ocean surface for all calculations is assumed in this study. Accordingly, the surface bistatic scattering function matrix is azimuthally independent and expressed using the

Fresnel reflection coefficients  $\overline{\overline{R}}(\mu)$ :

$$\overline{\overline{\gamma}}(x, y, \mu, \mu', \phi, \phi') = \mu \left| \overline{\overline{R}}(\mu) \right|^2 \delta(\mu - \mu') \delta(\phi - \phi') \quad (4.16)$$

Thus, the lower boundary condition can be formulated as:

$$\overline{\overline{I}}(x, y, 0, \mu, \phi) = \mu \left| \overline{\overline{R}}(\mu) \right|^2 \overline{\overline{I}}(x, y, 0, -\mu, \phi) + \left( \overline{\overline{I}} - \mu \left| \overline{\overline{R}}(\mu) \right|^2 \right) \overline{\overline{B}}(T_s) \quad (4.17)$$

Applying the azimuthal harmonic balancing, the lower boundary conditions corresponding to the sine and cosine harmonic perturbation RT equations (4.8) - (4.13) are:

$$\begin{aligned} \overline{\overline{I}}_{0c}^{(0)}(x, y, 0, \mu) &= \mu \left| \overline{\overline{R}}(\mu) \right|^2 \overline{\overline{I}}_{0c}^{(0)}(x, y, 0, -\mu) + \left( \overline{\overline{I}} - \mu \left| \overline{\overline{R}}(\mu) \right|^2 \right) \overline{\overline{B}}(T_s) \\ \overline{\overline{I}}_{mc}^{(n)}(x, y, 0, \mu) &= \mu \left| \overline{\overline{R}}(\mu) \right|^2 \overline{\overline{I}}_{mc}^{(n)}(x, y, 0, -\mu) \\ \overline{\overline{I}}_{ms}^{(n)}(x, y, 0, \mu) &= \mu \left| \overline{\overline{R}}(\mu) \right|^2 \overline{\overline{I}}_{ms}^{(n)}(x, y, 0, -\mu) \end{aligned} \quad (4.18)$$

The HI-UMRT algorithm begins with the zeroth order perturbation equation (4.8), which is a 1D planar-stratified radiative transfer equation readily solved using the existing UMRT numerical engine. HI-UMRT then proceeds to solve equations (4.9 - 4.13) for higher order of azimuthal harmonics and perturbations by repetitive use of this engine.

This iterative perturbation scheme with an inner loop for azimuthal harmonics and another outer loop for perturbations is illustrated in Figure 4.1. At any given order of  $m$  and  $n$ , the perturbation equation solution can be found using the 1D UMRT engine based on the predetermined matrix operators  $\overline{\overline{\kappa}}_a$ ,  $\overline{\overline{\kappa}}_e$ ,  $\overline{\overline{P}}$ , and  $\overline{\overline{P}}_m$  and the horizontal derivatives of radiances of lower order. HI-UMRT thus inherits the numerical stability and computational efficiency for all matrix operations in its perturbation series iteration by use of UMRT.

The truncation of the azimuthal harmonic expansion should be comparable to that of the elevation discretization. That is, the number of azimuthal harmonics  $M_\phi$  should be equal to the number of elevation streams  $2M_\theta$ . In this thesis, we use  $M_\phi = 2M_\theta = 16$  for numerical studies. This truncation scheme is analogous to that used in a standard finite spherical harmonic series expansion. Otherwise, numerical divided differencing method is used to estimate the required horizontal derivatives. A further discussion of discretization is in Section 4.3.

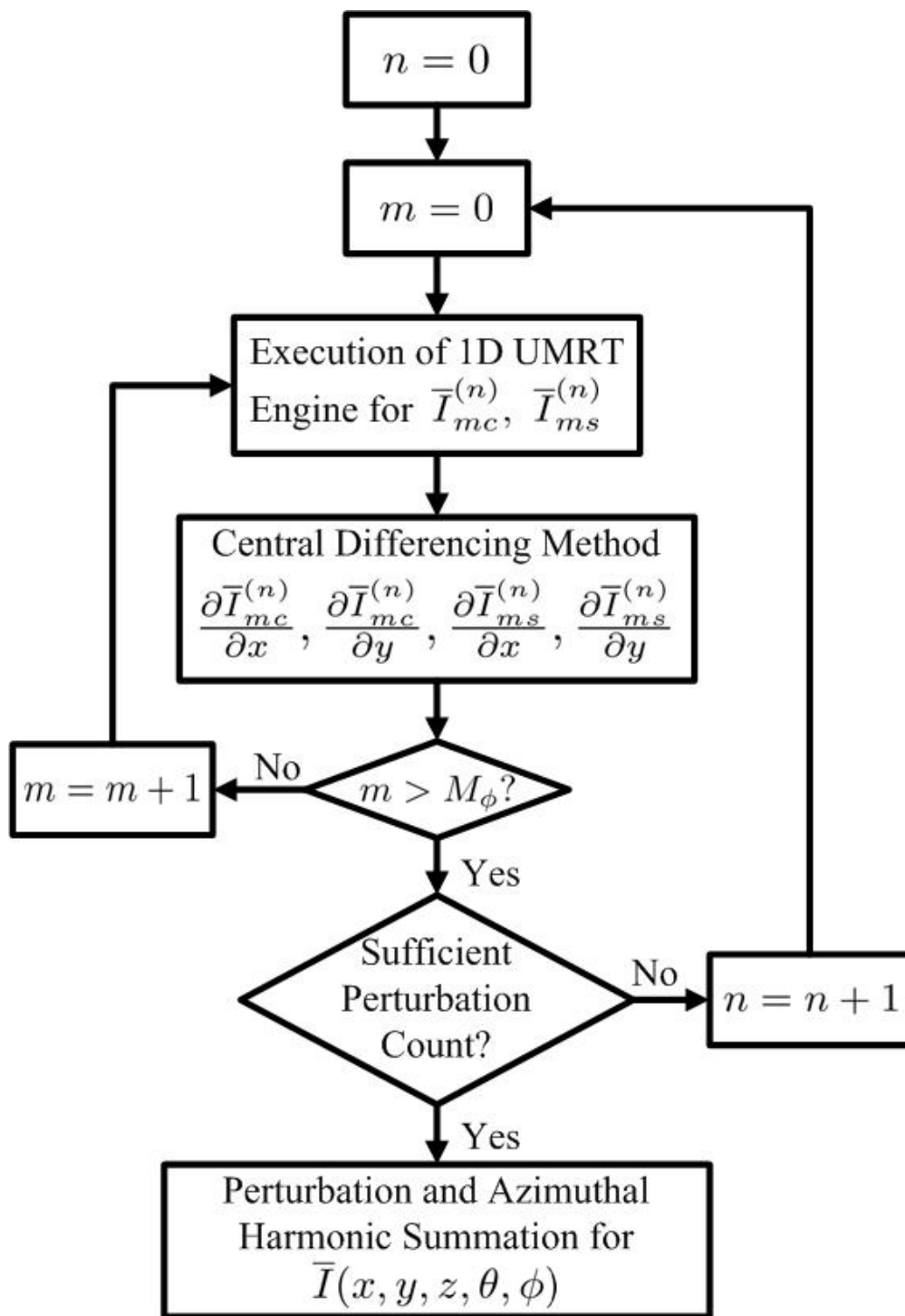


Figure 4.1: A flowchart of the HI-UMRT algorithm based on the existing 1D UMRT engine embedded within an iterative perturbation scheme.



### 4.2.2 Perturbation Source Analysis

The azimuthal harmonic and perturbation series equations (4.8) - (4.13) are solved using (respectively) the Planck function as a source for  $m = 0, n = 0$  and the horizontal derivatives in radiances of lower order as a source for  $m > 0$  or  $n > 0$ . For  $m > 0$  and  $n = 0$ , equations (4.10) - (4.11) are sourceless and thus dissipative, being only excited at the surface and top-of-atmosphere boundaries. The computing time for HI-UMRT is related to the maximum azimuthal harmonic order  $M_\phi$  and perturbation series order  $N$  used at truncation. However, not all azimuthal harmonic and perturbation terms up to a given required order are necessary in the solution. As shown in the perturbation source diagram of Figure 4.2, many such terms for isotropic surface and top-of-atmosphere boundary conditions are zero and thus not necessary to be computed. Accordingly, the required number of 1D UMRT calculations is determined:

$$L = \begin{cases} \frac{1}{2}(N+1)(N+2), & 0 \leq N \leq M_\phi \\ \frac{1}{2}(M_\phi+1)(M_\phi+2) + (N-M_\phi)M_\phi, & N > M_\phi \end{cases} \quad (4.19)$$

For example, if  $M_\phi = 2M_\theta = 16$  and  $N = 4$ , the required number of 1D UMRT engine iterations is  $L = 15$ .

From Figure 4.2, the computational complexity of the HI-UMRT algorithm is determined by considering only those non-trivial radiative transfer solution highlighted with a solid circle. For simplicity, the analysis assumes that the lower boundary has an azimuth-independent surface bistatic scattering function  $\bar{\gamma}(\theta, \theta')$  (e.g., specular calm ocean surface). The analysis is based on a 2-dimensional grid (see Figure 4.2) with each node representing a radiative transfer solution and its estimated horizontal gradients in a given azimuthal harmonic order  $m$  and perturbation order  $n$ . More specifically, the origin node at  $(m = 0, n = 0)$  represents the 1D UMRT solution of equation (4.8), the nodes along the two axes represent the solutions of (4.9) through (4.11), and all other nodes are for the solutions of (4.12) and (4.13). If a solution is purely dissipative and has no source at either boundary, then it is trivial and indicated by an empty circle. Otherwise, a node with a solid circle indicates that the 1D UMRT engine is required to be executed and followed by

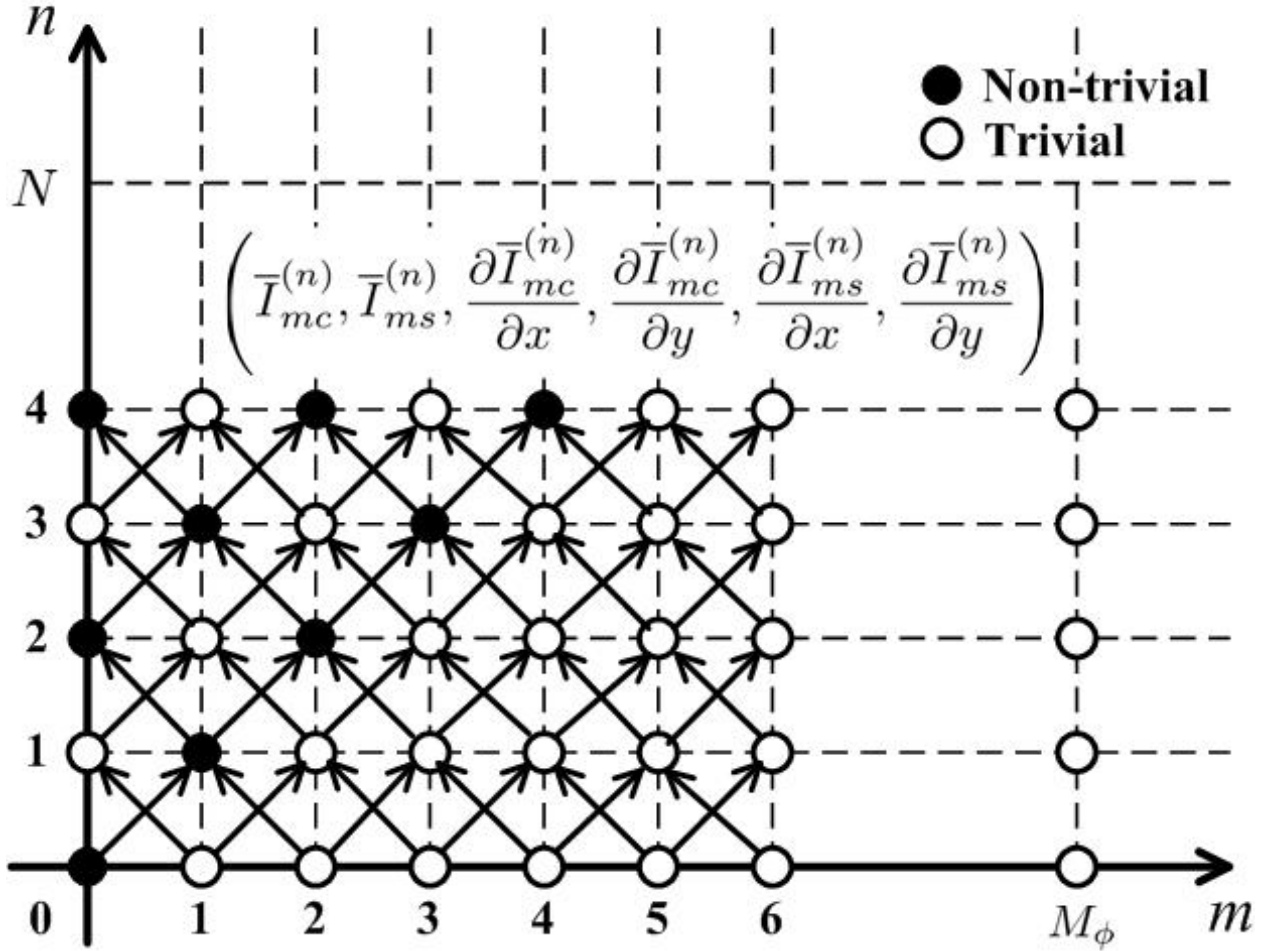


Figure 4.2: HI-UMRT perturbation source diagram for illustration of non-trivial RT solutions under the assumption of a specular surface as the lower boundary condition required calculations exist only at non-trivial azimuthal harmonics of order  $m$  and perturbation order  $n$ .

horizontal gradient estimation. The azimuthal harmonic perturbation equations (4.9) through (4.13) are coupled between adjacent perturbation orders. These coupling relations are illustrated using arrows. An arrow connects a source node where the horizontal gradient of the radiative field is a source function of the 1D equation but in one higher perturbation order. In general, each perturbed node has two lower-order source nodes except for those for the zeroth order azimuthal harmonics (i.e.,  $m = 0$ ). A perturbed node corresponds to a trivial radiative solution if the solutions of all source nodes are trivial.

Using the aforementioned coupling perturbation source relationships, the series is solved

beginning at the origin node of the grid where the 1D UMRT engine computes microwave radiances propagating through a presumed planar-stratified but vertically inhomogeneous atmosphere satisfying the requisite boundary conditions at the surface and cosmic background. Note that any higher order azimuthal harmonics (e.g.,  $m > 0$ ) of thermal emission from a specular surface and constant cosmic background radiation are zero, thus resulting in a series of trivial solutions of the radiative equations (4.10) and (4.11). The above result is represented as a solid circle at origin and empty circles along the azimuthal harmonic axis (i.e., the  $m$  axis).

The solution proceeds to the first perturbation order as follows. The horizontal derivative of the non-trivial 1D UMRT solution at  $(m = 0, n = 0)$  becomes the source function of the equations (4.12) and (4.13) with  $(m = 1, n = 1)$ , where only a single non-trivial first order perturbation solution exists. This result is represented using a solid circle at the grid point  $(m = 1, n = 1)$ . The perturbation source analysis for higher order perturbation solutions is repeated per Figure 4.2. Figure 4.2 shows that the UMRT engine needs to repeat 15 times for computing the perturbation corrections up to the fourth order. Consistent with equation (4.19), this iterative process is comprised of solving three equations with  $m = 0$ , and six sine harmonic and six cosine harmonic perturbation equations with  $(m > 0, n > 0)$ .

A theoretical flop-based computing time of the 1D UMRT engine was estimated to be  $\sim 65 \mu\text{sec}$  based on a 70 teraFLOPS (i.e., one trillion floating-point operations per second) supercomputer for a cloudy vertical profile with 60 levels and 8 discrete radiation streams [139]. This time excludes setup of the absorption vector, extinction matrix, and phase matrix and boundary condition variables. Using the result of the above perturbation source analysis, the computing time of 3D HI-UMRT with fourth-order perturbation corrections applied is thus  $\sim 1 \text{ msec}$  under the same atmospheric conditions. Furthermore, the 3D HI-UMRT algorithm could compute the forward microwave radiances within  $\sim 1$  minute over a  $\sim 1000 \times 1000 \text{ km}$  severe weather simulation domain with 5 km horizontal spacing. This estimated computing time is comparable to that required for a satellite to acquire microwave data during an overpass.

### 4.3 HI-UMRT Numerical Solution

#### 4.3.1 Angular Discretization of the Radiative Transfer Equations

The numerical solution of the discretized radiative transfer equations (4.12) and (4.13) is derived, where the horizontal derivatives in radiances of lower order are considered as the source function for higher order series terms. The brightness temperature vectors  $\bar{T}_{B,mc}^{(n)}$  and  $\bar{T}_{B,ms}^{(n)}$  based on the Rayleigh-Jean's approximation are used to represent the radiation fields in the azimuthal harmonic perturbation series in  $\bar{T}_{mc}^{(n)}$  and  $\bar{T}_{ms}^{(n)}$ .

Consider first the cosine harmonics of the differential radiative transfer equation (4.12). Discretizing (4.12) for the first two Stokes parameters  $\left(T_{Bv,mc}^{(n)} \text{ and } T_{Bh,mc}^{(n)}\right)$  over a set of Gaussian quadrature angles  $\theta_i$  [127] and separating the upwelling (+) and downwelling (-) components, a set of azimuthal harmonic coupled equations for  $m > 0$  are obtained:

$$\begin{aligned} \mu_i \frac{\partial T_{Bvi,mc}^{+(n)}}{\partial z} &= -\kappa_e T_{Bvi,mc}^{+(n)} \\ &+ \sum_{j=1}^{M_\theta} \gamma_j P_{m v v i j}^{+++} T_{Bv j,mc}^{+(n)} + \sum_{j=1}^{M_\theta} \gamma_j P_{m v v i j}^{+-} T_{Bv j,mc}^{-(n)} + \sum_{j=1}^{M_\theta} \gamma_j P_{m v h i j}^{+++} T_{Bh j,mc}^{+(n)} + \sum_{j=1}^{M_\theta} \gamma_j P_{m v h i j}^{+-} T_{Bh j,mc}^{-(n)} \\ &- \frac{1}{2} \sin \theta_i \frac{\partial}{\partial x} \left[ T_{Bvi,(m+1)c}^{+(n-1)} + T_{Bvi,(m-1)c}^{+(n-1)} \right] - \frac{1}{2} \sin \theta_i \frac{\partial}{\partial y} \left[ T_{Bvi,(m+1)s}^{+(n-1)} - T_{Bvi,(m-1)s}^{+(n-1)} \right] \end{aligned} \quad (4.20)$$

$$\begin{aligned} \mu_i \frac{\partial T_{Bhi,mc}^{+(n)}}{\partial z} &= -\kappa_e T_{Bhi,mc}^{+(n)} \\ &+ \sum_{j=1}^{M_\theta} \gamma_j P_{m h v i j}^{+++} T_{Bv j,mc}^{+(n)} + \sum_{j=1}^{M_\theta} \gamma_j P_{m h v i j}^{+-} T_{Bv j,mc}^{-(n)} + \sum_{j=1}^{M_\theta} \gamma_j P_{m h h i j}^{+++} T_{Bh j,mc}^{+(n)} + \sum_{j=1}^{M_\theta} \gamma_j P_{m h h i j}^{+-} T_{Bh j,mc}^{-(n)} \\ &- \frac{1}{2} \sin \theta_i \frac{\partial}{\partial x} \left[ T_{Bhi,(m+1)c}^{+(n-1)} + T_{Bhi,(m-1)c}^{+(n-1)} \right] - \frac{1}{2} \sin \theta_i \frac{\partial}{\partial y} \left[ T_{Bhi,(m+1)s}^{+(n-1)} - T_{Bhi,(m-1)s}^{+(n-1)} \right] \end{aligned} \quad (4.21)$$

$$\begin{aligned} -\mu_i \frac{\partial T_{Bvi,mc}^{-(n)}}{\partial z} &= -\kappa_e T_{Bvi,mc}^{-(n)} \\ &+ \sum_{j=1}^{M_\theta} \gamma_j P_{m v v i j}^{--} T_{Bv j,mc}^{+(n)} + \sum_{j=1}^{M_\theta} \gamma_j P_{m v v i j}^{--} T_{Bv j,mc}^{-(n)} + \sum_{j=1}^{M_\theta} \gamma_j P_{m v h i j}^{--} T_{Bh j,mc}^{+(n)} + \sum_{j=1}^{M_\theta} \gamma_j P_{m v h i j}^{--} T_{Bh j,mc}^{-(n)} \\ &- \frac{1}{2} \sin \theta_i \frac{\partial}{\partial x} \left[ T_{Bvi,(m+1)c}^{-(n-1)} + T_{Bvi,(m-1)c}^{-(n-1)} \right] - \frac{1}{2} \sin \theta_i \frac{\partial}{\partial y} \left[ T_{Bvi,(m+1)s}^{-(n-1)} - T_{Bvi,(m-1)s}^{-(n-1)} \right] \end{aligned} \quad (4.22)$$

$$\begin{aligned}
-\mu_i \frac{\partial T_{Bhi,mc}^{- (n)}}{\partial z} &= -\kappa_e T_{Bhi,mc}^{- (n)} \\
+ \sum_{j=1}^{M_\theta} \gamma_j P_{mhvij}^{-+} T_{Bvj,mc}^{+ (n)} &+ \sum_{j=1}^{M_\theta} \gamma_j P_{mhvij}^{--} T_{Bvj,mc}^{- (n)} + \sum_{j=1}^{M_\theta} \gamma_j P_{mhhi_j}^{-+} T_{Bhj,mc}^{+ (n)} + \sum_{j=1}^{M_\theta} \gamma_j P_{mhhi_j}^{--} T_{Bhj,mc}^{- (n)} \\
- \frac{1}{2} \sin \theta_i \frac{\partial}{\partial x} [T_{Bhi,(m+1)c}^{- (n-1)} &+ T_{Bhi,(m-1)c}^{- (n-1)}] - \frac{1}{2} \sin \theta_i \frac{\partial}{\partial y} [T_{Bhi,(m+1)s}^{- (n-1)} - T_{Bhi,(m-1)s}^{- (n-1)}]
\end{aligned} \quad (4.23)$$

where  $\mu_i = \cos \theta_i$ ,  $\{\theta_i\}$  are the Gauss-Lobatto quadrature angles, and  $\{\gamma_j\}$  is the respective Christoffel weights,  $M_\theta$  is the number of elevation quadrature streams between zenith and the horizon (e.g.  $M_\theta = 8$  in this thesis), and  $\kappa_e$  is a scalar extinction coefficient. The extinction coefficient includes both gaseous absorption and hydrometeor absorption and scattering presuming randomly oriented cloud particles.

The zeroth azimuthal harmonic Mie phase matrix has been proven to satisfy the requirements of transition matrix symmetry [122]. It is straightforward to show that the  $m^{\text{th}}$  azimuthal harmonic Mie phase matrix exhibits the same symmetric properties:

$$\begin{aligned}
P_{m\alpha\beta ij}^{++} &= P_{m\alpha\beta ij}^{--}, & P_{m\alpha\beta ij}^{+-} &= P_{m\alpha\beta ij}^{-+} \\
P_{m\alpha\beta ij}^{++} &= P_{m\beta\alpha ji}^{++}, & P_{m\alpha\beta ij}^{+-} &= P_{m\beta\alpha ji}^{-+} \\
\alpha, \beta &= v \text{ or } h
\end{aligned} \quad (4.24)$$

The above relationships show that the  $m^{\text{th}}$  azimuthal harmonic Mie phase matrix elements remain unchanged by either inversion of the signs of  $\mu_i$  and  $\mu_j$  or by permutation of both angular indexes and polarizations. Based on the findings in chapter 3, the above symmetry relations also apply to complex randomly oriented hydrometeors.

Applying the symmetry properties of (4.24) to the discretized radiative transfer equations (4.20) - (4.23), along with defining a new scaled intensity variable set:

$$\begin{aligned}
u_{vi,mc}^{(n)} &= \sqrt{\mu_i \gamma_i} T_{Bvi,mc}^{+ (n)}, & u_{hi,mc}^{(n)} &= \sqrt{\mu_i \gamma_i} T_{Bhi,mc}^{+ (n)} \\
v_{vi,mc}^{(n)} &= \sqrt{\mu_i \gamma_i} T_{Bvi,mc}^{- (n)}, & v_{hi,mc}^{(n)} &= \sqrt{\mu_i \gamma_i} T_{Bhi,mc}^{- (n)}
\end{aligned} \quad (4.25)$$

the matrix form of the discretized equations is obtained:

$$\frac{\partial}{\partial z} \underbrace{\begin{bmatrix} \bar{u}_{mc}^{(n)} \\ \bar{v}_{mc}^{(n)} \end{bmatrix}}_{4M_\theta \times 1} = \underbrace{\begin{bmatrix} -\bar{U}_m & -\bar{D}_m \\ \bar{D}_m & \bar{U}_m \end{bmatrix}}_{4M_\theta \times 4M_\theta} \underbrace{\begin{bmatrix} \bar{u}_{mc}^{(n)} \\ \bar{v}_{mc}^{(n)} \end{bmatrix}}_{4M_\theta \times 1} + \underbrace{\begin{bmatrix} \bar{f}_{1,mc}^{(n)} \\ \bar{f}_{2,mc}^{(n)} \end{bmatrix}}_{4M_\theta \times 1} \quad (4.26)$$

where

$$\bar{u}_{mc}^{(n)} \triangleq \begin{bmatrix} \bar{u}_{v,mc}^{(n)} \\ \bar{u}_{h,mc}^{(n)} \end{bmatrix}, \bar{v}_{mc}^{(n)} \triangleq \begin{bmatrix} \bar{v}_{v,mc}^{(n)} \\ \bar{v}_{h,mc}^{(n)} \end{bmatrix}, \quad (4.27)$$

$$\begin{bmatrix} -\bar{U}_m & -\bar{D}_m \\ \bar{D}_m & \bar{U}_m \end{bmatrix} = \begin{bmatrix} -\bar{A}_{m0} & -\bar{C}_{m0} & -\bar{B}_{m0} & -\bar{D}_{m0} \\ -\bar{E}_{m0} & -\bar{G}_{m0} & -\bar{F}_{m0} & -\bar{H}_{m0} \\ \bar{B}_{m0} & \bar{D}_{m0} & \bar{A}_{m0} & \bar{C}_{m0} \\ \bar{F}_{m0} & \bar{H}_{m0} & \bar{E}_{m0} & \bar{G}_{m0} \end{bmatrix} \quad (4.28)$$

and the elements of submatrices  $\bar{A}_{m0}$  through  $\bar{G}_{m0}$  are defined as:

$$\begin{aligned} A_{m0ij} &= \frac{\kappa_e}{\mu_i} \delta_{ij} - \sqrt{\frac{\gamma_i \gamma_j}{\mu_i \mu_j}} P_{m v v i j}^{+++} & B_{m0ij} &= -\sqrt{\frac{\gamma_i \gamma_j}{\mu_i \mu_j}} P_{m v v i j}^{+-} \\ C_{m0ij} &= -\sqrt{\frac{\gamma_i \gamma_j}{\mu_i \mu_j}} P_{m v h i j}^{+++} & D_{m0ij} &= -\sqrt{\frac{\gamma_i \gamma_j}{\mu_i \mu_j}} P_{m v h i j}^{+-} \\ E_{m0ij} &= -\sqrt{\frac{\gamma_i \gamma_j}{\mu_i \mu_j}} P_{m h v i j}^{+++} & F_{m0ij} &= -\sqrt{\frac{\gamma_i \gamma_j}{\mu_i \mu_j}} P_{m h v i j}^{+-} \\ G_{m0ij} &= \frac{\kappa_e}{\mu_i} \delta_{ij} - \sqrt{\frac{\gamma_i \gamma_j}{\mu_i \mu_j}} P_{m h h i j}^{+++} & H_{m0ij} &= -\sqrt{\frac{\gamma_i \gamma_j}{\mu_i \mu_j}} P_{m h h i j}^{+-} \end{aligned} \quad (4.29)$$

The source function vector for  $m > 0$  in (4.26) is composed of the horizontal gradient of radiances in low perturbation order. The elements of the vector are defined as:

$$\begin{aligned} \bar{f}_{1,mc}^{(n)} &= -\bar{\Lambda} \frac{\partial}{\partial x} \left[ \bar{u}_{(m+1)c}^{(n-1)} + \bar{u}_{(m-1)c}^{(n-1)} \right] \\ &\quad - \bar{\Lambda} \frac{\partial}{\partial y} \left[ \bar{u}_{(m+1)s}^{(n-1)} - \bar{u}_{(m-1)s}^{(n-1)} \right] \\ \bar{f}_{2,mc}^{(n)} &= +\bar{\Lambda} \frac{\partial}{\partial x} \left[ \bar{v}_{(m+1)c}^{(n-1)} + \bar{v}_{(m-1)c}^{(n-1)} \right] \\ &\quad + \bar{\Lambda} \frac{\partial}{\partial y} \left[ \bar{v}_{(m+1)s}^{(n-1)} - \bar{v}_{(m-1)s}^{(n-1)} \right] \end{aligned} \quad (4.30)$$

where  $\bar{\Lambda}$  is a  $2M_\theta \times 2M_\theta$  diagonal matrix with the  $i^{\text{th}}$  diagonal element  $\Lambda_{ii} = \frac{1}{2} \tan \theta_i$ . The boundary conditions simply become null for the higher order (i.e.  $m > 0$ ) azimuthal harmonics of both cosmic background radiation and specular surface thermal emission.

The sine harmonics of the differential equation (4.13) can be discretized using the same process as above, thus resulting in the same form of discretized equations as (4.26) except for the elements of the source function vector:

$$\begin{aligned}
\bar{f}_{1,ms}^{(n)} &= -\bar{\Lambda} \frac{\partial}{\partial x} \left[ \bar{u}_{(m+1)s}^{(n-1)} + \bar{u}_{(m-1)s}^{(n-1)} \right] \\
&\quad - \bar{\Lambda} \frac{\partial}{\partial y} \left[ \bar{u}_{(m-1)c}^{(n-1)} - \bar{u}_{(m+1)c}^{(n-1)} \right] \\
\bar{f}_{2,ms}^{(n)} &= +\bar{\Lambda} \frac{\partial}{\partial x} \left[ \bar{v}_{(m+1)s}^{(n-1)} + \bar{v}_{(m-1)s}^{(n-1)} \right] \\
&\quad + \bar{\Lambda} \frac{\partial}{\partial y} \left[ \bar{v}_{(m-1)c}^{(n-1)} - \bar{v}_{(m+1)c}^{(n-1)} \right]
\end{aligned} \tag{4.31}$$

Following the discussion of the UMRT and DOTLRT solutions in [122, 127], it is straightforward to show that both matrices  $\bar{\bar{A}}_m \triangleq \bar{\bar{U}}_m + \bar{\bar{D}}_m$  and  $\bar{\bar{B}}_m \triangleq \bar{\bar{U}}_m - \bar{\bar{D}}_m$  are symmetric and positive definite for the first two coupled Stokes parameters. Note that  $\bar{\bar{A}}_m$  and  $\bar{\bar{B}}_m$  are not the same as  $\bar{\bar{A}}_{m0}$  and  $\bar{\bar{B}}_{m0}$ . The proof is based on the fact that the extinction coefficient is always greater than or equal to the corresponding scattering coefficient for passive lossy media (e.g. atmosphere and clouds).

### 4.3.2 Solution for 3D Spatially Inhomogeneous Sparse Media

The azimuthal harmonic discrete ordinates of the radiative transfer equations (e.g., 4.26) are discretized in a spatial grid coinciding with that of a numerical weather model (e.g., WRF) where  $x$  and  $y$  are horizontal coordinates and  $z$  is height. The atmosphere with 3D inhomogeneous clouds is thus represented by non-overlapping cubic volumes seamlessly stacked along horizontal and vertical coordinates of the 3D grid. Within each cubic volume the medium radiative properties (e.g.  $\bar{\bar{A}}_m$ ,  $\bar{\bar{B}}_m$ ,  $\kappa_a$ , and  $T$ ) are assumed constant. The horizontal spatial derivatives of the discretized radiation fields are estimated using central finite differencing between adjacent grid nodes. The estimated horizontal derivatives are also assumed to be constant in height (i.e.  $z$ -independent) within any given layer but varying with quadrature stream angles. This assumption is made because each individual volume is considered homogeneous so that the horizontal radiation transported between adjacent volumes for a radiation stream can be modeled as constant in height. The overall solution

is thus obtained by first estimating the horizontal derivatives of the radiation fields and then using the layer-adding method in a recursion to calculate the radiation fields propagating through the vertically stacked volumes.

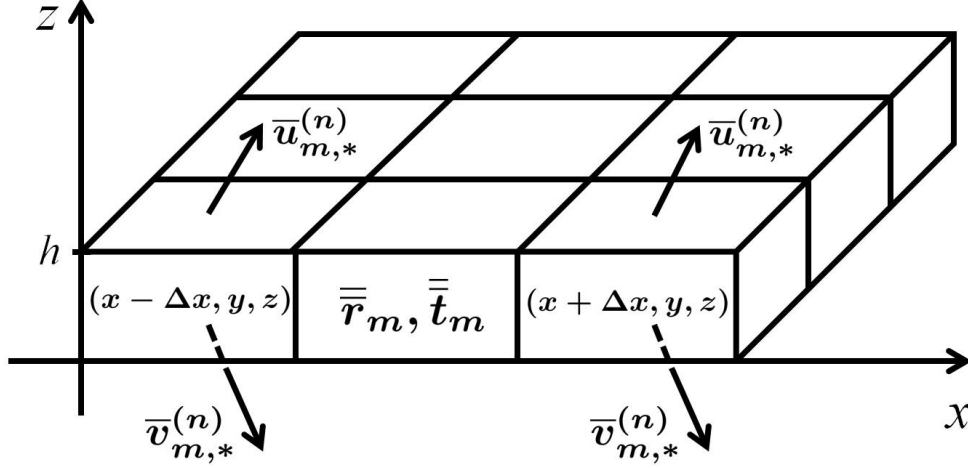


Figure 4.3: Calculation of the azimuthal harmonic reflection and transmission operators  $(\bar{\bar{r}}_m, \bar{\bar{t}}_m)$ , and the azimuthal harmonic perturbation self-radiation fields  $(\bar{u}_{m,*}^{(n)}, \bar{v}_{m,*}^{(n)})$  for a horizontal inhomogeneous layer with thickness  $h$ .

Figure (4.3) shows a single layer of horizontally inhomogeneous clouds divided into many homogeneous cubic volumes. The volumetric scattering and absorption inside a volume are described by the azimuthal harmonic reflection and transmission matrices  $(\bar{\bar{r}}_m, \bar{\bar{t}}_m)$ . Suppose an external radiation field of  $m^{\text{th}}$  azimuthal harmonic  $\bar{u}_{m,e}$  impinges upon the bottom of a cloud volume. In this case,  $(\bar{\bar{r}}_m, \bar{\bar{t}}_m)$  are implicitly defined as:

$$\begin{aligned} \bar{u}_m &= \bar{\bar{t}}_m \bar{u}_{m,e} & \text{at } z = h \\ \bar{v}_m &= \bar{\bar{r}}_m \bar{u}_{m,e} & \text{at } z = 0 \end{aligned} \quad (4.32)$$

Following UMRT [122], the azimuthal harmonic reflection and transmission matrices can be found using the homogeneous solution of the equation (4.26) and written in terms of the sub-block sum



and difference matrices of the transition matrix,  $\overline{\overline{A}}_m$  and  $\overline{\overline{B}}_m$  as:

$$\begin{aligned}\overline{\overline{t}}_m &= 2(\overline{\overline{c}}_m + \overline{\overline{B}}_m \overline{\overline{s}}_m + \overline{\overline{s}}_m \overline{\overline{A}}_m + \overline{\overline{c}}_m^T)^{-1} \triangleq 2\overline{\overline{Q}}_m^{-1} \\ \overline{\overline{r}}_m &= \overline{\overline{Q}}_m^{-1} (\overline{\overline{c}}_m + \overline{\overline{B}}_m \overline{\overline{s}}_m - \overline{\overline{s}}_m \overline{\overline{A}}_m - \overline{\overline{c}}_m^T)\end{aligned}\quad (4.33)$$

where

$$\begin{aligned}\overline{\overline{c}}_m &\triangleq \cosh\left(\sqrt{\overline{\overline{A}}_m \overline{\overline{B}}_m} h\right) \\ \overline{\overline{s}}_m &\triangleq \sinh\left(\sqrt{\overline{\overline{A}}_m \overline{\overline{B}}_m} h\right) \left(\overline{\overline{A}}_m \overline{\overline{B}}_m\right)^{-\frac{1}{2}}\end{aligned}\quad (4.34)$$

Note that a numerical failure will usually happen to the matrix inversion  $\overline{\overline{Q}}_m^{-1}$  for highly opaque and thick clouds due to ill-conditioning of  $\overline{\overline{Q}}_m$  caused by hyperbolic function calculations. Instead, analytic diagonalization and factorization of the symmetric and positive definite matrices  $\overline{\overline{A}}_m$  and  $\overline{\overline{B}}_m$  result in numerically stable matrix operations in calculating the azimuthal harmonic reflection and transmission matrices (see equations 48-49 in [122]). This process of stabilization is described in detail in [127].

Owing to thermal emission, an individual volume will generate 0<sup>th</sup> order azimuthal harmonic self-radiation streams at the top and bottom surfaces. Due to the horizontal gradient in radiances of low perturbation order, each individual volume might also generate the  $m^{\text{th}}$  azimuthal harmonic self-radiation streams at the top and bottom surfaces. Following the notation of UMRT, these streams are denoted by the subscript  $*$  (e.g.  $\overline{u}_{m,*}^{(n)}$  and  $\overline{v}_{m,*}^{(n)}$  in Figure 4.3). To solve for these self-radiation streams, the inhomogeneous solution of the radiative transfer equation (4.26) needs to be found by using the following shorthand notation for equation (4.26):

$$\frac{\partial}{\partial z} \overline{W}_{mc}^{(n)} = \overline{\overline{T}}_m \overline{W}_{mc}^{(n)} + \overline{F}_{mc}^{(n)} \quad (4.35)$$

where

$$\begin{aligned}\overline{W}_{mc}^{(n)} &\triangleq \begin{bmatrix} \overline{u}_{mc}^{(n)} \\ \overline{v}_{mc}^{(n)} \end{bmatrix}, \quad \overline{\overline{T}}_m \triangleq \begin{bmatrix} -\overline{\overline{U}}_m & -\overline{\overline{D}}_m \\ \overline{\overline{D}}_m & \overline{\overline{U}}_m \end{bmatrix} \\ \overline{F}_{mc}^{(n)} &\triangleq \begin{bmatrix} \overline{f}_{1,mc}^{(n)} \\ \overline{f}_{2,mc}^{(n)} \end{bmatrix}\end{aligned}$$

The complete solution of the equation (4.35) can be found using the matrix exponential operator and the integrating factor method [97], written as:

$$\overline{W}_{mc}^{(n)}(z) = e^{\overline{T}_m z} \overline{W}_{mc}^{(n)}(0) + e^{\overline{T}_m z} \int_0^z e^{-\overline{T}_m z'} \overline{F}_{mc}^{(n)} dz' \quad (4.36)$$

where  $\overline{W}_{mc}^{(n)}(0)$  is the azimuthal harmonic perturbation radiation field at  $z = 0$ . The source term  $\overline{F}_m^{(n)}$  is comprised of horizontal derivatives in radiances of azimuthal harmonics  $(m + 1)$  and  $(m - 1)$  in the perturbation order  $(n - 1)$ . Using the aforementioned assumption of the  $z$ -independence of the horizontal derivatives, the inhomogeneous solution of equation (4.35) would be found as:

$$\overline{W}_{mc,inh}^{(n)}(z) = -\overline{T}_m^{-1} \overline{F}_{mc}^{(n)} \quad (4.37)$$

The relationship between the above inhomogeneous solution and the azimuthal harmonic perturbation self-radiation fields can be established based on the same calculation as used in UMRT, thus expressed as:

$$\begin{aligned} \overline{u}_{mc,*}^{(n)}(h) &= \overline{u}_{mc,inh}^{(n)}(h) - \overline{r}_m \overline{v}_{mc,inh}^{(n)}(h) - \overline{t} \overline{u}_{mc,inh}^{(n)}(0) \\ \overline{v}_{mc,*}^{(n)}(0) &= \overline{v}_{mc,inh}^{(n)}(0) - \overline{r}_m \overline{u}_{mc,inh}^{(n)}(0) - \overline{t} \overline{v}_{mc,inh}^{(n)}(h) \end{aligned} \quad (4.38)$$

Finally, the horizontal derivative in radiances of cosine harmonics (subscript  $mc$ ) and perturbation order  $n$  required as part of the source function is estimated using the self-radiation fields  $(\overline{u}_{mc,*}^{(n)}, \overline{v}_{mc,*}^{(n)})$  based on the central differencing method as:

$$\begin{aligned} \frac{\partial}{\partial x} \overline{u}_{mc}^{(n)} &\approx \frac{\overline{u}_{mc,*}^{(n)}(x + \Delta x, y, h) - \overline{u}_{mc,*}^{(n)}(x - \Delta x, y, h)}{2\Delta x} \\ \frac{\partial}{\partial y} \overline{u}_{mc}^{(n)} &\approx \frac{\overline{u}_{mc,*}^{(n)}(x, y + \Delta y, h) - \overline{u}_{mc,*}^{(n)}(x, y - \Delta y, h)}{2\Delta y} \\ \frac{\partial}{\partial x} \overline{v}_{mc}^{(n)} &\approx \frac{\overline{v}_{mc,*}^{(n)}(x + \Delta x, y, 0) - \overline{v}_{mc,*}^{(n)}(x - \Delta x, y, 0)}{2\Delta x} \\ \frac{\partial}{\partial y} \overline{v}_{mc}^{(n)} &\approx \frac{\overline{v}_{mc,*}^{(n)}(x, y + \Delta y, 0) - \overline{v}_{mc,*}^{(n)}(x, y - \Delta y, 0)}{2\Delta y} \end{aligned} \quad (4.39)$$

The horizontal derivative of the sine harmonics can be estimated in an analogous manner using  $(\bar{u}_{ms,*}^{(n)}, \bar{v}_{ms,*}^{(n)})$  based on the central differencing method.

For a given azimuthal harmonic order  $m$  and perturbation order  $n$ , the total radiated and reflected stream vectors for a multilayer inhomogeneous medium can be computed based on the radiative solution of each horizontally inhomogeneous layer. These properties for an individual cubic volume are the azimuthal harmonic reflection and transmission matrices  $(\bar{r}_m, \bar{t}_m)$  and the azimuthal harmonic self-radiation vectors  $\bar{u}_{mc,*}^{(n)}, \bar{u}_{ms,*}^{(n)}, \bar{v}_{mc,*}^{(n)}, \bar{v}_{ms,*}^{(n)}$  at the top and bottom surface of the volume. The overall radiative properties of the vertically stacked volumes can thus be calculated by upward recursion based on the lower and upper boundary conditions (see [122], eq. 57).

Note that when  $m = 0$  and  $n = 0$  as the initial step of the HI-UMRT framework, the self-radiation fields  $(\bar{u}_{0c,*}^{(0)}, \bar{v}_{0c,*}^{(0)})$  due to thermal emission are obtained using the existing 1D UMRT algorithm. The horizontal gradients of the radiation fields  $\bar{u}_{0c}^{(0)}, \bar{v}_{0c}^{(0)}$  estimated using (4.39) construct the source function of the radiative transfer equation (4.26) in the 1<sup>th</sup> azimuthal harmonics and the 1<sup>th</sup> perturbation order. After that, the iterative perturbations begin and follow the paths shown in the perturbation source diagram (see Figure 4.2) till the convergence at the maximum perturbation order  $N$ .

### 4.3.3 Convergence Criterion

HI-UMRT needs a sufficient number of perturbation iterations to achieve the required precision in computed microwave radiance for practical applications. This precision is generally less than 2 K in brightness temperature. In general, the perturbation error caused by neglecting higher order perturbation corrections than  $N$  depends on the degree of horizontal inhomogeneity of the medium. For example, more iterations are expected over abrupt cloud edges than in stratiform clouds due to the discontinuity in radiation across the cloud horizontal boundaries. In this study, the maximum change of the brightness temperature at the observation level made by the  $n^{\text{th}}$  order perturbation correction is calculated and compared with a preset threshold in degrees Kelvin for terminating the maximum perturbation iteration required for acceptable convergence. The maximum perturbation

order  $N$  is determined using the condition below:

$$\max_{n=N} \{\bar{T}_B^{(n)} - \bar{T}_B^{(n-1)}\} < 0.2 \text{ K} \quad (4.40)$$

where  $\bar{T}_B^{(n)}$  is the brightness temperature vector at an observation level computed by the HI-UMRT algorithm using the accumulated  $n^{\text{th}}$  order perturbation corrections, and 0.2 K is (admittedly) somewhat arbitrary.

In practice, an comparable empirical convergence relationship of the maximum brightness temperature correction to the perturbation order can be found based on the numerical HI-UMRT solution over a challenging simulation domain. If the maximum brightness temperature correction decreases exponentially as the perturbation order increases, we can find an exponential function of maximum  $T_B$  correction by regression fitting the correction data to an exponential for the first 3 perturbation orders. Using this empirical relationship, the required perturbation order for achieving a preset precision (e.g.  $< 0.2$  K) can be determined after the 3<sup>rd</sup> order perturbation correction. This method for assessing convergence is illustrated in Section 5.1.

## Chapter 5

### Simulations of Microwave Radiances using 3D HI-UMRT Model

The impact of cloud horizontal inhomogeneities on computed microwave radiances can be assessed using radiative transfer simulations over clouds in severe weather, such as the intensified hurricane Sandy (October 29th, 2012) event. Meaningful simulations of such mesoscale events can be based on microphysical cloud profiles simulated using the Weather Research and Forecasting (WRF v3.5) model. A selected simulation domain covers a  $1000 \times 1000$  km region over the Atlantic Ocean and is discretized into 3D grids with  $5 \times 5$  km horizontal spacing and 60 vertical levels. This domain was selected to compute microwave radiances propagating through 3D inhomogeneous clouds near rain bands, the hurricane eyewall region, and surrounding deep convective towers.

The Reisner five-phase cloud model [98, 127] was used to simulate hydrometeor microphysical states, wherein five spherical hydrometeor phases are assumed. Liquid hydrometeors follow the Marshall-Palmer particle size distribution [85]. Exponential size distributions are applied to frozen and mixed-phase hydrometeors with a fixed number density of particles and a variable mean particle size to account for the total volumetric mass content of hydrometeors [103, 121]. For spherical hydrometeors, the single-scattering parameters (e.g. scalar extinction coefficient, absorption coefficient, and Stokes matrix) were calculated using Mie theory [41]. A total of 16 elevation angle quadrature streams, (i.e.,  $M_\theta = 16$ ), is used in the numerical examples. Based on the results from chapter 4, the number of azimuthal harmonics is thus set to  $M_\phi = 16$ . Note that the zeroth azimuthal harmonic and perturbation equation is the 1D radiative transfer equation under the planar-stratified assumption readily solvable using the 1D UMRT engine. The intercomparison of top-of-atmosphere

brightness temperatures computed using 3D HI-UMRT and 1D UMRT can be used to show the cumulative perturbation corrections to the planar-stratified radiative transfer solution. Frequencies of 166.31 and 240.70 GHz were chosen for the HI-UMRT/UMRT intercomparisons because the radiances at these frequencies are highly sensitive to cloud hydrometeor scattering and are strongly absorbed by water vapor in the lower troposphere, thus isolating the impact of the Earth’s surface reflection on the upwelling radiances.

In this chapter, numerical simulations are shown to illustrate the converged perturbation corrections and further understand 3D cloud radiative effects by comparing simulated upwelling brightness temperature imagery obtained using the 3D HI-UMRT algorithm to that obtained using the planar-stratified 1D UMRT model.

## 5.1 Convergent Perturbation Series

The first performance test was designed to verify the convergence of the iterative perturbation series used in the HI-UMRT model. Fig. 5.1 shows decreases in the maximum change of brightness temperature computed by HI-UMRT at each increasing perturbation order. At any given perturbation order  $n$ , HI-UMRT computes the upwelling brightness temperature as the summation of the sine and cosine azimuthal harmonics which are obtained by adding up the horizontal perturbation corrections up to  $n^{\text{th}}$  lower order. The maximum change of top-of-atmosphere brightness temperatures within eight elevation streams and two orthogonal linear polarizations between perturbation order  $n$  and  $n - 1$ , (i.e., maximum  $\{\overline{T}_B^{(n)} - \overline{T}_B^{(n-1)}\}$ ) can readily be found. After 15 perturbation iterations, the maximum brightness temperature corrections for the Sandy event are reduced to  $\sim 0.2$  K for 166.31 GHz and  $\sim 0.1$  K for 240.70 GHz (see Fig. 5.1).

Two dashed curves are also plotted in Figure 5.1 to show the predicted rate of convergence using nonlinear least-squares data fitting [19] applied to the data points computed using HI-UMRT with lower perturbation order in the corresponding solid curve. This data fitting method has been implemented using the curve fitting toolbox of the MATLAB software environment. The required number of perturbation iterations in the HI-UMRT algorithm can be estimated based

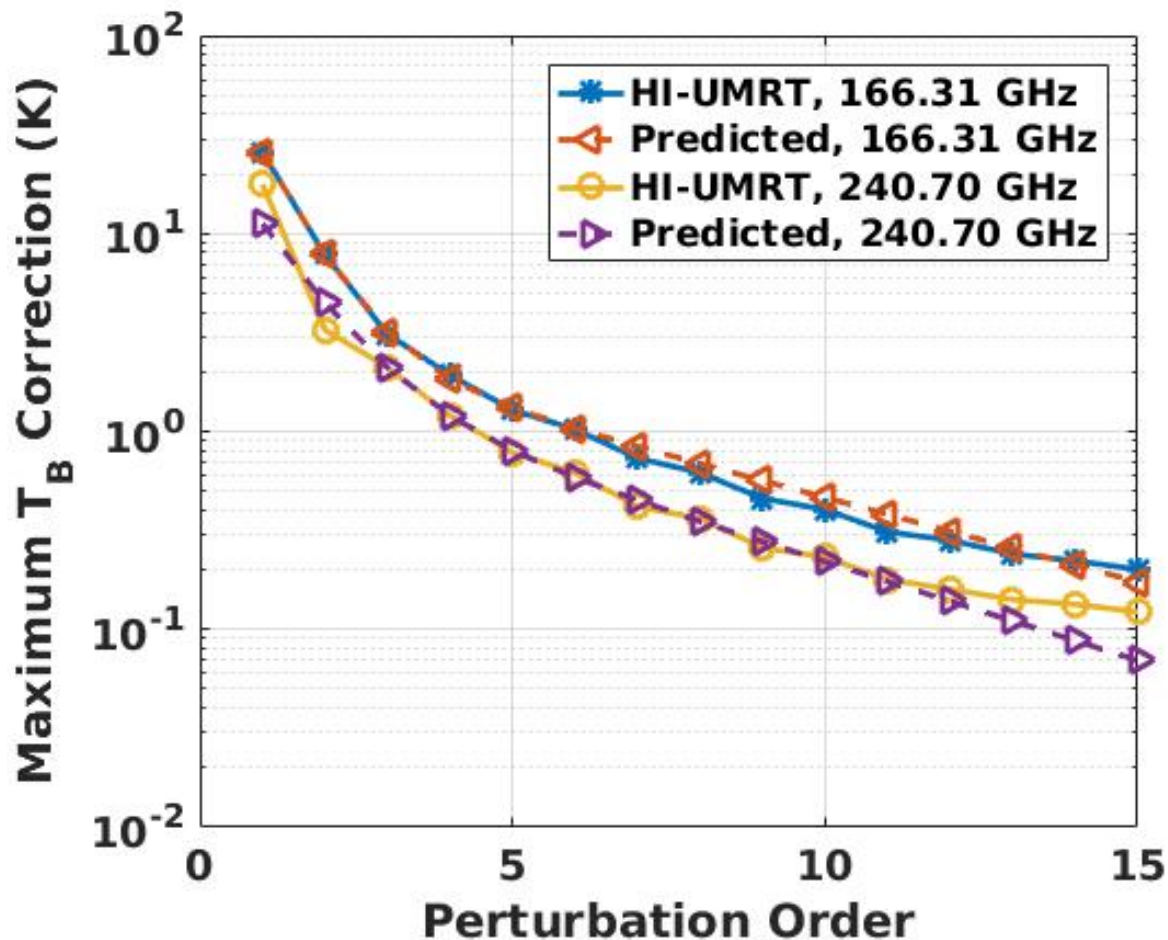


Figure 5.1: Relationship between the maximum perturbation correction and the perturbation order for upwelling brightness temperature simulations for hurricane Sandy at 166.31 GHz and 240.70 GHz. The maximum  $T_B$  change with the 15<sup>th</sup> order perturbation correction reaches the convergence threshold of 0.2 K. The solid curve for the perturbation corrections computed using HI-UMRT and the dashed curve for the predicted perturbation corrections.

on the brightness temperature corrections within the lower perturbation orders. For example at 166.31 GHz fifteen perturbation iterations are required to achieve  $< 0.2$  K  $T_B$  maximum correction upon completing the 6<sup>th</sup> order perturbation iteration. Based on the perturbation source diagram (see Figure 4.2) the 1D UMRT model thus needs to be repeated  $0.5 \times 16 \times 17 = 136$  times until convergence. Equivalently, the computing time for convergence on a 70 teraFLOPS machine is  $\sim 5$  minutes for a  $200 \times 200 \times 60$  3D grid based on the theoretical computational complexity analysis in Section 4.

## 5.2 Azimuthally Dependent 3D Radiation Effects

The HI-UMRT radiative solution is the superposition of 3D iterative perturbation corrections imposed on the 1D planar-stratified radiative solution. Thus, 3D radiation effects can be revealed by subtracting 1D brightness temperatures from the corresponding converged HI-UMRT solution for the entire simulation domain at the observation level of interest. These 3D radiation effects depend on both elevation angle  $\theta$  and azimuth angle  $\phi$ .

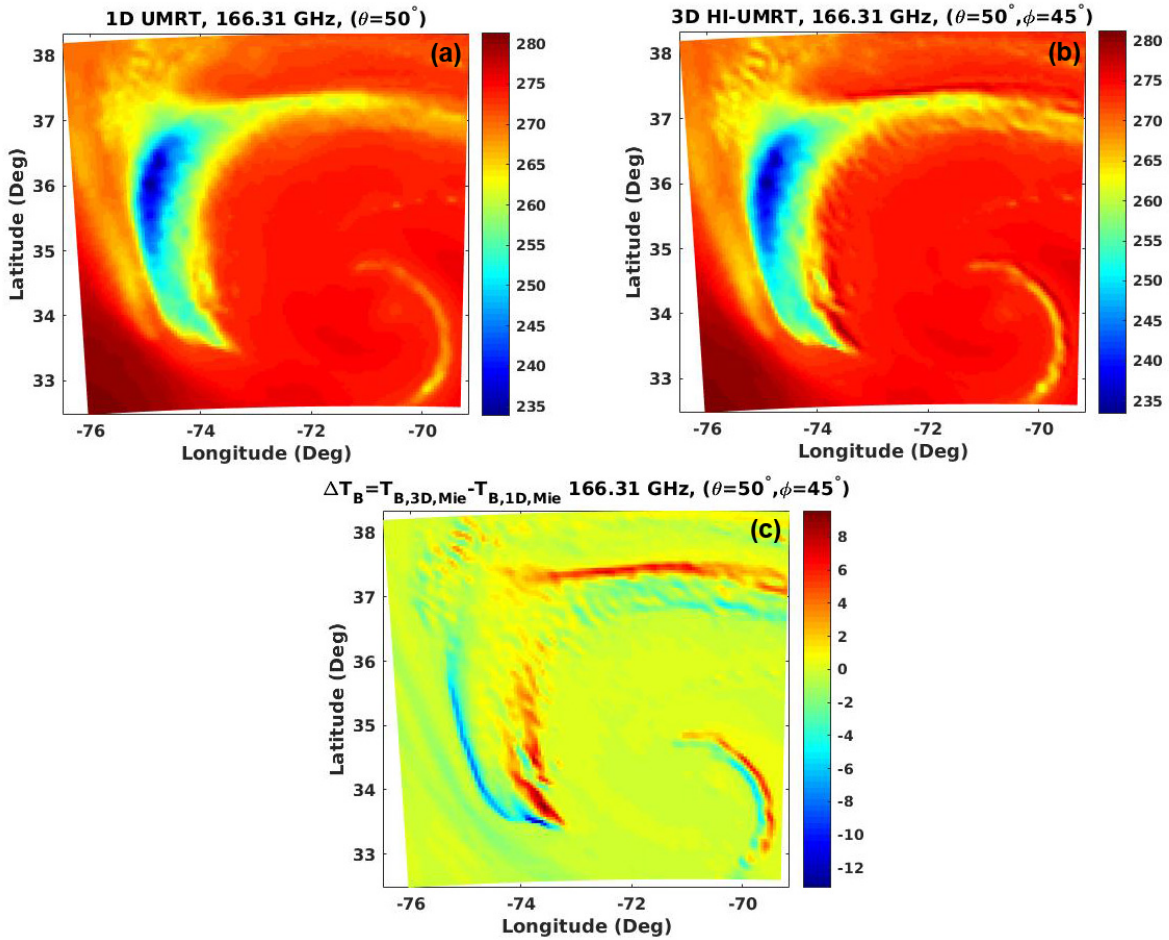


Figure 5.2: Simulation of 3D radiative transfer through opaque and horizontally inhomogeneous clouds in a simulation domain over hurricane Sandy 2012 at 166.31 GHz. The angular variables of the radiative transfer equation are set to be  $\theta = 50^\circ$  and  $\phi = 45^\circ$ . (a) 1D UMRT top-of-atmosphere brightness temperature image obtained using HI-UMRT with  $m = 0$  and  $n = 0$ ; (b) 3D HI-UMRT brightness temperature image computed up to 15<sup>th</sup> order perturbation corrections; (c) Difference between 3D and 1D radiative transfer solution (i.e. (b)-(a)).



Figure 5.2 shows a simulation of top-of-atmosphere brightness temperature image using HI-UMRT with  $\theta = 50^\circ$ ,  $\phi = 45^\circ$  at 166.31 GHz. Panel (c) shows the difference between brightness temperatures computed up to 15<sup>th</sup> order perturbation corrections (panel (b)) versus the 0<sup>th</sup> order perturbation solution (panel (a)). The azimuthal angle of  $45^\circ$  is used to simulate radiation streams propagating out of the image and being tilted toward the upper-right corner of the image (i.e., toward the northeast). The magnitude of the brightness temperature differences  $\Delta T_B$  within the simulation domain falls in the range between -12 K and +10 K. Importantly, one stripe of positive  $\Delta T_B$  always occurs in parallel with another stripe of negative  $\Delta T_B$  around the cloud edges of rain bands or close to a hurricane eye wall. This positive and negative  $\Delta T_B$  coupling phenomenon is caused by horizontal radiation transport within the underlying horizontally inhomogeneous clouds. The 1D radiative transfer model (e.g. UMRT) under the planar-stratified assumption and the independent-pixel approximation neglects these radiative interactions between adjacent cloud columns, thus introducing biases in brightness temperatures at the locations of horizontal cloud edges. In addition, the sign of the brightness temperature differences also indicates the direction of the effective horizontal radiative transfer within the clouds. For example, the sign of the image in panel (c) reverses for observations from  $\phi = 225^\circ$ .

Note that the HI-UMRT algorithm provides the radiative solution in a 5-dimensional space (i.e., 3 spatial variables plus 2 angular variables). Particularly, the 3D radiation field solutions  $T_B(x, y, z, \theta, \phi)$  vary with the azimuth angle  $\phi$ . Thus, the brightness temperature differences computed using 3D HI-UMRT versus 1D UMRT are expected to change with azimuth angle. Figure 5.3 illustrates the brightness temperature differences  $\Delta T_B$  simulated at four different azimuth angles from  $\phi = 0^\circ$  through  $\phi = 270^\circ$  at  $90^\circ$  intervals. Although the positive and negative  $\Delta T_B$  coupling phenomenon can be seen in all images with analogous magnitude, the coupled stripes are found to turn  $90^\circ$  counterclockwise in successive images. That is, the stripes are perpendicular to the azimuth angle. The spatial distribution of the coupled stripes also varies with the degree of effective horizontal radiative transfer gradient. For example, positive or negative stripes of brightness temperature differences (e.g. several Kelvin in absolute value) only appear at the tail of the large

cyclonic cloud band in Figure 5.3 at azimuth angles  $\phi = 90^\circ$  and  $\phi = 270^\circ$ .

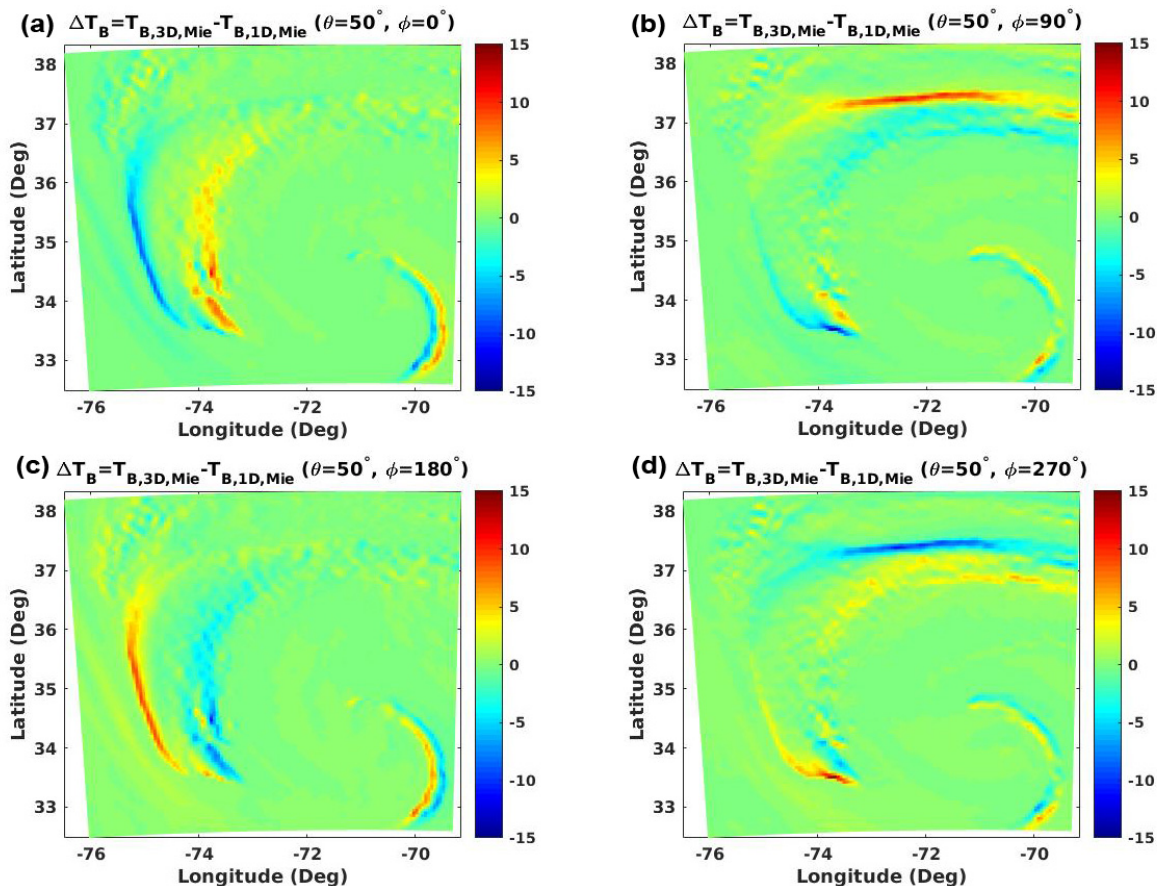


Figure 5.3: Simulation of brightness temperature differences for the Sandy 2012 event between 3D and 1D radiative transfer solutions at four different azimuth angles: (a)  $\phi = 0^\circ$ , (b)  $\phi = 90^\circ$ , (c)  $\phi = 180^\circ$ , (d)  $\phi = 270^\circ$ .

Finally, Table 5.1 compares attributes of 3D HI-UMRT with those of 1D UMRT along with the discrete-ordinate tangent linear radiative transfer (DOTLRT) model. The DOTLRT model originates the development of numerically stable and unconditionally computationally efficient plane parallel radiative transfer solution. The 3D HI-UMRT inherits all of the computational advantages of 1D model and extends the radiative transfer solution to the 3D case based on azimuthal harmonics of the radiation fields and an iterative perturbation series.

Table 5.1: Evolution of 3D HI-UMRT originating from 1D discrete-ordinate tangent linear RT (DOTLRT) model [127]

<b>Attribute</b>	<b>HI-UMRT</b>	<b>UMRT</b>	<b>DOTLRT</b>
Fast, Stable Analytic Matrix Inversion	Yes	Yes	Yes
3D Atmospheric Inhomogeneities	Perturbation series and azimuthal harmonics	No	No
Fast Jacobian	Yes	Yes	Yes
Phase Matrix	DDSCAT-based or Reduced Mie or DMRT (4x4)	Reduced Mie or DMRT (4x4)	Reduced HG (2x2)
Media	Sparse (and Dense)*	Sparse and Dense	Sparse
Polarization	Dual-polarization	Dual-polarization	Single-polarization
Interface Refraction / Internal Reflection	(Yes)*	Yes	No
Radiation Stream Interpolation	Yes, cubic spline	Yes, cubic spline	No
Layer Thermal Emission Approximation	Linear dependence	Linear dependence	Constant
Level/Layer Centric	Level	Level	Layer

\*Dense media surface emissivity extensions for complex surfaces (e.g., snow, unisotropic wind driven oceans) are under development.

## Chapter 6

### Microwave Radiances Assimilation Scheme: Precipitation Locking

To improve numerical weather forecast accuracy, a numerical weather model with realistic physical representation of the atmosphere and accurate knowledge of the atmospheric state vector used as initial conditions are required [59]. Direct observations of atmospheric state variables via *in situ* means such as sondes, aircraft, and weather stations can be used along satellite and surface weather radar data to improve the accuracy of the state vector [3]. Spaceborne and airborne observations based on remote sensing techniques are key sources of meteorological information, especially over the oceans and southern hemisphere. The process of using all of these types of observations for optimal atmospheric state vector update is known as data assimilation [105].

Methods of data assimilation have been developed over several decades, including the first empirical-based analysis approach known as the successive correction method (SCM) [21]. Multivariate analysis methods based on statistical estimation theory were subsequently introduced and have resulted in more accurate numerical weather model forecasts. Among these methods, the technique known as “Optimal Interpolation” (OI) was developed based on a linearized minimum mean square error (LMMSE) estimator to optimally correct the state vector using the criterion of orthogonality of the innovations and the estimation error. Equivalently, three-dimensional variational data assimilation (3D-VAR) was formulated based on the least mean squares solution to minimize the cost function, which is based on both a background error covariance and an observation error covariance matrix [82, 59]. The state vector in the cost function can be extended to 4-dimensions by considering the time evolution of the numerical weather model process. Accordingly,

the 4-dimensional variational assimilation (4D-VAR) scheme has been used to handle arbitrary observation times [72, 22, 59]. Modern data assimilation methods are based on either extended Kalman filtering or ensemble Kalman filtering schemes that update the background error covariance in each assimilation cycle [59].

## 6.1 Precipitation Locking Concept

The state vector update in a data assimilation cycle typically is made to only the thermodynamic variables (e.g. temperature  $T$ , pressure  $p$ , air density  $\rho$ , water vapor density  $q$ , and wind vector  $(u, v, w)$ ) at each grid point  $(x, y, z)$  and at any given analysis time  $t$ . These variables follow a complete set of seven governing equations for the atmosphere [59] based on the laws of conservation of momentum, energy, dry air mass, and moisture in all forms. However, hydrometeor variables for clouds and precipitation cells in numerical weather prediction (NWP) models can also be potentially corrected by directly assimilating microwave radiance observations which have all of: (i) a wide range of cloud penetrabilities, and (ii) high spatio-temporal resolution comparable to that of convective scales. General algorithms for microwave data assimilation into NWP models that correct both thermodynamic and hydrometeor variables are required to be developed with similar conservation law constraints based on flow-dependent nonlinear observation operators and background error covariance matrices. To this end, the concept of *precipitation locking* based on microwave radiances assimilation focuses on optimal updates of both thermodynamic and hydrometeor state variables in an NWP model:

$$\bar{x}(x, y, z, t) = \{T, q, \rho_c, \rho_r, \rho_i, \rho_s, \rho_g\} \quad (6.1)$$

where  $(\rho_c, \rho_r, \rho_i, \rho_s, \rho_g)$  are the bulk density in  $\text{g/m}^3$  for the five microphysical categories of hydrometeors: 1) cloud liquid water, 2) rain droplets, 3) ice, 4) snow, and 5) graupel (respectively).

When both the NWP model hydrometeor and thermodynamic state variables are close enough to the truth to permit linear state variable corrections it can be said that the model is “precipitation locked”. Precipitation locking is analogous to the locking of a phase locked loop in that linear phase

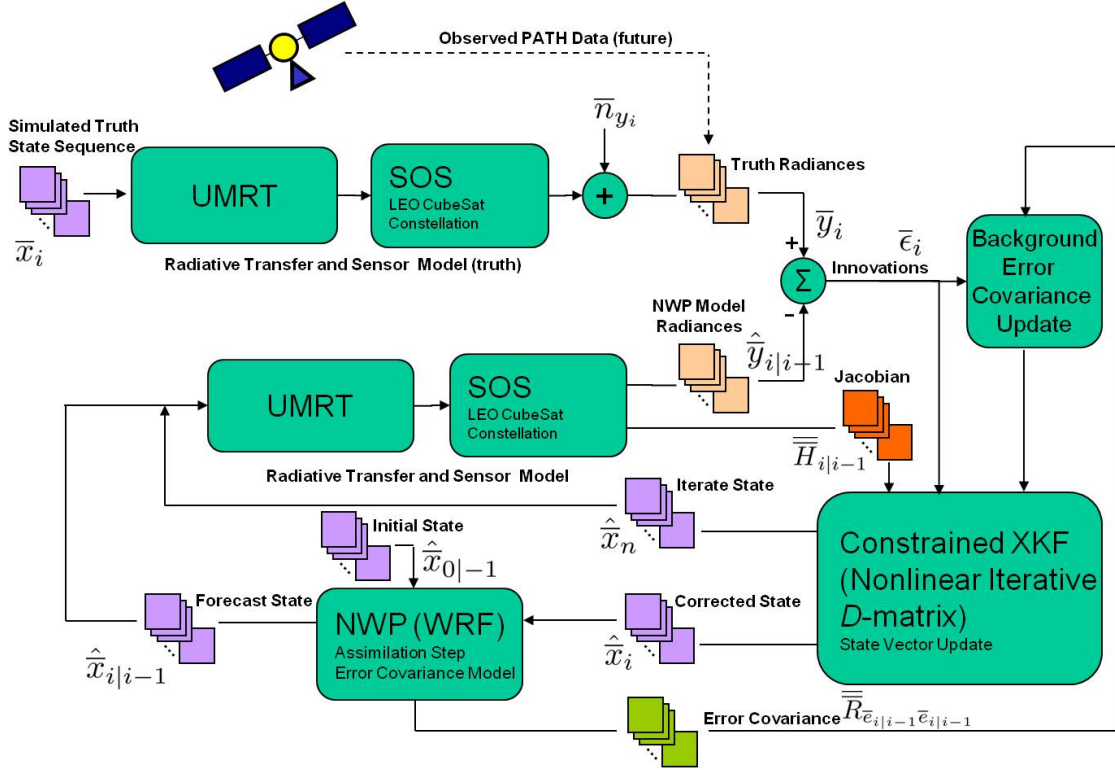


Figure 6.1: Precipitation locking simulation system under development at Center for Environmental Technology (CET) at University of Colorado at Boulder.

differencing is used to drive the loop oscillator phase to remain close to that of the input signal [40]. Departure of the input signal and oscillator phases by more than typically  $\sim \pi/3$  radians results in loss of lock and concomitant collapse of signal-to-noise ratio. Analogously, a precipitation-locked NWP model requires both hydrometeor and thermodynamic state variables to be close to the truth, thus permitting frequent linear corrections through the Kalman gain matrix to be applied to innovations to maintain near-truth (see Figure 6.1). High temporal resolution satellite data would be necessary to maintain precipitation lock along with the appropriate requisite sampling rate and spatial resolution.

## 6.2 Simulations of High-temporal Resolution Observations

To date, satellites providing sub-hourly microwave observations with spatial resolution of  $\sim 15\text{-}30$  km over mesoscale weather systems in tropical and extratropical regions remain in the

development stage for concept demonstration (e.g. CubeSat constellations of small satellites [11, 94]). Observing system simulation experiments (OSSEs) are thus required to provide experimental data for assisting both hardware development and subsequent efforts of assimilating microwave data into NWP models. To this end, a sequence of microwave antenna temperature images of the extratropical cyclone (hurricane) Sandy (2012) was simulated using the Weather Research and Forecasting (WRF v3.5) model and the 1D UMRT model for a CubeSat constellation overflying the event every 30 minutes. Simulations were carried out based on a standard WRF simulation domain configuration, individual CubeSat radiometer specifications, and anticipated CubeSat constellation orbit parameters.

The severe weather event in the simulation is hurricane Sandy during its intensification between October 29th and 30th, 2012. The 3D cubic simulation domain was configured to have 337 staggered grid points in the east-west direction and 301 staggered grid points in the north-south direction with 5 km horizontal spacing and 33 staggered vertical levels. The Weather Research and Forecasting model (WRF v3.5.1) was used to generate a truth state sequence of atmosphere prognostic variables (e.g. temperature, water vapor, and five-category hydrometeor densities) in the simulation domain at intervals of 30 minutes.

The observation system specifications of the 3U PolarCube and Orbital Micro System's (OMS) GEMSO1a CubeSat radiometer [94] developed at CU CET were applied to these truth radiance simulations. The PolarCube sensor (dubbed "MiniRad") uses a cross-track scanning total power radiometer to be deployed in an orbit of  $\sim 425$  km altitude and providing a  $\sim 900$  km wide swath. It operates at a center frequency of 118.75 GHz near the  $1^-$  oxygen absorption line with 8 sensing channels. The 3dB beam width at nadir is  $\sim 2.3^\circ$  and nadir footprint size  $\sim 17$  km. A quadratically-tapered aperture is assumed for all channels. The resulting antenna gain pattern can be described by [112]:

$$g(\theta) = g_o \left| \frac{J_{q+1}\left(\frac{\pi D}{\lambda} \sin \theta\right)}{\left(\frac{\pi D}{\lambda} \sin \theta\right)^{q+1}} \right|^2 \quad (6.2)$$

where  $g_o$  is a normalization constant,  $J_n$  is the  $n^{\text{th}}$  order Bessel function,  $q = 1$  is the quadratic taper

exponent,  $\theta$  denotes the angle from boresight,  $D$  is the aperture diameter, and  $\lambda$  is the wavelength. Since MiniRad uses cross-track scanning the linear polarization state of the antenna rotates with scan angle ( $\theta_s$ ) and thus incorporates mixed horizontal and vertical components. The resulting rotated linearly polarized antenna temperature measurement can be modeled as [133]:

$$T_A(\theta_s) = T_A^v \cos^2 \theta_s + T_A^h \sin^2 \theta_s \quad (6.3)$$

The GEMS CubeSat constellation concept uses  $\sim 50$  CubeSat-based small satellites deployed in multiple orbital planes, for example the International Space Station orbit with inclination of  $57.6^\circ$  or NASA A-train orbit with inclination of  $98.14^\circ$ . Figure 6.2 illustrates that  $\sim 15$ -30 minute mean revisit times are achievable using a modest 36-satellite constellation [44]. Top-of-atmosphere

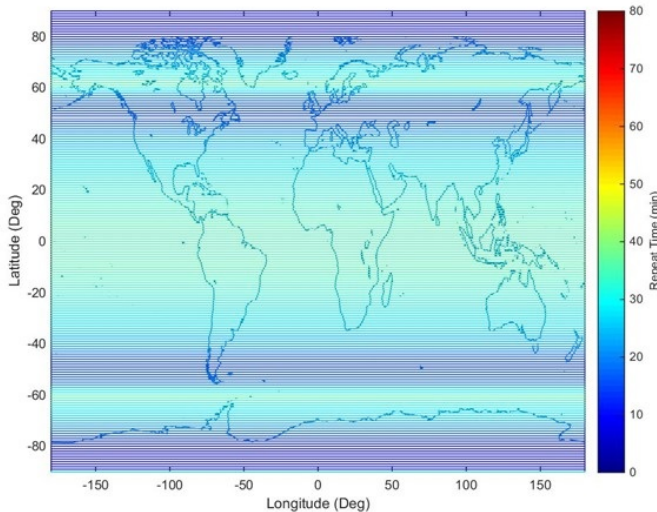


Figure 6.2: Sub-hourly repeat times for a 36-satellite CubeSat constellation [44].

brightness temperature  $T_B$  images for cross-track viewing were simulated using the UMRT model for four MiniRad channels with frequency offsets from the  $1^-$   $O_2$  line center of 0.7 GHz, 1.1 GHz, 1.5 GHz and 2.1 GHz. The rotated linear polarization antenna temperature images (see Figure 6.3) were subsequently computed by convolving the antenna gain patterns with the upwelling brightness temperature imagery. Key features of Sandy are revealed in all four selected channels. The warm core in the eye of the hurricane, the cold temperatures over the near-eyewall rain bands resulting



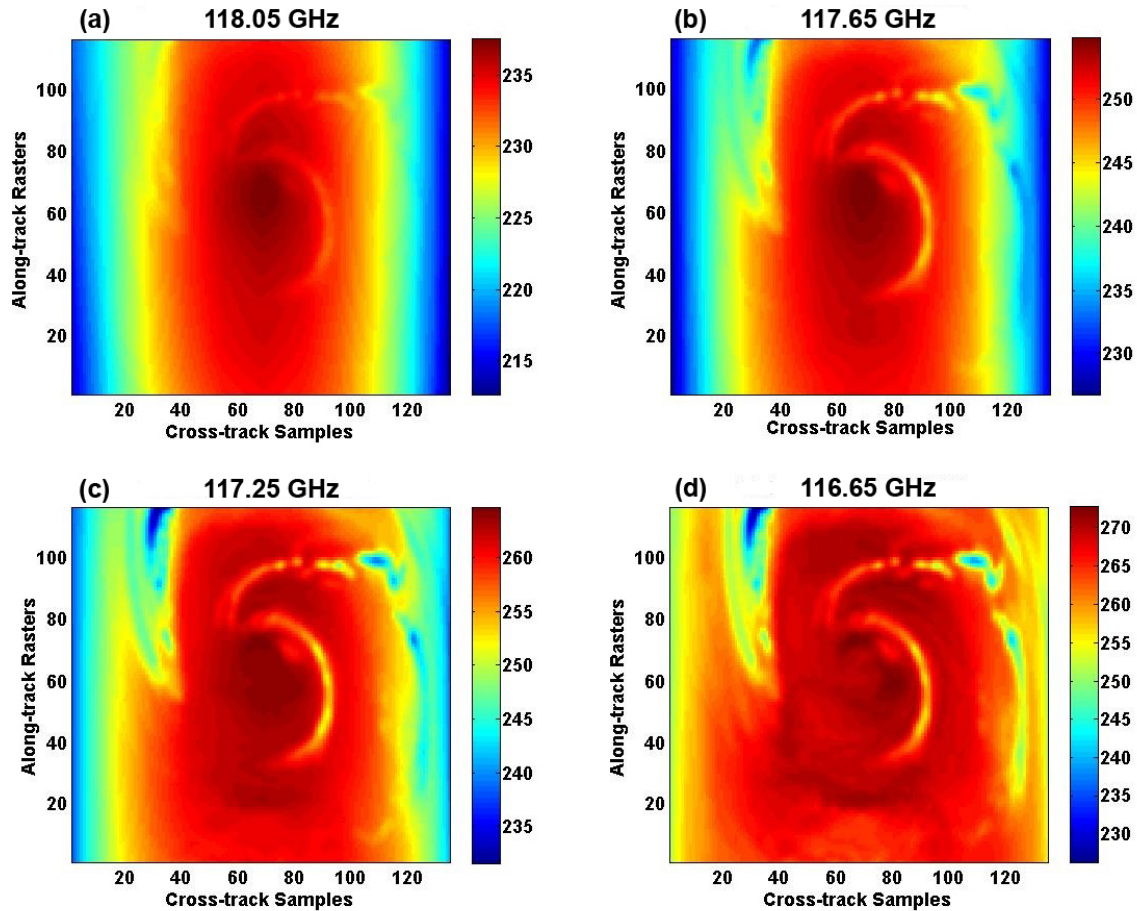


Figure 6.3: Simulated rotated linear polarization antenna temperature images for four selected MiniRad channels: (a) 118.05 GHz, (b) 117.65 GHz, (c) 117.25 GHz, (d) 116.65 GHz.

from strong scattering of dense cloud ice, and the thin cyclonic rain bands near the hurricane eye match the corresponding features in the upwelling brightness temperature imagery. However, the antenna temperature imagery is of coarser resolution compared to the simulation grid and contains geometric distortions at large scan angles along with anticipated limb darkening [43]. These differences between the brightness temperature and antenna temperature imagery are significant for radiance assimilation purposes and properly accounted for through the use of an appropriate instrument Jacobian, which describes the tangent linear response of instrument to the radiation field.

A 50 element CubeSat fleet is capable of providing observed data within time intervals within

which atmosphere state vector remains highly correlated. In order to illustrate this correlation, brightness temperature images at 117.25 GHz over two hours at 30 minute intervals were simulated (see Figure 6.4). It can be seen that the rain bands around the eyewall gradually develop over

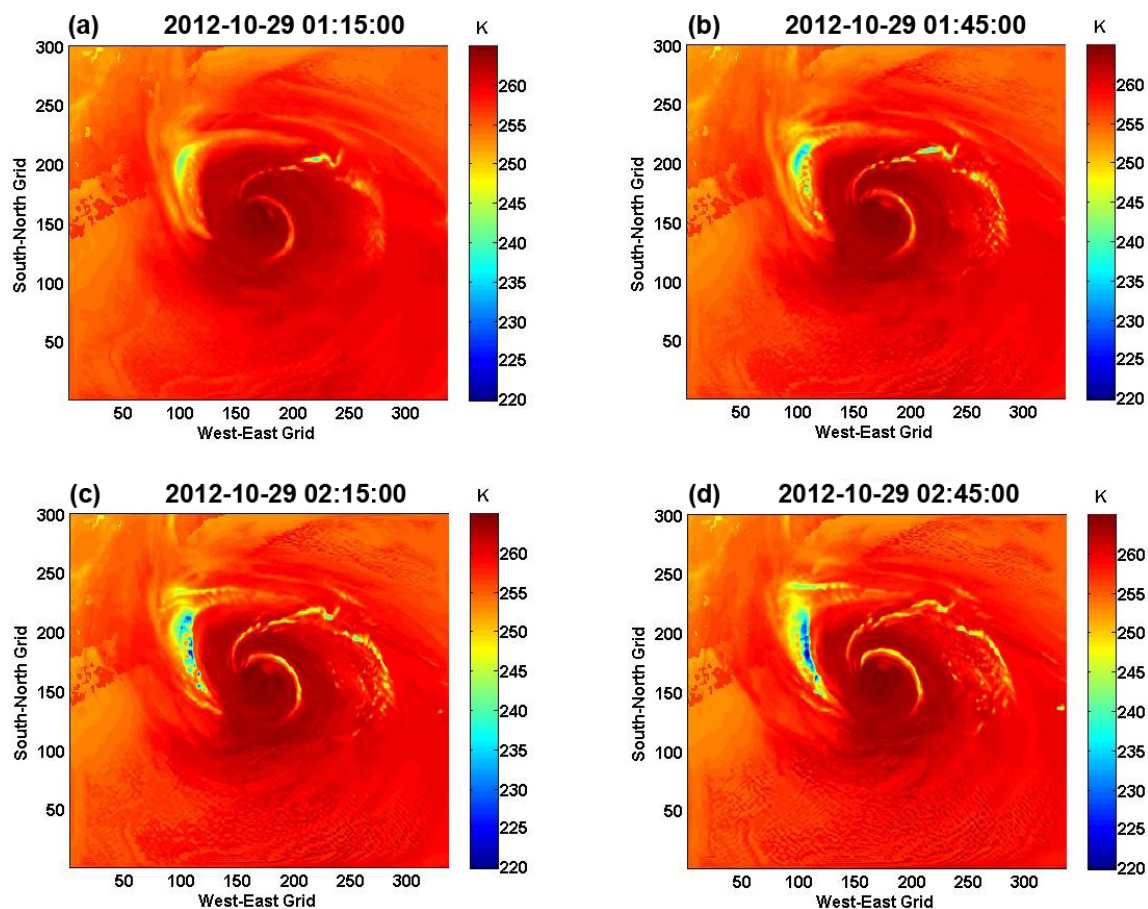


Figure 6.4: Brightness temperature images computed within two hours at intervals of 30 minutes: (a) 01:15:00, (b) 01:45:00, (c) 02:15:00, (d) 02:45:00.

this time interval. The correlation of strength and location of rain bands relative to the eyewall between adjacent images is evident, although the entire hurricane event exhibits regular displacement associated with the eyewall motion. The observed antenna temperature imagery reveals similar correlations between observations, but at lower resolution, and with anticipated distortion and limb darkening. Assimilation of the antenna temperature imagery at such short time intervals is anticipated to ultimately permit improved eyewall tracking and intensity change forecasting.

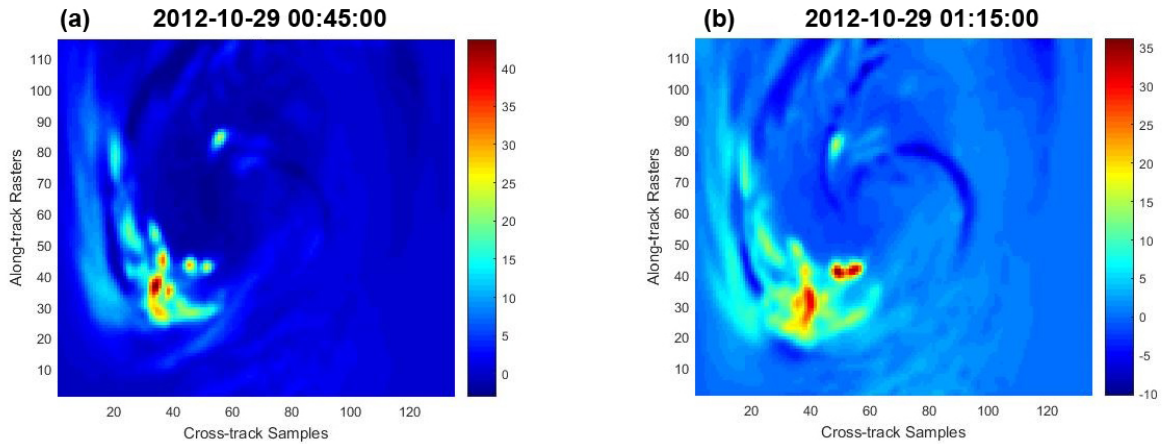


Figure 6.5: Innovations of 117.25 GHz channel. The observations were simulated based on two PolarCube or GEMS satellites flying over Hurricane Sandy at (a) October 29th, 00:45:00 and (b) October 29th, 01:15:00 on two different orbits.

The innovations, which are the differences in radiance between the MiniRad observations and the predictions by the NWP model (see Figure 6.1), form the basic data elements used for assimilation of the observations into the NWP model by minimizing a quadratic error function and generating optimal linear state vector updates. The innovations in the 117.25 GHz channel were computed at two assimilation times, October 29th 00:45:00 and October 29th 01:15:00 (see Figure 6.5). At each time, MiniRad observations were computed based on the simulated true state vectors in the NWP model. The true state vectors were subsequently perturbed by running the NWP forecast with a 24-hour earlier time shift, i.e. the model forecasting proceeded using the state vector at the analysis time of October 28th 00:00:00. The differences between what MiniRad would observe and what the perturbed model predicted are significantly greater than the root-sum-square combined instrument noise and NWP model error, particularly where the hydrometeors density is high and rain band structure is deeply convective. These simulated innovations are up to  $\pm 40$  Kelvin.

OSSEs in support of a low cost microwave imaging and sounding CubeSat constellation based on the MiniRad sensor are being developed and demonstrated as part of this thesis at CU CET. NWP simulations of the CubeSat fleet observation concept have been produced for assisting in the

engineering development of an evolved array constellation satisfying observation requirements on a global basis and for understanding the capabilities for short-term mesoscale forecasting using high spatio-temporal resolution microwave observations. The NWP-based simulations are being used to facilitate development and demonstration of precipitation locking using 30 minute microwave observations. These simulations are now discussed.

## **6.3 First-Frame Locking**

### **6.3.1 Primary Goals**

Precipitation locking of thermodynamic and hydrometeor state variables cannot be achieved spontaneously by the WRF model without properly assimilating observations at high spatio-temporal resolution [45, 139]. The evolution of WRF model errors for hydrometeors and associated thermodynamic variables (temperature, water vapor density, and wind velocity) can be modeled as a stochastic Brownian process over limited time scales due to the inherently noisy and effectively unobservable meteorological phenomena [109] that jointly influence these variables. Thus, the error covariance of WRF thermodynamic and hydrometeor state parameters grows linearly in time based on the joint Brownian process.

Extended Kalman filtering (XKF) advances data assimilation by recalculating the background error covariance matrix using the tangent linear numerical weather model at each assimilation cycle (e.g. at 6 hours intervals for current operational global models). However, beginning with only a poor estimation of the atmosphere thermodynamic state, extended Kalman filtering can require weeks of high performance computer processing to be able to provide the linear unbiased estimate of the atmospheric state and associated background error covariance matrices [59]. Within this transition period and for typical 6-hour assimilation cycles, atmosphere hydrometeor state variables are fully de-correlated, thus precluding any linear update of hydrometeor state variables in the model. Extended Kalman filtering thus requires more frequent observations to be assimilated for accurate estimation of the general background error covariance matrix [87]. Moreover, due to the

rapid evolution of clouds precipitation and short spatial scales any such general background error covariance matrix would be highly time-dependent and localized. This feature of hydrometeor variables significantly complicates optimal data assimilation at time and space scales required for precipitation locking.

The simulated PATH data observed over Sandy at intervals of 30 minutes begin to meet the above observation frequency requirement of extended Kalman filtering. The simulated observations are most useful for a precipitation locking demonstration when 1) the simulated observed data can be differenced with predictions of the observed radiances, and 2) the forecast state vector is uncorrelated to the truth state at the first-frame assimilation time. The innovation field  $\bar{\epsilon}_i$  is thus calculated by differencing simulated noise-corrupted truth radiances with WRF model observed radiances (see Figure 6.1):

$$\bar{\epsilon}_i(x, y, \theta, \phi, f) = \bar{y}_i(x, y, \theta, \phi, f) - \hat{y}_{i|i-1}(x, y, \theta, \phi, f) \quad (6.4)$$

where the innovation field varies with horizontal location  $(x, y)$ , observation angles  $(\theta, \phi)$ , frequency  $f$ , and time step index.

The time index  $i = 1$  corresponds to the presumed first-frame assimilation time 2012-10-29 06:00:00, at which time  $\bar{y}_1$  is the vector of simulated truth radiances in antenna temperature based on the North American Mesoscale (NAM) analyses at time index  $i = 1$ , and  $\hat{y}_{1|0}$  is the vector of predicted radiances in antenna temperature computed based on the forecast state vector launched from NAM analyses at the time index  $i = 0$ . The forecast NAM analysis is 24 hours before the first-frame assimilation time (i.e.  $i = 0$  corresponds to 2012-10-28 06:00:00) to ensure hydrometeor state de-correlation. For rapidly evolving mesoscale weather (e.g. Sandy), the 24-hour time difference for NAM analyses is long enough to ensure that the forecast state  $\hat{x}_{1|0}$  and truth state  $\bar{x}_1$  are uncorrelated.

A total of 12 sounding/imaging channels centered at the 118.7503 GHz oxygen line and the 183.310 GHz water vapor line (see Table 6.1) are selected for the first-frame locking study. Gaussian additive noise vector  $\bar{n}_{y_1}$  were added to the simulated observed data with the standard deviation

Table 6.1: List of frequencies used for the precipitation locking study.

Center Frequency (GHz)	Offset (MHz)	Bandwidth (MHz)
118.7503 (oxygen line)	$\pm 0.4$	200.0
	$\pm 0.7$	400.0
	$\pm 1.1$	400.0
	$\pm 1.5$	400.0
	$\pm 3.0$	1200.0
	$\pm 5.0$	2600.0
183.310 (water vapor line)	$\pm 0.9$	1500.0
	$\pm 1.65$	1500.0
	$\pm 3.0$	1500.0
	$\pm 5.0$	1500.0
	$\pm 7.0$	2000.0
	$\pm 17.0$	2000.0

calculated based on an assumed instrument noise figure of 3dB. Figure 6.6 illustrates the innovations computed by differencing brightness temperature imagery between truth radiances  $\bar{y}_1$  and predicted radiances  $\hat{\bar{y}}_{1|0}$  at selected observation channels and at nadir viewing angle ( $\theta = 0^\circ$ ). Note that cross-track geometry, polarization rotates and beam convolution are neglected here. In other words, the sensor observation simulation step in Figure 6.1 is skipped. The magnitude of innovations in general increases with the transparency of the observation channel. For example, the maximum absolute value of innovations reaches 60 Kelvin at  $118.7503 \pm 5.0$  GHz where the differences of hydrometeor distribution in the lower troposphere between the truth and the forecast state cause significant variations in observed brightness temperature. The state variable differences in a selected atmospheric column are illustrated in Figure 6.7. It is shown that all state variables in the 24-hour forecast deviate from the simulated truth. Small relative errors occur for the thermodynamic variables  $T$  and  $q$  and large relative errors for hydrometeor bulk densities (e.g. cloud liquid water density  $\rho_c$  and snow bulk density  $\rho_s$ ).

The first-frame locking aims to optimally correct the state variable errors at the time of the first arrival of available observations using nonlinear iterative statistical estimation for prognostic variables. Three main goals in the first-frame locking are attempted simultaneously: 1) the

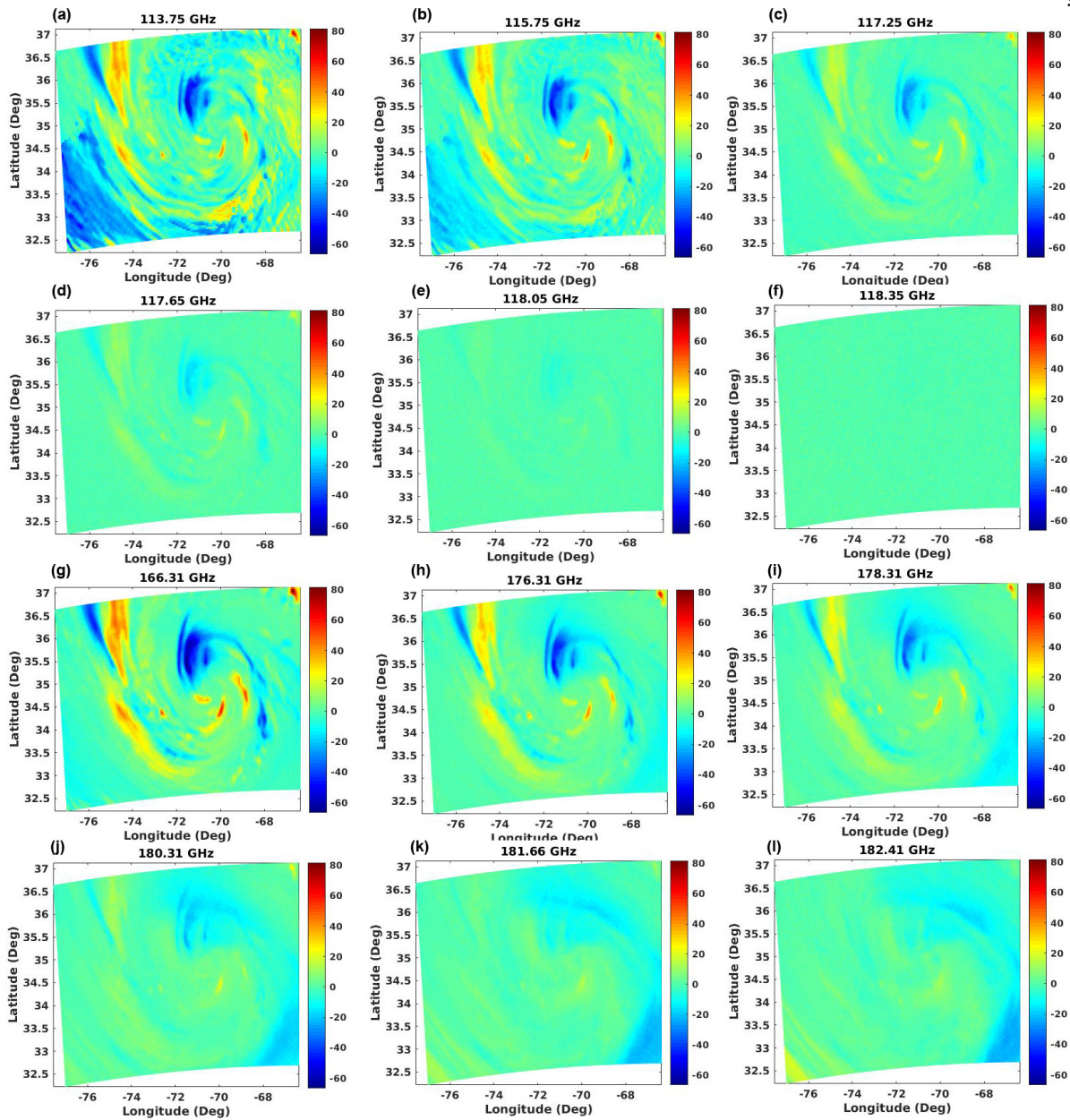


Figure 6.6: Brightness temperature innovations of 12 selected channels at nadir viewing angle. (a)-(f) sounding channels offset to the 118.7503 GHz oxygen absorption line center, (g) window channel at 166.31 GHz, and (h)-(l) sounding channels offset to the 183.310 GHz water vapor absorption line center.

innovation fields in all selected channels are reduced to a minimum, 2) hydrometeor state variables in atmospheric columns are updated to be close to the true state by use of the Kalman gain, and 3) the process of thermodynamic variable update is effectively stabilized to avoid diverging from the

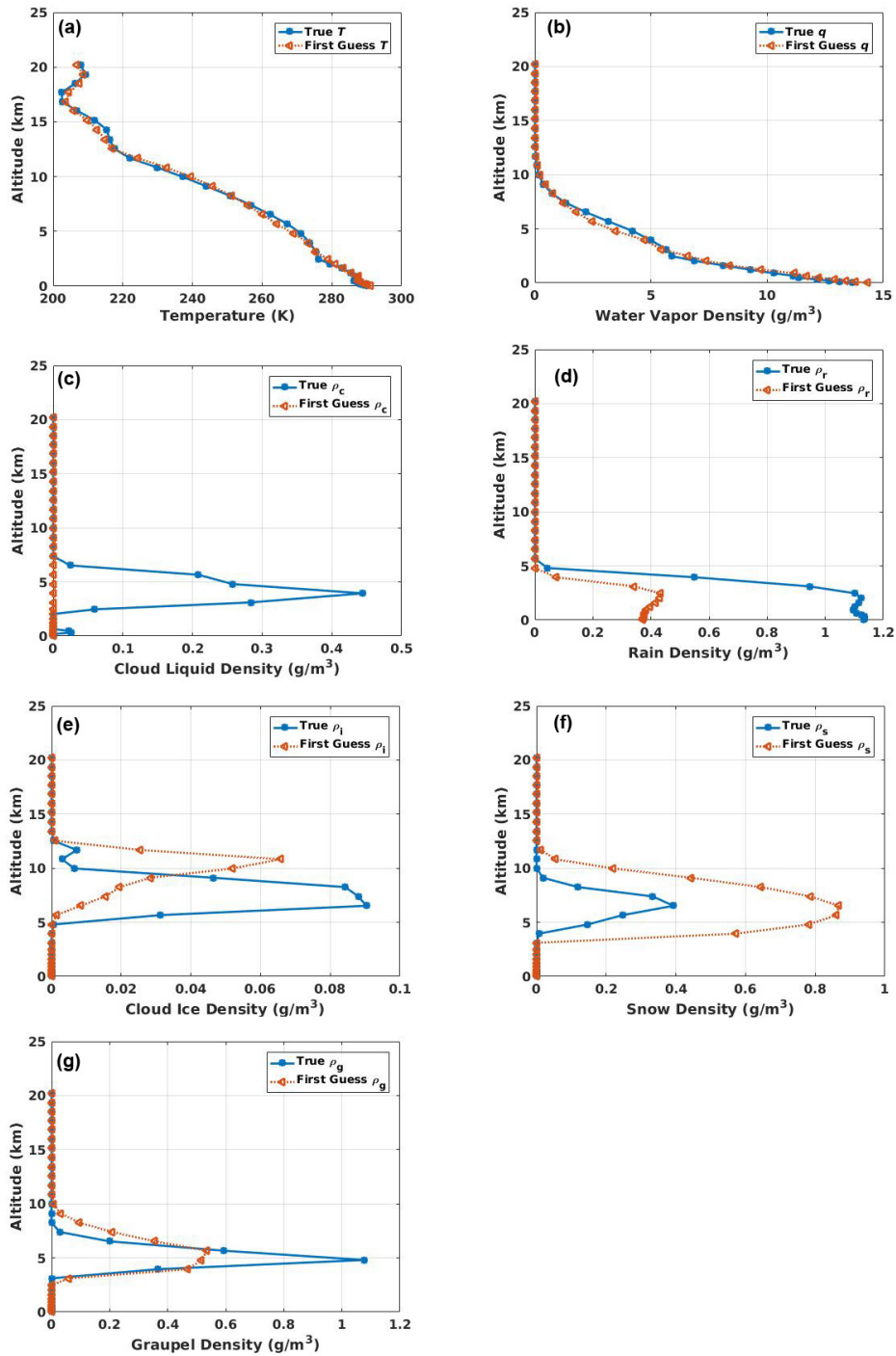


Figure 6.7: Comparisons of the state variable between the truth and forecast in a selected atmospheric column with the grid indexes ( $x = 175$ ,  $y = 128$ ) in the simulation domain: (a) temperature in Kelvin, (b) water vapor bulk density in  $\text{g/m}^3$ , and (c)-(g) the bulk density of hydrometeor in  $\text{g/m}^3$  of five microphysical phases.



true state.

### 6.3.2 Assimilation Method: Extended Kalman Filtering

Extended Kalman filtering (XKF) is applicable to estimation and prediction of the state of any nonlinear physical system with either a linear or nonlinear observation model. By linearizing both physical process and the observation model, XKF provides a means of optimally updating physical state variables and error covariance matrices based on the statistical linearized minimum mean square error (LMMSE) estimator, which is also known as nonlinear iterative D-matrix estimator. For the precipitation locking assimilation system, the WRF NWP model and the nonlinear observation process associated with satellite microwave radiometry can be generalized in the following form:

$$\bar{x}_{i+1} = \bar{A}(\bar{x}_i) + \bar{B}(\bar{x}_i)\bar{n}_{x_i} \quad (6.5)$$

$$\bar{y}_i = \bar{W}(\bar{x}_i) + \bar{n}_{y_i} \quad (6.6)$$

where  $\bar{x}_i$  is the vector of atmospheric state variables defined in (6.1) with time index  $i$ ,  $\bar{y}_i$  is the vector of observed brightness temperatures defined in (6.4),  $\bar{B}(\bar{x}_i)$  is the atmospheric process noise matrix, and  $\bar{A}(\cdot)$  and  $\bar{W}(\cdot)$  are the governing nonlinear operators for the WRF forecast and the observation model. Noise statistics can be defined using the model noise covariance matrix  $\bar{R}_{n_{x_i}n_{x_i}}$  and the observation noise covariance matrix  $\bar{R}_{n_{y_i}n_{y_i}}$ :

$$\langle \bar{n}_{x_i} \bar{n}_{x_i'}^t \rangle = \bar{R}_{n_{x_i}n_{x_i}} \delta_{ii'} \quad (6.7)$$

$$\langle \bar{n}_{y_i} \bar{n}_{y_i'}^t \rangle = \bar{R}_{n_{y_i}n_{y_i}} \delta_{ii'} \quad (6.8)$$

$$\langle \bar{x}_i \bar{n}_{x_i'}^t \rangle = \langle \bar{x}_i \bar{n}_{y_i'}^t \rangle = 0 \quad (6.9)$$

where superscript  $t$  indicates the transpose of a vector.

At any assimilation time, the innovation field defined in (6.4) can be calculated based on the observation equation (6.6):

$$\bar{\epsilon}_i = \bar{y}_i - \hat{\bar{y}}_{i|i-1} = \bar{W}(\bar{x}_i) + \bar{n}_{y_i} - \bar{W}(\hat{\bar{x}}_{i|i-1}) \quad (6.10)$$

The linearization of the observation equation is required for the LMMSE estimator to be applied.

The Taylor series expansion of  $\overline{W}(\overline{x}_i)$  around the forecast state vector  $\hat{x}_{i|i-1}$  is given by:

$$\overline{W}(\overline{x}_i) = \overline{W}(\hat{x}_{i|i-1}) + \overline{H}(\hat{x}_{i|i-1})(\overline{x}_i - \hat{x}_{i|i-1}) + \mathcal{O}((\overline{x}_i - \hat{x}_{i|i-1})(\overline{x}_i - \hat{x}_{i|i-1})^t) \quad (6.11)$$

where  $\overline{H}(\hat{x}_{i|i-1})$  is the Jacobian matrix of the observation system given the underlying atmospheric state vector  $\hat{x}_{i|i-1}$ , and is defined as:

$$\overline{H}(\hat{x}_{i|i-1}) = (\mathcal{D}\overline{W})|_{\hat{x}_{i|i-1}} \triangleq \overline{H}_{i|i-1}, \quad \text{i.e., } \{H_{jk}\} = \left\{ \frac{\partial W_j}{\partial x_k} \Big|_{\hat{x}_{i|i-1}} \right\} \quad (6.12)$$

Bringing (6.11) into (6.10) and neglecting higher order terms in the expansion, the innovation field can be linearized as:

$$\begin{aligned} \bar{\epsilon}_i &\approx \overline{W}(\hat{x}_{i|i-1}) + \overline{H}_{i|i-1}(\overline{x}_i - \hat{x}_{i|i-1}) + \overline{n}_{y_i} - \overline{W}(\hat{x}_{i|i-1}) \\ &= \overline{H}_{i|i-1}(\overline{x}_i - \hat{x}_{i|i-1}) + \overline{n}_{y_i} \\ &= \overline{H}_{i|i-1}\bar{e}_{i|i-1} + \overline{n}_{y_i} \end{aligned} \quad (6.13)$$

where  $\bar{e}_{i|i-1} \triangleq \overline{x}_i - \hat{x}_{i|i-1}$  is the vector of background state vector errors. The linear relationship between the innovation field and the vector of background errors allows the statistical LMMSE estimator to be straightforwardly applied. In doing so, the atmospheric state vector can be optimally estimated from the innovations via a linear inversion matrix  $\overline{D}$ :

$$\hat{e}_{i|i-1} = \overline{D}\bar{\epsilon}_i = \left( \overline{R}_{\bar{e}_{i|i-1}\bar{\epsilon}_i} \overline{R}_{\bar{\epsilon}_i\bar{\epsilon}_i}^{-1} \right) \bar{\epsilon}_i \quad (6.14)$$

where  $\bar{e}_{i|i-1}$  and  $\bar{\epsilon}_i$  both have zero means,  $\overline{R}_{\bar{e}_{i|i-1}\bar{\epsilon}_i}$  is the cross covariance of background errors and innovations,  $\overline{R}_{\bar{\epsilon}_i\bar{\epsilon}_i}$  is the auto-covariance of innovations. The matrix  $\overline{D} = \overline{R}_{\bar{e}_{i|i-1}\bar{\epsilon}_i} \overline{R}_{\bar{\epsilon}_i\bar{\epsilon}_i}^{-1}$  is obtained using the criterion of orthogonality of the innovations and background errors. This result is based on the weak form of the general orthogonality principle that is fundamental to statistical estimation theory and is identical to multivariate linear least squares fit.

Using the linearized innovation field (6.13) and the noise characteristics (6.9), the covariance matrices are determined as:

$$\overline{R}_{\bar{e}_{i|i-1}\bar{\epsilon}_i} \triangleq \left\langle \bar{e}_{i|i-1} \left( \overline{H}_{i|i-1}\bar{e}_{i|i-1} + \overline{n}_{y_i} \right)^t \right\rangle = \left\langle \bar{e}_{i|i-1} \bar{e}_{i|i-1}^t \right\rangle \overline{H}_{i|i-1}^t \quad (6.15)$$

$$\begin{aligned}
\overline{\overline{R}}_{\bar{e}_i \bar{e}_i} &\triangleq \left\langle \left( \overline{\overline{H}}_{i|i-1} \bar{e}_{i|i-1} + \bar{n}_{y_i} \right) \left( \overline{\overline{H}}_{i|i-1} \bar{e}_{i|i-1} + \bar{n}_{y_i} \right)^t \right\rangle \\
&= \overline{\overline{H}}_{i|i-1} \left\langle \bar{e}_{i|i-1} \bar{e}_{i|i-1}^t \right\rangle \overline{\overline{H}}_{i|i-1}^t + \overline{\overline{R}}_{n_{y_i} n_{y_i}}
\end{aligned} \tag{6.16}$$

Further, define the background error covariance matrix  $\overline{\overline{R}}_{\bar{e}_{i|i-1} \bar{e}_{i|i-1}}$  (also notated as the  $\overline{\overline{B}}$  matrix in NWP data assimilation literature (e.g. [59, 3])):

$$\overline{\overline{R}}_{\bar{e}_{i|i-1} \bar{e}_{i|i-1}} \triangleq \left\langle \bar{e}_{i|i-1} \bar{e}_{i|i-1}^t \right\rangle = \left\langle (\bar{x}_i - \hat{x}_{i|i-1}) (\bar{x}_i - \hat{x}_{i|i-1})^t \right\rangle \tag{6.17}$$

Substituting the cross- and auto-covariance matrices (6.15) and (6.16) into (6.14), the optimal correction to the state variable  $\bar{x}_i$  can be determined as:

$$\begin{aligned}
\hat{x}_i &= \hat{x}_{i|i-1} + \overline{\overline{D}} (\bar{y}_i - \overline{\overline{W}}(\hat{x}_{i|i-1})) \\
\overline{\overline{D}} &= \overline{\overline{R}}_{\bar{e}_{i|i-1} \bar{e}_{i|i-1}} \overline{\overline{H}}_{i|i-1}^t \left( \overline{\overline{H}}_{i|i-1} \overline{\overline{R}}_{\bar{e}_{i|i-1} \bar{e}_{i|i-1}} \overline{\overline{H}}_{i|i-1}^t + \overline{\overline{R}}_{n_{y_i} n_{y_i}} \right)^{-1}
\end{aligned} \tag{6.18}$$

where  $\overline{\overline{D}}$  is the Kalman gain. The Kalman gain is completely determined by 3 components: 1) the background error covariance matrix  $\overline{\overline{R}}_{\bar{e}_{i|i-1} \bar{e}_{i|i-1}}$ , 2) the observation Jacobian  $\overline{\overline{H}}_{i|i-1}$  given the WRF forecast state vectors, and 3) the observation noise covariance matrix  $\overline{\overline{R}}_{n_{y_i} n_{y_i}}$ . The observation Jacobian can be quickly computed using radiative transfer models such as HI-UMRT, UMRT [122], and DOTLRT [127], which include the tangent linear response of the observed brightness temperature to multiphase hydrometeor bulk density parameters. The observation noise covariance is modeled based on hardware design and operational parameters of the observation system. Importantly, the matrix  $\overline{\overline{R}}_{\bar{e}_{i|i-1} \bar{e}_{i|i-1}}$  describing the statistical properties of the WRF model state error is a key element in calculating the Kalman gain and subsequently determining the state vector correction  $\hat{x}_i$  in each assimilation cycle. Instead of a static climatological background error covariance, a flow-dependent background error covariance model [3] is critical to precipitation locking assimilation.

### 6.3.3 Background Error Covariance Modeling

A flow-dependent routine is required to estimate background error covariances for WRF forecast state variables and to readily provide the needed background error covariance matrices  $\overline{\overline{R}}_{\bar{e}_{i|i-1} \bar{e}_{i|i-1}} \triangleq \overline{\overline{R}}_{ee}$  used in data assimilation. The size of the background error covariance matrix

is typically on the order of  $10^7 \times 10^7$  when all relevant atmospheric state variables in WRF 3D grids over mesoscale sized weather systems are all considered. One way to deal with the large size of  $\overline{\overline{R_{ee}}}$  is to reduce the rank of a static background error covariance matrix via the control variables transformation [38]. This method has been embodied in the WRF data assimilation (WRFDA) system, which includes a stand-alone module (i.e. the `genbe` program) for the estimation of background error covariance matrices for WRFDA. The basic structure of the matrix  $\overline{\overline{R_{ee}}}$  in WRFDA models is the statistics of only a few thermodynamic variables (e.g zonal wind, meridional wind, pressure and potential temperature) [3]. Other control variables can be added to advance the applicability of  $\overline{\overline{R_{ee}}}$  [4]. However, hydrometeor state variables (e.g. ice water mass per unit volume, cloud liquid mass per unit volume, etc) are not included in the structure of the background error covariance matrix in WRFDA as of this writing, thus precluding the direct application of WRFDA in precipitation locking.

As applicable in microwave precipitation assimilation, the structure of the matrix  $\overline{\overline{R_{ee}}}$  is comprised of seven variables (two thermodynamic and five hydrometeor state variables) that have been defined in (6.1). The background error covariance matrix is highly flow-dependent especially during convection, and neglect of this state dependency has shown to result in rapid error growth of poorly observable prognostic variable modes [4]. In this thesis, a parameterized approach that is an empirical flow-dependent 1D vertical error covariance matrix estimate has been developed to facilitate precipitation locking via extended Kalman filtering method.

Consider an ensemble of cloud vertical profiles in NWP model reanalyses for mesoscale severe weather (e.g. hurricanes). Each NWP vertical profile is defined as a single column of  $M$  elements for both thermodynamic and cloud hydrometeor state variables at all vertical levels (e.g.  $M = 224$  for a 32-level NWP profile). Based on the altitude-density model [42] which is a finite-parameter precipitation cell model, each vertical cloud profile can be represented by a vector of 15 parameters:

$$\overline{H} = (\langle h_i \rangle, \sigma_{h_i}, \rho_{h_i}), \quad i = [1, \dots, 5] \quad (6.19)$$

where  $\langle h_i \rangle$  denotes the mean of the precipitation cell altitude,  $\sigma_{h_i}$  denotes the standard deviation

of the precipitation cell altitude,  $\rho_{h_i}$  is the column integrated hydrometeor content of the  $i^{\text{th}}$  hydrometeor category for the cell, and  $i$  is the index of microphysical hydrometeor categories including cloud liquid water, rain, cloud ice, snow and graupel [98].

The ensemble of vertical precipitation profiles can subsequently be classified into multiple hydrometeor modes using clustering analysis methods such as the K-means algorithm [10]. Using K-means, vertical profiles described using an altitude-density representation are optimally partitioned into  $K$  clusters so that a metric distance between the vertical profile set and assigned cluster means is minimized. Each cluster corresponds to a precipitation cell mode and should contain a number of precipitation profiles greater than the size of the 1D background error covariance matrix to preclude rank deficiency. Within each cluster, covariance of vertical state variables can be estimated using an unbiased covariance matrix estimator. When the mean of the vertical profiles in a given cluster is treated as the true state of the corresponding cell mode, the estimator should give a measure of the background error covariance matrix for 1D vertical cloud variables given that cell is in that mode.

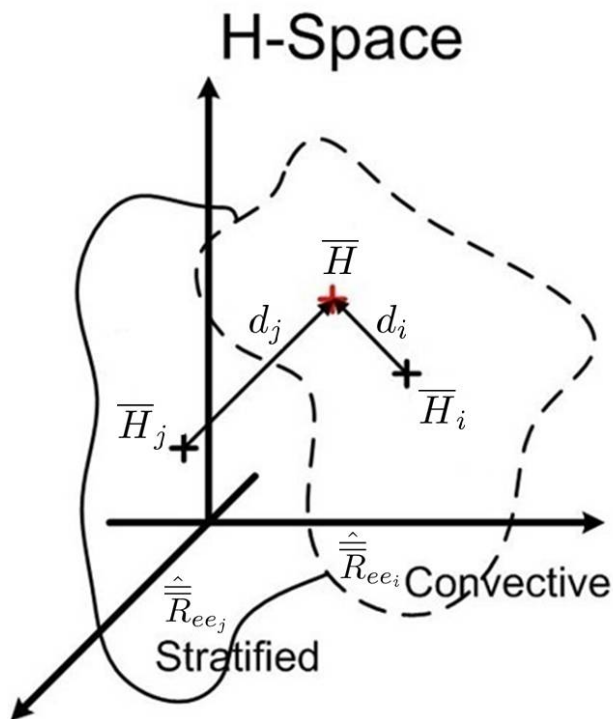


Figure 6.8: Sample precipitation cell modes, e.g. stratified and convective modes in a 15-dimensional H-space for estimating the background error covariance matrix under flow-dependent conditions.

The cell profile classification and covariance estimation method can be illustrated in Figure 6.8 for an idealized case with  $K = 2$  (i.e. only stratified and convective cell modes). Each mode is represented by a closed region in a 15-dimensional space with each point representing the mapping from a vertical precipitation profile to the H-space. The cluster means of these two modes are denoted as black cross markers with the mode representation vectors  $\bar{H}_i$  and  $\bar{H}_j$ . The background error covariance matrix of each mode is computed using the set of cell profiles in the K-means classification. Given a total of  $N$  cell profiles in the convective cluster organized as a  $M \times N$  data matrix  $\bar{\bar{X}}_i$ , the data variation matrix is  $\delta\bar{\bar{X}}_i = \bar{\bar{X}}_i - \langle\bar{\bar{X}}_i\rangle_c$ , where  $\langle\cdot\rangle_c$  is the column-wise mean of  $\bar{\bar{X}}_i$ . An unbiased covariance matrix estimator for this cluster can now be used to compute a covariance matrix  $\hat{\hat{R}}_{ee_i}$  which we can *roughly interpret* as the background error covariance matrix for the cluster as:

$$\hat{\hat{R}}_{ee_i} = \frac{1}{N-1} \delta\bar{\bar{X}}_i \delta\bar{\bar{X}}_i^t \quad (6.20)$$

The above equation can similarly be used to compute  $\hat{\hat{R}}_{ee_j}$  for the stratified cluster. For any vertical profile which is not used in the classification, the flow-dependent 1D vertical background error covariance matrix can be estimated by weighted interpolation between  $\hat{\hat{R}}_{ee_i}$  and  $\hat{\hat{R}}_{ee_j}$ :

$$\hat{\hat{R}}_{ee} = \frac{d_j}{d_i + d_j} \hat{\hat{R}}_{ee_i} + \frac{d_i}{d_i + d_j} \hat{\hat{R}}_{ee_j} \quad (6.21)$$

where  $d_i$  and  $d_j$  are the metric distance between the interpolated point and the cluster centroids  $i$  and  $j$ . This distance is defined as the norm of vector difference:

$$d_i = |\bar{H} - \bar{H}_i|, \quad d_j = |\bar{H} - \bar{H}_j| \quad (6.22)$$

In general, the number of clusters  $K$  can be expected to be significantly larger than 2. The flow-dependent 1D vertical background error covariance matrix of any cloud profile can be determined for any such  $K$  by inverse distance weighting with Shepard's method [108]:

$$\hat{\hat{R}}_{ee}(\bar{H}) = \frac{\sum_{k=1}^K w_k(\bar{H}_k) \hat{\hat{R}}_{ee_k}}{\sum_{k=1}^K w_k(\bar{H}_k)} \quad (6.23)$$

where  $\hat{\hat{R}}_{ee}(\bar{H})$  is the  $M \times M$  background error covariance matrix of the vertical cloud profile mapped into the point  $\bar{H}$ , and  $\hat{\hat{R}}_{ee_k}$  is the background error covariance matrix of the cell mode  $k$ . The inverse distance weighting function  $w_k(\bar{H}_k)$  is defined as:

$$w_k(\bar{H}_k) = \frac{1}{d(\bar{H}, \bar{H}_k)^p} = \frac{1}{|\bar{H} - \bar{H}_k|^p} \quad (6.24)$$

where  $d(\bar{H}, \bar{H}_k)$  is the Euclidean distance between the point  $\bar{H}$  and the mode centroid  $\bar{H}_k$  in H-space, and the parameter  $p$  is a positive real number known as the power parameter. Larger values of  $p$  result in greater weights for points closest to the interpolated point. We note that the choice of  $p$  is somewhat arbitrary. However, following the methods used in the 2-dimensional version of this problem (i.e. known as Kriging [2]), a power of proportional to the number of clusters is reasonable. Accordingly, we use  $p = 2K$  in the inverse distance weighting calculation.

The above flow-dependent modeling of background error covariance was applied to NAM model reanalyses of the hurricane Sandy at the analysis time 2012-10-29 00:00:00 (i.e., 6 hours before the first-frame time). This state vector provided  $264 \times 408$  cloud profiles with 32 vertical levels. These cloud profiles were partitioned into 20 clusters using the K-means algorithm based on the altitude-density model. Figure 6.9 illustrates the horizontal distribution of cloud profile clusters within the simulation domain over Sandy. Cloud profiles with the least amount of hydrometeor content are classified into one cluster (i.e. the 10<sup>th</sup> cluster). Cloud profiles within rain bands are divided into multiple clusters based on the altitude and density distribution of the cells.

Next, the background error covariance matrix of each cluster  $\hat{\hat{R}}_{ee_k}$ ,  $k = \{1, \dots, 20\}$  was computed using (6.20). Figure 6.10 illustrates the structure of each 1D vertical background error covariance matrix in the case study of Sandy. The resulting matrices are readily used in the Kalman gain calculation by the inverse distance weighting interpolation.

### 6.3.4 Constrained Extended Kalman Filtering

In this section, constraints on the atmospheric state vectors are considered in the extended Kalman filtering process in order to stabilize both thermodynamic and hydrometeor state variable

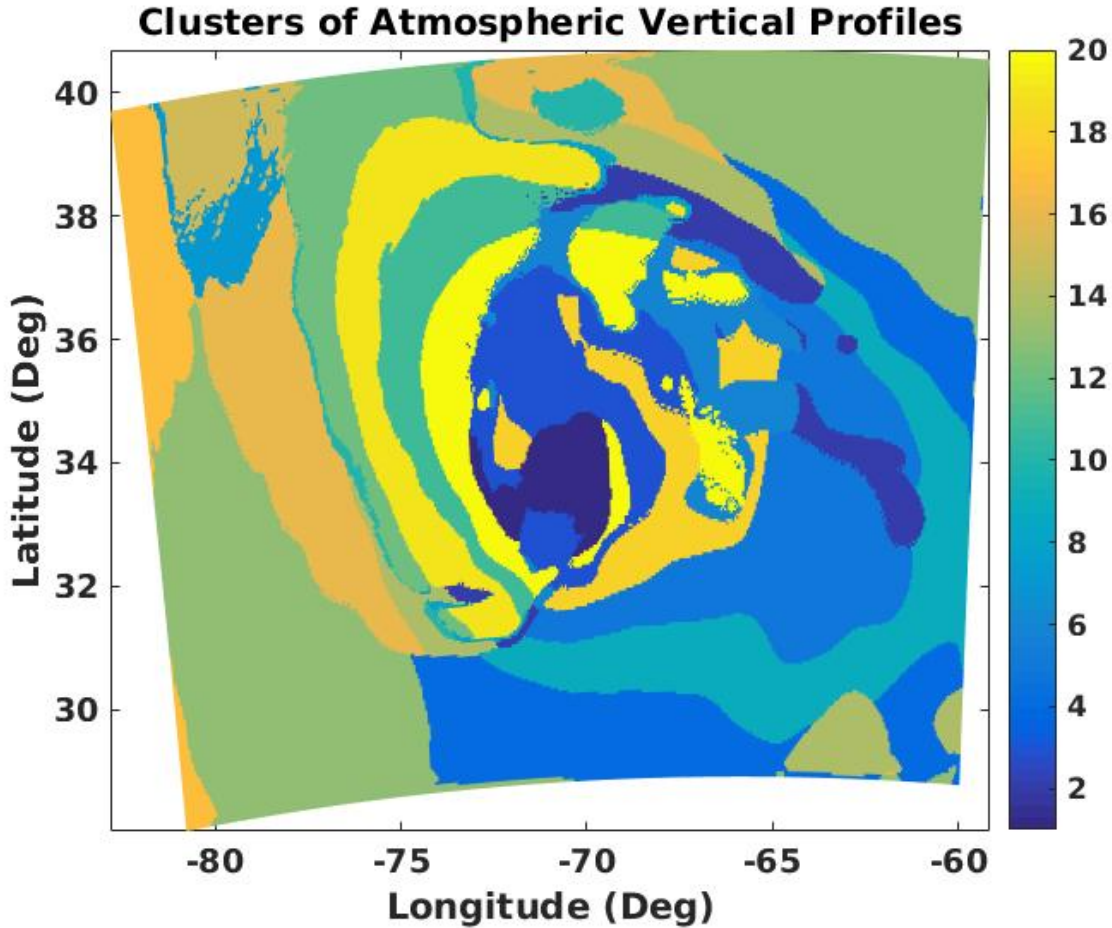


Figure 6.9: Cloud vertical profiles in NAM reanalyses classified into 20 clusters using the K-means algorithm based on the altitude-density model.

update. The atmospheric state vectors are optimally updated using the extended Kalman filtering equations (6.18) based on estimated statistics of NWP model errors and observation errors. However, since extended Kalman filtering is based on unconstrained Gaussian assumptions [59], the statistically optimal update of state variables can become invalid because of the violation of natural constraints on those variables (e.g. non-negative values of ice water content in the atmosphere).

Therefore, extended Kalman filtering with inequality constraints imposed on individual state variables must be defined and applied in precipitation assimilation process. As discussed by Simon et al. [110] and Zhang et al. [138], this problem can be formulated as a quadratic programming problem [39] with linear inequality constraints. In the context of precipitation locking, the constrained



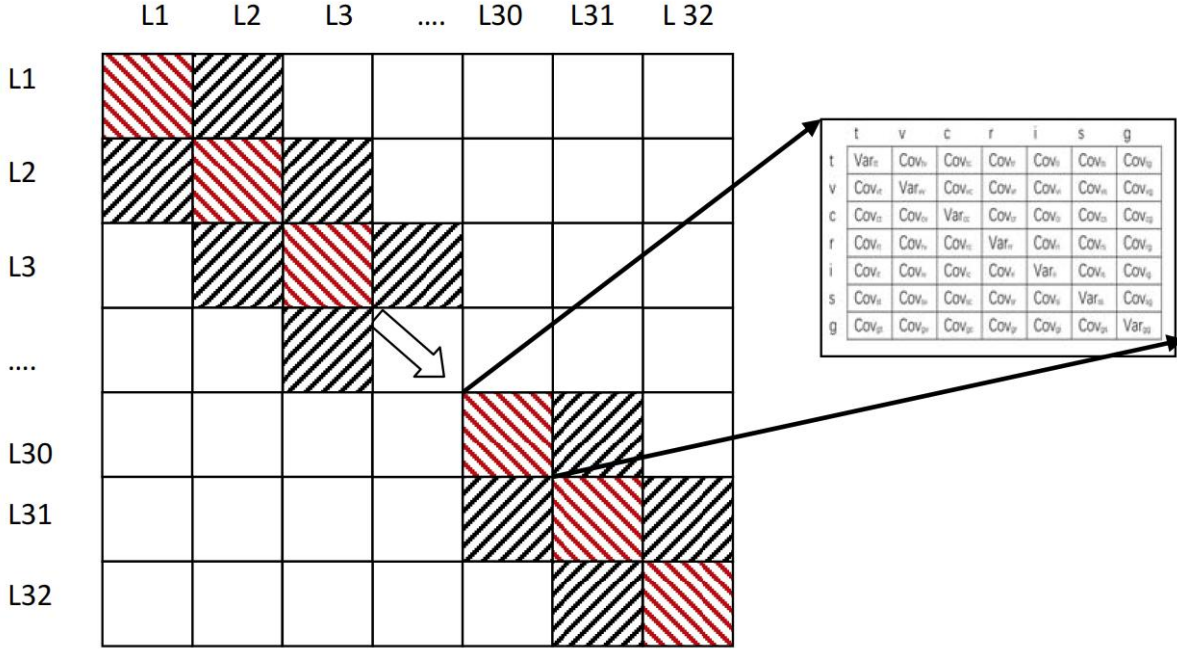


Figure 6.10: Schematic diagram of the background error covariance matrix for cloud hydrometeor variables at 32 vertical levels. Red squares on the diagonal represent variances and covariances among multivariate states in the same level. Black squares along the off-diagonal are variances and covariances between adjacent levels. The enlarged table illustrates variances and covariances of seven state variables at a given level: temperature  $t$ , vapor density  $v$ , cloud water density  $c$ , rain droplet density  $r$ , cloud ice density  $i$ , snow density  $s$ , and graupel density  $g$ .

optimization formulation under absolute fixed constraints after each state update can be expressed as:

$$\min_{\bar{x}} \left[ (\bar{x} - \hat{x}_i)^t \overline{\overline{R}}_{\bar{e}_i | \bar{e}_i}^{-1} (\bar{x} - \hat{x}_i) \right]$$

subject to  $\bar{x}_{lb} \leq \bar{x} \leq \bar{x}_{ub}$

(6.25)

where  $\hat{x}_i$  is the corrected state vector with time index  $i$  defined in (6.18), and  $\bar{x}_{lb}$  and  $\bar{x}_{ub}$  are vectors of the lower bound and upper bound for the optimized state vector  $\bar{x}$ . The matrix  $\overline{\overline{R}}_{\bar{e}_i | \bar{e}_i}$  is the analysis error covariance matrix which is defined in extended Kalman filtering [59] and can be computed using matrix quantities in (6.18) as:

$$\overline{\overline{R}}_{\bar{e}_i | \bar{e}_i} = \overline{\overline{R}}_{\bar{e}_i | \bar{e}_i} - \overline{\overline{D}} \overline{\overline{H}}_{i|i-1} \overline{\overline{R}}_{\bar{e}_i | \bar{e}_i}$$
(6.26)

Note that the corrected state vector  $\hat{x}_i$  at time index  $i$  can also be treated as the maximum  $a$

*posteriori* (MAP) estimate [138] given the observations at time index  $i$  and the prior state vector statistics at time index  $(i - 1)$ . Thus, the posterior state vector distribution can be reconstructed using the Gaussian distribution function as:

$$f(\bar{x}) = \frac{1}{\sqrt{(2\pi)^n |\overline{\overline{R}}_{\bar{e}_i | \bar{e}_i}|}} \exp\left\{-\frac{1}{2}(\bar{x} - \hat{x}_i)^t \overline{\overline{R}}_{\bar{e}_i | \bar{e}_i}^{-1} (\bar{x} - \hat{x}_i)\right\} \quad (6.27)$$

where superscript  $n$  denotes the size of state vector  $\bar{x}$ . Therefore, the solution of the constrained optimization in (6.25) is identical to the following optimization formulation:

$$\begin{aligned} & \max_{\bar{x}} f(\bar{x}) \\ & \text{subject to } \bar{x}_{lb} \leq \bar{x} \leq \bar{x}_{ub} \end{aligned} \quad (6.28)$$

The solutions of (6.25) or (6.28) are based on a hard-clipping process. The elements in the corrected state vector  $\hat{x}_i$  are hard-clipped if they violate the lower or upper bound. These clipped elements are set to corresponding element values in  $\bar{x}_{lb}$  or  $\bar{x}_{ub}$ . Thus, the clipping action is equivalent to adding equality constraints to the optimization problem as shown in either (6.25) or (6.28).

We can use the lower bound  $\bar{x}_{lb}$  to demonstrate this clipping process. Suppose the set  $\{i_c\}$  contains indexes of clipped elements and the set  $\{i_u\}$  is the complement of the set  $\{i_c\}$ . The optimization with equality constraints (i.e., clipping) can be defined to maximize the following conditional state vector distribution:

$$\max_{\bar{x}(\{i_u\})} f(\bar{x}(\{i_u\}) | \bar{x}(\{i_c\}) = \bar{x}_{lb}(\{i_c\})) \quad (6.29)$$

The solution of the above optimization formula has been found [110, 138]:

$$\begin{aligned} \bar{x}(\{i_u\}) &= \hat{x}_i(\{i_u\}) + \overline{\overline{R}}_{12} \overline{\overline{R}}_{22}^{-1} (\bar{x}(\{i_c\}) - \hat{x}_i(\{i_c\})) \\ \bar{x}(\{i_c\}) &= \bar{x}_{lb}(\{i_c\}) \end{aligned} \quad (6.30)$$

where  $\overline{\overline{R}}_{12}$  and  $\overline{\overline{R}}_{22}$  are block sub-matrices of the permuted  $\overline{\overline{R}}_{\bar{e}_i | \bar{e}_i}$  according to the index sets  $\{i_c\}$  and  $\{i_u\}$ :

$$\bar{x}' = \begin{bmatrix} \bar{x}(\{i_u\}) \\ \bar{x}(\{i_c\}) \end{bmatrix} = \begin{bmatrix} \bar{x}_1 \\ \bar{x}_2 \end{bmatrix} \quad (6.31)$$

$$\overline{\overline{R}}_{\bar{e}_{i|i}\bar{e}_{i|i}} = \begin{bmatrix} \overline{\overline{R}}_{11} & \overline{\overline{R}}_{12} \\ \overline{\overline{R}}_{21} & \overline{\overline{R}}_{22} \end{bmatrix} \quad (6.32)$$

The general solution of the constrained optimization problem (6.25) can thus be found by clipping the invalid state update to the lower or upper bounds and recalculating the state update for intact state variables according to the near-optimal solution in (6.30). Note that the hard-clipping process needs to be iteratively executed until all elements of  $\bar{x}$  in (6.25) are under constraint.

In summary, the discussion of extended Kalman filtering, background error covariance modeling, and inequality constraints imposed on the state vector update can be embodied in a comprehensive flowchart for first-frame precipitation locking (see Figure 6.11). It has been shown [67] that iterative state vector updates with scaling factors are necessary because of the nonlinear relationships between observations and the underlying state variables. The vector of scaling factors  $\text{diag}(\alpha_{ii})$  can be determined based on the degree of nonlinearity of the observation operator. The scaling factors are introduced in each iteration to limit the step size in  $\hat{x}_n$  so that the tangent linear approximation to  $\overline{W}(\cdot)$  is maintained.

### 6.3.5 Preliminary Results

The simulated antenna temperature  $T_A$  images as shown in section 6.2 are the results of the convolution between the antenna gain pattern and brightness temperature  $T_B$  images simulated using UMRT. The instrument Jacobians that describe the response of instrument (e.g. MiniRad) to the radiation field are required in the overall observation system Jacobians to complete the derivative chain rule for calculating the tangent linear response of instrument to the geophysical state variables of interest. However, for simplicity, the extended Kalman filtering study in this chapter uses the full resolution brightness temperature  $T_B$  imagery with additive Gaussian noise as equivalent observations for precipitation assimilation experiments.

For any given atmospheric vertical profile, two kinds of inequality constraints are imposed on each individual state variable at all discrete levels: 1) lower bounds for all hydrometeor densities

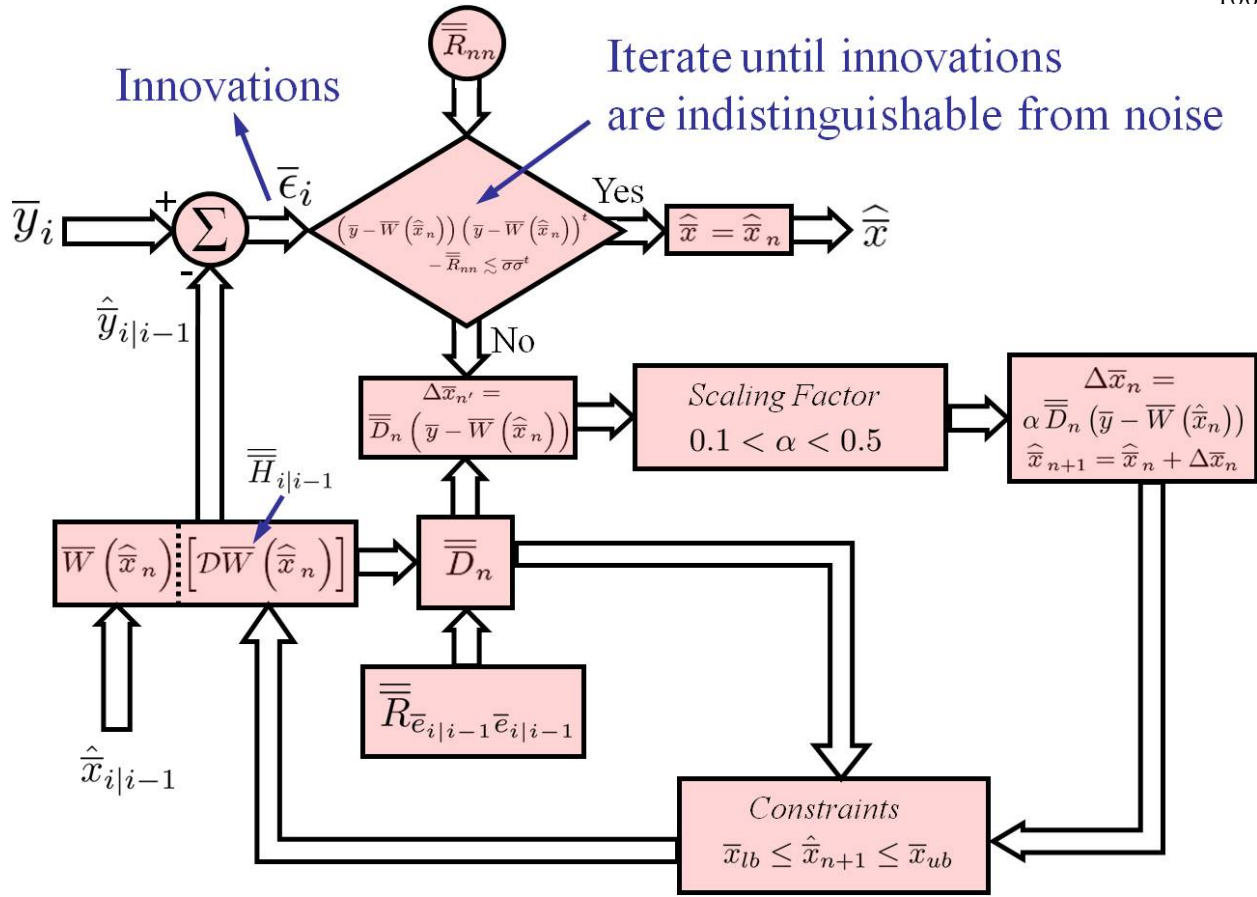


Figure 6.11: Schematic flowchart of constrained extended Kalman filtering used for iterative update for atmospheric state vectors. Modified from Skofronick-Jackson [112].

(i.e.  $\bar{\rho}_c > 0$ ,  $\bar{\rho}_r > 0$ ,  $\bar{\rho}_i > 0$ ,  $\bar{\rho}_s > 0$ ,  $\bar{\rho}_g > 0$ ), and 2) upper and lower bounds for relative humidity (0 - 100%). As shown in Appendix (D.6) at a given level is determined by the water vapor density, the temperature, and the saturation vapor pressure at that temperature. Therefore, the second constraint simultaneously stabilizes both water vapor density and temperature by implicitly setting lower and upper bounds. For any given vapor density, temperature should be maintained to be above a minimum value so that the water vapor density will not condense out (i.e. the relative humidity will not exceed 100%). For any given temperature, the vapor density is linearly related to the relative humidity, thus forming both lower and upper bounds to the vapor density. When constraints take effect, the violated variable is set to be the value of corresponding bound. One exception is when the relative humidity is updated to exceed 100%, both temperature and vapor density are

reset to be the values of first guess that is the WRF forecast based on the initial atmospheric state.

This adjustment is equivalent to specify steady-state variables during XKF iterations.

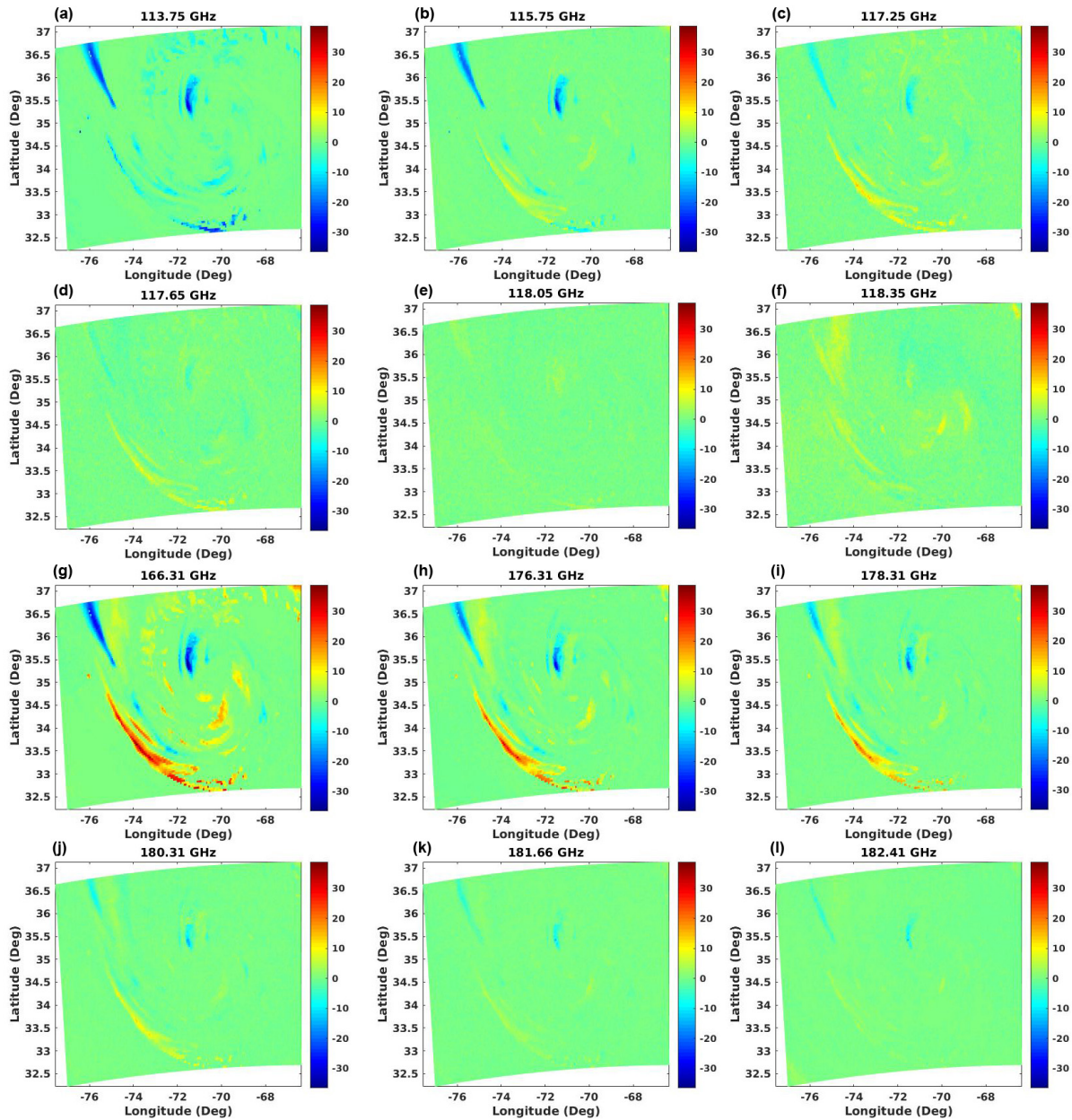


Figure 6.12: Residual  $T_B$  innovations of 12 selected channels at nadir viewing angle after 20 XKF iterates. (a)-(f) sounding channels offset to the 118.7503 GHz oxygen absorption line center, (g) window channel at 166.31 GHz, and (h)-(l) sounding channels offset to the 183.310 GHz water vapor absorption line center.

Figure 6.12 illustrates residual  $T_B$  innovations after 20 iterations of the state update using

extended Kalman filtering with the aforementioned constraints. Within each iterate, a scaling factor  $\alpha = 0.3$  is applied to maintain a valid tangent linear update. In general, the innovations of all channels within the scene under examination considerably decrease, even for the regions near rain bands. In the worst case, the 118.35 GHz channel, which is sensitive to the scattering of cloud ice in the upper troposphere, exhibits an innovation increase by a few Kelvin at the 20<sup>th</sup> iterate. Inaccurate estimates of Jacobians for state variables at upper tropospheric levels might cause this increase of innovation amplitude, in particular close to rain bands. The modeling error in the background error covariance matrices might be another source of this problem.

The statistical convergence of the innovation field over the scene with XKF iteration count is one of key criteria for assessing the performance of the XKF assimilation method. Figure 6.13 shows the innovation mean, standard deviation, minimum and maximum calculated using all pixels over the scene (see Figure 6.12) for each iteration and frequency. Except for the 118.35 GHz channel, the statistical variation of the innovation fields is reduced with iteration count. The standard deviation for nearly all channels is converged at the 20<sup>th</sup> iterate with different  $\sigma_{T_B}$  values which are noticeably smaller relative to the  $\sigma_{T_B}$  of the initial innovation field.

As another key criterion, thermodynamic and hydrometeor state variables after 20 XKF iterations are compared with both the simulated true state vector and the WRF forecast state vector (i.e. the first guess) for assessing the locking status of the WRF model. Note that precipitation locking is a highly flow-dependent assimilation process, thus the locking status depends on the physical properties of the atmosphere vertical profiles. Usually, cloudy and clear sky condition are two distinguishable states in data assimilation. In this thesis, we classify cloud vertical profiles into two primary categories, thin clouds and thick clouds, by using the integrated cloud ice content in the profile. One category of thin clouds includes profiles with integrated cloud ice content  $< 0.1 \text{ kg/m}^2$  and the other includes profiles with integrated cloud ice content  $\geq 0.1 \text{ kg/m}^2$ . This threshold  $0.1 \text{ kg/m}^2$  is somewhat arbitrarily selected based on the histogram of integrated cloud ice content of profiles in the testing domains, whereby a roughly equal number of profiles is present in each category.

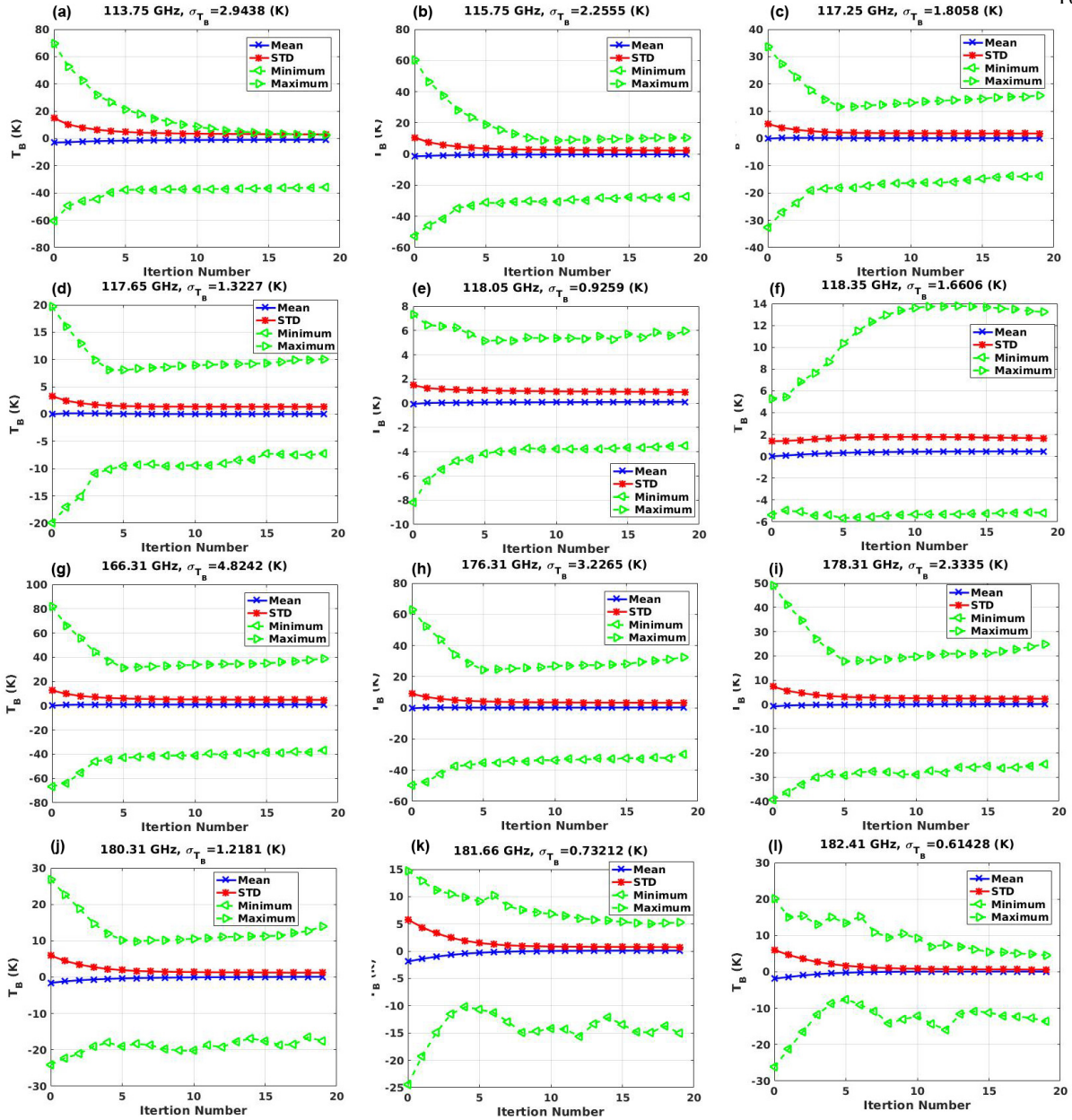


Figure 6.13: Statistics of the innovation variations with XKF iterations. Each figure shows mean, standard deviation, minimum and maximum value of the innovations over the entire testing scene for (a) - (l) sounding/imaging channels centered at 118.7503 GHz and 183.310 GHz. The standard deviation of residual  $T_B$  innovations after 20 iterations is shown in each sub-figure title.

The comparisons of atmospheric state variables between the truth, the first guess, and the 20<sup>th</sup> iterate thus proceeds within each of these two categories. Figure 6.14 shows comparisons of atmospheric state variables between the mean truth, the mean first guess, and the mean and STD

of the 20<sup>th</sup> iterate for thin clouds. The statistical quantities are calculated based on vertical profiles within the thin cloud category. In this case, the mean hydrometeor variables of the 20<sup>th</sup> iterate overestimate the truth for all hydrometeor phases and perform even worse than the first guess on average. The minimum values however are absolute zero, which is evidence that the constraints with lower bounds imposed on hydrometeor densities take effect during XKF iterations. The mean thermodynamic variables of the 20<sup>th</sup> iterate stay close to the mean truth with reasonably small variance compared to the maximum. However, both minimum and maximum curve drift away from the mean truth, which indicates that the XKF fails to correctly update temperature and water vapor density at some points during iterations, thus resulting in large differences between the mean and the maximum values (e.g. up to  $\sim 70$  K for temperature and  $\sim 40$  g/m<sup>3</sup> for vapor density).

Figure 6.15 shows similar comparisons of atmospheric state variables for thick clouds. As expected, the averaged hydrometeor profiles of the 20<sup>th</sup> iterate have estimates to the truth compared to the first guess, in particular, for rain and cloud ice density. The mean thermodynamic variables of the 20<sup>th</sup> iterate closely follow the trend of the mean truth as in the thin cloud case. However, the minimum and maximum values have considerably smaller dynamic range relative to the case of thin clouds. This smaller variation of minimum and maximum values shows that the constrained XKF can effectively constrain the thermodynamic state update errors for thick clouds. Overall, comparing Figures 6.14 and 6.15, the constrained XKF state variable updates for thick clouds exhibit statistically smaller errors for both thermodynamic and hydrometeor variables. The improved results using the XKF method for thick clouds is suspected to be due to better estimates of the hydrometeor background error covariance using thick cloud profiles than was achieved for thin cloud profiles.

The degree of precipitation locking can also be quickly assessed by the state variable error defined as the difference between an iterate state and the true state. Three scalar quantities of the temperature error are defined: 1) the error of mean temperature from surface to 1 km height, 2) the error of temperature at 500 mb, and 3) the error of temperature at 700 mb. The integrated vapor mass content per unit area (i.e. in kg/m<sup>2</sup>) along with hydrometeor mass content per unit area are also defined and used for precipitation locking assessment.



Figure 6.16 shows the above defined variable errors after 20 XKF iterations over the scene of hurricane Sandy. Exceptionally, large temperature errors (e.g., up to 60 K) simultaneously occur at different pressure levels over a few small regions near rain bands. These errors reveal that iterate temperature profiles in those regions diverge from the simulated true values. However, temperature errors are relatively smaller over most of the scene area. A similar situation occurs for the integrated vapor errors over the scene. For hydrometeor state variables, the constrained XKF is capable to iteratively reduce the state error of the precipitation cells over the simulated scene, although the state error grows larger (i.e., about  $\pm 10 \text{ kg/m}^2$ ) for integrated cloud water and rain over a small region of the scene. These large state errors show that the constraints used in the XKF algorithm cannot alone stabilize the state update when a poor estimate of background error covariance is used.

Finally, statistics of prognostic variable errors are computed at each XKF iteration based on atmospheric vertical profiles in the thin and thick cloud categories defined above. Figures 6.17 and 6.18 show the changing statistics of prognostic variable errors with XKF iteration for these thin cloud and thick cloud category (respectively). The constrained XKF shows better statistical results for thick clouds. For example, the mean error in integrated vapor content iteratively decreases from  $\sim 15 \text{ kg/m}^2$  to  $\sim 2 \text{ kg/m}^2$  for the thick cloud case. However, the mean error increases by  $\sim 10 \text{ kg/m}^2$  for the thin cloud case. The maximum errors grow larger during XKF iterations for nearly all prognostic variables because the XKF fails to update the state vector correctly for a small number of profiles within the testing scene. *Therefore, stabilizing the increasing errors for small number prognostic variable profits becomes the major issue in achieving precipitation locking. As we discussed before, an accurate estimate of a flow-dependent background error covariance matrix is fundamental to the tasks of simultaneously decreasing both thermodynamic and hydrometeor state variable errors.*

#### 6.4 Suggested Future Research on Precipitation Locking

The potential for locking the WRF model to the hydrometeor state using microwave satellite observations over precipitation cells and heavy cloud features within rapidly evolving mesoscale

convection such as hurricane rain bands and frontal boundaries requires three critical components functioning efficiently and cooperatively: 1) background error covariance matrix providing the flow-dependent joint error statistics for all hydrometeor and thermodynamic state variables, 2) fast and accurate Jacobians describing the tangent linear relationship between the observed satellite radiances and the atmospheric state, and 3) physically-based constraints imposed on prognostic state variables so that the variable update suggested by the extended Kalman filter is stabilized and maintains conservation laws. Although it was not fully quantified in this thesis, error statistics in the forward radiative transfer model over clouds and precipitation are also anticipated to play a key role in XKF stabilization.

Among these requirements, the background error covariance matrix plays perhaps the most important role in meteorological variational data assimilation systems based on passive microwave satellite data and iterative extended Kalman filtering. The background error covariance must also be flow-dependent and rapidly calculable over all relevant meteorological scenarios. To this end, a Brownian-based background error covariance model for both hydrometeor and thermodynamic variables is being developed at CU CET in collaboration with Dr. Jieying He of the Chinese National Space Science Center. This model is based on the "NMC method" under which the prognostic variable state increments are small enough that both hydrometeor and thermodynamic state variables can be assumed to be Brownian processes whose error covariances grow linearly with time. Under the Brownian assumption the error covariance matrix can be developed from increments in the forecast state variables, which are themselves jointly Gaussian for short enough time periods. The research focuses on the appropriate time differences to be used to justify the Brownian assumption for both hydrometeor (e.g., rain, cloud liquid water, cloud ice, snow, and graupel density) and thermodynamic variables (e.g. temperature, water vapor) within the framework of the WRF model. It specially addresses the determination of the proper scaling factor between the time difference increments and the resulting background error covariance matrix.

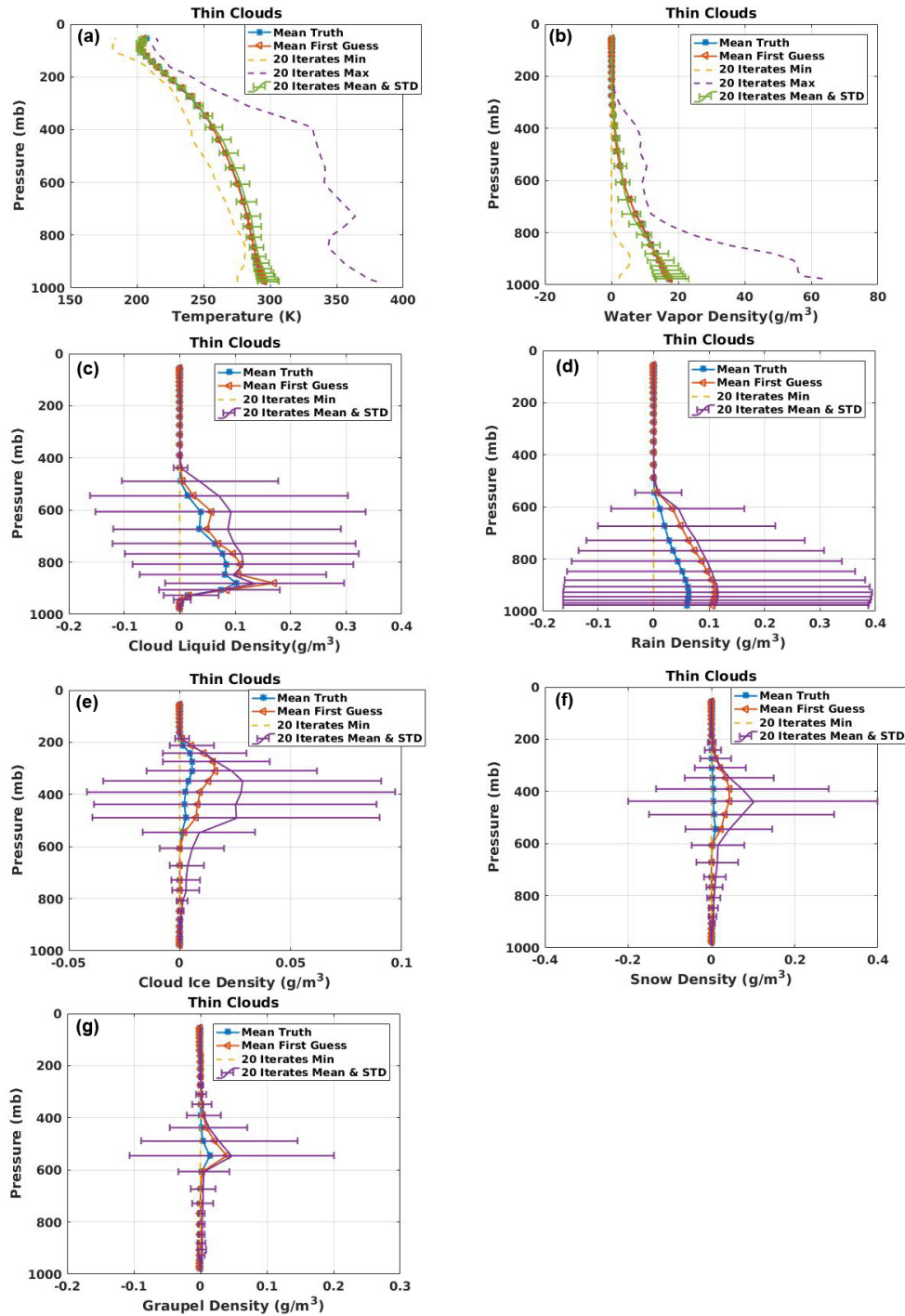


Figure 6.14: Comparisons of atmospheric state variables for thin clouds between the mean truth (line with stars), the mean first guess (line with triangles), and the 20<sup>th</sup> iterate mean and STD profiles (line with error bars), (a) temperature in Kelvin, (b) water vapor bulk density in  $\text{g/m}^3$ , (c)-(g) the bulk density of hydrometeor in  $\text{g/m}^3$  of five microphysical phases. The minimum and maximum values of temperature and vapor density in the 20<sup>th</sup> iterate are shown in (a) and (b). Only the minimum values of hydrometeor density in the 20<sup>th</sup> iterate are included in (c)-(g) for good display.

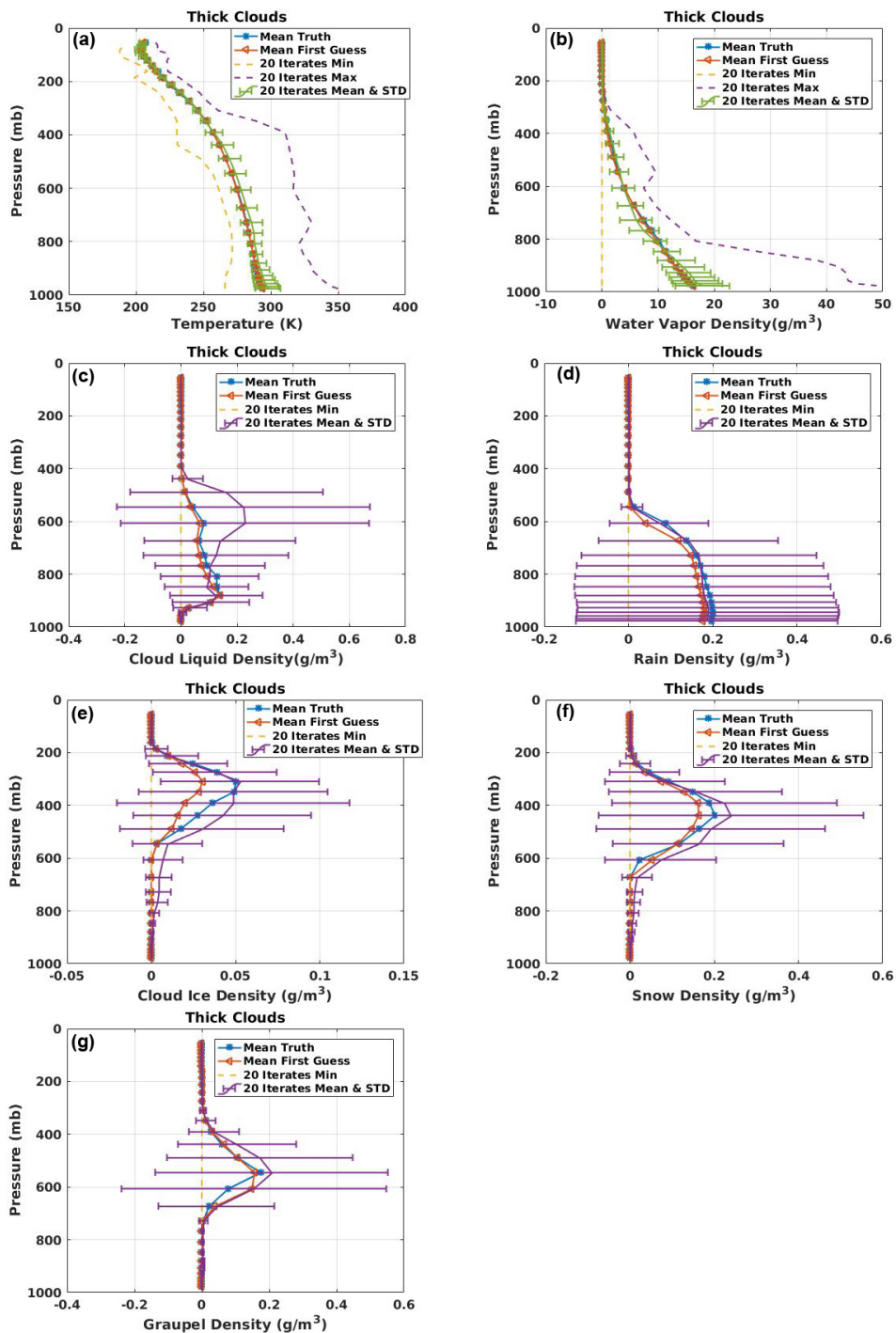


Figure 6.15: Similar to Figure 6.14, but comparisons of atmospheric state variables for thick clouds.

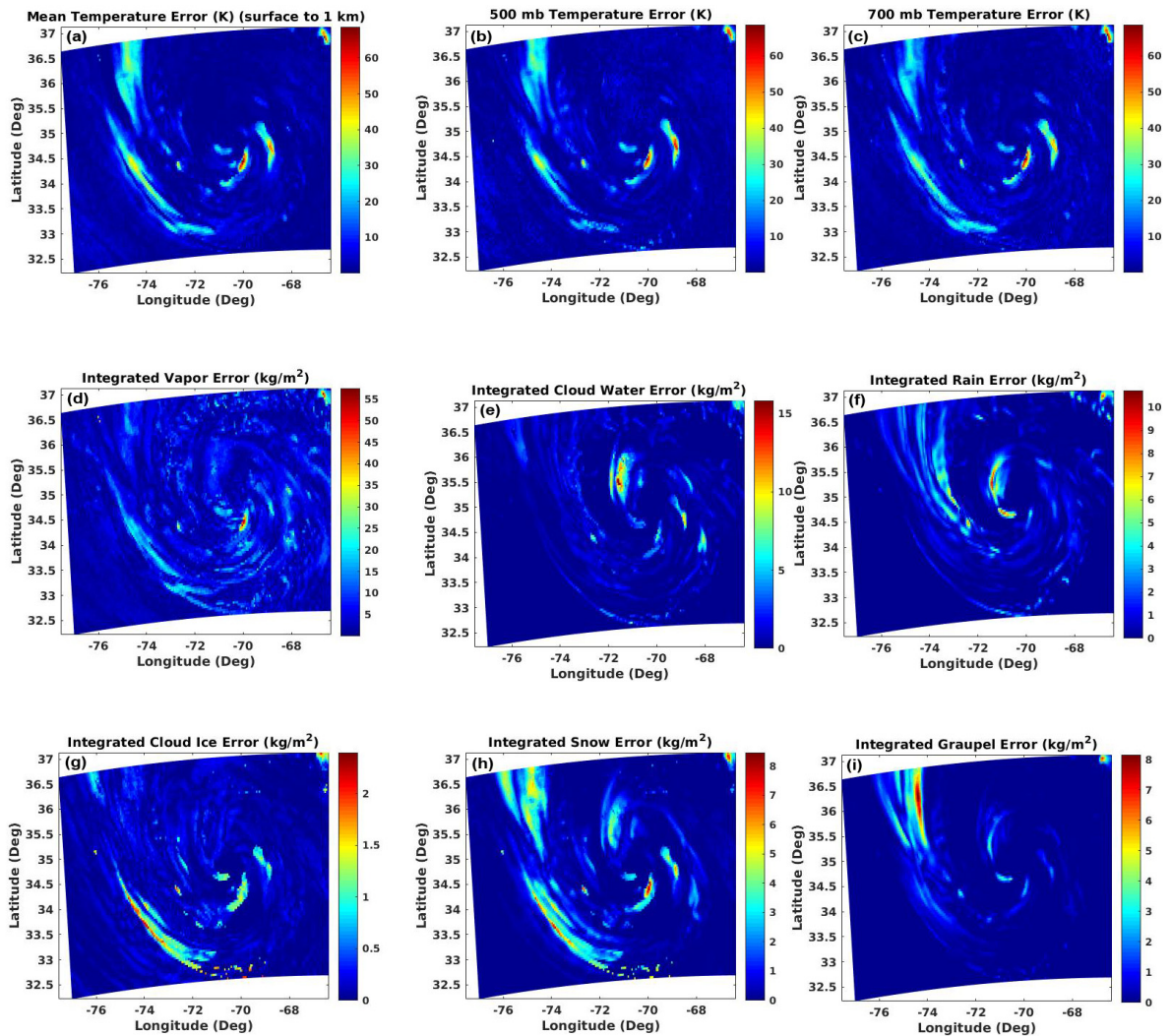


Figure 6.16: Prognostic variable errors at the 20<sup>th</sup> iterate used for assessing the degree of precipitation locking, (a) mean temperature error evaluated from surface to 1 km height, (b) temperature error at 500 mb, (c) temperature error at 700 mb, (d) integrated vapor content error in  $\text{kg}/\text{m}^2$ , (e) integrated cloud water path error in  $\text{kg}/\text{m}^2$ , (f) integrated rain error in  $\text{kg}/\text{m}^2$ , (g) integrated cloud ice path error in  $\text{kg}/\text{m}^2$ , (h) integrated snow path error in  $\text{kg}/\text{m}^2$ , (i) integrated graupel path error in  $\text{kg}/\text{m}^2$ .

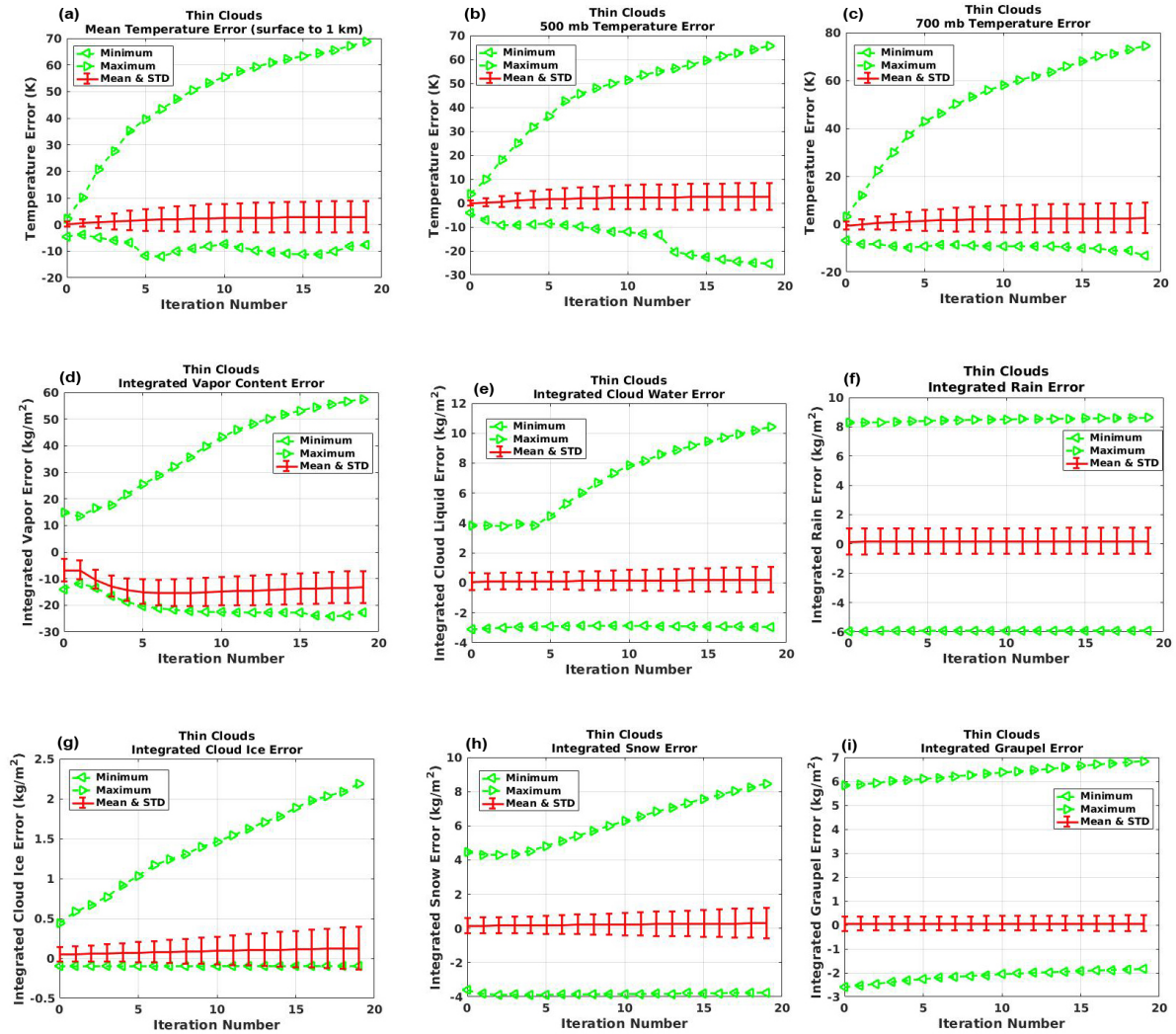


Figure 6.17: Statistics of prognostic variable errors changed during XKF iterate. Each figure shows the error mean, standard deviation, minimum and maximum values calculated using atmospheric profiles categorized as thin clouds. (a) mean temperature error evaluated from surface to 1 km height, (b) temperature error at 500 mb, (c) temperature error at 750 mb, (d) integrated vapor content error in  $\text{g/m}^2$ , (e) integrated cloud water path error in  $\text{g/m}^2$ , (f) integrated rain error in  $\text{g/m}^2$ , (g) integrated cloud ice path error in  $\text{g/m}^2$ , (h) integrated snow path error in  $\text{g/m}^2$ , (i) integrated graupel path error in  $\text{g/m}^2$ .

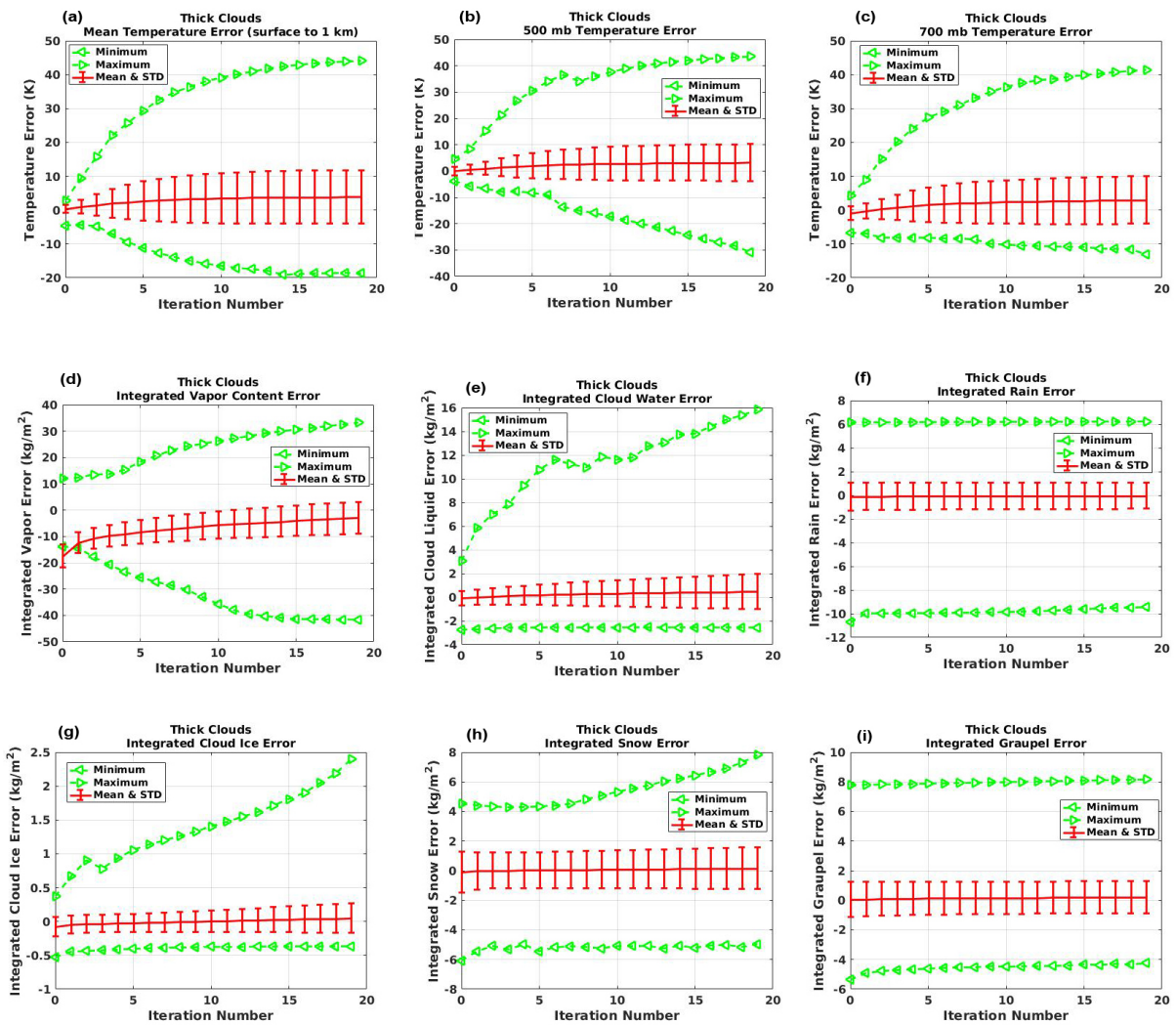


Figure 6.18: Similar to Figure 6.17 but for statistics of prognostic variable errors calculated using profiles of thick clouds.

## Chapter 7

### Conclusions

In this thesis, the UMRT model is applied to multilayer clouds composed of a wide variety of aspherical OpenSSP hydrometeors under the approximation of transition matrix subblock sum and difference [SBSD] symmetry. Within a two Stokes parameter framework, transition matrix SBSB symmetry is imposed using the block-diagonal elements of the Stokes matrix for randomly oriented frozen OpenSSP hydrometeors, thereby neglecting the asymmetric component of the transition matrix caused by the arbitrary geometrical structure of these hydrometeors. An upper bound on the brightness temperature errors incurred by neglecting the asymmetric component is shown to be sufficiently small under even extreme atmospheric hydrometeor conditions for frequencies up to  $\sim 1$  THz. Hence, the OpenSSP complex hydrometeor database can be incorporated into the UMRT framework for stable and efficient forward radiative simulations under all weather conditions for the first two Stokes parameters.

For broadband simulations of microwave radiances using UMRT, a scattering function matrix database based on the geometrical properties of OpenSSP hydrometeors was created using the discrete dipole scattering code. The database was established for a small but representative portion (e.g. 203 samples) of the complete aspherical OpenSSP hydrometeor database and is applicable at key microwave frequencies from 10 GHz to 874 GHz. The maximum diameter ( $D_{\max}$ ) of selected hydrometeors for a given habit reaches  $\sim 4,500 \mu\text{m}$ , which is similar to the maximum particle dimensions used in previous studies of ice hydrometeor scattering.

Microwave radiance intercomparison simulations were carried out by alternately incorporating



multi-habit aspherical OpenSSP hydrometeors and mass-equivalent ice spheres at key sensing frequencies between 10 and 874 GHz. The resulting top-of-atmosphere brightness temperatures over a WRF-based hurricane Sandy simulation were compared with respect to polarization, viewing angle, and frequency. The statistics of brightness temperature images for such a severe weather event show the considerable impact of aspherical frozen hydrometeors on computed forward radiances, where the impact depends heavily on both frequency and viewing angle. For the sounding channels of the upcoming ICI mission, simulated radiances exhibit high sensitivity to complex (versus spherical) geometrical hydrometeor structure. The strong impact of aspherical hydrometeors can also be found at off-nadir views for other channels above 300 GHz. These broadband simulations provide quantitative statistics useful for improving the interpretation of ice cloud remote sensing observations.

The horizontally inhomogeneous unified microwave radiative transfer (HI-UMRT) model has been developed to solve the 3D radiative transfer equation using the existing 1D planar-stratified UMRT model embedded in a convergent horizontal perturbation series. The iterative perturbation begins with the 1D UMRT solution as an initial guess to the microwave radiation fields in a 3D inhomogeneous medium. This stable and accurate 1D numerical solution for multi-stream and coupled dual-polarization microwave radiances plays a key role in a rapid convergence of the perturbation series.

A perturbation source function analysis based on the decomposed azimuthal harmonic and iterative perturbation equations was performed in order to identify the radiative equations with non-trivial solutions based on the upper cold space and lower surface atmospheric boundary conditions. With the assumption of an azimuthally-independent surface bistatic scattering function, such as for a specular ocean surface, only a small portion of the decomposed equations have non-trivial radiative transfer solution, thus reducing the number of 1D model executions in the perturbation process and shortening the computing time for achieving the convergent threshold.

An intercomparison of upwelling brightness temperatures simulated using 3D HI-UMRT and 1D UMRT shows considerable impact of cloud horizontal inhomogeneities on the computed microwave radiances. This impact varies with the azimuth angle used in a simulation and becomes

strong near cloud edges or over clouds with a high degree of horizontal inhomogeneity. The 3D radiation effects due to medium horizontal inhomogeneities can be identified using the computed brightness temperature difference images where coupled stripes of positive and negative differences appear due to the effective horizontal radiation transport in clouds. These considerable 3D radiation effects are expected to be of concern in passive remote sensing observations since the radiation fields within the upwelling radiation of a sensing beam can not be treated as uniform over horizontally inhomogeneous clouds.

The HI-UMRT model is applicable to forward microwave radiances simulation for a 3D inhomogeneous medium and provides the 3D radiative solution with numerical stability and computational efficiency to meet the operational requirements for either cloud property retrieval or microwave radiances assimilation.

An important application of 3D HI-UMRT incorporating aspherical hydrometeors in microwave radiances assimilation has been explored by first introducing the concept of precipitation locking. The potential of locking the precipitation cells in NWP models is based on extended Kalman filtering with accurate estimate of background error covariance and Jacobians. A background error covariance model for cloud vertical profiles based on cluster classification and error covariance interpolation was developed. The estimated background error covariances for 1D vertical atmospheric state variables are used in first-frame locking experiments. Two types of inequality constraints are imposed on the state variables during extended Kalman filtering iterations. The simulation results show the potential of precipitation locking over the scene of simulated hurricane Sandy, where prognostic variable errors simultaneously decrease with noticeable amount after 20 iterates of extended Kalman filtering.

## Bibliography

- [1] R. Anthes and B. Moore, editors. Earth Science and Applications from Space: National Imperatives for the Next Decade and Beyond. January 2007.
- [2] Olena Babak and Clayton V. Deutsch. Statistical approach to inverse distance interpolation. Stochastic Environmental Research and Risk Assessment, 23(5):543–553, July 2009.
- [3] R. N. Bannister. A review of forecast error covariance statistics in atmospheric variational data assimilation. I: Characteristics and measurements of forecast error covariances. Quarterly Journal of the Royal Meteorological Society, 134(637):1951–1970, October 2008.
- [4] R. N. Bannister. A review of forecast error covariance statistics in atmospheric variational data assimilation. II: Modelling the forecast error covariance statistics. Quarterly Journal of the Royal Meteorological Society, 134(637):1971–1996, October 2008.
- [5] Peter Bartello and Herschel L. Mitchell. A continuous three-dimensional model of short-range forecast error covariances. Tellus A: Dynamic Meteorology and Oceanography, 44(3):217–235, January 1992.
- [6] Peter Bauer, Thomas Auligné, William Bell, Alan Geer, Vincent Guidard, Sylvain Heilliette, Masahiro Kazumori, Min-Jeong Kim, Emily H.-C. Liu, Anthony P. McNally, Bruce Macpherson, Kozo Okamoto, Richard Renshaw, and Lars-Peter Riishøjgaard. Satellite cloud and precipitation assimilation at operational NWP centres. Quarterly Journal of the Royal Meteorological Society, 137(661):1934–1951, October 2011.
- [7] Peter Bauer, Alan J. Geer, Philippe Lopez, and Deborah Salmond. Direct 4d-Var assimilation of all-sky radiances. Part I: Implementation. Quarterly Journal of the Royal Meteorological Society, 136(652):1868–1885, October 2010.
- [8] Bryan A. Baum, Ping Yang, Andrew J. Heymsfield, Carl G. Schmitt, Yu Xie, Aaron Bansemer, Yong-Xiang Hu, and Zhibo Zhang. Improvements in Shortwave Bulk Scattering and Absorption Models for the Remote Sensing of Ice Clouds. Journal of Applied Meteorology and Climatology, 50(5):1037–1056, December 2010.
- [9] M. Bergadá, M. Labriola, R. González, M. A. Palacios, D. Marote, A. Andrés, J. L. García, D. S. Pascuala, L. Ordóñez, M. Rodríguez, M. T. Ortín, V. Estesó, J. Martínez, and U. Klein. The Ice Cloud Imager (ICI) preliminary design and performance. In 2016 14th Specialist Meeting on Microwave Radiometry and Remote Sensing of the Environment (MicroRad), pages 27–31, April 2016.

- [10] Christopher M. Bishop. Pattern recognition and machine learning. Information science and statistics. Springer, New York, 2006.
- [11] William Blackwell, G. Allen, C. Galbraith, R. Leslie, I. Osaretin, M. Scarito, Mike Shields, E. Thompson, D. Toher, D. Townzen, A. Vogel, R. Wezalis, Kerri Cahoy, David Miller, Anne Marinan, Ryan Kingsbury, Evan Wise, Sung Wook Paek, Eric Peters, Meghan Prinkey, Pratik Davé, Brian Coffee, and Neal Erickson. MicroMAS: A First Step Towards a Nanosatellite Constellation for Global Storm Observation. AIAA/USU Conference on Small Satellites, August 2013.
- [12] Craig F. Bohren and Donald R. Huffman. Absorption and scattering of light by small particles. Wiley, New York, 1983.
- [13] Giovanni Botta, Kultegin Aydin, Johannes Verlinde, Alexander E. Avramov, Andrew S. Ackerman, Ann M. Fridlind, Greg M. McFarquhar, and Mengistu Wolde. Millimeter wave scattering from ice crystals and their aggregates: Comparing cloud model simulations with X- and Ka-band radar measurements. Journal of Geophysical Research: Atmospheres, 116(D1), January 2011.
- [14] Michael A. Box. Radiative perturbation theory: a review. Environmental Modelling & Software, 17(1):95–106, January 2002.
- [15] Michael A. Box, Igor N. Polonsky, and Anthony B. Davis. Higher order perturbation theory applied to radiative transfer in non-plane-parallel media. Journal of Quantitative Spectroscopy and Radiative Transfer, 78(1):105–118, April 2003.
- [16] S. A. Buehler, C. Jiménez, K. F. Evans, P. Eriksson, B. Rydberg, A. J. Heymsfield, C. J. Stubenrauch, U. Lohmann, C. Emde, V. O. John, T. R. Sreerekha, and C. P. Davis. A concept for a satellite mission to measure cloud ice water path, ice particle size, and cloud altitude. Quarterly Journal of the Royal Meteorological Society, 133(S2):109–128, October 2007.
- [17] Mark Buehner. Ensemble-derived stationary and flow-dependent background-error covariances: Evaluation in a quasi-operational NWP setting. Quarterly Journal of the Royal Meteorological Society, 131(607):1013–1043, April 2005.
- [18] S. Chandrasekhar. Radiative transfer. Dover Publications, New York, 1960.
- [19] T. Coleman and Y. Li. An Interior Trust Region Approach for Nonlinear Minimization Subject to Bounds. SIAM Journal on Optimization, 6(2):418–445, May 1996.
- [20] C. Cornet, L. C-Labonnote, and F. Szczap. Three-dimensional polarized Monte Carlo atmospheric radiative transfer model (3dmcpol): 3d effects on polarized visible reflectances of a cirrus cloud. Journal of Quantitative Spectroscopy and Radiative Transfer, 111(1):174–186, January 2010.
- [21] George P. Cressman. An operational objective analysis system. Monthly Weather Review, 87(10):367–374, October 1959.
- [22] John C. Derber. Variational Four-dimensional Analysis Using Quasi-Geostrophic Constraints. Monthly Weather Review, 115(5):998–1008, May 1987.

- [23] G. Desroziers, L. Berre, B. Chapnik, and P. Poli. Diagnosis of observation, background and analysis-error statistics in observation space. Quarterly Journal of the Royal Meteorological Society, 131(613):3385–3396, October 2005.
- [24] Bruce T. Draine and Piotr J. Flatau. Discrete-Dipole Approximation For Scattering Calculations. JOSA A, 11(4):1491–1499, April 1994.
- [25] D. W. Draper, D. A. Newell, F. J. Wentz, S. Krimchansky, and G. M. Skofronick-Jackson. The Global Precipitation Measurement (GPM) Microwave Imager (GMI): Instrument Overview and Early On-Orbit Performance. IEEE Journal of Selected Topics in Applied Earth Observations and Remote Sensing, 8(7):3452–3462, July 2015.
- [26] C. Emde, S. A. Buehler, C. Davis, P. Eriksson, T. R. Sreerekha, and C. Teichmann. A polarized discrete ordinate scattering model for simulations of limb and nadir long-wave measurements in 1-D/3-D spherical atmospheres. Journal of Geophysical Research: Atmospheres, 109(D24):D24207, December 2004.
- [27] C. Emde, R. Buras, B. Mayer, and M. Blumthaler. The impact of aerosols on polarized sky radiance: model development, validation, and applications. Atmospheric Chemistry and Physics, 10(2):383–396, January 2010.
- [28] Claudia Emde, Vasileios Barlakas, Céline Cornet, Frank Evans, Sergey Korin, Yoshifumi Ota, Laurent C. Labonnote, Alexei Lyapustin, Andreas Macke, Bernhard Mayer, and Manfred Wendisch. IPRT polarized radiative transfer model intercomparison project – Phase A. Journal of Quantitative Spectroscopy and Radiative Transfer, 164:8–36, October 2015.
- [29] Claudia Emde, Vasileios Barlakas, Céline Cornet, Frank Evans, Zhen Wang, Laurent C. Labonnote, Andreas Macke, Bernhard Mayer, and Manfred Wendisch. IPRT polarized radiative transfer model intercomparison project – Three-dimensional test cases (phase B). Journal of Quantitative Spectroscopy and Radiative Transfer, 209:19–44, April 2018.
- [30] Patrick Eriksson, Robin Ekelund, Jana Mendrok, Manfred Brath, Oliver Lemke, and Stefan A Buehler. A general database of hydrometeor single scattering properties at microwave and sub-millimetre wavelengths. page 26, 2018.
- [31] K. Franklin Evans. The Spherical Harmonics Discrete Ordinate Method for Three-Dimensional Atmospheric Radiative Transfer. Journal of the Atmospheric Sciences, 55(3):429–446, February 1998.
- [32] K. Franklin Evans and Graeme L. Stephens. Microwave Radiative Transfer through Clouds Composed of Realistically Shaped Ice Crystals. Part I. Single Scattering Properties. Journal of the Atmospheric Sciences, 52(11):2041–2057, June 1995.
- [33] K. Franklin Evans and Graeme L. Stephens. Microwave Radiative Transfer through Clouds Composed of Realistically Shaped Ice Crystals. Part II. Remote Sensing of Ice Clouds. Journal of the Atmospheric Sciences, 52(11):2058–2072, June 1995.
- [34] K. Franklin Evans, Steven J. Walter, Andrew J. Heymsfield, and Merritt N. Deeter. Modeling of Submillimeter Passive Remote Sensing of Cirrus Clouds. Journal of Applied Meteorology, 37(2):184–205, February 1998.

- [35] K. Franklin Evans, Steven J. Walter, Andrew J. Heymsfield, and Greg M. McFarquhar. Submillimeter-Wave Cloud Ice Radiometer: Simulations of retrieval algorithm performance. Journal of Geophysical Research: Atmospheres, 107(D3):AAC 2–1, February 2002.
- [36] K. Franklin Evans, James R. Wang, Paul E. Racette, Gerald Heymsfield, and Lihua Li. Ice Cloud Retrievals and Analysis with the Compact Scanning Submillimeter Imaging Radiometer and the Cloud Radar System during CRYSTAL FACE. Journal of Applied Meteorology, 44(6):839–859, June 2005.
- [37] Brad Schoenberg Ferrier, Wei-Kuo Tao, and Joanne Simpson. A Double-Moment Multiple-Phase Four-Class Bulk Ice Scheme. Part II: Simulations of Convective Storms in Different Large-Scale Environments and Comparisons with other Bulk Parameterizations. Journal of the Atmospheric Sciences, 52(8):1001–1033, April 1995.
- [38] Mike Fisher. `Assimilation_techniques_4dvar`. page 9, 2002.
- [39] R. Fletcher. Practical Methods of Optimization. John Wiley & Sons, Incorporated, New York, UNITED KINGDOM, 2013.
- [40] Floyd Martin Gardner. Phaselock techniques. John Wiley, Hoboken, NJ, 3rd ed edition, 2005.
- [41] A. J. Gasiewski. Microwave radiative transfer in hydrometeors. In M. A. Janssen, editor, Atmospheric remote sensing by microwave radiometry, Wiley series in remote sensing, pages 91–144. Wiley, New York, 1993.
- [42] A. J. Gasiewski and D. H. Staelin. Numerical modeling of passive microwave O<sub>2</sub> observations over precipitation. Radio Science, 25(3):217–235, May 1990.
- [43] A.J. Gasiewski. Atmospheric temperature sounding and precipitation cell parameter estimation using passive 118-ghz o<sub>2</sub> observations. Ph.D. thesis, MIT, 1998.
- [44] A.J. Gasiewski, B. T. Sanders, and D. W. Gallaher. Realization of path goals using a small satellite constellation. 95th AMS Annual Meeting, Phoenix, Arizona, 2015.
- [45] A.J. Gasiewski, A.G. Voronovich, B.L. Weber, D. F. Smith, Timothy L. Schneider, and Jian-Wen Bao. Fast forward radiative transfer modeling for microwave radiance assimilation. JCSDA Science Workshop, Camp Springs, MD, 2005.
- [46] Gene H. Golub and Charles F. Van Loan. Matrix computations. Johns Hopkins studies in the mathematical sciences. Johns Hopkins University Press, Baltimore, MD, 3rd ed edition, 1996.
- [47] Janko Gravner and David Griffeath. Modeling snow-crystal growth: A three-dimensional mesoscopic approach. Physical Review E, 79(1):011601, January 2009.
- [48] Mircea Grecu and William S. Olson. Precipitating Snow Retrievals from Combined Airborne Cloud Radar and Millimeter-Wave Radiometer Observations. Journal of Applied Meteorology and Climatology, 47(6):1634–1650, June 2008.
- [49] Ji-Hyun Ha and Dong-Kyou Lee. Effect of length scale tuning of background Error in WRF-3dvar system on assimilation of high-resolution surface data for heavy rainfall simulation. Advances in Atmospheric Sciences, 29(6):1142–1158, November 2012.

- [50] Jieying He, K. Zhang, and A. J. Gasiewski. Brownian-based background error covariance matrix for hydrometeor and thermodynamic variables. In preparation for submission, 2018.
- [51] Andrew J. Heymsfield, Sharon Lewis, Aaron Bansemer, Jean Iaquinta, Larry M. Miloshevich, Masahiro Kajikawa, Cynthia Twohy, and Michael R. Poellot. A General Approach for Deriving the Properties of Cirrus and Stratiform Ice Cloud Particles. Journal of the Atmospheric Sciences, 59(1):3–29, January 2002.
- [52] Andrew J. Heymsfield, Larry M. Miloshevich, Carl Schmitt, Aaron Bansemer, Cynthia Twohy, Michael R. Poellot, Ann Fridlind, and Hermann Gerber. Homogeneous Ice Nucleation in Subtropical and Tropical Convection and Its Influence on Cirrus Anvil Microphysics. Journal of the Atmospheric Sciences, 62(1):41–64, January 2005.
- [53] Andrew J. Heymsfield, Carl Schmitt, and Aaron Bansemer. Ice Cloud Particle Size Distributions and Pressure-Dependent Terminal Velocities from In Situ Observations at Temperatures from 0° to -86°C. Journal of the Atmospheric Sciences, 70(12):4123–4154, March 2013.
- [54] Gang Hong. Radar backscattering properties of nonspherical ice crystals at 94 GHz. Journal of Geophysical Research: Atmospheres, 112(D22), November 2007.
- [55] Gang Hong, Ping Yang, Bryan A. Baum, Andrew J. Heymsfield, Fuzhong Weng, Quanhua Liu, Georg Heygster, and Stefan A. Buehler. Scattering database in the millimeter and submillimeter wave range of 100–1000 GHz for nonspherical ice particles. Journal of Geophysical Research: Atmospheres, 114(D6):D06201, March 2009.
- [56] P. L. Houtekamer and Herschel L. Mitchell. A Sequential Ensemble Kalman Filter for Atmospheric Data Assimilation. Monthly Weather Review, 129(1):123–137, January 2001.
- [57] Akira Ishimaru. Wave propagation and scattering in random media. Academic Press, New York, 1978.
- [58] Heikki Järvinen. Temporal evolution of innovation and residual statistics in the ECMWF variational data assimilation systems. Tellus A: Dynamic Meteorology and Oceanography, 53(3):333–347, January 2001.
- [59] Eugenia Kalnay. Atmospheric modeling, data assimilation, and predictability. Cambridge University Press, Cambridge, U.K. ; New York, 2003.
- [60] C. Kenney and A. Laub. Condition Estimates for Matrix Functions. SIAM Journal on Matrix Analysis and Applications, 10(2):191–209, April 1989.
- [61] L. Klein and C. Swift. An improved model for the dielectric constant of sea water at microwave frequencies. IEEE Journal of Oceanic Engineering, 2(1):104–111, January 1977.
- [62] Marian Klein and Albin J. Gasiewski. Nadir sensitivity of passive millimeter and submillimeter wave channels to clear air temperature and water vapor variations. Journal of Geophysical Research: Atmospheres, 105(D13):17481–17511, July 2000.
- [63] Prashant Kumar, C. M. Kishtawal, and P. K. Pal. Impact of satellite rainfall assimilation on Weather Research and Forecasting model predictions over the Indian region. Journal of Geophysical Research: Atmospheres, 119(5):2017–2031, March 2014.

- [64] C. Kummerow, J. Simpson, O. Thiele, W. Barnes, A. T. C. Chang, E. Stocker, R. F. Adler, A. Hou, R. Kakar, F. Wentz, P. Ashcroft, T. Kozu, Y. Hong, K. Okamoto, T. Iguchi, H. Kuroiwa, E. Im, Z. Haddad, G. Huffman, B. Ferrier, W. S. Olson, E. Zipser, E. A. Smith, T. T. Wilheit, G. North, T. Krishnamurti, and K. Nakamura. The Status of the Tropical Rainfall Measuring Mission (TRMM) after Two Years in Orbit. Journal of Applied Meteorology, 39(12):1965–1982, December 2000.
- [65] C. Kummerow and J. A. Weinman. Determining microwave brightness temperatures from precipitating horizontally finite and vertically structured clouds. Journal of Geophysical Research: Atmospheres, 93(D4):3720–3728, April 1988.
- [66] Karl S. Kunz and Raymond J. Luebbers. The Finite Difference Time Domain Method for Electromagnetics. CRC Press, May 1993. Google-Books-ID: 00on9fRvJqIC.
- [67] C. C. Kuo, D. H. Staelin, and P. W. Rosenkranz. Statistical iterative scheme for estimating atmospheric relative humidity profiles. IEEE Transactions on Geoscience and Remote Sensing, 32(2):254–260, March 1994.
- [68] Kwo-Sen Kuo, William S. Olson, Benjamin T. Johnson, Mircea Grecu, Lin Tian, Thomas L. Clune, Bruce H. van Aartsen, Andrew J. Heymsfield, Liang Liao, and Robert Meneghini. The Microwave Radiative Properties of Falling Snow Derived from Nonspherical Ice Particle Models. Part I: An Extensive Database of Simulated Pristine Crystals and Aggregate Particles, and Their Scattering Properties. Journal of Applied Meteorology and Climatology, 55(3):691–708, February 2016.
- [69] Kwo-Sen Kuo, R. C. Weger, R. M. Welch, and S. K. Cox. The picard iterative approximation to the solution of the integral equation of radiative transfer—part II. Three-dimensional geometry. Journal of Quantitative Spectroscopy and Radiative Transfer, 55(2):195–213, February 1996.
- [70] R. Paul Lawson, Brad Baker, Bryan Pilson, and Qixu Mo. In Situ Observations of the Microphysical Properties of Wave, Cirrus, and Anvil Clouds. Part II: Cirrus Clouds. Journal of the Atmospheric Sciences, 63(12):3186–3203, December 2006.
- [71] Henriette M. Lemke and Markus Quante. Backscatter characteristics of nonspherical ice crystals: Assessing the potential of polarimetric radar measurements. Journal of Geophysical Research: Atmospheres, 104(D24):31739–31751, December 1999.
- [72] John M. Lewis and John C. Derber. The use of adjoint equations to solve a variational adjustment problem with advective constraints. Tellus A: Dynamic Meteorology and Oceanography, 37(4):309–322, January 1985.
- [73] J. Li, D. J. W. Geldart, and Petr Chýlek. Second order perturbation solution for radiative transfer in clouds with a horizontally arbitrary periodic inhomogeneity. Journal of Quantitative Spectroscopy and Radiative Transfer, 53(4):445–456, April 1995.
- [74] L. Liao, R. Meneghini, H. K. Nowell, and G. Liu. Scattering Computations of Snow Aggregates From Simple Geometrical Particle Models. IEEE Journal of Selected Topics in Applied Earth Observations and Remote Sensing, 6(3):1409–1417, June 2013.
- [75] Hans J. Liebe. An updated model for millimeter wave propagation in moist air. Radio Science, 20(5):1069–1089, September 1985.



- [76] Hans J. Liebe, George A. Hufford, and Takeshi Manabe. A model for the complex permittivity of water at frequencies below 1 THz. International Journal of Infrared and Millimeter Waves, 12(7):659–675, July 1991.
- [77] B. Lim, T. Gaier, P. Kangaslahti, B. Lambbrigtsen, and A. Tanner. Initial results from the GeoSTAR-II laboratory demonstrator. In 2012 IEEE International Geoscience and Remote Sensing Symposium, pages 1282–1285, July 2012.
- [78] C. Liu, P. Yang, P. Minnis, N. Loeb, S. Kato, A. Heymsfield, and C. Schmitt. A two-habit model for the microphysical and optical properties of ice clouds. Atmos. Chem. Phys., 14(24):13719–13737, December 2014.
- [79] Guosheng Liu. A Database of Microwave Single-Scattering Properties for Nonspherical Ice Particles. Bulletin of the American Meteorological Society, 89(10):1563–1570, October 2008.
- [80] H. Liu, J. Wu, S. Zhang, J. Yan, L. Niu, C. Zhang, W. Sun, H. Li, and B. Li. The Geostationary Interferometric Microwave Sounder (GIMS): Instrument overview and recent progress. In 2011 IEEE International Geoscience and Remote Sensing Symposium, pages 3629–3632, July 2011.
- [81] Quanhua Liu, Clemens Simmer, and Eberhard Ruprecht. Three-dimensional radiative transfer effects of clouds in the microwave spectral range. Journal of Geophysical Research: Atmospheres, 101(D2):4289–4298, February 1996.
- [82] A. C. Lorenc. Analysis methods for numerical weather prediction. Quarterly Journal of the Royal Meteorological Society, 112(474):1177–1194, October 1986.
- [83] Yinghui Lu, Zhiyuan Jiang, Kultegin Aydin, Johannes Verlinde, Eugene E. Clothiaux, and Giovanni Botta. A polarimetric scattering database for non-spherical ice particles at microwave wavelengths. Atmospheric Measurement Techniques, 9(10):5119–5134, October 2016.
- [84] Alexander Marshak and Anthony Davis, editors. 3D Radiative Transfer in Cloudy Atmospheres. Springer Science & Business Media, March 2006. Google-Books-ID: NR8yY6M6I2QC.
- [85] J. S. Marshall and W. Mc K. Palmer. The distribution of raindrops with size. Journal of Meteorology, 5(4):165–166, August 1948.
- [86] T. Meissner and F. J. Wentz. The complex dielectric constant of pure and sea water from microwave satellite observations. IEEE Transactions on Geoscience and Remote Sensing, 42(9):1836–1849, September 2004.
- [87] Robert N. Miller, Michael Ghil, and François Gauthiez. Advanced Data Assimilation in Strongly Nonlinear Dynamical Systems. Journal of the Atmospheric Sciences, 51(8):1037–1056, April 1994.
- [88] Michael I. Mishchenko. Multiple scattering, radiative transfer, and weak localization in discrete random media: Unified microphysical approach. Reviews of Geophysics, 46(2):RG2003, June 2008.

- [89] Michael I. Mishchenko, Joop W. Hovenier, and Larry D. Travis, editors. Light scattering by nonspherical particles: theory, measurements, and applications. Academic Press, San Diego, 2000.
- [90] C. Mätzler, editor. Thermal Microwave Radiation: Applications for Remote Sensing. IET, 2006. Google-Books-ID: K\_LywiWmDeEC.
- [91] T. Nakajima and M. Tanaka. Matrix formulations for the transfer of solar radiation in a plane-parallel scattering atmosphere. Journal of Quantitative Spectroscopy and Radiative Transfer, 35(1):13–21, January 1986.
- [92] Holly Nowell, Guosheng Liu, and Ryan Honeyager. Modeling the microwave single-scattering properties of aggregate snowflakes. Journal of Geophysical Research: Atmospheres, 118(14):7873–7885, July 2013.
- [93] William S. Olson, Lin Tian, Mircea Grecu, Kwo-Sen Kuo, Benjamin T. Johnson, Andrew J. Heymsfield, Aaron Bansemer, Gerald M. Heymsfield, James R. Wang, and Robert Meneghini. The Microwave Radiative Properties of Falling Snow Derived from Nonspherical Ice Particle Models. Part II: Initial Testing Using Radar, Radiometer and In Situ Observations. Journal of Applied Meteorology and Climatology, 55(3):709–722, January 2016.
- [94] L. Periasamy and A. J. Gasiewski. Prelaunch performance of the 118 GHz polarcube 3utemperature sounding radiometer. In 2017 IEEE International Geoscience and Remote Sensing Symposium (IGARSS), pages 2137–2140, July 2017.
- [95] Grant W. Petty and Wei Huang. Microwave Backscatter and Extinction by Soft Ice Spheres and Complex Snow Aggregates. Journal of the Atmospheric Sciences, 67(3):769–787, March 2010.
- [96] J. R. Piepmeier and A. J. Gasiewski. High-resolution passive polarimetric microwave mapping of ocean surface wind vector fields. IEEE Transactions on Geoscience and Remote Sensing, 39(3):606–622, March 2001.
- [97] Louis A. Pipes. A perturbation method for the solution of linear matrix differential equations. Journal of the Franklin Institute, 283(5):357–371, May 1967.
- [98] J. Reisner, R. M. Rasmussen, and R. T. Bruintjes. Explicit forecasting of supercooled liquid water in winter storms using the MM5 mesoscale model. Quarterly Journal of the Royal Meteorological Society, 124(548):1071–1107, April 1998.
- [99] Clifford A. Reiter. A local cellular model for snow crystal growth. Chaos, Solitons & Fractals, 23(4):1111–1119, February 2005.
- [100] J. R. Roche. On the sensitivity of the matrix exponential problem. RAIRO. Analyse numérique, 15(3):249–255, 1981.
- [101] Roddy Rhodes Rogers. A short course in cloud physics. Pergamon Press, 1979. Google-Books-ID: \_D5RAAAAMAAJ.
- [102] R. D. Rosenkrantz. Where Do We Stand on Maximum Entropy? (1978). In R. D. Rosenkrantz, editor, E. T. Jaynes: Papers on Probability, Statistics and Statistical Physics, Synthese Library, pages 210–314. Springer Netherlands, Dordrecht, 1989.

- [103] Steven A. Rutledge and Peter Hobbs. The Mesoscale and Microscale Structure and Organization of Clouds and Precipitation in Midlatitude Cyclones. VIII: A Model for the “Seeder-Feeder” Process in Warm-Frontal Rainbands. Journal of the Atmospheric Sciences, 40(5):1185–1206, May 1983.
- [104] Matthew N. O. Sadiku. Refractive index of snow at microwave frequencies. Applied Optics, 24(4):572–575, February 1985.
- [105] Thomas W. Schlatter. Variational assimilation of meteorological observations in the lower atmosphere: A tutorial on how it works. Journal of Atmospheric and Solar-Terrestrial Physics, 62(12):1057–1070, August 2000.
- [106] Carl G. Schmitt and Andrew J. Heymsfield. Observational quantification of the separation of simple and complex atmospheric ice particles. Geophysical Research Letters, 41(4):2013GL058781, February 2014.
- [107] R. S. Sekhon and R. C. Srivastava. Snow Size Spectra and Radar Reflectivity. Journal of the Atmospheric Sciences, 27(2):299–307, March 1970.
- [108] Donald Shepard. A two-dimensional interpolation function for irregularly-spaced data. In Proceedings of the 1968 23rd ACM national conference on -, pages 517–524, Not Known, 1968. ACM Press.
- [109] Glenn Shutts. A kinetic energy backscatter algorithm for use in ensemble prediction systems. Quarterly Journal of the Royal Meteorological Society, 131(612):3079–3102, October 2005.
- [110] D. Simon and D. L. Simon. Kalman filtering with inequality constraints for turbofan engine health estimation. IEE Proceedings - Control Theory and Applications, 153(3):371–378, May 2006.
- [111] William C Skamarock, Joseph B Klemp, Jimmy Dudhia, David O Gill, Dale M Barker, Michael G Duda, Xiang-Yu Huang, Wei Wang, and Jordan G Powers. A Description of the Advanced Research WRF Version 3. page 125.
- [112] G. M. Skofronick-Jackson and A. J. Gasiewski. Nonlinear statistical retrievals of ice content and rain rate from passive microwave observations of a simulated convective storm. IEEE Transactions on Geoscience and Remote Sensing, 33(4):957–970, July 1995.
- [113] Gail Skofronick-Jackson, Andrew Heymsfield, Eric Holthaus, Cerese Albers, and Min-Jeong Kim. Nonspherical and spherical characterization of ice in Hurricane Erin for wideband passive microwave comparisons. Journal of Geophysical Research: Atmospheres, 113(D6):D06201, March 2008.
- [114] Gail Skofronick-Jackson and Benjamin T. Johnson. Surface and atmospheric contributions to passive microwave brightness temperatures for falling snow events. Journal of Geophysical Research: Atmospheres, 116(D2):D02213, January 2011.
- [115] Roy W. Spencer. A Satellite Passive 37-GHz Scattering-based Method for Measuring Oceanic Rain Rates. Journal of Climate and Applied Meteorology, 25(6):754–766, June 1986.

- [116] DH Staelin, AJ Gasiewski, JP Kerekes, MW Shields, and FJ Solman III. Concept proposal for a geostationary microwave (gem) observatory. Prepared for the NASA/NOAA Advanced Geostationary Sensor (AGS) Program, 23, 1998.
- [117] Knut Stamnes and Jakob J. Stamnes. Radiative Transfer in Coupled Environmental Systems: An Introduction to Forward and Inverse Modeling. John Wiley & Sons, Incorporated, Berlin, GERMANY, 2015.
- [118] Knut Stamnes, S.-Chee Tsay, Warren Wiscombe, and Kolf Jayaweera. Numerically stable algorithm for discrete-ordinate-method radiative transfer in multiple scattering and emitting layered media. Applied Optics, 27(12):2502–2509, June 1988.
- [119] Julius Adams Stratton. Electromagnetic theory. International series in physics. McGraw-Hill, New York ; London, 1st ed edition, 1941.
- [120] Chinnawat Surussavadee and David H. Staelin. Millimeter-Wave Precipitation Retrievals and Observed-versus-Simulated Radiance Distributions: Sensitivity to Assumptions. Journal of the Atmospheric Sciences, 64(11):3808–3826, November 2007.
- [121] W. K. Tao. Goddard Cumulus Ensemble Model. Part I : Model Description. Terrestrial, Atmos. Oceanic Sci., 4:35–72, 1993.
- [122] M. Tian and A. J. Gasiewski. A Unified Microwave Radiative Transfer Model for General Planar Stratified Media: Slab Formulation. IEEE Transactions on Geoscience and Remote Sensing, 51(7):4103–4118, July 2013.
- [123] Leung Tsang, Jin Au Kong, and Robert T. Shin. Theory of microwave remote sensing. Wiley series in remote sensing. Wiley, New York, 1985.
- [124] J. Tyynelä and V. Chandrasekar. Characterizing falling snow using multifrequency dual-polarization measurements. Journal of Geophysical Research: Atmospheres, 119(13):8268–8283, July 2014.
- [125] H. C. van de Hulst. Light scattering by small particles. Dover Publications, New York, 1981.
- [126] C. Van Loan. The Sensitivity of the Matrix Exponential. SIAM Journal on Numerical Analysis, 14(6):971–981, December 1977.
- [127] A. G. Voronovich, A. J. Gasiewski, and B. L. Weber. A fast multistream scattering-based Jacobian for microwave radiance assimilation. IEEE Transactions on Geoscience and Remote Sensing, 42(8):1749–1761, August 2004.
- [128] Tamás Várnai and Roger Davies. Effects of Cloud Heterogeneities on Shortwave Radiation: Comparison of Cloud-Top Variability and Internal Heterogeneity. Journal of the Atmospheric Sciences, 56(24):4206–4224, December 1999.
- [129] Tamás Várnai and Alexander Marshak. Statistical Analysis of the Uncertainties in Cloud Optical Depth Retrievals Caused by Three-Dimensional Radiative Effects. Journal of the Atmospheric Sciences, 58(12):1540–1548, June 2001.
- [130] Tamás Várnai and Alexander Marshak. Observations of Three-Dimensional Radiative Effects that Influence MODIS Cloud Optical Thickness Retrievals. Journal of the Atmospheric Sciences, 59(9):1607–1618, May 2002.

- [131] Zhen Wang, Shengcheng Cui, Jun Yang, Haiyang Gao, Chao Liu, and Zhibo Zhang. A novel hybrid scattering order-dependent variance reduction method for Monte Carlo simulations of radiative transfer in cloudy atmosphere. Journal of Quantitative Spectroscopy and Radiative Transfer, 189:283–302, March 2017.
- [132] Stephen G. Warren and Richard E. Brandt. Optical constants of ice from the ultraviolet to the microwave: A revised compilation. Journal of Geophysical Research: Atmospheres, 113(D14):D14220, July 2008.
- [133] F. Weng, H. Yang, and X. Zou. On Convertibility From Antenna to Sensor Brightness Temperature for ATMS. IEEE Geoscience and Remote Sensing Letters, 10(4):771–775, July 2013.
- [134] Yu-lin Xu. Electromagnetic scattering by an aggregate of spheres. Applied Optics, 34(21):4573–4588, July 1995.
- [135] Chun Yang, Zhiquan Liu, Jamie Bresch, Syed R. H. Rizvi, Xiang-Yu Huang, and Jinzhong Min. AMSR2 all-sky radiance assimilation and its impact on the analysis and forecast of Hurricane Sandy with a limited-area data assimilation system. Tellus A: Dynamic Meteorology and Oceanography, 68(1):30917, December 2016.
- [136] Jun-Ichi Yano, Andrew J. Heymsfield, and Vaughan T. J. Phillips. Size Distributions of Hydrometeors: Analysis with the Maximum Entropy Principle. Journal of the Atmospheric Sciences, 73(1):95–108, September 2015.
- [137] Maxim A. Yurkin and Alfons G. Hoekstra. The discrete-dipole-approximation code ADDA: Capabilities and known limitations. Journal of Quantitative Spectroscopy and Radiative Transfer, 112(13):2234–2247, September 2011.
- [138] Haizheng Zhang, Ravi Seshadri, A. Arun Prakash, Francisco C. Pereira, Constantinos Antoniou, and Moshe E. Ben-Akiva. Improved Calibration Method for Dynamic Traffic Assignment Models. Transportation Research Record: Journal of the Transportation Research Board, 2667:142–153, January 2017.
- [139] K. Zhang and A. J. Gasiewski. Microwave CubeSat fleet simulation for hydrometric tracking in severe weather. In 2016 IEEE International Geoscience and Remote Sensing Symposium (IGARSS), pages 5569–5572, July 2016.
- [140] Kun Zhang and Albin J. Gasiewski. Multiband Simulations of Multistream Polarimetric Microwave Radiances Over Aspherical Hydrometeors. Journal of Geophysical Research: Atmospheres, 123(22):12,738–12,761, November 2018.
- [141] J. M. Ziman. Elements of advanced quantum theory. Cambridge U.P, London, 1969.

## Appendix A

### Example Input Files for DDSCAT v7.3.1

An external file *ior-266K.dat* is created to specify the refractive index of ice for OpenSSP frozen hydrometeors based on the Warren and Brandt 2008 model [132]. This file is used in the simulations of microwave radiances based on the OpenSSP database as well as in the UMRT Mie scattering calculations for a spherical shaped ice particle. The file is constructed in three data columns. Each data row contains the real and imaginary part of the complex refractive index of ice at a discrete wavelength in microns. A portion of the file *ior-266K.dat* corresponding to the microwave frequencies from 10 GHz to 1 THz (i.e. wavelength between  $\sim 30,000 - 300 \mu m$ ) is shown below. DDSCAT v7.3.1 code performs linear interpolation for any microwave frequency not shown in the table.

<i>Wavelength(um)</i>	<i>Re(n)</i>	<i>Im(n)</i>
$3.000E + 002$	1.7989	$2.549E - 002$
$5.000E + 002$	1.7908	$1.405E - 002$
$1.300E + 003$	1.7868	$5.173E - 003$
$5.000E + 003$	1.7861	$1.337E - 003$
$1.900E + 004$	1.7861	$3.574E - 004$
$3.900E + 004$	1.7861	$1.839E - 004$

A parameter file named *ddscat.par* is required for each execution of the program *ddscat*. The file specifies the parameters for the discrete dipole algorithm, the initial memory allocation, the

target geometry and composition, wavelength, the incident and scattered directions, and the target orientations etc. An itemized explanation of this parameter file can be found in the user guide of DDSCAT v7.3.1 (<http://ddscat.wikidot.com/user-guide>).

We have modified the parameter file so that DDSCAT v7.3.1 writes out the scattering parameters as needed for: 1) dual-polarization, 2) each target orientation, 3) the orientational average of  $18 \times 19 \times 18$  random orientations over three Eulerian angles, 4) nine upper triangle elements of the Stokes matrix except  $S_{44}$  (following the Stokes matrix notation of Bohren and Huffman [12]), and 5) the scattering plane at  $\phi = 0$ . An example of modified portion of a *ddscat.par* file is shown below.

---

```

***** Define Incident Polarizations *****
2 = IORTH (=1 to do only pol. state e01; =2 to also do orth. pol. state)
***** Specify which output files to write *****
1 = IWRKSC (=0 to suppress, =1 to write '.sca' file for each target orient.
***** Specify Target Rotations *****
0.0 360.0 18 = BETAMI, BETAMX, NBETA (beta=rotation around a1)
0.0 180.0 19 = THETMI, THETMX, NTHETA (theta=angle between a1 and k)
0.0 360.0 18 = PHIMIN, PHIMAX, NPHI (phi=rotation angle of a1 around k)
***** Select Elements of S Matrix to Print *****
9 = NSMELTS = number of elements of S to print (not more than 9)
11 12 13 14 22 23 24 33 34 = indices ij of elements to print
***** Specify Scattered Directions *****
1 = NPLANES = number of scattering planes
0.0 0.0 180.0 1.0 = phi, thetamin, thetamax, dtheta (deg) for the plane

```

---

## Appendix B

### Transition Matrix Symmetry Induced by Block-diagonal Stokes Matrix

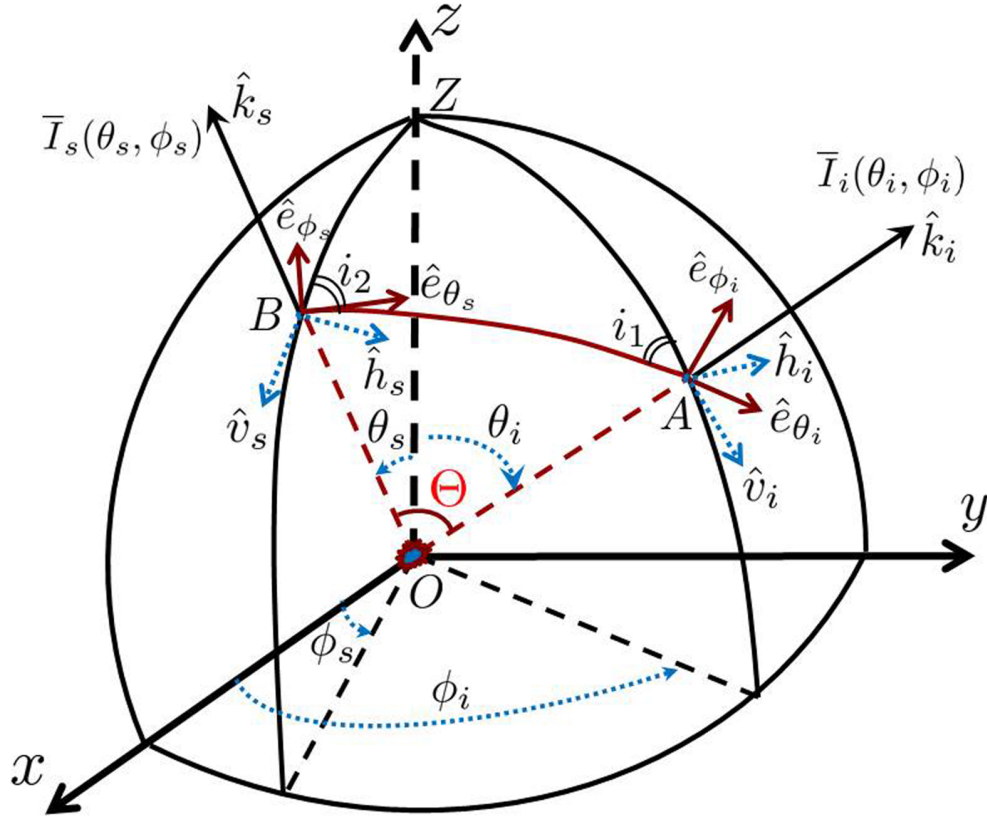


Figure B.1: Geometry of the scattering problem by a single aspherical particle with random orientations at origin. The incident wave propagates along  $\hat{k}_i$  defined by  $(\theta_i, \phi_i)$  and the scattered wave along  $\hat{k}_s$  defined by  $(\theta_s, \phi_s)$  is considered. The forward scattering angle  $\Theta$  is defined in a scattering plane spanned by  $\hat{k}_i$  and  $\hat{k}_s$ . The polarization vectors of the incident and the scattered wave in the scattering plan are drawn in red arrows.

The Stokes matrix in the block-diagonal form of (3.27) relates the incident and scattered



radiations in the scattering plane of OAB shown in Figure B.1. In order to connect the incident radiation  $\bar{I}_i(\theta_i, \phi_i)$  to the scattered one  $\bar{I}_s(\theta_s, \phi_s)$ , two rotation matrices are needed [89, 117]:  $\bar{\bar{R}}(-i_1)$  rotates the incident polarization components of  $(\hat{v}_i, \hat{h}_i)$  from the plane of OAZ to OAB in the counter-clockwise direction with respect to an observer looking into  $\hat{k}_i$  and coincides with the polarization components of  $(\hat{e}_{\theta_i}, \hat{e}_{\phi_i})$ ;  $\bar{\bar{R}}(\pi - i_2) = \bar{\bar{R}}(-i_2)$  rotates the scattered polarization components of  $(\hat{e}_{\theta_s}, \hat{e}_{\phi_s})$  from OAB to OBZ in the clockwise direction with respect to an observer looking into  $\hat{k}_s$  and aligns with  $(\hat{v}_s, \hat{h}_s)$ .

$$\bar{\bar{R}}(-i_{1,2}) = \begin{bmatrix} \cos^2 i_{1,2} & \sin^2 i_{1,2} & 0.5 \sin 2i_{1,2} & 0 \\ \sin^2 i_{1,2} & \cos^2 i_{1,2} & -0.5 \sin 2i_{1,2} & 0 \\ -\sin(2i_{1,2}) & \sin(2i_{1,2}) & \cos(2i_{1,2}) & 0 \\ 0 & 0 & 0 & 1 \end{bmatrix} \quad (\text{B.1})$$

where  $i_1$  is the spherical surface angle between OAZ and OAB,  $i_2$  is the spherical surface angle between OAB and OBZ. The relation of  $\bar{I}_i(\theta_i, \phi_i)$  and  $\bar{I}_s(\theta_s, \phi_s)$  can thus be found in (B.2).

$$\begin{aligned} \bar{I}_s(\theta_s, \phi_s) &= \langle \bar{L} \rangle_o(\theta_s, \theta_i, \Delta\phi) \bar{I}_i(\theta_i, \phi_i) \\ &= \bar{\bar{R}}(-i_2) \langle \bar{L} \rangle_o(\Theta) \bar{\bar{R}}(-i_1) \bar{I}_i(\theta_i, \phi_i) \end{aligned} \quad (\text{B.2})$$

where  $\Delta\phi = \phi_i - \phi_s$ , and  $\Theta$ ,  $i_1$ , and  $i_2$  are functions of the incident and scattering angles  $(\theta_s, \theta_i, \Delta\phi)$  [89, 90, 117, 122],

$$\begin{aligned} \cos \Theta &= \cos \theta_s \cos \theta_i + \sin \theta_s \sin \theta_i \cos \Delta\phi \\ \cos i_1 &= \frac{-\cos \theta_s + \cos \theta_i \cos \Theta}{\sin \theta_i \sin \Theta} \\ \cos i_2 &= \frac{-\cos \theta_i + \cos \theta_s \cos \Theta}{\sin \theta_s \sin \Theta} \end{aligned} \quad (\text{B.3})$$

Applying the Stokes matrix (3.27) to (B.2) and integrating  $\langle \bar{L} \rangle_o(\theta_s, \theta_i, \Delta\phi)$  with respect to  $\Delta\phi$  over  $2\pi$ , two symmetric relations regarding the change of  $\theta_i$  and  $\theta_s$  are subsequently determined,

$$\langle \bar{L} \rangle_o(-\theta_s, -\theta_i) = \bar{\Delta}_{34} \langle \bar{L} \rangle_o(\theta_s, \theta_i) \bar{\Delta}_{34} \quad (\text{B.4})$$

$$\langle \bar{L} \rangle_o(\theta_i, \theta_s) = \bar{C}_1^{-1} \langle \bar{L} \rangle_o^T(\theta_s, \theta_i) \bar{C}_1 \quad (\text{B.5})$$

where the superscript  $T$  denotes the matrix transpose,

$$\overline{\overline{C}}_1 = \text{diag}\{2, 2, -1, 1\}, \quad (\text{B.6})$$

and

$$\overline{\overline{\Delta}}_{34} = \text{diag}\{1, 1, -1, -1\}. \quad (\text{B.7})$$

The relation of (B.4) shows that the first  $2 \times 2$  sub-matrix along the diagonal are unchanged to the simultaneous change of the sign of  $\theta_i$  and  $\theta_s$ . The other relation of (B.5) shows that the diagonal elements of  $\langle \overline{\overline{L}} \rangle_o(\theta_s, \theta_i)$  are unaltered due to the interchange of  $\theta_i$  and  $\theta_s$ , and  $\langle L_{vh} \rangle_o(\theta_s, \theta_i) = \langle L_{hv} \rangle_o(\theta_i, \theta_s)$ . Discretizing the relations of (B.4) and (B.5) into multiple quadrature angles and considering the first two Stokes parameters, it's straightforward to show that the transition matrix symmetry requirements (3.24) and (3.25) are fulfilled.

## Appendix C

### Small Valued Asymmetric Components of the OpenSSP Stokes Matrix

A method based on DDSCAT v7.3.1 code implementation [24] is elaborated in this section for directly calculating the complex  $2 \times 2$  scattering function matrix of a particle and then deriving the full Stokes matrix,  $\overline{\overline{L}}(\theta_s, \phi_s, \theta_i, \phi_i; D, i_s, \beta, \Theta, \Phi)$ , at a particular orientation determined by three Eulerian angles  $\beta$ ,  $\Theta$ , and  $\Phi$ . The method is developed to calculate the full Stokes matrix in a single execution, not limited to the maximum of 9 elements as DDSCAT v7.3.1 does. Furthermore, the method is applicable for averaging Stokes matrix elements over either uniform or preferential orientation distribution. In this study, the method is used to provide an empirical validation that the random orientation-averaged Stokes matrix of an arbitrary OpenSSP hydrometeor exhibits small deviation from the required symmetry of (3.24) and (3.25) due to the relatively small value of the asymmetric component  $\langle \overline{\overline{L}} \rangle_{o, \text{asym}}(\theta_s, \theta_i)$  (3.28).

It has been found that DDSCAT code cannot directly estimate the full Stokes matrix of a particle at a given orientation,  $\overline{\overline{L}}(\theta_s, \phi_s, \theta_i, \phi_i; D, i_s, \beta, \Theta, \Phi)$ , defined in a primary coordinate system as shown in Figure B.1, due to the restriction that the propagation direction of the incident wave is fixed to be one of the coordinate axes in DDSCAT framework. In the primary coordinates, the incident wave propagation direction and polarization vectors form an orthonormal system and are

defined in (C.1). The orthonormal system of the scattered wave is defined similarly.

$$\begin{aligned}
\hat{k}_i &= \sin \theta_i \cos \phi_i \hat{x} + \sin \theta_i \sin \phi_i \hat{y} + \cos \theta_i \hat{z} \\
\hat{h}_i &= \frac{\hat{k}_i \times \hat{z}}{|\hat{k}_i \times \hat{z}|} = \sin \phi_i \hat{x} - \cos \phi_i \hat{y} \\
\hat{v}_i &= \hat{h}_i \times \hat{k}_i \\
&= -\cos \theta_i \cos \phi_i \hat{x} - \cos \theta_i \sin \phi_i \hat{y} + \sin \theta_i \hat{z}
\end{aligned} \tag{C.1}$$

The particle orientation is defined using three unit vectors  $(\hat{a}_1, \hat{a}_2, \hat{a}_3)$  described by three Eulerian angles  $(\beta, \Theta, \Phi)$  [24].

$$\begin{aligned}
\hat{a}_1 &= \cos \Theta \hat{x} + \sin \Theta \cos \Phi \hat{y} + \sin \Theta \sin \Phi \hat{z} \\
\hat{a}_2 &= -\sin \Theta \cos \beta \hat{x} + (\cos \Theta \cos \Phi \cos \beta - \sin \Phi \sin \beta) \hat{y} \\
&\quad + (\cos \Theta \sin \Phi \cos \beta + \cos \Phi \sin \beta) \hat{z} \\
\hat{a}_3 &= \sin \Theta \sin \beta \hat{x} - (\cos \Theta \cos \Phi \sin \beta + \sin \Phi \cos \beta) \hat{y} \\
&\quad - (\cos \Theta \sin \Phi \sin \beta - \cos \Phi \cos \beta) \hat{z}
\end{aligned} \tag{C.2}$$

It is recognized that DDSCAT solves the single-scattering problem in the coordinates of  $(\hat{k}_i, \hat{v}_i, \hat{h}_i)$  shown in Figure C.1 (a) and computes the complex scattering function matrix in (C.3) based on the coordinate-transformed particle orientation  $(\beta', \Theta', \Phi')$  and the forward scattering angles  $(\theta', \phi')$  as shown in (C.4) and (C.5), respectively.

$$\begin{bmatrix} \overline{E}_s(\vec{r}) \cdot \hat{e}_{\theta_s} \\ \overline{E}_s(\vec{r}) \cdot \hat{e}_{\phi_s} \end{bmatrix} = \frac{e^{-jkr}}{r} \begin{bmatrix} \tilde{f}_{\theta v} & \tilde{f}_{\theta h} \\ \tilde{f}_{\phi v} & \tilde{f}_{\phi h} \end{bmatrix} \begin{bmatrix} \overline{E}_i(\vec{r}) \cdot \hat{v}_i \\ \overline{E}_i(\vec{r}) \cdot \hat{h}_i \end{bmatrix} \tag{C.3}$$

$$\begin{aligned}
\Theta' &= \arccos(\hat{a}_1 \cdot \hat{k}_i) \\
\Phi' &= \operatorname{atan2}(\hat{a}_1 \cdot \hat{h}_i, \hat{a}_1 \cdot \hat{v}_i) \\
\beta' &= \operatorname{atan2}(\hat{a}_3 \cdot \hat{k}_i, -\hat{a}_2 \cdot \hat{k}_i)
\end{aligned} \tag{C.4}$$

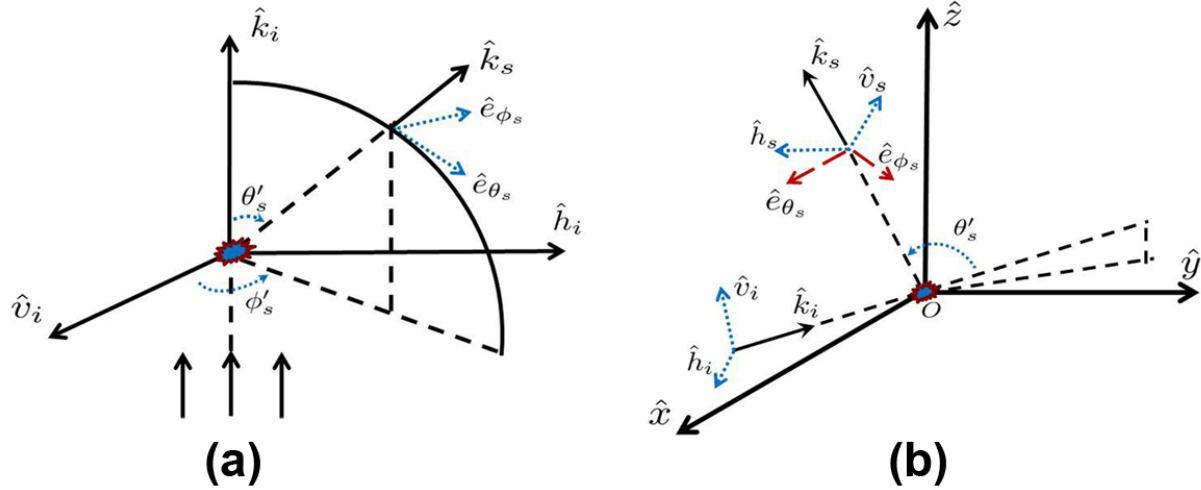


Figure C.1: Scattering coordinate system wherein DDSCAT computes complex scattering function matrix. (a) Forward scattering angles ( $\theta'$ ,  $\phi'$ ) and the particle orientation ( $\beta'$ ,  $\Theta'$ ,  $\Phi'$ ) are redefined in a forward scattering coordinate system. (b) Transform of DDSCAT-based scattered electric fields (dashed arrows) into the required scattered components in vertical and horizontal polarization.

$$\begin{aligned}\theta'_s &= \text{acos}(\hat{k}_s \cdot \hat{k}_i) \\ \phi'_s &= \text{atan2}(\hat{k}_s \cdot \hat{h}_i, \hat{k}_s \cdot \hat{v}_i)\end{aligned}\quad (\text{C.5})$$

The polarization unit vectors ( $\hat{e}_{\theta_s}, \hat{e}_{\phi_s}$ ) of the scattered electric fields illustrated in Figure C.1 (b) are further transformed into the vertical and horizontal polarization components ( $\hat{v}_s, \hat{h}_s$ ) through a transformation matrix found in (C.6).

$$\begin{bmatrix} \overline{E}_s(\vec{r}) \cdot \hat{v}_s \\ \overline{E}_s(\vec{r}) \cdot \hat{h}_s \end{bmatrix} = \begin{bmatrix} \hat{e}_{\theta_s} \cdot \hat{v}_s & \hat{e}_{\phi_s} \cdot \hat{v}_s \\ \hat{e}_{\theta_s} \cdot \hat{h}_s & \hat{e}_{\phi_s} \cdot \hat{h}_s \end{bmatrix} \begin{bmatrix} \overline{E}_s(\vec{r}) \cdot \hat{e}_{\theta_s} \\ \overline{E}_s(\vec{r}) \cdot \hat{e}_{\phi_s} \end{bmatrix}\quad (\text{C.6})$$

Bringing (C.3) into (C.6), the complex scattering function matrix  $\overline{\overline{F}}(\theta_i, \phi_i, \theta_s, \phi_s; \beta, \Theta, \Phi)$  relating the incident electric field to the scattered field is found in (C.7). It is computed as a multiplication of two matrices: the first is determined by the scattering geometry and the second is provided by

DDSCAT.

$$\overline{\overline{F}}(\theta_i, \phi_i, \theta_s, \phi_s; \beta, \Theta, \Phi) = \begin{bmatrix} f_{vv} & f_{vh} \\ f_{hv} & f_{hh} \end{bmatrix} = \begin{bmatrix} \hat{e}_{\theta_s} \cdot \hat{v}_s & \hat{e}_{\phi_s} \cdot \hat{v}_s \\ \hat{e}_{\theta_s} \cdot \hat{h}_s & \hat{e}_{\phi_s} \cdot \hat{h}_s \end{bmatrix} \begin{bmatrix} \tilde{f}_{\theta v} & \tilde{f}_{\theta h} \\ \tilde{f}_{\phi v} & \tilde{f}_{\phi h} \end{bmatrix} \quad (\text{C.7})$$

Applying (C.7) to the definitions of modified Stokes parameters, the Stokes matrix defined in the primary coordinate system is obtained by:

$$\overline{\overline{L}}(\theta_i, \phi_i, \theta_s, \phi_s; \beta, \Theta, \Phi) = \begin{bmatrix} |f_{vv}|^2 & |f_{vh}|^2 \\ |f_{hv}|^2 & |f_{hh}|^2 \\ 2\text{Re}\{f_{vv}f_{hv}^*\} & 2\text{Re}\{f_{vh}f_{hh}^*\} \\ 2\text{Im}\{f_{vv}f_{hv}^*\} & 2\text{Im}\{f_{vh}f_{hh}^*\} \\ \text{Re}\{f_{vv}f_{vh}^*\} & -\text{Im}\{f_{vv}f_{vh}^*\} \\ \text{Re}\{f_{hv}f_{hh}^*\} & -\text{Im}\{f_{hv}f_{hh}^*\} \\ \text{Re}\{f_{vv}f_{hh}^* + f_{vh}f_{hv}^*\} & -\text{Im}\{f_{vv}f_{hh}^* - f_{vh}f_{hv}^*\} \\ \text{Im}\{f_{vv}f_{hh}^* + f_{vh}f_{hv}^*\} & \text{Re}\{f_{vv}f_{hh}^* - f_{vh}f_{hv}^*\} \end{bmatrix} \quad (\text{C.8})$$

Finally, the reduced Stoke matrix as a function of  $(\theta_s, \theta_i)$  is obtained by averaging over all possible orientations based on a specific orientation distribution, followed by azimuthal average over  $2\pi$ . For the case of random orientations, it's straightforward to average Stokes matrix using composite Simpson's rule.

The above method was applied to 60 representative snow aggregates selected from the OpenSSP database at a frequency of 118.75 GHz. For each selected aggregate, the Stokes matrix  $\overline{\overline{L}}(\theta_s, \phi_s, \theta_i, \phi_i; D, i_s, \beta, \Theta, \Phi)$  is discretized over 16 Gauss-Legendre quadrature elevation angles, 24 uniformly-sampled azimuthal angles, and 1,008 discrete random orientations (i.e. uniformly sampled over  $\beta$ ,  $\Theta$ , and  $\Phi$  with  $30^\circ$  spacing). The degree of symmetry of orientation-averaged Stokes matrix is evaluated by the fractional errors between two pairs of matrices (C.9) with simultaneous permutation

of angular indexes and up-/down-welling indexes.

$$\begin{aligned}\langle \bar{L} \rangle_o(\theta_s, \theta_i; D, i_s) &\stackrel{?}{=} \langle \bar{L} \rangle_o^T(\theta_i, \theta_s; D, i_s) \\ \langle \bar{L} \rangle_o(\theta_s, \theta_i; D, i_s) &\stackrel{?}{=} \langle \bar{L} \rangle_o(\pi - \theta_s, \pi - \theta_i; D, i_s)\end{aligned}\tag{C.9}$$

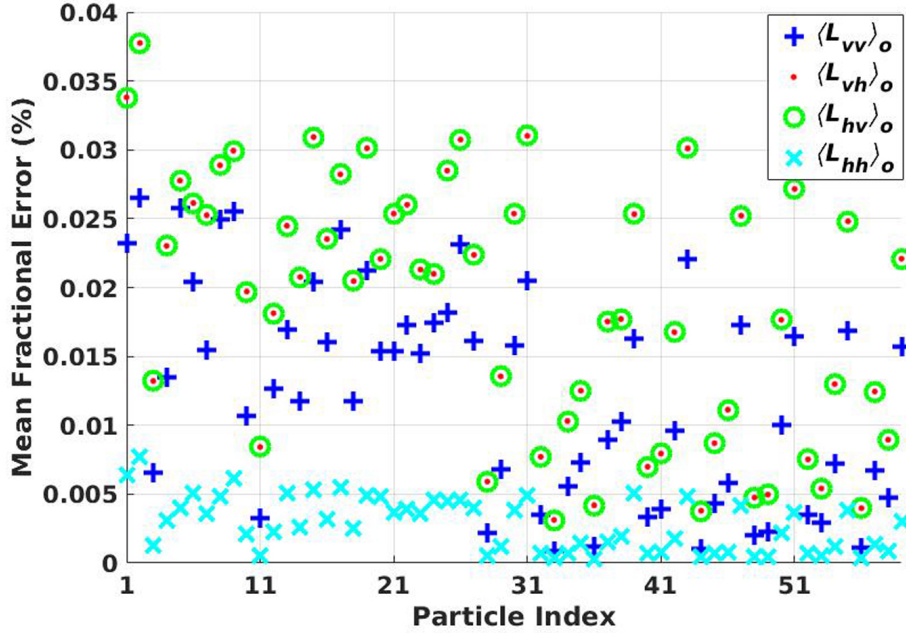


Figure C.2: Mean fractional errors between the pairs of Stokes matrix elements with simultaneous permutation of angular and up-/down-welling indexes.

Figure C.2 shows that the mean fractional errors over all possible permutations of 16 discrete elevation angles are limited to  $< 4 \times 10^{-4}$ , which have general agreement with the analytic analysis of Stokes matrix structure for OpenSSP hydrometeors in section 2.2. The impact of such small relative errors on the computed dual-polarization radiances becomes negligible based on the transition matrix perturbations analysis to the DRTE in (3.17).

## Appendix D

### Calculations of Atmospheric Prognostic Variables Based on WRF Simulations

The WRF v3.5 model is used to simulate atmospheric state vectors of intensified hurricane Sandy over north Atlantic Ocean near the coastal area of New York City between October 28th, 2012 and October 30th, 2012. State variables in WRF outputs are defined on the C grid (see Figure D.1) based on horizontal and vertical staggering [111].

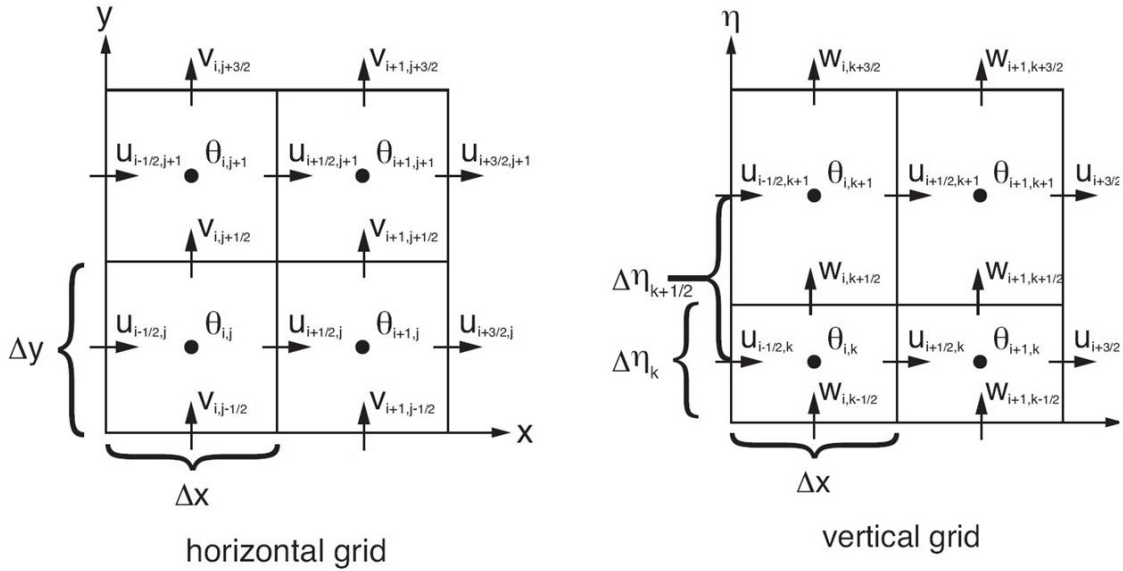


Figure D.1: Horizontal and vertical grids of the WRF (known as the C grid) where thermodynamic and hydrometeor state variables  $\theta_{ij}$  are defined at the center of the grid cell, and the components of winds ( $U_{ij}$ ,  $V_{ij}$ ,  $W_{ij}$ ) are defined along the normal cell face.  $\Delta x$  and  $\Delta y$  are the east-west resolution and the north-south resolution of the grid (respectively). The vertical grid length  $\Delta \eta$  is not a constant and is specified in the WRF model initialization.

Prognostic variables of interest in this thesis are: 1) the level height in meters, 2) the level



temperature in Kelvins, 3) Pressure in mb, 4) water vapor bulk density in  $g/m^3$ , and 5) five-phase hydrometeor bulk density in  $g/m^3$ . These variables can be computed based on the WRF output defined at the grid cell center (see Figure D.2).

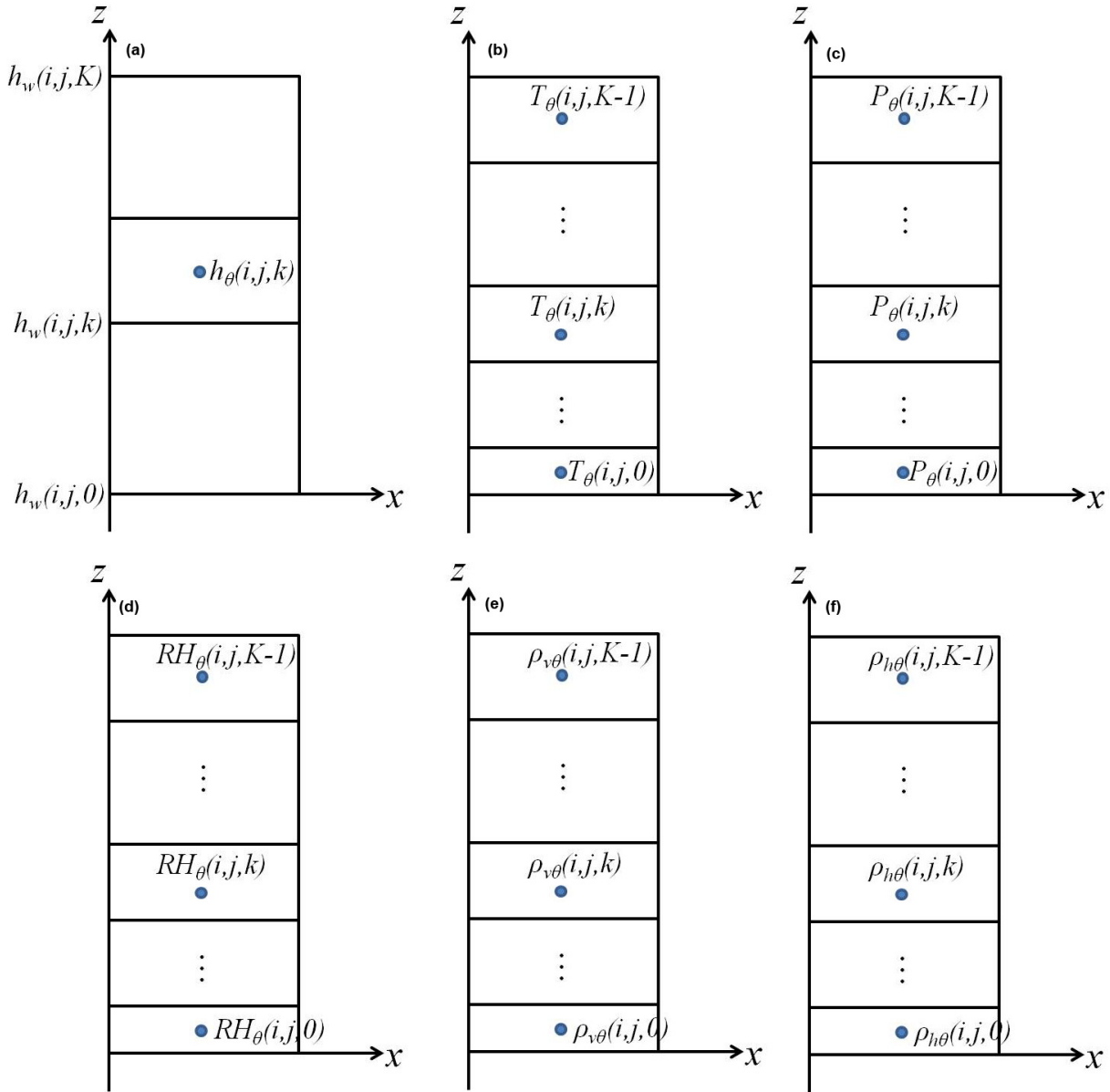


Figure D.2: Atmospheric state variables defined at the center of the WRF grid cell. (a) height in meters, (b) temperature in Kelvins, (c) pressure in mb, (d) relative humidity in %, (e) water vapor density in  $g/m^3$ , and (f) hydrometeor bulk density in  $g/m^3$ .

The height of the grid cell center can be calculated using the base-state geopotential and

perturbation geopotential defined at the upper and lower cell face:

$$\begin{aligned} h_w(i, j, k) &= (\text{PHB}(i, j, k) + \text{PH}(i, j, k)) / G \\ h_\theta(i, j, k) &= \frac{1}{2}(h_w(i, j, k) + h_w(i, j, k + 1)) \end{aligned} \quad (\text{D.1})$$

where  $\text{PHB}(i, j, k)$  is the base-state geopotential defined at variable locations with the variable indices  $(i, j, k)$ ,  $\text{PH}(i, j, k)$  is the perturbation geopotential in the unit of  $m^2/s^2$ , and  $G$  is the standard Earth's gravity (i.e.  $9.81m/s^2$ ). Note that the terrain height is calculated as  $h_w(i, j, 0)$ .

The temperature at the grid cell center can be calculated by:

$$T_\theta(i, j, k) = \theta_{t_o} \left( \frac{P}{P_o} \right)^{R/C_p} \quad (\text{D.2})$$

where  $\theta_{t_o}$  is the potential temperature for air and  $P$  is the total pressure. Both quantities are calculated by WRF.  $P_o = 1000mb$  is the standard reference pressure,  $R = 287.0 J K g^{-1} K^{-1}$  is the specific gas constant of dry air, and  $C_p$  is the specific heat capacity at a constant pressure.

The relative humidity RH is defined as the ratio of the vapor pressure  $e$  and the saturation vapor pressure  $e_s(T)$ , which is determined by temperature  $T$  alone. The saturation vapor pressure  $e_s(T)$  can be estimated by the Goff-Gratch equation which is reliable in a range of  $-50^\circ$  to  $102^\circ$  [101]. The saturation vapor pressure over liquid water  $e_{sw}$  is given by the Goff-Gratch equation:

$$\begin{aligned} \log(e_{sw}) &= -7.90298(373.16/T - 1) + 5.02808 \log(373.16/T) \\ &\quad -1.3816 \times 10^{-7} (10^{11.344(1-T/373.16)-1}) \\ &\quad + 8.1328 \times 10^{-3} (10^{-3.49149(373.16/T-1)} - 1) + \log(1013.246) \end{aligned} \quad (\text{D.3})$$

The corresponding saturation mixing ratio  $Q_{vs}$  can thus be found as:

$$Q_{vs} = \epsilon \frac{e_{sw}}{P - e_{sw}} \approx 0.622 \frac{e_{sw}}{P - e_{sw}} \quad (\text{D.4})$$

The relative humidity is obtained using the water vapor mixing ratio  $Q_v$  calculated by WRF and the saturation mixing ratio  $Q_{vs}$ :

$$\text{RH} = \frac{100Q_v}{Q_{vs}} \quad (\text{D.5})$$

The water vapor density  $\rho_v$  in  $g/m^3$  can be obtained as:

$$\rho_v = \frac{RH e_{sw}}{R_v T} \quad (D.6)$$

where  $R_v = 0.4615 J g^{-1} K^{-1}$  is the individual gas constant for water vapor.

Finally, hydrometeor densities for cloud liquid water, rain, cloud ice, snow, and graupel can be calculated as the ratio of hydrometeor mixing ratio and water vapor mixing ratio:

$$\rho_h = \frac{Q_h}{Q_v} \rho_v \quad (D.7)$$

where  $Q_h$  is the hydrometeor mixing ratio calculated by WRF for cloud  $Q_{cl}$ , rain  $Q_r$ , cloud ice  $Q_i$ , snow  $Q_s$  and graupel  $Q_g$ .